



DOKTORARBEIT

**Simulating Palaeolithic Human Dispersal
Using Human Existence Potential and
Constrained Random Walk Model**

Inaugural-Dissertation zur Erlangung des Doktorgrades
der Mathematisch-Naturwissenschaftlichen Fakultät
der Universität zu Köln,

vorgelegt von

Konstantin Klein

aus Köln,
Deutschland.

Köln, der 04.10.2021.

Berichterstatter/ Gutachter: Prof. Dr. Yaping Shao
Jun.-Prof. Dr. Andreas Maier
Prof. Dr. Gerd-Christian Weniger

Vorsitz der Prüfungskommission: Prof. Dr. Martin Melles

Beisitzer: Dr. Cendrick Ansorge

Disputationstermin: 22.12.2021

UNIVERSITY OF COLOGNE

*Abstract*Faculty of Mathematics and Natural Sciences
Institute for Geophysics and Meteorology

Doctor of Philosophy

**Simulating Palaeolithic Human Dispersal Using Human Existence
Potential and Constrained Random Walk Model**

by Konstantin KLEIN

Our knowledge regarding the history of mankind and the way that led us from Africa to Europe shows gaps in time and space, despite intensive research. Archaeological discoveries, genetic analyzes or dating provide novel results, which, however, do not always fit into the assumed migration process and cause controversy. To estimate the settlement in regions and time periods without archaeological information or to test hypotheses, numerical human dispersal models can provide answers. The expansion of the Paleolithic hunter-gatherers is a complex and non-linear process influenced by many factors, such as environmental conditions, resource occurrences, population sizes, social components like conflict or exchange, or the presence of other species. One crucial factor for the dispersal is the climate, which determines the living conditions of humans as well as food and water resources. For the quantitative evaluation of the settlement and spread of Paleolithic hunter-gatherers, two numerical models are developed, the Human Existence Potential (HEP) and the Constrained Random Walk Model (CRWM).

The HEP allows a static analysis of the habitats of a human culture under climatic and environmental conditions. By using logistic regression, archaeological and climatic data are combined in order to determine a spatial potential for settlement. The HEP is then adjusted by the environmental conditions, such as the topography, glaciers or water bodies, which influence the accessibility of the resources. In addition to the spread, the HEP is used to determine contact probabilities and regionalizations, and the influence of climate changes. The CRWM is a dynamic model that simulates the dispersal of populations through the individual movement of humans. The human movement is described by a stochastic differential equation, i.e. it consists of a deterministic drift and a stochastic component. The direction of the drift is determined by the HEP and other humans, whose presence has both positive effects, since they ensure survival, and negative effects, since they consume the available resources. The stochastic movement reflects the individuality and unpredictability of human behavior. In addition, births and deaths are integrated in the CRWM. The likelihood of both depends on the size of the population and the resources available. Both models are calibrated, validated, tested and then applied to case studies.

In a first case study, it is shown that the Solutrean in western Europe were cut off by an environmental barrier from the Epigravettian in eastern Europe during the Last Glacial Maximum. The expansion and contact within the Solutrean took place along the coast of Iberia, with corridors opening up inland in times of favorable climate. Another case study shows that the first phase of immigration into Europe of the modern humans of the Aurignacian came to an end in northern Iberia. The environmental conditions prevented them from spreading further south. The Neanderthals, who

populated the Iberian Peninsula at the time, were well adapted to the environmental conditions there and colonized large areas of Iberia. Due to the climate change caused by an Heinrich event, Neanderthal social networks collapsed. This particularly affected the north and south of Iberia. Assuming the Neanderthals lived in significantly lower population densities than modern humans, the Heinrich event presumably led to a complete extinction of the Neanderthals on the Iberian peninsula. Overall, it can be concluded that the extinction of the Neanderthals in Iberia can be attributed more likely to the effects of an Heinrich event than to the appearance of modern humans.

Acknowledgements

A doctoral thesis is always a collaborative project and this is especially true for this work. First of all, I would like to thank my main supervisor Yaping Shao, who designed the research project, always stood by my side, developed and integrated many ideas and concepts and supported me not only in research but also in my private life. Another important support for my work was the collaboration with Gerd-Christian Weniger, who gave advice on all archaeological questions, developed the archaeological case studies and accompanied and promoted my research from the start.

I would particularly like to highlight the collaboration with Christian Wegener. The discussion that took place on an almost daily basis and the joint development of the Our Way Model was essential for the outcome of our project. Important collaborations were also established with Isabell Schmidt, through whom many ideas were developed and the case study on the Last Glacial Maximum was implemented, and with Patrick Ludwig, who contributed the climate simulations and provided climatological advice.

I would like to specifically highlight the work within the Collaborative Research Center 806 (CRC806) and thank for the fruitful collaborations and the support. Especially the collaborations with Andreas Hense, Andreas Zimmermann, Heiko Limberg, Andreas Maier, Frank Schäbitz, Jürgen Richter, Sven Ulbrich, and all PhD students in the IRTG, actively contributed to the research through discussions and suggestions.

In particular, I would like to thank my colleagues from the Institute for Geophysics and Meteorology, where I was able to spend four wonderful years and who certainly influenced my research in one way or another. Special thanks also go to the employees from the atmospheric modeling group.

Special thanks go to the supervisors of both Graduate Schools: Karin Boessenkool from the Graduate School of Geosciences, and Daniela Holst and Hannah Hartung from the Integrated Research Training Group of the CRC806. You gave us students the structure to complete the doctoral thesis within the given time frame and provided us many occasions to learn new skills and improve ourselves.

Last but not least, I would like to thank the most important people in my life, my family and friends, who accompanied me during my doctoral thesis and who gave me emotional support in difficult phases. Without you I wouldn't have had the persistence and perseverance to finish the work.

Contents

| | |
|---|-----------|
| Acknowledgements | v |
| 1 Introduction and motivation | 1 |
| 1.1 Collaborative Research Center 806 'Our Way to Europe' | 4 |
| 1.1.1 Project E6 | 5 |
| 1.1.2 Our Way Model | 5 |
| 1.2 Human migration modeling | 7 |
| 1.2.1 Species distribution modeling (SDM) | 7 |
| 1.2.2 Agent based modeling (ABM) | 8 |
| 1.2.3 Differential equation modeling (DEM) | 9 |
| 2 HEP in Europe during the LGM | 13 |
| 3 Impact of HE4 on human populations in Iberia (2): HEP | 35 |
| 3.1 Introduction | 36 |
| 3.2 Results | 38 |
| 3.3 Discussion | 40 |
| 3.4 Materials and methods | 42 |
| 3.4.1 Archeological data | 43 |
| 3.4.2 Climate data | 44 |
| 3.4.3 Predictor selection | 44 |
| 3.4.4 Statistical evaluation | 46 |
| 4 Constrained Random Walk Model (CRWM) | 49 |
| 4.1 Introduction | 49 |
| 4.1.1 Human dispersal driven by climatic and environmental conditions | 50 |
| 4.1.2 Stochastic mobility of individuals | 51 |
| 4.1.3 Overpopulation and population clustering | 51 |
| 4.1.4 Population growth and decline | 52 |
| 4.1.5 Outlook | 53 |
| 4.2 Mathematical description of the CRWM: Main equations | 53 |
| 4.2.1 HEP based drift component | 54 |
| 4.2.2 Stochastic component | 55 |
| 4.2.3 Compound equations | 56 |
| 4.3 Parameterization of the main equations | 57 |
| 4.3.1 Drift parameters | 57 |
| 4.3.2 Stochastic parameters | 59 |
| 4.4 Population attractiveness function | 60 |
| 4.4.1 Definition | 60 |
| 4.4.2 Example | 63 |
| 4.5 Birth and death module | 63 |
| 4.5.1 Definition | 65 |
| 4.6 Numerical Implementation | 68 |

| | | |
|----------|---|-----------|
| 4.6.1 | Main equations | 68 |
| 4.6.2 | Gradient | 68 |
| 4.6.3 | Population attractiveness | 69 |
| 4.6.4 | Initial conditions | 71 |
| 4.6.5 | Boundary conditions | 71 |
| 4.7 | Summary | 72 |
| 5 | Calibration and evaluation of the CRWM | 75 |
| 5.1 | Calibration | 75 |
| 5.1.1 | Calibration of the drift component | 75 |
| | Sensitivity of the friction according to D_t | 76 |
| | Calibration of G_d and D_t | 78 |
| 5.1.2 | Calibration of the stochastic component | 80 |
| 5.1.3 | Calibration of the population attractiveness function | 82 |
| | Calibration of η and ϵ | 83 |
| 5.1.4 | Calibration of the birth and death module | 85 |
| | Determination of Δt^{bd} | 87 |
| | Determination of κ | 89 |
| 5.2 | Test and numerical evaluation of the equations of motion | 90 |
| 5.2.1 | Experiment G1 | 90 |
| 5.2.2 | Experiment G2 | 92 |
| 5.2.3 | Experiment G3 | 94 |
| 5.3 | Summary | 95 |
| 6 | Impact of HE4 on human populations in Iberia (2): CRWM | 97 |
| 6.1 | Introduction | 97 |
| 6.2 | Migration of the Aurignacian to the Iberian Peninsula | 97 |
| 6.2.1 | Calibration of Δt^{bd} | 98 |
| 6.2.2 | First experiment: the standard configuration | 99 |
| | Migration over time | 100 |
| | Settlement statistics | 101 |
| | Source and sink regions | 102 |
| | Population flow | 103 |
| 6.2.3 | Parameter testing | 104 |
| | Growth rate r | 105 |
| | Maximal cultural carrying capacity ρ_{max} | 107 |
| | Maximal migration velocity u_{max} and individual mobility σ_u | 108 |
| 6.2.4 | Monte Carlo experiment | 110 |
| | Migration to Iberia | 111 |
| | Impact of the Heinrich Event 4 | 113 |
| 6.2.5 | Summary | 114 |
| 6.2.6 | Discussion | 116 |
| 6.3 | Neanderthals in Iberia during MIS 3 and the effects of an Heinrich Event | 117 |
| 6.3.1 | Moderate population experiment | 118 |
| | Interstadial conditions | 118 |
| | Heinrich event conditions | 120 |
| 6.3.2 | Small population experiment | 122 |
| | Interstadial conditions | 122 |
| | Heinrich event conditions | 124 |
| 6.3.3 | Large population experiment | 126 |
| | Interstadial conditions | 126 |

| | |
|--|------------|
| Heinrich event conditions | 126 |
| 6.3.4 Summary | 128 |
| 6.3.5 Discussion | 129 |
| 7 Discussion | 133 |
| 8 Conclusions and outlook | 137 |
| A Constrained random walk model | 155 |
| A.1 Mathematical definitions | 155 |
| A.1.1 Probability theory | 155 |
| A.1.2 Markov process | 156 |
| A.1.3 Itô stochastic differential equation | 157 |
| A.2 Component equations in spherical coordinates | 158 |
| B Impact of Heinrich Event 4 on human populations in Iberia | 163 |
| B.1 Climate maps | 163 |
| B.2 HEP estimation | 164 |
| B.3 CRWM Iberia | 168 |

List of Figures

| | | |
|-----|--|----|
| 1.1 | Project arrangement of the CRC 806 (from https://www.sfb806.uni-koeln.de/). | 5 |
| 1.2 | Geographical classification of the regional projects of the CRC 806 and regions in which archaeological excavations or geological investigations took place along the routes from Africa to Europe (from https://www.sfb806.uni-koeln.de/). | 7 |
| 3.1 | HEP of the NEA for GI9 (a) and HE4 (b) conditions based on the MP sites (white squares) and the logistic regression coefficients estimated by the GI9 bioclimatic variables. | 38 |
| 3.2 | HEP of the AMHs for GI9 (a, c) and HE4 (b, d) conditions based on all sites of the AUR (AUR All) (a, b) and the sites of the AUR Phase 1 (AUR P1) (c, d) and the logistic regression coefficients estimated by the GI9 bioclimatic variables. | 40 |
| 3.3 | Topographic distributions of the archaeological sites of the Aurignacian (AUR) and Middle Paleolithic (MP); <i>left</i> : topographic height, and <i>right</i> : topographic roughness, i.e. the standard deviation of topography around the site. | 43 |
| 3.4 | Dendrogram correlation cluster of the bioclimatic variables for (a) GI9 and (b) HE4, and separation into climate groups: mean temperature (green), temperature variation (red), daily temperature variation (blue), mean precipitation (magenta), precipitation variation (yellow) and mean dryness (cyan). | 44 |
| 4.1 | Schematic description of the Constrained Random Walk Model (CRWM). Blue colored are the main modules of the CRWM and yellow colored is the model input. | 53 |
| 4.2 | Schematic illustration of the macroscopic drift in one dimension with friction (black line, $\alpha = 1$ and $\gamma = 0.05$) and without friction (green line, $\alpha = 1$ and $\gamma = 0$); depicted are the velocity (top) and the position (bottom) for a constant HEP for 1000 time steps with $u(t_0) = 0$, $x(t_0) = 0$, and $\Delta t = 0.5$. | 56 |
| 4.3 | Population attractiveness function (f_{pa}) defined in Eq. 4.22, based on the population density (ρ) in hms/100 km ² for the parameters $\eta = 1.6$ and $\epsilon = 0.4$ and different cultural carrying capacities (ρ_c). | 62 |
| 4.4 | Theoretical illustration of the effect of the population attractiveness function (f_{pa}) for $\eta = 1.6$, $\epsilon = 0.3$ and $\rho_{max} = 6$ hms/100 km ² , considering a random HEP distribution Φ (<i>top</i>), and a randomly generated population density ρ in [hms/100 km ²] (<i>middle</i>); depicted is the resulting available HEP calculated by $\Phi_{av} = f_{pa} \cdot \Phi$ (<i>bottom</i>). | 64 |
| 4.5 | Framework of the birth and death module. It is determined separately for each grid cell C_{ij} by random variables ζ_{ij} whether a new human is born or a human dies in the CRWM. | 65 |

| | | |
|------|--|----|
| 4.6 | (A) Gaussian probability density $p_\zeta(x)$ with $\mu_\zeta = 1$ and $\sigma_\zeta = 1$ used to estimate the random variable ζ ; the green and grey shaped areas are the probabilities of ζ being either positive, $P(\zeta \geq 0)$, or negative, $P(\zeta < 0)$, respectively. (B) The probabilities $P(\zeta \geq 0)$ and $P(\zeta < 0)$ for different mean values μ_ζ | 66 |
| 4.7 | Mean of the Gaussian distribution $\mu_{\zeta_{ij}}$ (Eq. 4.35) defining the probability density of the random variable ζ_{ij} , determined by the population density (ρ) for a cultural carrying capacity of $\rho_c = 6$ hms/100 km ² . Shown are different realization according to the growth rate r with $\kappa = 1$ | 67 |
| 4.8 | Illustration of the grid of the HEP (Φ) based on the longitude ($\check{\phi}$) and latitude ($\check{\lambda}$) to better understand the numerical calculation of the gradient used to estimate the drift determining the macroscopic mobility of a human H (green diamond). | 69 |
| 4.9 | Definition of the area $A_{i,j}$ of an grid cell used to calculate the population density. | 70 |
| 4.10 | Representation of the boundary conditions used in the CRW model; the black lines show the outer boundary of the research area, HEP values are set to -1 for water bodies. | 72 |
| 5.1 | Input Gaussian HEP and initial position of the human (H) used for calibration and validation of the constrained random walk model. | 76 |
| 5.2 | Examples for the trajectory of human H with initial condition $(\lambda_0, \phi_0) = (2^\circ, 2^\circ)$ and $(u_0, v_0) = (0, 0)$ km/year determined by the drift of the CRWM (Eq. 5.1 and 5.2) for different setups determining the friction of the model as defined in Tab. 5.1 with $u_{max} = 10$ km/yr. Black dots indicate the position of the human in 100 year time steps. Setup (D) delivers the desired results, a calibrated model without large-scale overshooting. | 77 |
| 5.3 | <i>Left:</i> Maximal absolute velocity M as defined in Eq. 5.6 of human H in Fig. 5.1 for different configurations of u_{max} with $D_t = 2$ years. <i>Right:</i> Combined deviation of M from u_{max} for the different u_{max} configurations (2.5, 5, 7.5, and 10 km/yr) as defined in Eq. 5.7. | 79 |
| 5.4 | Absolute velocities for the human H in Fig. 5.1 for different u_{max} with $G_d = 247$ km/yr, $D_t = 2$ yr, and a time period of 500 years. The maximal absolute velocity M for each configuration is specified. | 80 |
| 5.5 | Example of how the stochastic component is validated in the CRWM: 1000 people are randomly distributed around the Gaussian HEP; after an initialization period of 500 years, the distance from the center of the population is evaluated. 34% of the population is located within a 50 km radius from the center, 76% within a 100 km radius, 94% within a 150 km radius and 99% within a 200 km radius. | 81 |
| 5.6 | Percentage of the population which are located inside circles around the center with different radii defined by the individual mobility σ_u of the CRWM run, with $u_{max} = 5$ km/yr. For $\tau = 6$ yr, all four curves exceed the 75% threshold line. | 81 |
| 5.7 | Shape of the population attractiveness function for different values of the parameters η and ϵ , for $\rho_c = \rho_{max} = 6$ humans/100 km ² | 83 |
| 5.8 | Initial positions of the 3000 humans (left) and initial population density (right) of the experiments used to calibrate the parameter η and ϵ of the population attractiveness function. | 84 |

| | | |
|------|--|----|
| 5.9 | Population density averaged over the 100 years of the simulation for the initial setup shown in Fig. 5.8 for different values of the parameters η and ϵ . | 86 |
| 5.10 | Timely mean of the maximal population density per time step based on the population attractiveness function for different setups of η and ϵ . | 87 |
| 5.11 | Calibration of the time interval of the birth and death module (Δt^{bd}). (A) Amount of deaths compared to the total population per year for different Δt^{bd} for the setup as specified in Tab. 5.5 and the Gaussian HEP in Fig. 5.1. The straight line is the mean of the death rate (r_d), disregarding the spinup time. (B) Amount of humans modelled for differently resolved HEP distributions with 0.125° , 0.25° and 0.5° , for different Δt^{bd} , with the setup of Tab. 5.5 by changing ρ_{max} to 10 hms/100 km ² . | 88 |
| 5.12 | Modelled population growth rate r_{mod} for different κ for a chosen growth rate of $r = 0.03 \text{ yr}^{-1}$; the setup of the experiment is taken from Tab. 5.7 for the Gaussian HEP on Fig. 5.1. | 89 |
| 5.13 | 2d Gaussian HEP distribution with 1.25° resolution used for CRWM evaluation, encompassed by a rectangle of simulated water with HEP = -1. | 91 |
| 5.14 | Experiment G1: Test of the macroscopic forces for two humans, H1 (black lines) with initial conditions $\mathbf{x}_1(t_0) = (10^\circ, 10^\circ)$ and $\mathbf{u}_1(t_0) = (0, 0)$, and H2 (yellow lines) with initial conditions $\mathbf{x}_2(t_0) = (10^\circ, 40^\circ)$ and $\mathbf{u}_2(t_0) = (0, 0)$ for 1800 years with $\Delta t = 0.01$, and a Gaussian HEP by switching of the random part of the CRW model. The maximal migration velocity is chosen to be $u_{max} = 3.2 \text{ km/year}$. Shown on the upper figure is the migration trajectory in space. Depicted on the bottom figure is the absolute velocity of both humans (Eq. 5.5) in continuous lines, and the distance from the center at $(25^\circ, 25^\circ)$ (Eq. 5.11) in dashed lines. On both figures the dots indicate 100-yearly time steps. | 92 |
| 5.15 | Experiment G2: Test of the numerical stability of the CRWM for different time increments Δt with $u_{max} = 3.2 \text{ km/year}$ for human H1 of EG1; (A): absolute velocity $ \mathbf{u} $ and (B): distance from center; from 0 – 1500 yr (left) and from 1500 – 3000 yr (right). The right figures illustrate the oscillations around the center of the HEP distribution for different Δt , they are displayed in logarithmic scale. | 93 |
| 5.16 | Experiment G3: Test of CRWM with the model setup as in EG1 for human H1 for similar HEP distributions with different resolutions: in brown, absolute velocity for an HEP with 0.25° resolution; in black, absolute velocity for an HEP with 1.25° resolution, in black dashed, difference of the distance from center of model with HEP 0.25° and HEP 1.25° (eq. 5.14). | 95 |
| 6.1 | Calibration of Δt^{bd} by the death rate (number of deaths in relation to the total population per year) for the AUR migration defined by the setup in Tab. 6.1. r_d is the average death rate, disregarding the initial phase. | 99 |

| | | |
|------|--|-----|
| 6.2 | Dispersal of the humans of the Aurignacian based on the standard configuration (Tab. 6.2). It shows the total number of humans and the population density averaged over the color-coded time periods. The marked periods are in cyan 0 - 1k yrs, in blue 16k - 20k yrs, in red 22k-24k yrs, in yellow 40k - 41k yrs, in green 66.5k - 71k yrs, and in magenta 87k - 100k yrs. | 101 |
| 6.3 | Percentage of time steps (from 16k - 100k) at which the grid points were populated ($\rho_{ij} > 0$) based on the experiment from Tab. 6.2. Grid cells that were populated less than 5% of the time are not shown. . . . | 102 |
| 6.4 | Timely averaged births minus deaths in each grid cell (C_{ij}), while only those time steps are considered at which $\rho_{ij} > 0$. The source and sink regions are indicated by red and blue circles, respectively. | 104 |
| 6.5 | Population flow calculated by the sum of the velocities of all humans within a grid cell in $\text{km}/(\text{yr} \cdot 100 \text{ km}^2)$, averaged over the 100k year time period (black arrows); and the HEP of AUR All. | 105 |
| 6.6 | Percentage of time from 16k - 100k yrs in which the regions were populated by humans of the Aurignacian ($\rho > 0$), based on slightly modified experiments of the CRWM to the standard configuration of the 1st experiment (Tab. 6.2) for testing the parameter influence, with the modified parameter is shown in the caption. | 106 |
| 6.7 | Number of humans in the 100k yrs CRWM simulation of the dispersal of the humans of the AUR, for modified experiments to the standard configuration (Tab. 6.2), with the modified parameters being listed in the legends. | 109 |
| 6.8 | Number of humans of the 120 CRWM runs of the Monte Carlo experiment (with different random numbers) based on the setup in Tab. 6.3 (black lines), and the ensemble mean of the 120 runs (yellow line). After 7000 years the HEP changes to the conditions of HE4. | 110 |
| 6.9 | Different time steps of the simulated migration of the AMH to Iberia based on the Monte Carlo experiment with 120 runs and the setup in Tab. 6.3. Shown are the averaged population density at that point in time for all model runs in which the population density of the cells are unequal zero (colored grid cells), and the population spread in percentages of model runs, in black $> 95\%$, in grey $> 75\%$, in cyan $> 50\%$, in magenta $> 25\%$, in pink $> 5\%$ and in green $> 1\%$ (contour lines). . . . | 112 |
| 6.10 | Same as in Fig. 6.9 with times after the HE4. It occurs after 7k years and within 100 years and remains until the end of the 10k year time series. | 114 |
| 6.11 | Number of Neanderthals for the 100 runs of the moderate population experiment, i.e. $\rho_{max} = 5 \text{ hms}/100 \text{ km}^2$ (Tab. 6.4), and the ensemble mean (yellow). The interstadial HEP conditions apply for the first 20k years, these are then changed within 100 years to the HEP conditions of the Heinrich event and simulated for a further 10k years. | 119 |
| 6.12 | Settlement probability and population density of the Neanderthals in Iberia during MIS 3 depending on the 100 runs of the moderate population experiment with the same coloring as in Fig. 6.9. Shown are time segments at the beginning of the experiment, after 1k years, at the steady state of the interglacial conditions, after 20k years, immediately after the onset of the Heinrich event, after 20.2k years, and at the end of the time series, after 30k years. | 120 |

| | | |
|----------|--|-----|
| 6.13 | Settlement dynamics of the Neanderthals represented by the population flow (black arrows) and the coefficient of variation (CoV) of the population density (colored grid cells) averaged over the 100 runs of the moderate population experiment and over the time period (A) of 10k - 20k years (interstadial steady state) and (B) of 25k - 30k years ago (Heinrich event steady state). | 121 |
| 6.14 | Time-averaged births minus deaths per grid cell for the time period of (A) 10,000 - 20,000 years (interstadial steady state) and (B) 25k - 30k years (Heinrich event steady state), averaged over the 100 runs of the moderate population experiment. Pronounced or noticeable source and sink regions are marked with red and blue circles, respectively. | 122 |
| 6.15 | Same as in Fig. 6.11 but for the small population experiment ($\rho_{max} = 4$ hms/100 km ²). | 123 |
| 6.16 | Same as in Fig. 6.12 but for the small population experiment ($\rho_{max} = 4$ hms/100 km ²) | 124 |
| 6.17 | Same as in Fig. 6.13 for the small population experiment ($\rho_{max} = 4$ hms/100 km ²) for the time period (A) 10,000 - 20,000 years (interstadial steady state) and (B) of 25k - 30k years ago (Heinrich event steady state). | 125 |
| 6.18 | Same as in Fig. 6.14 but for the small population experiment ($\rho_{max} = 4$ hms/100 km ²) for (A) 10k - 20k years (interstadial steady state) and (B) 20.2k - 30k years (Heinrich event steady state). | 125 |
| 6.19 | Same as in Fig. 6.11 but only one run and for the large population experiment ($\rho_{max} = 7$ hms/100 km ²) | 127 |
| 6.20 | Timely averaged population density of the large population experiment ($\rho_{max} = 7$ hms/100 km ²) for (A) interstadial conditions, from 10k - 20k years, and (B) Heinrich event conditions, from 25k - 30k years. | 127 |
| 6.21 | Same as in Fig. 6.13 but for only one run and the large population experiment ($\rho_{max} = 7$ hms/100 km ²) and over the time period (A) of 10k - 20k years (interstadial steady state) and (B) of 25k - 30k years ago (Heinrich event steady state). | 128 |
| 6.22 | Same as in Fig. 6.14 but for only one run and the large population experiment ($\rho_{max} = 7$ hms/100 km ²) for (A) 10k - 20k years (interstadial steady state) and (B) 25k - 30k years (Heinrich event steady state). | 128 |
| A.2.1(A) | Change of the unit vector \mathbf{i} according to the longitude λ . (B) Division of $\delta\mathbf{i}$ into the northward and vertical components depending on the latitude ϕ . Both figures are from Holton and Hakim (2013) | 159 |
| A.2.2(A) | Longitudinal change of the unit vector \mathbf{j} . (B) Latitudinal change of unit vector \mathbf{j} . Both figures are from Holton and Hakim (2013) | 160 |
| B.1.1 | Annual mean temperature (Bio1) | 163 |
| B.1.2 | Temperature seasonality (Bio4) | 163 |
| B.1.3 | Precipitation seasonality (Bio15) | 164 |
| B.1.4 | Precipitation of wettest quarter (Bio16) | 164 |
| B.1.5 | Precipitation of driest quarter (Bio17) | 164 |
| B.2.1 | Climatic conditions at the presence and absence points based on the sites distribution of the Aurignacian (AUR All) and Middle Paleolithic (MP) technocomplexes for the GI9 climate simulation. Human presence is considered in a radius of 20 km around each archaeological site, human absence everywhere else. | 165 |

| | |
|--|-----|
| B.2.2MP HEP derived by the bioclimatic variables Bio 1/4/19/15/18 (a) and (b) and Bio 1/4/12/15/18 (c) and (d) for GI9 (a) and (c) and HE4 (b) and (d) estimated by the GI9 bioclimatic variables. Deviation the HEP Bio 1/4/16/15/17 (Fig. 1) from the mean of the three runs for GI9 (e) and HE4 (f). | 166 |
| B.2.3Aur HEP derived by the bioclimatic variables Bio 1/4/19/15/18 (a) and (b) and Bio 1/4/12/15/18 (c) and (d) for GI9 (a) and (c) and HE4 (b) and (d) estimated by the GI9 bioclimatic variables. Deviation the HEP Bio 1/4/16/15/17 (Fig. 1) from the mean of the three runs for GI9 (e) and HE4 (f). | 167 |
| B.3.1Same as in Fig. 6.18b but calculated from 25k - 30k years. | 168 |

List of Tables

| | | |
|-----|---|-----|
| 3.1 | Variance inflation factor (VIF) of the bioclimatic variables from the mean temperature (T mean), temperature variation (T var), mean precipitation (P mean), precipitation variation (P var), and mean dryness (D mean) groups. The upper four factors correspond to the GI9 and the lower ones to the HE4 climate. | 46 |
| 3.2 | Area under a receiver operating characteristics curve (AUC) and Brier skill score (BSS) for the HEP fits shown in Fig. 3.1 and 3.2. | 46 |
| 4.1 | Key parameters of the CRWM. | 73 |
| 5.1 | Experimental setup of Fig. 5.3 to test the friction component of the CRWM. | 77 |
| 5.2 | Calibrated parameters D_t and G_d | 79 |
| 5.3 | Percentage of the population (averaged from years 500 to 1000) that is located within the circle (PiC) with radius r around the HEP center in Fig. 5.1, with a starting population of 1000 humans that are randomly distributed around the center with a Gaussian probability and a standard deviation of 2° . In the CRWM, the parameters u_{max} and σ_u are specified in the table, and $\tau = 6$ yr. | 82 |
| 5.4 | Experimental setup to calibrate the population attractiveness function (f_{pa}). Further parameters are defined as: $D_t = 2$ yrs, $G_d = 247$ km, and $\tau = 6$ yrs. | 84 |
| 5.5 | Experimental setup to calibrate Δt^{bd} in the the birth and death module. | 87 |
| 5.6 | Experimental setup to calibrate κ in the the birth and death module. | 89 |
| 5.7 | Experimental setup to calibrate κ in the the birth and death module. | 90 |
| 5.8 | Experiments with different model setups based on different HEP distributions to evaluate and test the equations of motion. | 90 |
| 5.9 | Order of convergence, error in position and runtime of the CRWM based on the time increment Δt for $u_{max} = 3.2$ km/year. | 94 |
| 6.1 | Experimental setup to calibrate Δt^{bd} for the simulation of the AUR dispersal. | 99 |
| 6.2 | Parameter of the standard configuration to model the Aurignacian dispersal. | 99 |
| 6.3 | Parameters of the Monte Carlo experiment to model the Aurignacian dispersal. | 110 |
| 6.4 | Setup of the three Neanderthal experiments, the moderate population experiment (M), the small population experiment (S) and the large population experiment (L), with T_I being the time frame of the interstadial and T_H the time frame of the Heinrich event, and the other parameters as in Tab. 6.2 | 118 |

List of Abbreviations

| | |
|--------|---|
| ABM | Agent Based Model |
| AMH | Anatomical Modern Human |
| AUC | Area Under the Receiver Operating Characteristics (ROC) Curve |
| AUC | Aurignacian |
| BIO | Bioclimatic variable |
| BP | Before Present |
| BPP | Best Potential Path |
| BSS | Brier Skill Score |
| CoV | Coefficient of Variation |
| CRC806 | Collaborative Research Center 806 |
| CRWM | Constrained Random Walk Model |
| DEM | Differential Equation Model |
| EHC | Environmental Human Catchment |
| GI | Greenland Interstadial |
| GS | Greenland Stadial |
| HDM | Human Dispersal Model |
| HE | Heinrich Event |
| HEP | Human Existence Potential |
| LGM | Last Glacial Maximum |
| MIS | Marine Isotope Stage |
| MP | Middle Paleolithic |
| NEA | Neanderthal |
| PMIP | Paleoclimate Modelling Intercomparison Project |
| SDE | Stochastic Differential Equation |
| SDM | Species Distribution Model |
| VIF | Variance Inflation Factor |
| WRF | Weather Research and Forecasting model |

Chapter 1

Introduction and motivation

The evolution of humans and their spread over the earth, up to the settlement of Europe by modern humans, was a non-linear process of expansion that span over more than a hundred thousand years. Even though much is known about "Our Way to Europe", new archaeological discoveries and research findings often lead to controversies and reinterpretations of history. What seems certain is that the origin of modern humans lies in Africa. Through genetic analysis, the cradle of humankind could be located in South and East Africa ([Ramachandran et al., 2005](#); [Henn et al., 2011](#)). The exact dating of the emergence of modern humans, however, as well as the time of the exodus from Africa and the migration to Europe, are anything but proven facts but rather controversial. For example, a discovery from [Hublin et al. \(2017\)](#) moves the origin of Homo sapiens 100,000 years into the past to 315,000 years before present (BP) and relocates the place of origin from Ethiopia to Morocco. Two published datings of modern humans outside of Africa from Misliya Cave in Israel, dated to 177,000 to 194,000 years BP ([Hershkovitz et al., 2018](#)), and from Apidima Cave in Greece, dated to about 220,000 years BP ([Harvati et al., 2019](#)), were significantly older than previous datings and give rise to speculation. Diverse and interdisciplinary research helps to shed more light on our history. Scientific methods, such as genetic analysis and migration modeling, are gaining relevance in archeology and enabling investigations that were previously not possible. As a result, hypotheses can now be tested and analyzes carried out from time periods and regions in which no archaeological data are available.

Even though our assumptions about history are constantly changing and may continue to do so in the future, it is undisputed that the climate and its changes have a significant influence on humans and their migration. For instance, phases in which the Sahara was green, made it possible to migrate through ([Larrasoña et al., 2013](#)), and phases in which the Bering Strait was glaciated, made the settlement of North America possible in the first place. The climate on our planet is determined by an interplay of processes within and between the atmosphere, cryosphere, lithosphere, biosphere and hydrosphere. The main source of energy and driver of these processes is solar radiation. As shown in geological studies (so-called proxy data) and proven by physics, the climate is subject to constant fluctuations, which can mainly be attributed to changes in solar radiation. Due to the gravitational influences of several orbital bodies, the Earth's movement is not periodic but changes with time. It is thereby characterized by three time-variant parameters, the eccentricity, describing the distance of the Earth's orbit around the sun, the obliquity, the angle between the rotating axis of the Earth and the orbital axis, and the precession, the direction at which the Earth's rotating axis is pointing. Changes in those parameters lead to permanently fluctuating glacial and interglacial periods, the so called Milanchovich cycle ([Berger, 1988](#)).

In addition to this cycle, there have been short-term climatic fluctuations that strongly

shaped the conditions over centuries or millennia, the Dansgaard-Oeschger cycle. This cycle was discovered in the Arctic ice and leads to a constant change of stadials (cold phases) and interstadials (warm phases) as a result of changes in the thermohaline circulation (Dansgaard et al., 1993). In some stadials there were also so-called Heinrich events, in which large icebergs drift into the North Atlantic, melt there and significantly change the climate in Europe for centuries. The change of the climatic phases between glacial and interglacial as well as stadal and interstadial could be classified by proxy data in marine isotope stages. These periods are also mostly used in archeology and assigned to certain archaeological events. Climate changes have differencing effects from region to region (Voelker, 2002) and the effects on humans are not always clear. A milder climate can lead to a deterioration of the conditions for humans. The interaction between climate and humans is anything but trivial and must be viewed both in the overall picture and regionally.

Hunter-gatherers in the Paleolithic lived in close coalescence with their surroundings. The resources they used and consumed were provided by the environment which is for the major part governed by the climate, mainly by the temperature and precipitation. Moreover, humans are very flexible and able to adapt to various environments. Due to this adaptability the anatomical modern human (AMH) managed to populate the whole planet from tropical and subtropical regions at the equator to polar regions close to the poles. The adaptation of AMH to new conditions needed time; the AMH did not populate the Earth all at once. Archaeological findings indicate that the colonization took place in several migration waves (e.g., Bae et al., 2017). In addition to the step-wise migration process of alternating adaptation and exploration phases, humans experienced several phases of precarious conditions that forced them to retreat to refugia or, in extreme cases, led to the extinction of populations (e.g., Bradtmöller et al., 2012). In most cases, these changes in conditions can be correlated to climatic change and subsequent environmental change scenarios (Hublin and Roebroeks, 2009; Morgan, 2009; Hamilton et al., 2016; Grove, 2018; Raia et al., 2020).

In my doctoral thesis, models are developed with which the interaction between humans of the Paleolithic and the climate can be quantified and the migration of the humans can be calculated with climate / environment being the driving factor. The study is interdisciplinary and combines concepts and theories from archeology, anthropology, meteorology and physics. The models developed here are consistent with the repeated replacement model by Bradtmöller et al. (2012) and integrate results from ethnological case studies on hunters-gatherers (mainly from Binford, 2002; Kelly, 2013). Moreover, concepts from fluid dynamics, machine learning and probability theory are used. The results are based on extensive data analysis using archaeological site and climate modeling data. The developed models and presented studies could only be implemented in cooperation with many colleagues, especially from archeology, hence it was very fortunate for me to have written my doctoral thesis in the Collaborative Research Center 806 "Our Way to Europe". Since the work within the CRC806 made the doctoral thesis possible in the first place, the structure and the goals are briefly presented in the following (Sec. 1.1), with a special focus on the project E6 "Palaeoclimate and Palaeoenvironmental Reconstructions Using a Computational Regional Environmental Modeling System and Statistical Methods" in which my doctoral thesis is to be classified. Furthermore, there are of course other studies that have used similar procedures and methods to quantitatively determine the migration of humans and their adaptation to environmental conditions. This includes species distribution models, agent based models and differential equation models, which will be briefly presented below (Sec. 1.2).

The doctoral thesis can roughly be divided into two parts. In the first part the human

existence potential (HEP) is developed, which acts as a driving force in the constrained random walk model (CRWM) developed in the second part. The HEP reflects the adaptation of humans to the given environmental conditions and assigns each region a suitability score that defines the potential settlement. The HEP is calculated using machine learning methods and data from archaeological sites, climate models and environmental reconstructions. The development of the HEP was realized with several colleagues and has already been published, in the paper "Human Existence Potential in Europe during the Last Glacial Maximum" (Klein et al., 2021) which is presented in Chapter 2, in which I am the main author and did the data analysis and wrote a large part of the text. The case study highlights the different adaptations during the LGM of the hunter-gatherers of the Solutrean techno-complex in Western Europe and the Epigravettian techno-complex in Eastern Europe. In addition, through the integration of settlement core areas, it is classified whether regions were continuously populated, such as Franco-Cantabria and the Iberian coast, or only in intermittent phases of changing climate, such as central Iberia or regions close to the Scandinavian Ice Sheet in Eastern Europe. Chapter 3 presents another HEP study from an unpublished manuscript being the basis for the CRWM calculation in Chapter 6. In this manuscript, I am the main author and have carried out the data analysis and written a large part of the text. There, the archaeological history of the Neanderthals on the Iberian Peninsula during Marine Isotope Stage 3 and the immigrating modern humans of the Aurignacian are illuminated and evaluated using the HEP. The adaptation to interstadial conditions and the effects of a Heinrich event on the human populations are examined.

The CRWM is then presented in Chapter 4. In contrast to the static approach of the HEP, in the CRWM the dynamics of populations is determined by simulating the movement and reproduction or death of humans. The HEP is the driving factor that influences both the human movement and the growth or decrease of the population. The CRWM is mainly based on random processes that reflect the individuality of humans as well as the unpredictability of behavior and environmental factors. The human movement is solved mathematically by a stochastic differential equation, so it represents a random walk with a drift in the direction of good HEP conditions. In addition, the population attractiveness function integrates the presence of other humans into the simulated movement. As a result, population clustering occurs, but also the dispersal of humans due to local population pressure is implemented in the CRWM. Whether humans are born or die is treated separately in the model and is a random factor. The probability for this depends on the size of the population and the environmental conditions. The individual model components are introduced conceptually and mathematically in Chapter 4 and the numerical implementation is explained. In addition to the key parameters that significantly determine the outcome of the CRWM, some secondary parameters are defined, which are calibrated in Chapter 5 on the basis of idealized experiments. Care is taken to ensure that the model provides physically as well as archaeologically meaningful and comprehensible results. In addition, in Chapter 5 the model is validated for numerical stability and convergence.

In Chapter 6, an extensive case study of the modern humans of the Aurignacian who immigrated to the Iberian Peninsula and the Neanderthals residing there at the time is carried out with the CRWM. Determined thereby are which areas were potentially populated by the two human species, in which time period the migration took place, where the mobility was particularly high so that there was contact between neighboring settlement areas, and where noticeably many people were born (source regions)

or died (sink regions). Furthermore, the effects of the Heinrich event on the hunter-gatherers of both species who adapted to interstadial conditions is evaluated. Since the CRWM is a stochastic model, the same starting conditions can lead to different results due to random processes. In order to cover all random fluctuations, the simulation time periods in the experiments are chosen to be very long. In addition, a Monte Carlo experiment is carried out for both populations: The same experiment (with identical input parameters) is repeated 100 times and both the ensemble mean of all runs and the deviations are used for the evaluation. Since the choice of parameters has a decisive influence on the results, experiments with different input parameters are carried out for the two populations. For the modern humans of the Aurignacian, the dependency on all key parameters are tested and a Monte Carlo experiment is carried out with a configuration that give realistic results based on the archaeological history. Since the parameter dependencies from the Aurignacian experiments can be transferred to the Neanderthals, the analysis is limited to the parameter "cultural carrying capacities". This parameter defines the size of the population and thus largely determines the results. Three Monte Carlo experiments are carried out with small, moderate and large populations and effects on settlement behavior during interstadial conditions and the effects of the Heinrich event are evaluated.

Finally, Chapter 7 discusses modeling in general and HEP and CRWM in particular. In Chapter 8, the modeling approaches and results are summarized, conclusions are drawn and an outlook on possible follow-up studies and model extensions is given.

1.1 Collaborative Research Center 806 'Our Way to Europe'

The main goal of the CRC 806, which started in 2009 as a joint project of the Universities of Cologne, University Bonn and the RWTH University Aachen, was to bring together experts from various fields in archeology, natural sciences, anthropology and philosophy in order to be able to draw a comprehensive picture of the migration history of modern humans from Africa to Europe. This joined approach resulted in a number of collaborations which led to many sub-projects and interdisciplinary working groups. The general structure of the 3rd phase of the CRC is shown in Fig. 1.1, whereby the projects are divided into regional and superregional groups or assigned to the timelines and central tasks group. The human history in parts of Europe, Africa and the Levant was processed in various regional subgroups through archaeological excavations and analyzes. The superregional systems combined the regional results and placed them in a larger-scale context in terms of space and time. The dating of material were provided by the timeline groups, conceptual and overarching considerations were sought in the central task group.

The natural scientists involved in the CRC provided expertise in the areas of dating (luminescence, radiocarbon, archaeomagnetic), proxy and stratigraphy analyzes and climate modeling. In addition to the climate simulations, terrestrial and aquatic archives were recorded and evaluated in a number of field studies in order to reconstruct the environmental conditions and the climate history along the route to Europe (Figure 1.2). All data that were collected within the CRC were also made available to the public in an online database¹. With the completion of the CRC, it will be remembered as a very successful project after 12 years of research through numerous highly ranked published papers, many organized conferences and workshops, and other outreach activities, such as a jointly written book.

¹<https://crc806db.uni-koeln.de/start/>

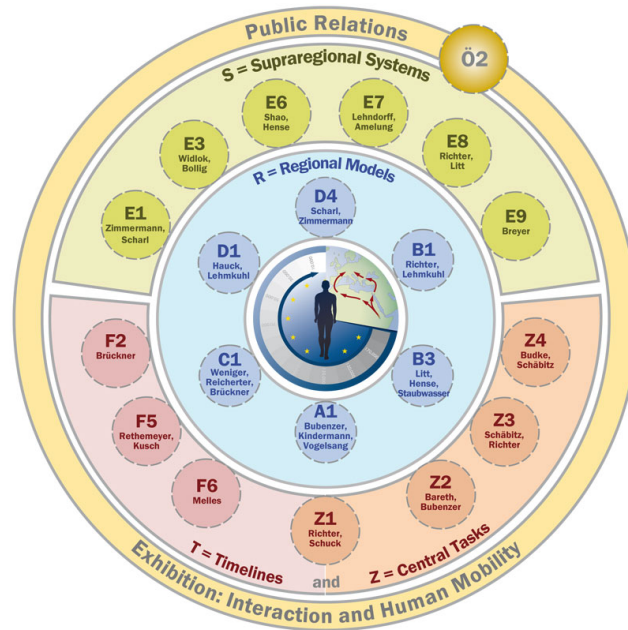


FIGURE 1.1: Project arrangement of the CRC 806 (from <https://www.sfb806.uni-koeln.de/>).

1.1.1 Project E6

My project was embedded in the superregional system E6. The aim of this subsector in the first two phases was to provide reliable climate modeling and environmental data for the CRC study domains to support the research on the movement of the modern humans from Africa to Europe. The research resulted in publications on paleoclimatic conditions (Ludwig et al., 2016, 2017, 2019; Weitzel et al., 2019), aeolian dust transport and loess deposition (Schaffernicht et al., 2019; Nett et al., 2021), and environmental reconstructions (Shao et al., 2018; Miebach et al., 2019). In the further course of the CRC, the focus of the E6 evolved towards the development of numerical models for the dispersal and settlement behavior of early humans, with a special focus on the development of the Our Way Model.

Without the collaboration with many colleagues within the CRC, the work would not have been possible. The collaboration consisted of the exchange of data as well as theories, concepts and hypotheses. An important collaboration arose with the E1 and D4 projects. Through the exchange of many ideas and the integration of the archaeological data, the publication Klein et al. (2021) was created, which is presented in Chapter 2. Another relevant collaboration arose with the C1 project resulting in the unpublished paper presented in Chapter 3 and the case study presented in Chapter 6. Furthermore, many basics for the development of the CRWM were worked out.

1.1.2 Our Way Model

The main goal of our working group in the last phase of the project was to develop a prognostic model for human dispersal. The Our Way Model simulates the dispersal of humans through the combination of the social, biological and climatological dimensions and the integration of concepts from the natural and social sciences. By using archaeological and climate / environment data, the aim is to integrate model and data. With the Our Way Model we are trying to implement a complex model from simple assumptions by combining and integrating multiscale models. The human

dispersal model (HDM) simulates the large-scale expansion of population densities, while the constrained random walk model (CRWM) simulates the mobility of individual humans. Both models are inherent in that they use the human existence potential as the main driving force for migration. The Our Way Model framework is a platform to test archaeological hypotheses, such as the effects of climate change on populations or the adaptations of people to given conditions. Due to the different approaches in relation to scales and times, population dynamics analysis can be carried out and thus the possible reasons for the spread of humans can be studied more profoundly. The Our Way Model is continuously in development and the integration of new data and concepts can significantly improve model performance in the future.

Both the CRWM and the HEP are the subject of this doctoral thesis, so the concept and the functionality of the Our Way Model will be further elaborated in the course of the thesis. The HDM was mainly developed within the doctoral thesis of Christian Wegener and should be briefly mentioned here. The overview is limited to the main components of the model. The dispersal of humans in the HDM is simulated by the two-dimensional Fisher-Kolmogorov Equation of a time-dependent population density ($\rho(x, y)$):

$$\frac{d\rho}{dt} = -\vec{\nabla} \cdot (\vec{v}\rho) + \vec{\nabla} \cdot (K\vec{\nabla}\rho) + B - D, \quad (1.1)$$

with the movement speed and direction $\vec{v}(x, y)$, diffusion coefficient $K(x, y)$, and sources $B(x, y)$ and sinks $D(x, y)$. The equation describes a temporal change in the population density, caused by an advection-governed population migration, a population diffusion and a population growth and decrease. The directional movement, so the migration velocity, is determined by the available human existence potential (Φ):

$$\vec{v}(t_i) = \gamma \vec{\nabla}\Phi, \quad (1.2)$$

with a parameter γ defining the migration speed. The available HEP integrates environmental preferences and population features and is also part of the CRWM and defined in Chapter 2 and Chapter 4. With the cultural carrying capacity calculated from the accessible HEP (Φ_{acc}) and the parameter *maximal cultural carrying capacity* (ρ_{max}):

$$\rho_c = \rho_{max} \cdot \Phi_{acc}, \quad (1.3)$$

the available HEP is calculated using the scaled Weibull function with the scaling parameters C , η and ϵ :

$$\Phi = C \cdot \Phi_{acc} \cdot \left(\frac{\eta}{\epsilon}\right) \cdot \left(\frac{\rho}{\epsilon \cdot \rho_c}\right)^{\eta-1} \cdot \exp\left[-\left(\frac{\rho}{\epsilon \cdot \rho_c}\right)^\eta\right]. \quad (1.4)$$

This implements two processes in Φ : (1) humans who are already in the area reduce the available resources and thus reduce the attractiveness of the area for other humans; and (2) low population densities are unattractive as they make survival much more difficult. Population growth or population decrease is implemented in the model by the following function:

$$B - D = \rho \cdot r_B \cdot \left[3 \exp\left(-\frac{\rho}{2 \rho_c}\right) - 2\right], \quad (1.5)$$

with the parameter *population growth rate* (r_B).

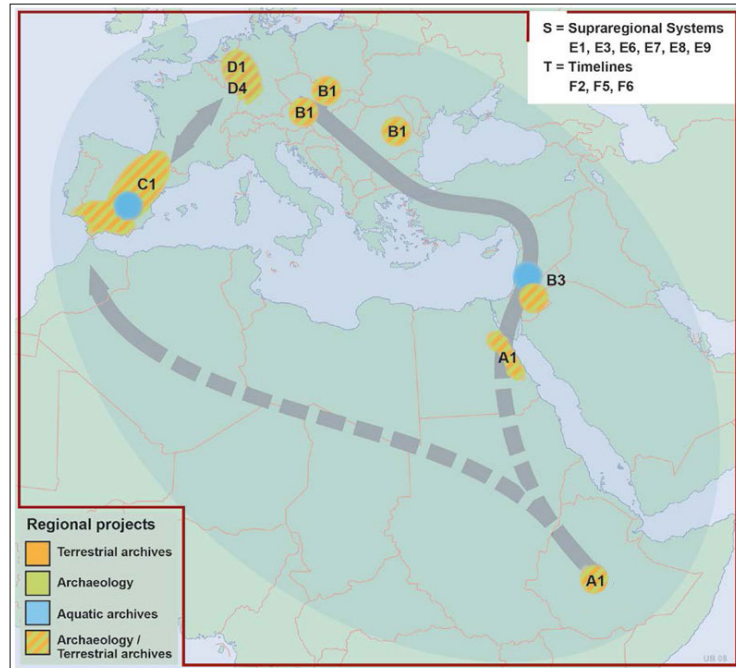


FIGURE 1.2: Geographical classification of the regional projects of the CRC 806 and regions in which archaeological excavations or geological investigations took place along the routes from Africa to Europe (from <https://www.sfb806.uni-koeln.de/>).

1.2 Human migration modeling

In archaeological and anthropological research there were several approaches that dealt with the modeling of human migration. A distinction can be made between two types of modeling, agent-based modeling (ABM) and differential equation modeling (DEM). While the ABM primarily deals with microscale phenomena, the DEM usually acts on the macro scale. The Constrained random walk model developed here can be seen as a kind of interface between the macro and micro scale. There, the movement of individual agents is modeled based on stochastic differential equations, so concepts from both ABM and DEM are integrated. Therefore, a brief overview of the general functionality of ABM and DEM is given here and the latest and most important publications in both areas in the field of archaeology are presented.

The human existence potential is based on concepts from Species Distribution Modeling, in which observation data are coupled with environmental and climatic data using machine learning methods in order to obtain a prediction of the spatial distribution of the species. The concept of the modeling and studies in the field of archeology are also presented below.

1.2.1 Species distribution modeling (SDM)

The so-called species distribution modeling (SDM), also known as habitat suitability, ecological niche or climate envelope modeling is a tool from the field of biology for determining the distribution and adaptation of species in an environment. The aim of the models is to determine a relationship between local data points or observations and environmental data, convert it into a score and extrapolate it onto a map. The environmental data can be of a climatic or topographical nature, whereby in many studies so-called bioclimatic variables are used, covering the mean temperature and

precipitation values as well as their variations and seasonal characteristics. On the basis of the observations, the presence and absence data sets are determined and thus the climatic / topographical range is determined to which the species are adapted. Since the connection between climate and observation is usually not trivial, but is made up of several predictors, machine learning methods are used, such as regression methods, random forest, support vector machines or MaxEnt (Elith et al., 2006), whereby an ensemble of methods can also be used (Araujo and New, 2007). However, there are some pitfalls of the SDMs, so it must be ensured that the predictors used hardly correlate (Braunisch et al., 2013) and are not colinear (Dormann et al., 2013), that there the data points and the number of predictors are sufficient so that the result is not overfitted, and that there is no spatial autocorrelation between the observation data, which would also lead to falsified results (Boria et al., 2014). Each SDM result must first be statistically evaluated in order to determine whether the model result is meaningful. For this purpose, the input data is split up into a training and test data set, the latter being used for evaluation. For evaluation, e.g. the Brier Skill Score or the area under the receiver operating characteristic curve (AUC) are calculated. The results of the SDM can then determine the effects of climate change on certain species by extrapolating to other climatic conditions or the spread of invasive species by extrapolating to other regions (Elith and Leathwick, 2009).

With the assumption that humans are a species whose survival is strongly influenced by external conditions, the methodology can be transferred to archeology. The presence / absence distribution is obtained either from archaeological sites (e.g., Banks et al., 2008; Burke et al., 2017) or from ethnological data (Tallavaara et al., 2015). The climatic predictors come from climate models, with a distinction being made between global and regional models with higher resolution. The simulations of the Paleoclimate Modelling Intercomparison Project (PMIP) (Braconnot et al., 2012), which is now in the 4th phase (Kageyama et al., 2018), are mostly used for climate reconstruction. There, in addition to the pre-industrial conditions, the climate of the phases Mid Holocene, Last Glacial Maximum and the Last Interglacial are reconstructed with global climate models. Especially for the Last Glacial Maximum, a large number of SDM studies have been published (Burke et al., 2014, 2017; Banks et al., 2006, 2008, 2009; Tallavaara et al., 2015). Furthermore, climate simulations were carried out to enable SDM studies on other settlement phases (Banks et al., 2006, 2013; Giampoudakis et al., 2017) and other human species such as the Neanderthal (Banks et al., 2008; Benito et al., 2017). Due to the increase in paleoclimatic reconstructions through projects such as PalMod², archaeological SDM studies are likely to gain in importance in the future. Finally, SDM results were also used as input for further calculations, e.g. to determine migration routes through least cost paths (Kondo et al., 2018) or as an environment for agent-based models (Wren and Burke, 2019, see the next Sec. 1.2.2).

1.2.2 Agent based modeling (ABM)

ABMs are computer models to investigate how the individual parts of a coherent system function and interact, whereby the individual parts are referred to as agents (Wurzer et al., 2015). They are used in many specialist areas such as philosophy, history or social science (Klein et al., 2018), whereby "agents" stands for different subjects, such as individual humans or a car in a traffic jam, or more abstract structures, such as states or companies, depending on the application. For applications in archeology, it is mostly used with individuals, groups or tribes. The principles and

²<https://www.palmod.de/>

methodology of ABMs presented here are largely based on [Wurzer et al. \(2015\)](#). The agents are located in an artificial environment, mostly characterized by climatic or environmental conditions, and their behavior within the environment is determined by certain conditions. In addition, conditions are defined that integrate the interactions between the agents in the model. What type of interaction depends entirely on the model study and can look very different, such as environmental change through resource consumption by agents or climate change, group formation, reproduction through births and deaths, or learning and memorizing about the environment. In [Macal and North \(2006\)](#) and [Wurzer et al. \(2015\)](#), some rules that must apply to agents in ABMs have been defined, which reflect the functionality of ABMs well: an agent has to 1) be uniquely identifiable, 2) cohabit an environment with other agents, and be able to communicate with them, 3) be able to act targeted, 4) be autonomous and independent, and 5) be able to change its behaviour. The great advantage of ABMs is that they are able to map heterogeneous populations ([Klein et al., 2018](#)), despite being computationally expensive. Furthermore, a distinction is made between deterministic and stochastic ABMs and between discrete and continuous environments.

In the study by [Wren and Burke \(2019\)](#), an ABM is combined with a habitat suitability (HS) model to create an environment in which the "agents", here families of hunters and gatherers, interact to study the regionalization of material cultures in Western Europe during the Last Glacial Maximum. The HS environment determines the birth and death rate and the movement of the agents, which is a random walk that is weighted by the HS score and the distance to the next uninhabited grid cell. In addition, a gene code is assigned to each agent, which represents the region from which it comes and which is passed on to offspring, this being made up of the gene codes of two agents at random. They came to the conclusion that the increased population growth in south France and north-east Spain led to continuous emigration from these regions, which led to genetic homogeneity in Western Europe.

In the ABM study by [Cucart-Mora et al. \(2018\)](#), the Upper to Middle Paleolithic transition, i.e. the transition from Neanderthals to modern humans, was simulated on the Iberian Peninsula. The agents, groups of 25 people, move in a random direction within a specified mobility range and reproduction takes place when there is enough space, depending on the birth rate. The parameters defining the mobility and reproduction in the model are obtained from ethnographic studies and adapted to the Neanderthal population. Each agent is assigned a gene code that identifies them as Neanderthals, modern humans or hybrids. The authors come to the conclusion that the extinction of the Neanderthals can be related to a lower growth rate compared to modern humans, or to a higher mobility; and that cultural barriers prevented inter-specific reproduction. This enabled them to reproduce the archaeological history of the Iberian Peninsula and show that there is little introgression of the Neanderthal genes in the genome of modern humans.

1.2.3 Differential equation modeling (DEM)

A good summary of DEM in archaeology can be found in [Steele \(2009\)](#), I will give a brief overview of his results here. The human dispersal in a DEM is usually simulated by a reaction-diffusion equation (Eq. 1.6, the notation is adapted to the notation of the doctoral thesis) which has first been applied to population studies by Skellam (1951). The dispersal of populations is governed by two processes, a population growth and

a spatial spreading, by estimating the timely change of a population density ρ :

$$\frac{\partial \rho}{\partial t} = f(\rho, r, K) + D \nabla^2 \rho, \quad (1.6)$$

with D being the Diffusion coefficient. The function $f(\rho, r, K)$ determines the population growth or decline and is usually defined by the logistic growth law, first established by [Verhulst \(1838\)](#):

$$f(\rho, r, K) = \rho r \cdot \left(1 - \frac{\rho}{K}\right). \quad (1.7)$$

The parameter r is the maximum population growth rate and the parameter K is the carrying capacity and defines a threshold for population growth. The quantity K can be specified according to the environmental conditions. A simple application of the model can be found in [Young and Bettinger \(1995\)](#). There, the spread of modern humans from Africa across world was simulated for different parameter configurations. Somewhat more complex models determine the parameters using archaeological data, such as radiocarbon dating ([Mellars, 2006](#)), or ethnographic studies of today's hunter-gatherer groups ([Fort et al., 2004](#)). [Ammermann and Cavalli-Sforza \(1979\)](#) developed the "wave of advance model" from the reaction-diffusion equation (Eq. 1.6) to estimate the spread of the Neolithic in Europe by fitting the parameters with radiocarbon data. However, both radiocarbon and ethnographic data have certain pitfalls that can lead to incorrect assumptions, such as the inaccuracy of the dating or the influence of sedentary people on the lives of today's hunters and gatherers.

Other studies have added additional components to the reaction-diffusion equation that have made the model more realistic, but the increasing complexity also increases the degrees of freedom in the model. In [Lewis and Kareiva \(1993\)](#), an additional term is introduced to depict the Allee effect, which states that the population decreases at low densities. Other studies integrated anisotropy in the population propagation either through spatial or temporal heterogeneity of the parameters ([Steele et al., 1998](#); [Martino et al., 2007](#)) or by including an advection term ([Davison et al., 2006](#)). Advection accelerates the dispersal in the direction of more favorable regions, which means that less favorable regions are more likely to be avoided. In [Davison et al. \(2006\)](#), this was used to accelerate the Neolithic migration along rivers in the model. An advanced DEM was published by [Timmermann and Friedrich \(2016\)](#). They simulated human dispersal by assuming the diffusion to be isotropic, while population growth and mortality are functions that depended on climatic variables. Through a global climate simulation of the last 300,000 years, they were able to simulate the entire pre-historic migration of modern humans. Many of the simulated arrival times in different parts of the world correspond to the archaeological dates, with some deviations being explained by interactions with other human species. However, their model depends on many parameters and it is at least questionable whether the results are representative or if the model is overfitted.

Another important factor that plays a role in migration is, in addition to the human-environment interaction, the interaction between humans. The human interaction was integrated, for example, by simulating the propagation of two different groups of people and including interaction terms in the Fisher-Skellam equation, such as in [Fort](#)

et al. (2008):

$$\frac{\partial \rho_1}{\partial t} = D_1 \nabla^2 \rho_1 + r_1 \rho_1 \left(1 - \frac{\rho_1}{K_1} \right) + \Gamma \rho_1 \rho_2, \quad (1.8)$$

$$\frac{\partial \rho_2}{\partial t} = D_2 \nabla^2 \rho_2 + r_2 \rho_2 \left(1 - \frac{\rho_2}{K_2} \right) - \Gamma \rho_1 \rho_2. \quad (1.9)$$

In Fort et al. (2008), population 1 represents the Mesolithic hunter-gatherers and population 2 the Neolithic farmers. The interaction parameter Γ determines the transition from hunter-gatherers to farmers. They found that both populations can coexist stably if the hunter-gatherer birth rate is high enough to compensate for the internal loss rate of farmers (Steele, 2009). Another two-population model was developed by Timmermann (2020) to simulate the extinction of the Neanderthals (ρ_n) in interaction with modern humans (ρ_s), whereby both competitive and interbreeding terms were included in the equations:

$$\frac{\partial \rho_n}{\partial t} = \nabla (D_n \nabla \rho_n) + r_n \rho_n \left(1 - \frac{\rho_n + \beta_{NS} \rho_s}{K_n} \right) \quad (1.10)$$

$$+ \gamma_I [r_n \rho_s \Theta(\rho_n - \rho_s) - r_s \rho_n \Theta(\rho_s - \rho_n)],$$

$$\frac{\partial \rho_s}{\partial t} = \nabla (D_s \nabla \rho_s) + r_s \rho_s \left(1 - \frac{\rho_s + \beta_{SN} \rho_n}{K_s} \right) \quad (1.11)$$

$$+ \gamma_I [r_n \rho_s \Theta(\rho_n - \rho_s) - r_s \rho_n \Theta(\rho_s - \rho_n)].$$

The parameters β_{NS} and β_{SN} control the effectiveness of food exploitation of a species in comparison to the other species, which integrates food competition between Neanderthals and modern humans in the equation. The interbreeding is governed by the Heaviside-function Θ , while the parameter γ_I is the average interbreeding factor. When both species populate the same grid cell, the larger group grows by interbreeding, while the offspring comes from the shrinking smaller group. The parameters $D_{n,s}$, $r_{n,s}$ and $K_{n,s}$ in Eq. 1.10 and 1.11 are also climate dependent. The main outcome of the study is that Neanderthal extinction could occur when Homo sapiens were more effective in exploiting glacial food resources in comparison to Neanderthals.

Chapter 2

Human Existence Potential in Europe during the Last Glacial Maximum

Authors

- Konstantin Klein, Institute for Geophysics and Meteorology, Cologne, Germany.
- Christian Wegener, Institute for Geophysics and Meteorology, Cologne, Germany.
- Isabell Schmidt, Department of Prehistoric Archaeology, University of Cologne.
- Masoud Rostami, Institute for Geophysics and Meteorology, Cologne, Germany.
- Patrick Ludwig, Karlsruhe Institute of Technology, Karlsruhe, Germany.
- Sven Ulbrich, Deutscher Wetterdienst, Offenbach, Germany.
- Jürgen Richter, Department of Prehistoric Archaeology, University of Cologne, Cologne, Germany.
- Gerd-Christian Wegener, Neanderthal Museum, Mettmann, Germany.
- Yaping Shao, Institute for Geophysics and Meteorology, Cologne, Germany.

Reference

Konstantin Klein, Christian Wegener, Isabell Schmidt, Masoud Rostami, Patrick Ludwig, Sven Ulbrich, Jürgen Richter, Gerd-Christian Weniger, and Yaping Shao: Human existence potential in Europe during the Last Glacial Maximum, *Quaternary International*, Volumes 581–582, 2021, Pages 7-27, ISSN 1040-6182, <https://doi.org/10.1016/j.quaint.2020.07.046>.

Contents lists available at [ScienceDirect](https://www.sciencedirect.com)

Quaternary International

journal homepage: www.elsevier.com/locate/quaint

Human existence potential in Europe during the Last Glacial Maximum

Konstantin Klein^{a,1}, Christian Wegener^{a,1}, Isabell Schmidt^{b,1}, Masoud Rostami^{a,1},
Patrick Ludwig^c, Sven Ulbrich^{a,d}, Jürgen Richter^{b,1}, Gerd-Christian Weniger^{e,1},
Yaping Shao^{a,*}

^a Institute of Geophysics and Meteorology, University of Cologne, Cologne, Germany

^b Department of Prehistoric Archaeology, University of Cologne, Cologne, Germany

^c Institute of Meteorology and Climate Research, Karlsruhe Institute of Technology, Karlsruhe, Germany

^d Deutscher Wetterdienst, Offenbach, Germany

^e Neanderthal Museum, Mettmann, Germany

ARTICLE INFO

Keywords:

Human existence potential
Last glacial maximum (LGM)
Solutrean
Epigravettian
Environmental human catchment
Best potential path
Logistic regression

ABSTRACT

Archaeological records indicate that many regions in Europe remained unoccupied by hunter-gatherers during the Last Glacial Maximum (LGM), probably due to the harsh climatic conditions and glacial extent. In the populated regions of southwestern Europe, a new technocomplex, the Solutrean, is known to have emerged among hunter-gatherers but did not reach the regions east of 10°E. To better understand human occupation of Europe during the LGM, Human Existence Potential (HEP) is presented, which expresses the suitability of a region with given environmental conditions for habitation by hunter-gatherers. We estimate the HEP based on archaeological site locations and reconstructed climate/environment data. By geostatistically upscaling archaeological site distributions into Core Areas, we distinguish areas that were likely to have been continuously occupied by hunter-gatherers from areas intermittently occupied. The use of Core Areas in the model improves the description of regions of continuous human presence, removing some of the previously observed mismatches between reconstructions and archaeological records. Using HEP, important anthropological and archaeological questions can be studied. Environmental Human Catchment (EHC) and Best Potential Path (BPP) are applied to quantify an area of HEP attraction and the lowest-cost path between two areas, respectively. With these tools, we characterize the potential connections between the Core Areas, the environmental barriers and possible social and technological interactions. A clear difference in environmental adaptation is found between the populations in western and eastern Europe, with a significant climate barrier preventing the propagation of the Solutrean to eastern Europe.

1. Introduction

Human demography and adaptation during the Last Glacial Maximum (LGM) have been investigated intensively during the past decade using a diverse set of methods (Banks et al., 2009; Tallavaara et al., 2015; Maier et al., 2016; Burke et al., 2017; Bocquet-Appel et al., 2005; French and Collins, 2015; Weniger et al., 2019). Many researchers agree that hunter-gatherers in Europe were facing extreme climate during this time period with colder and drier conditions compared to the present-day (e.g., Bartlein et al., 2011; Annan and Hargreaves, 2013). Furthermore, evidence of human presence at the time is scarce for northern Europe, but more abundant for most parts of southwestern

Europe, with the currently known distribution of archaeological sites probably shaped by the limits imposed by climatic conditions (see discussion in Tallavaara et al., 2015).

Cultural developments differed considerably within the inhabited regions. A suite of new lithic technologies and implements, the Solutrean technocomplex, appeared throughout southwestern Europe, with regionally distinct lithic point types presumably reflecting human adaptations to specific ecological niches (Banks et al., 2009; Schmidt, 2015b). In eastern Europe, the Epigravettian technocomplex constituted a cultural development strongly rooted in the preceding Gravettian. Studies about this large-scale division suggest an environmental rupture that separated the populations of the two regions (Banks et al., 2009;

* Corresponding author.

E-mail address: yshao@uni-koeln.de (Y. Shao).

¹ Member of the Collaborative Research Centre (CRC) 806, 'Our Way to Europe'.

<https://doi.org/10.1016/j.quaint.2020.07.046>

Received 14 October 2019; Received in revised form 15 July 2020; Accepted 25 July 2020

Available online 26 August 2020

1040-6182/© 2020 Elsevier Ltd and INQUA. All rights reserved.

Maier et al., 2016).

In contrast to scenarios of a population crisis during the LGM (Straus, 1990a, b; Tallavaara et al., 2015), diachronic studies on population size (e.g., Maier and Zimmermann, 2017; Maier et al., 2016; French and Collins, 2015) suggest that human populations had already experienced a massive decrease - local extinctions and a breakdown of trans-continental social networks - during the preceding final Gravettian period when the climate changed, insolation decreased, the vegetation-growth period shortened, and glaciers extended (Maier et al., 2020). Estimates indicate that populations recovered during the LGM, and the northern regions of Europe were finally repopulated during the succeeding Magdalenien. These Upper Paleolithic population changes in Europe have been illustrated by the repeated replacement model, as proposed by Bradtmöller et al. (2012).

To expand these insights and to further investigate human-environment interactions, we assume that (1) similar environmental conditions have the same potential for human existence and (2) they act as the dominant driver for human dispersal at the time. Working under these two premises, which are in line with many previous studies (van Andel and Davies, 2003; Bocquet-Appel et al., 2005; Tzedakis et al., 2007; Müller et al., 2011; Schmidt et al., 2012; Banks et al., 2013; Ludwig et al., 2018), we use a set of climate variables to estimate the Human Existence Potential (HEP), which defines the probability of hunter-gatherers existence for given technocomplexes, depending on available resources and climate and environment conditions. Resources in some areas are difficult to access, HEP is thus modified by additional parameters such as topography, glaciers, water bodies, and forests.

Using the HEP-model, we explore and quantify some important aspects of human-environment relations. Under the assumption that the mobility of hunter-gatherers - and thus contacts between groups - was facilitated by favorable environmental conditions at broader temporal and spatial scales, we consider a high HEP to positively affect the establishment and maintenance of human social networks. Kondo et al. (2018) suggested that paths along favorable environmental conditions can be used to describe migration routes between two points. This idea can be readily incorporated in HEP framework. The Best Potential Path (BPP) can be calculated by integrating HEP along the routes between two points. Note that this definition should be distinguished from the Least Cost Path - which is usually defined in archaeology by the walking speed in relation to the topography (e.g., White and Surface-Evans, 2012; Becker et al., 2017). We apply the BPP approach to the Solutrean network by calculating the BPP between the centres of different Core Areas. Furthermore, we analyze the cost of every BPP (T_{BPP}) to estimate the probability of contact between two Core Areas.

To gain further insight into population dynamics, we introduce a new concept, the Environmental Human Catchment (EHC), defined as an area delimited by minima in the HEP distribution. Our definition of catchments is different from that of Vita-Finzi et al. (1970), in which hunting-gathering and agricultural economies were considered. If the assumption that LGM hunter-gatherers preferred living in areas of high HEP is correct, their movements were probably oriented in the direction towards HEP maximums on longer time scales. Therefore, the HEP maximums define catchments and are used to identify the EHCs. The EHC corresponding to a HEP maximum is obtained by following the “upflow” of each grid point into the maximum. We assume that hunter-gatherers left an EHC only if forced to by external or internal factors such as environmental or socio-cultural factors.

To improve the previous approaches for characterizing environment conditions of LGM-human-occupation, we implement an up-scaling procedure of the archaeological data in the model. Given that the archaeological data, i.e., the geographic positions of sites dated to the LGM (Maier et al., 2016), constitute the evidence from a palimpsest of several thousand years, they probably contain outliers. The climate data used to derive the HEP, in contrast, represent large-scale and time-averaged conditions for the entire LGM. By spatially up- and temporally down-scaling archaeological data into Core Areas, the

temporal scale coincides better with the temporal scale of the climate data. Such an up- and down-scaling procedure has been used in several studies (e.g., Zimmermann et al., 2004, 2009; Kretschmer, 2015). In a case-by-case analysis of the HEP, we compare the results obtained from all sites with those obtained from sites in Core Areas. By doing so, we identify the likely areas of continuous human settlement in Europe during the whole LGM period, and the likely areas of intermittent settlement during certain LGM phases when climate conditions were favorable.

2. Data

2.1. Archaeological data

The presence of hunter-gatherers was determined by using 396 archaeological sites across Europe assigned to the LGM (Maier and Zimmermann, 2015). This database is available online.² It specifies the geographical position and cultural attribution of each assemblage. It includes radiocarbon-dated sites from the period between 25 ka and 20 ka cal BP and sites typologically attributed to the Solutrean, Badegoulian or Epigravettian technocomplex. Due to constraints in the applied method and datasets in Italy and the Balkan region, these areas were excluded from the further analysis (cf. Discussion in Maier et al., 2016), reducing the archaeological sites from 396 to 358 in total (Fig. 1). We used two datasets to create and test the HEP model:

- (i) Dataset All (DatALL): all sites of the dataset,
- (ii) Dataset Core Areas (DatCA): sites located within Core Areas.

DatCA becomes a subset of DatALL by applying an up-scaling procedure to the archaeological data following the protocol described elsewhere (Zimmermann et al., 2004; Schmidt et al., 2020). The protocol uses a site-density based geostatistical procedure to identify Core Areas (CA; Schmidt et al., 2020), which represent clusters of archaeological sites, interpreted as continuously and permanently settled regions (Maier et al., 2016; Zimmermann et al., 2009). For an analysis such as ours, which covers a period of several thousand years, CA clustering appears to be an appropriate spatial up-scaling procedure for archaeological sites. The CA comprised in total 310 archaeological sites across Europe.

We divided Europe along the 10°E longitude into a western and an eastern population (Fig. 1). Archaeologically, this division reflects the border between the Solutrean technocomplex to the west and the Epigravettian technocomplex to the east. The number of sites in Europe assigned to the western and eastern areas is given in Table 1.

2.2. Paleoenvironmental and paleoclimatic data

The climate data, basically temperature and precipitation, in this study were obtained from a 30-year regional climate simulation for LGM conditions (Ludwig et al., 2017) using the Weather Research and Forecasting (WRF) model (Skamarock et al., 2008). The WRF model was nested in the LGM run of the global earth system model MPI-ESM-P (Stevens et al., 2013), which was part of the Paleoclimate Modeling Intercomparison Project (PMIP3) (Braconnot et al., 2012). The WRF model used a much higher spatial resolution (50 km grid spacing) compared to the MPI-ESM-P (approx. 200 km) and thus provided more detailed information on the climate in Europe under glacial conditions. More details about the benefits of regional paleo-climate modeling are given in Ludwig et al. (2019). To take into account the glacial boundary conditions, the WRF model input data were modified in the extent and height of the Eurasian ice sheet, lowered sea level, and displaced

² <https://crc806db.uni-koeln.de/dataset/show/crc806e1lgmsitesdatabase201503131428396059/>.

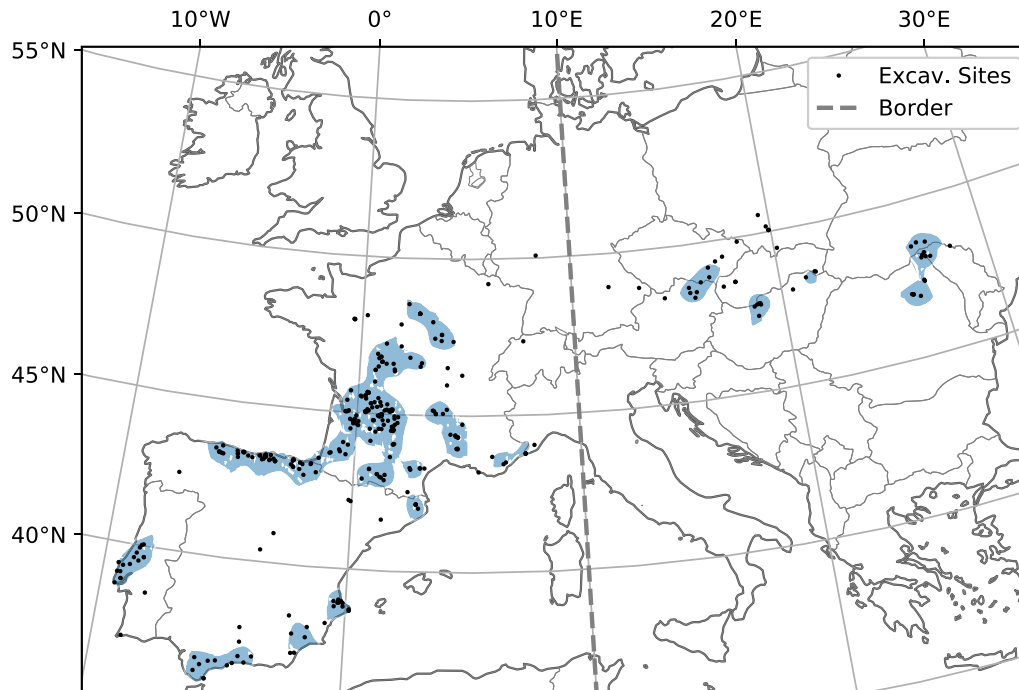


Fig. 1. Archaeological sites dated or assigned to the LGM (black dots, after Maier and Zimmermann (2015)), Core Areas are encircled by the “Optimally Describing Isoline” (blue shading, after Maier et al. (2016)) and the boundary between the western and eastern population (dashed gray line). (For interpretation of the references to color in this figure legend, the reader is referred to the Web version of this article.)

Table 1

The number of archaeological sites depending on the classification into the populations as shown in Fig. 1; (i) DatALL: all sites, (ii) DatCA: sites within Core Areas.

| | Western Population | Eastern Population |
|--------|--------------------|--------------------|
| DatALL | 307 | 51 |
| DatCA | 278 | 32 |

coastline. These conditions were adjusted based on the PMIP3 protocol for LGM simulations. Finally, the paleo-vegetation data were obtained from a global vegetation reconstruction for the LGM from Shao et al. (2018). The paleo-vegetation reconstruction and the PMIP3 data were also used to determine the HEP accessibility described in Section 3.4.

3. Definition of the human existence potential

In general, humans are capable of adapting to various environmental conditions if food and water supply are ensured. Both resources are mainly controlled by temperature and precipitation. However, adaptation to certain environmental conditions may also prohibit humans from occupying all potentially inhabitable areas. Instead, they may prefer familiar environmental conditions and continue living under these if possible. Given this cultural selective factor, it is legitimate to use archaeological data to train the Human Existence Potential (HEP) on archaeological site distribution.

Four subsets of archaeological site data, as defined in Table 1, are used to model the HEP. We thereby distinguish between HEP derived by sites affiliated to the Solutrean technocomplex in western Europe ($\leq 10^\circ\text{E}$) and sites affiliated to the Epigravettian technocomplex in eastern Europe ($>10^\circ\text{E}$); and DatAll sites (HEP_{ALL}), and DatCA sites (HEP_{CA}). The four different HEPs are west HEP_{ALL}, west HEP_{CA}, east HEP_{ALL}, and east HEP_{CA}. Given the interpretation of Core Areas, HEP_{CA} can be interpreted as representing the suitability of regions for continuous settlement for a given technocomplex. As the climate data is

considered to represent the mean conditions of the LGM, we, furthermore, assume that HEP_{CA} reflects the mean HEP for continuous settlement. As DatALL includes archaeological outliers, i.e., sites that are considered to be only temporarily occupied, the difference $\Delta\text{HEP} = \text{HEP}_{\text{CA}} - \text{HEP}_{\text{ALL}}$ points to temporary variations from the mean conditions. In particular, negative ΔHEP regions were probably settled in intermittent phases of favorable climatic conditions.

The HEP is calculated by applying logistic regression with second-degree polynomials on a presence and absence record for suitable climatic predictors. The different bioclimatic predictors are derived by monthly mean temperature, daily maximum and minimum temperature, and monthly precipitation. The resulting HEP is a function of climatological predictors that presents the least to most desirable conditions for human existence with corresponding scores from zero to one. The resulting HEP is modified by functions based on topography, glaciers, water bodies, and vegetation, to account for the accessibility. A description of the HEP model setup and the evaluation of the model is given in the next subsections and summarized in Fig. 2.

3.1. Variable selection

From the 19 different bioclimatic variables (Hijmans et al., 2005; O'Donnell and Ignizio, 2012), calculated using the WRF (Weather Research and Forecast) model output (see Table 2), the predictors for the logistic regression are chosen. A description of how the bioclimatic variables are computed is included in Section A in the Appendix. The variables Bio 8 and Bio 9 (Fig. A.1e and Fig. A.1f) are excluded from the analysis, because the regression coefficients did not converge due to strong temperature variations, in particular in Eastern Europe.

In a regression analysis, collinearity can cause errors in categorizing the importance of a predictor by overestimating the variance of the regression parameters (Dormann et al., 2013). A standard method in statistics to overcome this problem is the evaluation of the variance inflation factor (VIF; Alin, 2010). This factor estimates how much of the variance of a regression model is inflated in comparison to the same

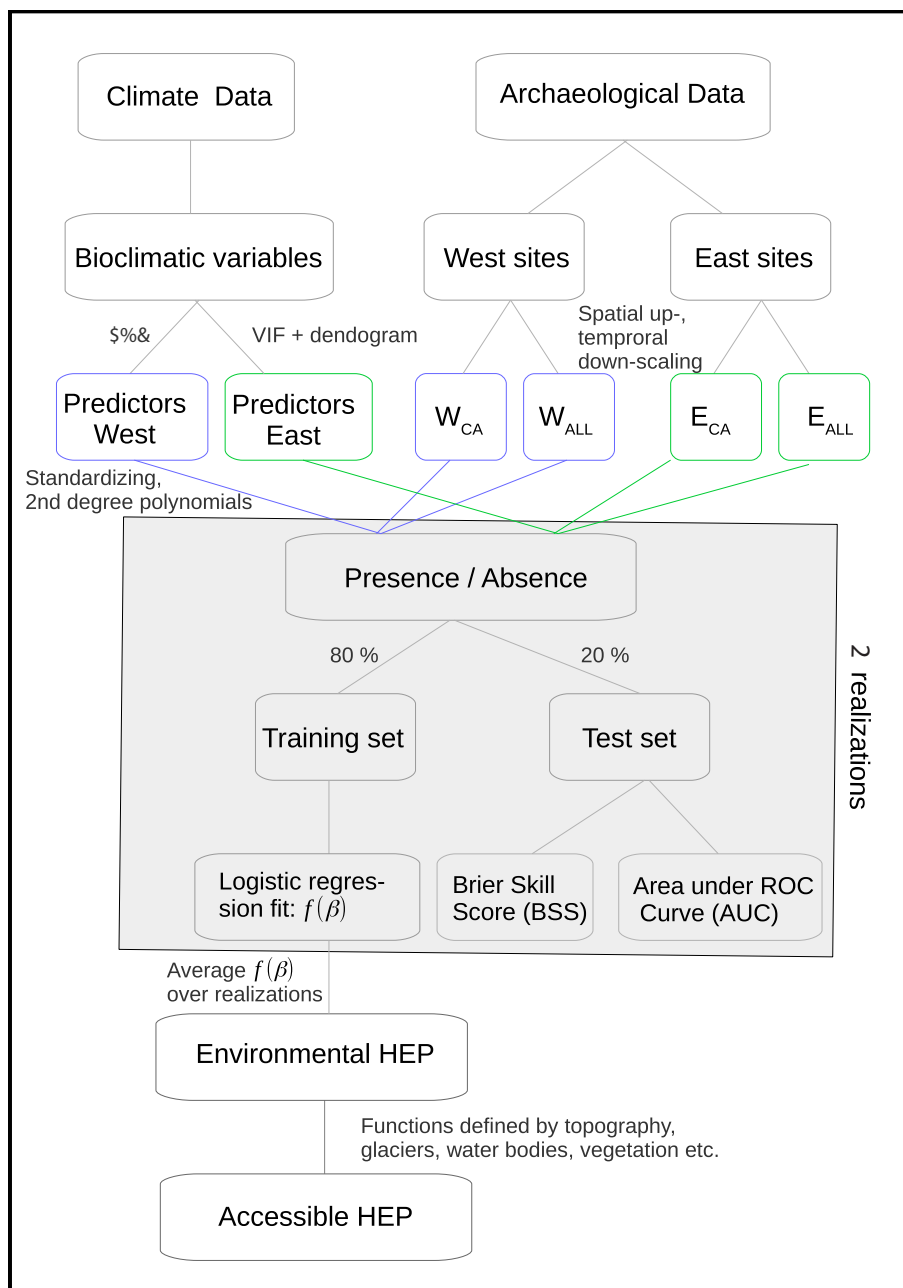


Fig. 2. Modeling framework of the Human Existence Potential (HEP).

model without collinearity. The VIF of each bioclimatic variable (b_i) is obtained by determining the Coefficient of Determination (R) from the ordinary least square regression with b_i as the predictand and the other bioclimatic variables as the predictors. The VIF of b_i is then:

$$VIF = \frac{1}{1 - R^2} \tag{1}$$

The VIF of each bioclimatic variable is required to be less than 10. We calculate the VIF of each variable and exclude the one with the highest VIF, except for Bio 4 or Bio 15, because both, namely the seasonality of temperature and precipitation, are known to be high impact predictors for the population of hunter-gatherers, as suggested by Grove (2018), and should be part of the analysis. We repeat the above step until the requirement ($VIF < 10$) is satisfied for all remaining variables. The distributions of the final seven variables used in the regression Bio 1, 3, 4, 14, 15, 18 and 19 are shown in Fig. 3.

The seven variables are used to estimate the HEP of the western

population. For the eastern population, it is necessary to adjust the HEP model due to the low density and amount of archaeological sites (Table 1). The number of predictors have to be decreased to reduce errors from an under-parameterized model. We, therefore, further analyze the mutual correlations of the seven variables. The correlations are converted into a distance matrix by calculating the distance scores between two bioclimatic variables b_i and b_j with $i, j \in [1, 3, 4, 14, 15, 18, 19]$, by:

$$d_{i,j} = 1 - |corr(b_i, b_j)|, \tag{2}$$

while $corr(b_i, b_j)$ is the correlation coefficient between b_i and b_j . By joining two clusters of the resulting distance matrix into a single new cluster until one final node is left (Müllner, 2013), a hierarchical dendrogram correlation clustering can be drawn (Fig. B1). The distances between two clusters are the minimum distances between the corresponding variables. We choose a distance threshold of 0.3 to define the

Table 2
Definition of the 19 Bioclimatic variables as candidate predictors of the HEP. The corresponding definition for each of the variables is shown in the Appendix.

| Bioclimatic Variable | Definition |
|----------------------|-------------------------------------|
| Bio 1 | Annual Mean Temperature |
| Bio 2 | Mean Diurnal Range |
| Bio 3 | Isothermality |
| Bio 4 | Temperature seasonality |
| Bio 5 | Max Temperature of Warmest Month |
| Bio 6 | Min Temperature of Coldest Month |
| Bio 7 | Temperature Annual Range |
| Bio 8 | Mean Temperature of Wettest Quarter |
| Bio 9 | Mean Temperature of Driest Quarter |
| Bio 10 | Mean Temperature of Warmest Quarter |
| Bio 11 | Mean Temperature of Coldest Quarter |
| Bio 12 | Annual Precipitation |
| Bio 13 | Precipitation of Wettest Month |
| Bio 14 | Precipitation of Driest Month |
| Bio 15 | Precipitation Seasonality |
| Bio 16 | Precipitation of Wettest Quarter |
| Bio 17 | Precipitation of Driest Quarter |
| Bio 18 | Precipitation of Warmest Quarter |
| Bio 19 | Precipitation of Coldest Quarter |

main branches of the dendrogram, the largest (positive or negative) correlation between any two parameters from different branches is then in the range from -0.7 to 0.7 . As already discussed, Bio 4 and Bio 15 are kept as predictors. In addition, Bio 1 is kept to retain the information of the temperature extremes. The extracted four variables, Bio 1, 4, 15 and 19, are used for modeling the HEP based on sites of the eastern population.

3.2. Model fitting

All climate variables are standardized by removing the mean ($\langle b_i \rangle$) and normalizing with the standard deviation (σ_{b_i}):

$$b_i^s = \frac{b_i - \langle b_i \rangle}{\sigma_{b_i}} \quad (3)$$

Second-order polynomials of the standardized climate variables are then used as predictors (\vec{p}) to fit the logistic regression (Eq. (4)).

The logistic regression model (Tibshirani, 1996; Hastie and Friedman, 2008) needs to be fitted with the human presence and absence records. Human presence is assumed in the circle with a 50 km radius centered at each archaeological site. The climate state at a grid point lying inside the circles is affiliated with the presence record, while each state is only once included to the record (total number: N_{pre}). A radius of 50 km is assumed, so that the number of presence points is sufficiently large for model convergence. The pseudo-absence record is assumed by the absence of archaeological sites in a region, and therefore consists of all grid points lying outside the circles (total number: N_{abs}). The pseudo-absence points for Italy and the Balkans are excluded to avoid false assumptions on human absence due to above mentioned constraints (Maier et al., 2016). Moreover, the climatic states for Africa, any islands, water bodies and areas north of 56°N are omitted from the analysis. The locations of presence (from eastern and western population combined) and absence points for DatALL are shown in Fig. 4.

We carry out 1000 calculations. For each, we randomly split 80% of the presence and 80% of the absence record into a training dataset, and the remaining 20% of both datasets into a test dataset. The coefficients $\vec{\beta}$ and the intercept β_0 are determined by the logistic function of the training data:

$$y_i^{train} = \{1 + \exp[-(\beta_0 + \vec{\beta} \cdot \vec{p}_i^{train})]\}^{-1} \quad (4)$$

with $y_i^{train} = 1$ for presence and $y_i^{train} = 0$ for absence points, for $i = 1, \dots, 0.8 \cdot (N_{pre} + N_{abs})$. The presence and absence input are weighted by the

amount of presence and pseudo-absence points, respectively. The logistic regression involves 36 terms for the western and 15 terms for the eastern population, but not all terms are important. For that, LASSO (Least Absolute Selection and Shrinkage Operator) regularization (Tibshirani, 1996; Hastie and Friedman, 2008; Marami Milani et al., 2016) is used in the training process to exclude irrelevant terms of the polynomials.

The trained model (f) is then applied to the whole study area and the averaged outcome over the 1000 realizations is the HEP for Europe.

$$\begin{aligned} \text{HEP} &= \frac{1}{1000} \sum_{j=1}^{1000} f_j(\vec{p}) \\ &= \frac{1}{1000} \sum_{j=1}^{1000} \{1 + \exp[-(\beta_{0j} + \vec{\beta}_j \cdot \vec{p})]\}^{-1} \end{aligned} \quad (5)$$

3.3. Model evaluation

The test dataset is applied for cross validation. Different skill scores are determined to evaluate the uncertainty of the model, where the prediction $f(\vec{p}^{test})$ of each realization is compared to the classification \vec{y}^{test} (1 for presence and 0 for absence). The ‘‘Area under a Receiver Operating Characteristics Curve’’ (AUC) is determined to estimate the rate of cases which the method classifies correctly (Hanley and McNeil, 1982). The AUC values range from 0 to 1, while 0 means that all predictions are classified wrongly and 1 that all predictions are classified correctly. The Brier Score for each of the 1000 realization is calculated by:

$$BS = \frac{1}{N_{test}} \sum_{i=1}^{N_{test}} (f(\vec{p}_i^{test}) - y_i^{test})^2 \quad (6)$$

with $N_{test} = 0.2 \cdot (N_{pre} + N_{abs})$. By comparing the Brier Score of the trained model (BS_f) with the Brier Score of the same model where all coefficients except the intercept are set to zero (BS_{β_0}), the Brier Skill Score (BSS) can be estimated to measure the accuracy of a model:

$$BSS = 1 - BS_f / BS_{\beta_0} \quad (7)$$

The mean and the standard deviation of BSS and AUC of all 1000 realizations are calculated. In addition, the total variance (Var) of the 1000 predictions ($f(\vec{p})$) is computed to get a measure of the robustness of the output according to the input data. The results of the evaluation for all four model setups are shown in Table 3.

For all four subsets of archaeological site data, the model shows robustness to the input variables, as indicated by the low total variances shown in Table 3. Sensitivity analysis (Fig. D.1 in the Appendix) shows that local variances are generally low despite a few regions, e.g. the Pyrenees. The relatively high local variances are probably due to the inclusion of climatological outliers into the presence record. Both BSS and AUC suggest that model prediction work properly for all four setups (Table 3). As both AUC and BSS show low standard deviations, we suppose that the model output differs only marginally for different random setups. Thus, we suppose, that the occurrence of new archaeological findings would have only minor and rather local effects on the resulting HEP.

3.4. Accessibility

The HEP covers the main climate factors influencing the habitability, but the accessibility of resources is not considered. To account for important limiting factors such as orography and water bodies, several functions are introduced to modify the HEP. The result (HEP_{Acc}) is still referred to as HEP in the following discussions (Eq. (8)).

$$\text{HEP}_{Acc} = \text{HEP} \cdot g_{ice} \cdot g_{ele} \cdot g_{for} \dots \quad (8)$$

The modification functions, unless stated otherwise, are linear functions of the structure depicted in Eq. (9), with the input variable x ,

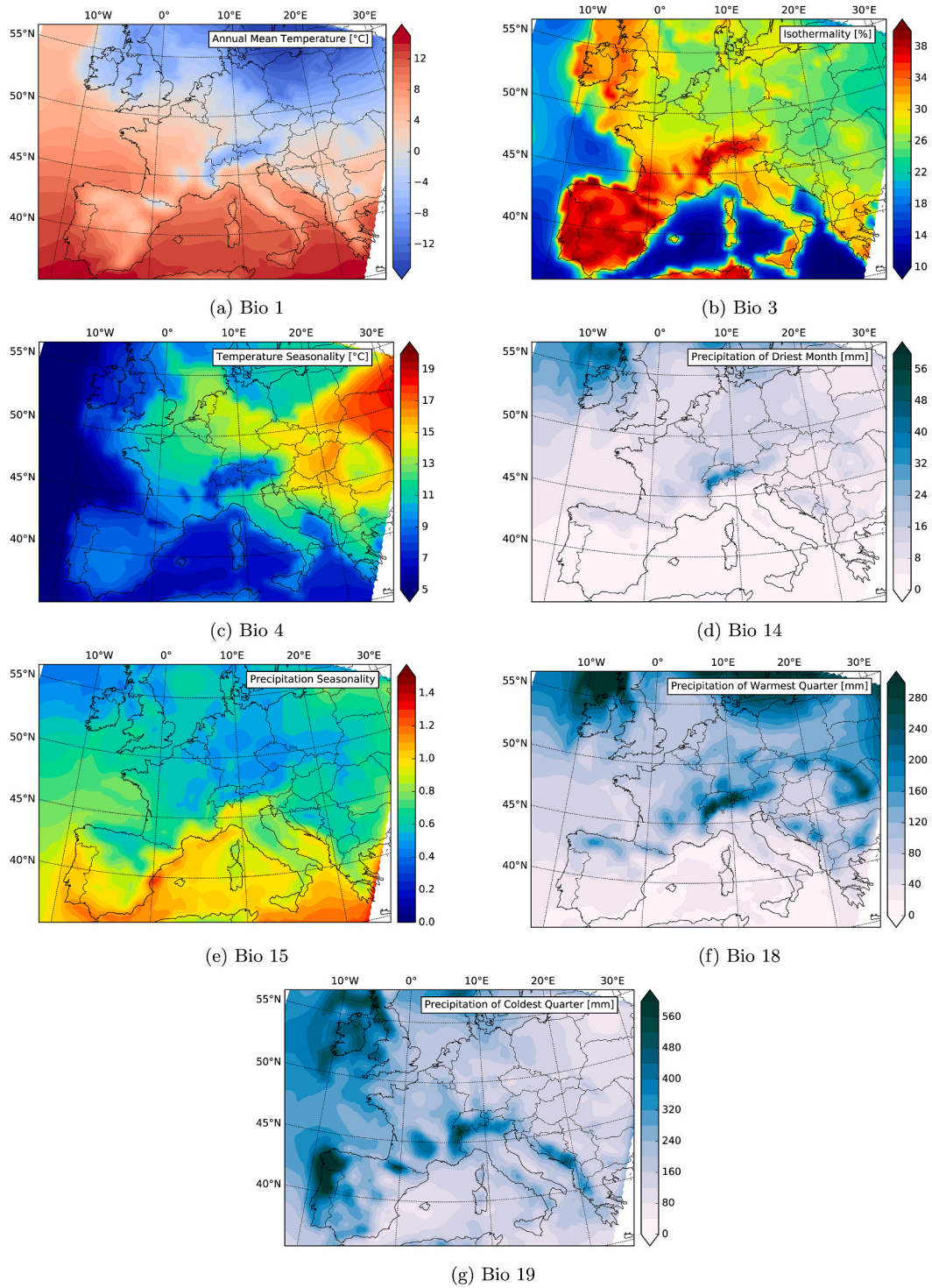


Fig. 3. Climate maps of the seven predictors used to calculate the Human Existence Potential (HEP).

the upper and lower limits x_u and x_l , and the slope m between the limits. Each modification function can diminish the HEP by up to 20% if the upper limit is reached. The empirical chosen parameters are listed in Table 4.

$$g(x)_{par} = \begin{cases} 1.0, & x < x_l \\ 1.0 - (x - x_l) \cdot m, & x_l \leq x < x_u \\ 0.8, & x \geq x_u \end{cases} \quad (9)$$

3.4.1. Ice, glaciers and water bodies

The permanent presence of sea ice and glaciers act as natural barriers

for hunter-gatherers. As no vegetation or wildlife is in these areas to sustain humans, the HEP is set to zero. Natural water bodies such as oceans and large lakes act as impassable borders and are masked out. We use the PMIP3 reconstruction of the glaciers and the LGM coastline (Braconnot et al., 2012).

$$g_{water,ice} = \begin{cases} 0, & \text{if gridpoint is water or ice} \\ 1, & \text{otherwise} \end{cases} \quad (10)$$

3.4.2. Orography

A crucial limiting factor of available resources is the orography. In

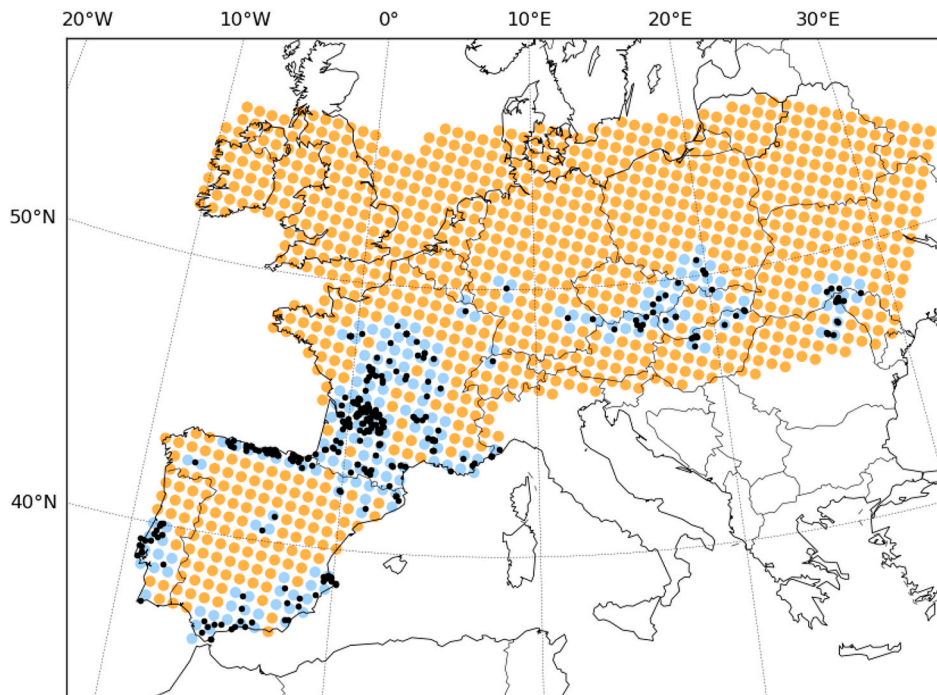


Fig. 4. Black dots: archaeological sites of DatALL (eastern and western sites combined) according to Table 1 across Europe. The underlying presence (blue) and pseudo-absence points (orange) for the calculation of the HEP are depicted. (For interpretation of the references to color in this figure legend, the reader is referred to the Web version of this article.)

Table 3

Mean and standard deviation of Area under a Receiver Operating Characteristics Curve (AUC) and Brier Skill Score (BSS) for the 1000 realizations, and total variance of the 1000 realizations (Var) of the prediction f , derived by the model setups W_{CA} , W_{All} , E_{CA} and E_{All} .

| | W_{CA} | W_{All} | E_{CA} | E_{All} |
|-----|-----------------|-----------------|-----------------|-----------------|
| AUC | 0.94 ± 0.02 | 0.94 ± 0.02 | 0.95 ± 0.03 | 0.93 ± 0.02 |
| BSS | 0.6 ± 0.05 | 0.56 ± 0.05 | 0.63 ± 0.05 | 0.54 ± 0.06 |
| Var | 0.02 | 0.013 | 0.001 | 0.001 |

Table 4

List of parameters used in each modification function.

| Parameterization | Variable x | Slope m | Lower limit x_l | Upper limit x_u |
|---|--------------|------------------------|-------------------|-------------------|
| Elevation g_{ele} | h | $0.1212 \cdot 10^{-3}$ | 350 m | 2000 m |
| Standard deviation of elevation g_{std} | h_σ | $0.5714 \cdot 10^{-3}$ | 50 m | 400 m |
| Vegetation g_{for} | f_f | 0.4 | 0.5 | 1 |

complex terrains (such as mountains, valleys, and cliffs), topographic obstacles make hunting and gathering more difficult so that the accessibility of resources is reduced in these regions. However, some complexity may be more favorable than flat terrain to find shelter, raw materials for tools and a higher diversity of resources. The elevation and complexity of the landscape are taken into account to evaluate the orographic influences.

Histograms (Fig. C.1 and Fig. C.2, see appendix) of the elevation of sites and the standard deviation of the elevation around the sites are created using a 30 s topography dataset. The standard deviation is used to estimate the roughness of the terrain in a grid cell of the climate data. The ordinate shows the normalized number of site bins of 50 m width (10 m width for standard deviation). Fig. C.1 shows that elevations (h) of 200 m–300 m are more frequent, while sites with higher altitudes are

less frequent. We set the interval for the HEP decline from 350 m to 2000 m. For the standard deviation (h_σ), the terrain featuring variations above 50 m is less occupied than nearly flat terrains. A low number of sites are found near high altitude variations. The boundaries are set to 50 m and 400 m to formulate g_{std} .

3.4.3. Forest and dense vegetation

Dense vegetation makes the transport more difficult while gathering, hunting or dispersing. We assume that areas with a large forest cover were less favorable. Humans could still survive in dense forests, but plant based foods are less accessible, e.g. higher up in the canopy or within the thicket (Kelly, 2013; Binford, 2002). We apply the global vegetation reconstruction of the LGM from Shao et al. (2018), focusing on the forest fraction. The potential is not altered for a forest fraction (f_f) below 0.5. For larger fractions, the potential is lowered with a linear function starting at 0.5 and ending at 1 for a full forest cover.

4. Best Potential Path and Environmental Human Catchment

We estimate BPP using a similar method as in Kondo et al. (2018). For a given grid, a cost function, C , is defined as $1/HEP$ (for $HEP \leq 10^{-5}$, C is set to 10^5). The total cost T between points A and B along a path s is:

$$T = \int_A^B C ds, \quad (11)$$

while we scale the distance between two grid points by $1/100 \text{ km}^{-1}$. From all possible paths between the two points, the BPP is the one of the lowest T , referred to as T_{BPP} . We compute the exchange network of the Solutrean technocomplex by determining the BPPs between the adjacent Core Areas.

To determine the EHC, we first extract catchments from the HEP pattern by identifying the local maxima and determining the associated upflow of each grid point to the maxima. By our definition, only catchments with a local maximum greater than 0.85 are specified as an EHC. We implement several rules so that catchments with lower maxima

merge into more substantial neighbouring catchments if they are not separated by low HEP < 0.5. Also, two EHCs with a direct transition are combined. The decision tree is shown in Fig. 5 and explained as follows:

1. If the HEP of the local maximum of a catchment (HEP_{LM}) is less than or equal to 0.85, it is surveyed if an adjacent catchment is an EHC ($HEP_{LM} > 0.85$). If yes, the catchment is merged with the EHC if they have more than two adjacent grid points with $HEP > 0.5$. If two or more adjacent catchments are EHCs, the catchment is merged into the one which has the lowest the minimum difference between the adjacent grid points.
2. Two adjacent EHCs are merged, if there are adjacent grid points with $HEP \geq 0.8$.

We repeat these steps ten times to capture all catchments which would merge. The resulting catchments satisfying $HEP_{LM} > 0.85$ are the EHCs.

5. Results

We estimate the HEP using either DatCA or DatALL and denote the results respectively as HEP_{CA} and HEP_{ALL} . While HEP_{CA} describes as reference the time averaged potential during the LGM, which enables continuous human occupation, the difference $\Delta HEP = HEP_{CA} - HEP_{ALL}$ provides insights in the potential variations which allow intermittent human occupations. In order to investigate the separation between the Solutrean and Epigravettian technocomplexes, HEP_{CA} and HEP_{ALL} are computed individually for western and eastern Europe. In the following, the HEP results are first described and then the BPP and EHC results. To facilitate discussion, regions with $HEP \geq 0.5$ are referred to as high HEP regions.

5.1. Western population

For the population in western Europe, or simply western population, the highest HEP_{CA} are located in the Franco-Cantabria with values exceeding 0.9 throughout the region (Fig. 6a). On the Iberian Peninsula, HEP_{CA} shows suitable conditions along the northern, southern and southeastern coasts (e.g. $HEP_{CA} \geq 0.7$), but generally unsuitable conditions in the northwestern and central parts. The great mountain ranges in Europe, such as the Alps, the Pyrenees and the Massif Central in France are generally unfavorable for LGM hunter-gatherers with low HEP_{CA} , as expected. Outside the known regions of the Solutrean technocomplex, potential refugia with high HEP_{CA} occur in Italy and the Balkans, although the archaeological sites in these areas are excluded in the

model training process (see Sec. 2.1). The regions with high HEP_{CA} east of Italy calculated using the model setup W_{CA} are exclusively located along the Mediterranean coast.

The spatial patterns of HEP_{ALL} (Fig. 6b) and HEP_{CA} partially differ. The most obvious differences occur in the inland regions of the Iberian Peninsula, northwestern Europe, and the Balkans (Fig. 8a). Clear differences can be seen in the Iberian Peninsula interior where HEP_{CA} is much lower than HEP_{ALL} . Similarly, high differences are observed at the northern and eastern margins of western Europe: high HEP_{ALL} regions extend to the northern border of France and southern parts of Great Britain, while high HEP_{CA} regions are confined more to the southwest. The upper Rhine rift valley, between southwestern Germany and France, has the largest ΔHEP . The highly suitable living conditions reflected in HEP_{ALL} almost entirely disappear in HEP_{CA} . The maximum ΔHEP here reaches around -0.5 (Fig. 8a). In eastern Europe, an increase can be observed for HEP_{CA} along the Adriatic Coast, while values for the hinterland conspicuously decrease. In Italy, the comparison shows higher HEP_{CA} in the Po valley, and lower values for the central region (Fig. 8a).

5.2. Eastern population

For the population in eastern Europe, or simply eastern population, HEP_{CA} indicates favorable living conditions around the Core Areas and some areas in Germany, the Czech Republic, and the Balkans (Fig. 7a). The highest HEP_{CA} of 0.97 is located in northeastern Hungary. The pattern is interrupted by low HEP_{CA} related to topographic features such as the High Tatras and the Carpathian Mountains. In northern Germany, there is an apparent mismatch between HEP_{CA} and the archaeological record, repeatedly reported in the literature (e.g., Maier et al., 2016). Interestingly, evidence of human presence (cf. archaeological sites in Fig. 7b) fits well with the southern boundary of HEP_{CA} -area in southern Germany (Fig. 7a).

The HEP_{ALL} shows high HEP regions in a rather continuous band stretching from the Netherlands to Moldavia in the east, and from the edge of the Scandinavian ice sheet to the northern Balkans in the south (Fig. 7b). The HEP_{CA} displays a less homogeneous pattern and a shrinkage of the western (i.e. Netherlands, Germany and western Poland) and northern extent of the band. The ΔHEP in Fig. 8b reveals the striking decrease of the HEP in these areas. Especially at the edge of the Scandinavian ice sheet, the HEP_{CA} deviates considerably from HEP_{ALL} , with a difference of up to 0.64. The pattern of ΔHEP in Fig. 8b shows positive values in regions in eastern Europe stretching from 46° to 48° N and negative values north and south of it.

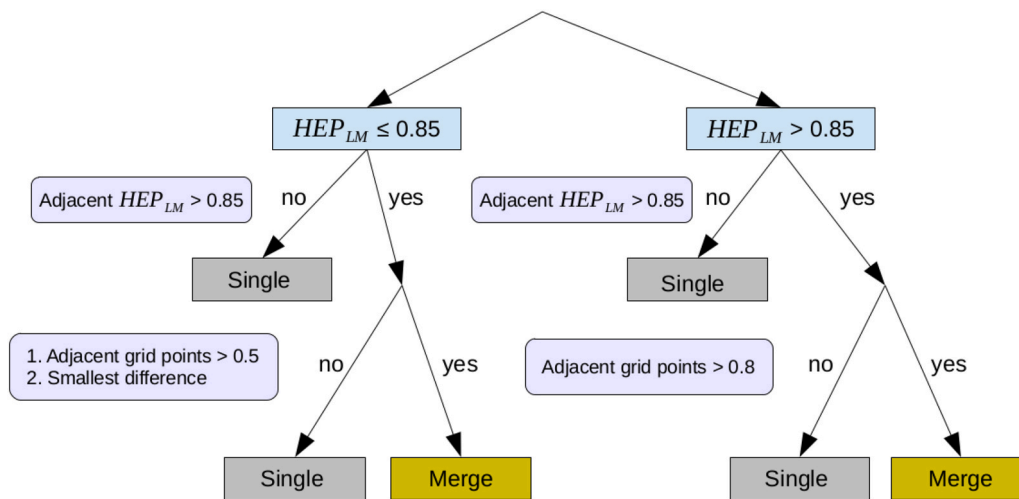


Fig. 5. Decision tree to illustrate when catchments are merged together. $HEP_{LM} > 0.85$ is the local maximum of HEP of the catchment.

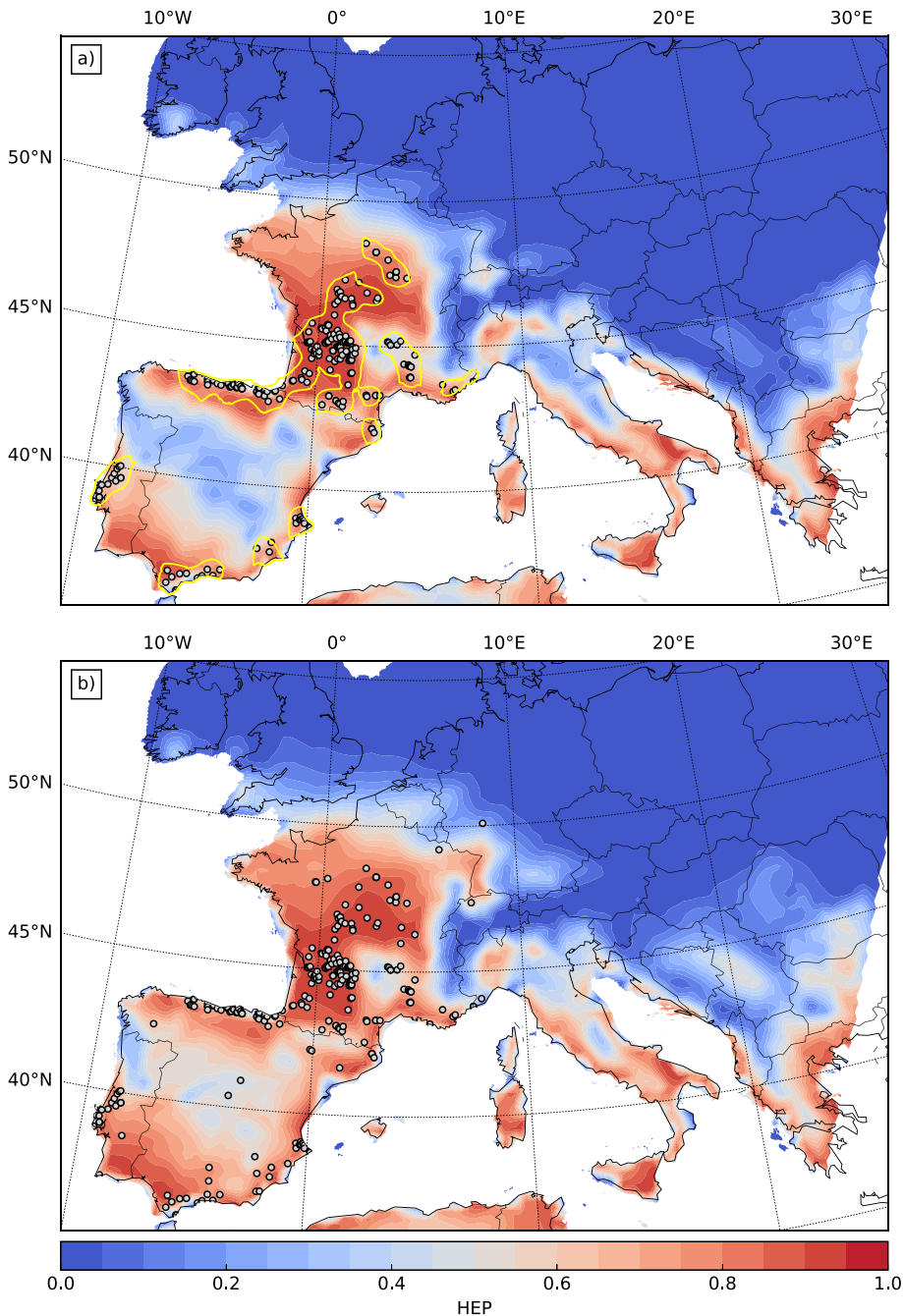


Fig. 6. Human Existence Potential (HEP) derived by logistic regression with the bioclimatic variables Bio 1, Bio 3, Bio 4, Bio 14, Bio 15, Bio 18 and Bio 19 and archaeological sites of the western population (west of 10°E). Thereby we incorporated for a) HEP_{CA} sites from Core Areas (DatCA) indicated by yellow lines, and for b) HEP_{ALL} all sites (DatALL). Gray dots: archaeological sites assigned to the LGM and incorporated in the model. (For interpretation of the references to color in this figure legend, the reader is referred to the Web version of this article.)

5.3. Application of the Best Potential Path to LGM Core Areas

We use BPP to investigate possible routes of the Solutrean social network across western Europe. To this end, we examine the BPP between Core Area centres in western Europe which are more than three grid points apart from each other. We provide two scenarios by calculating the BPP based on either HEP_{CA} (Fig. 9a) or HEP_{ALL} (Fig. 9b) of the western population with a total of 12 pairs of starting and ending points. Thereby, the BPP estimates how the social network of hunter-gatherers might have changed in intermittent phases of climate amelioration (considering HEP_{ALL}) in comparison to the continuous LGM conditions

(considering HEP_{CA}). We arrange the total costs of the BPP (T_{BPP}) in five categories to get an estimate of the proximity of contact.

For both scenarios, the same distribution of BPPs is found between the Core Area centered in the Dordogne and the Core Areas in northern France, Cantabria and Catalonia. This stable pattern is corroborated by the low costs of the BPPs ($T_{BPP} < 6$). Contact between these Core Areas is expected to have been intensive and stable. The BPPs connecting the Rhône valley with Franco-Cantabria and Catalonia run along the coast and the low T_{BPP} indicate a stable contact between these Core Areas. While the cost of BPP between the north of France and the Rhône valley reaches to $T_{BPP} > 9$ considering HEP_{CA}, the cost sinks when considering

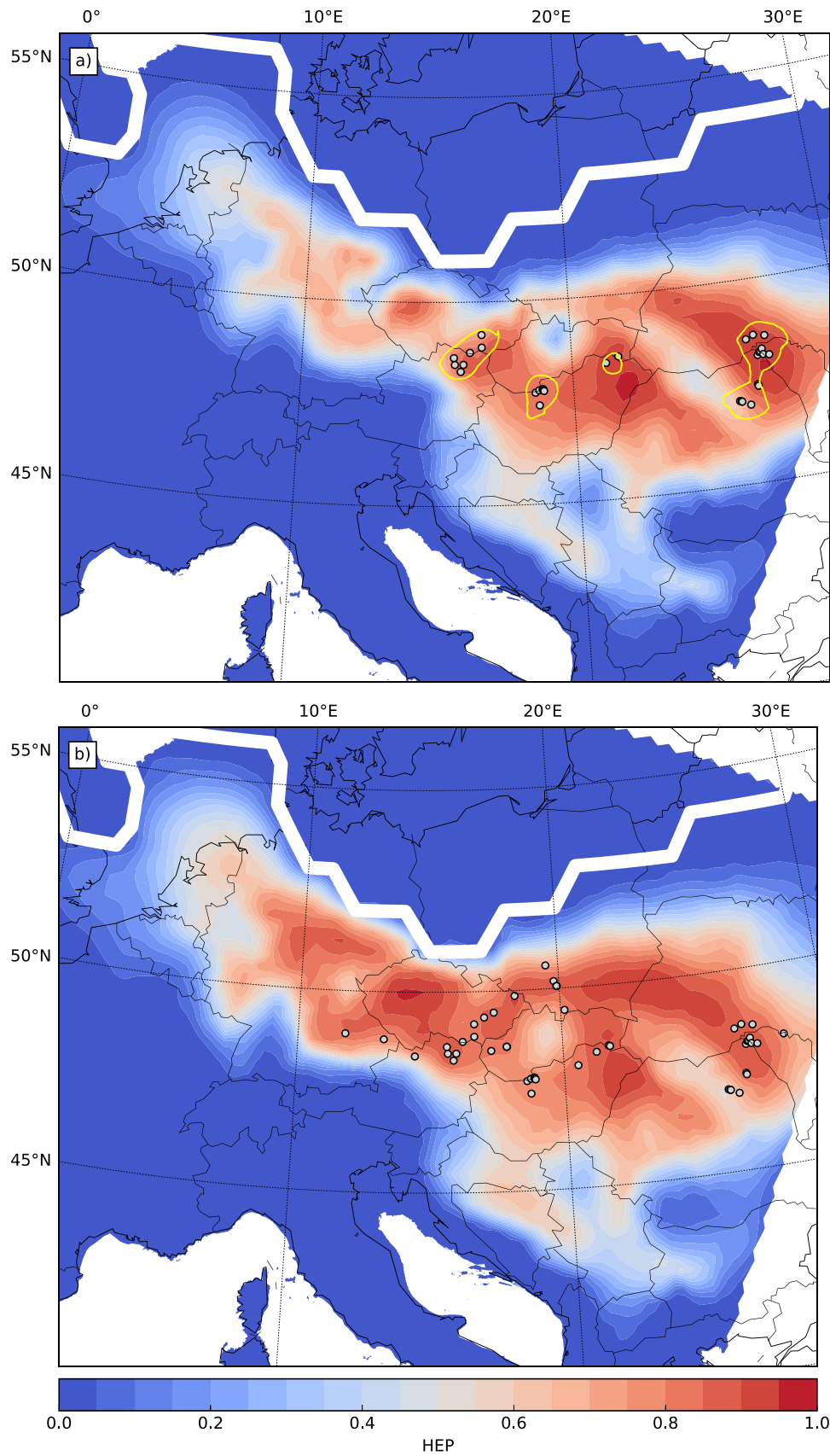


Fig. 7. Human Existence Potential (HEP) derived by logistic regression with the bioclimatic variables Bio 1, Bio 4, Bio 15 and Bio 19 and archaeological sites of the eastern population (east of 10°E). Thereby we incorporated for a) HEP_{CA} sites from Core Areas (DatCA) indicated by yellow lines, and for b) HEP_{ALL} all sites (DatALL). Gray dots: archaeological sites assigned to the LGM and incorporated in the model, white line: glacier extent from PMIP3-reconstructions. (For interpretation of the references to color in this figure legend, the reader is referred to the Web version of this article.)

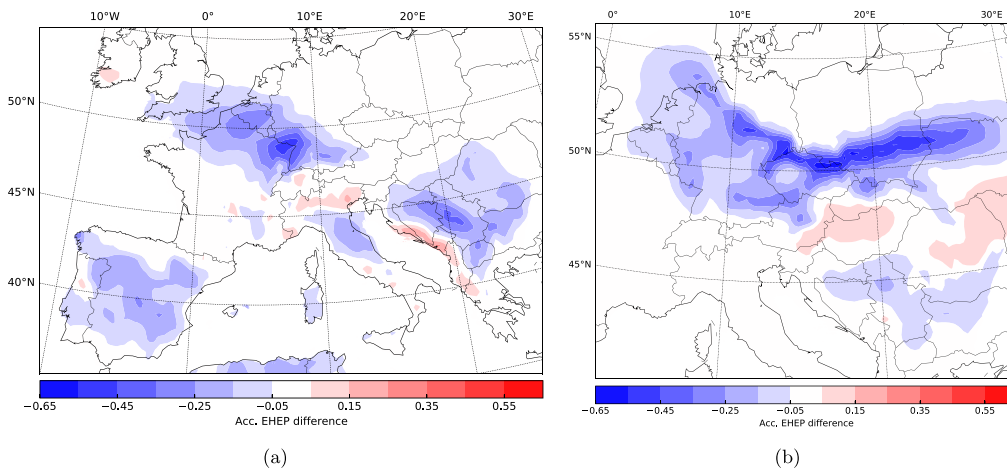


Fig. 8. Difference between the HEP derived using sites from Core Areas (HEP_{CA}) and the HEP derived using all sites (HEP_{ALL}): $\Delta HEP = HEP_{CA} - HEP_{ALL}$; for a) the western population, and b) the eastern population.

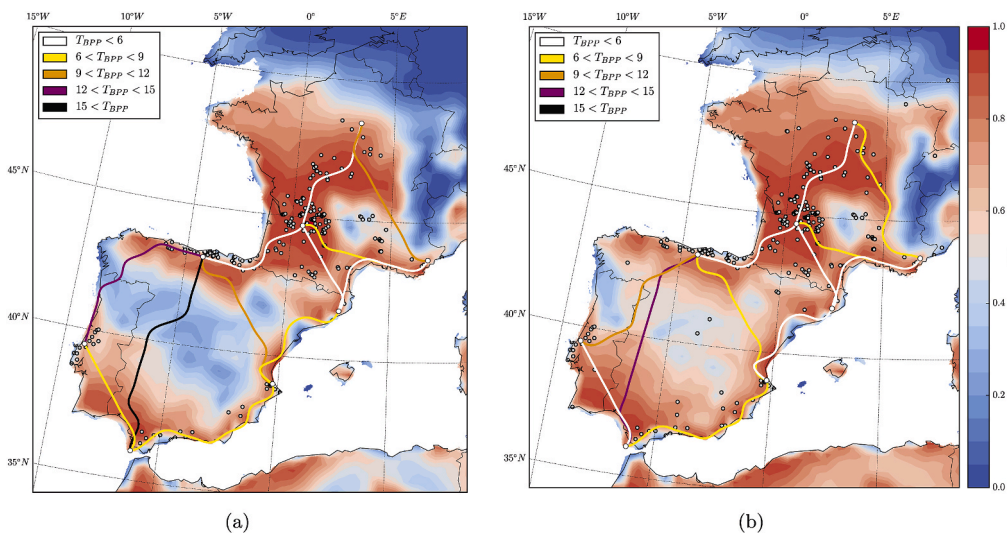


Fig. 9. Solutrean social networks across western Europe established by computing the BPP between centres of Core Areas. The BPP is derived by either (a) using HEP_{CA} or (b) using HEP_{ALL} . The cost of the BPP (T_{BPP}) is indicated by the color. Gray dots: archaeological sites incorporated in the HEP model. (For interpretation of the references to color in this figure legend, the reader is referred to the Web version of this article.)

HEP_{ALL} . The BPP then crosses the Core Area at the Massif Central.

On the Iberian Peninsula, BPPs between the Core Areas located at the Mediterranean coast follow the course of the coastline, and for both scenarios the connections have relatively low costs ($T_{BPP} < 9$). The two BPPs going through the inland of Iberia, in contrast, display much higher costs, which are, however, somewhat lower if the BPPs are determined based on HEP_{ALL} . The BPP connecting the Core Areas between the north coast and the west coast of Iberia is associated with high cost based on the HEP_{CA} ($T_{BPP} > 12$). With HEP_{ALL} , the course of the BPP moves further inland, along the Vale de Côa, and the cost is lower.

5.4. Environmental Human Catchment

To evaluate the HEP for Europe as a whole during the LGM, we combine the HEPs of the western and eastern population into a single

pattern. Since the high HEP regions of the western and eastern populations do not overlap (cf. Figs. 6 and 7), we take at each grid point the largest HEP_{CA} for either the eastern or the western population (Fig. 10). Next, the EHCs of the combined HEP_{CA} are identified by using the rules outlined in Fig. 5 and described in Sec. 4. In total, 15 EHCs are identified in Europe, with 12 associated with the western population and 3 associated with the eastern population (Fig. 10).

The biggest EHC of the western population comprises most parts of France and stretches from the south of Great Britain to the northwest of the Iberian Peninsula. It includes the Core Areas in Franco-Cantabria and northern France, and nine maximums with $HEP > 0.85$ (here after referred to as high local maxima). An EHC, incorporating the Rhône valley's, Catalanian and Massif Central's Core Area, is located along the Mediterranean coast. The Iberian Peninsula is separated into four additional EHCs, one covering the southwestern part and three dividing

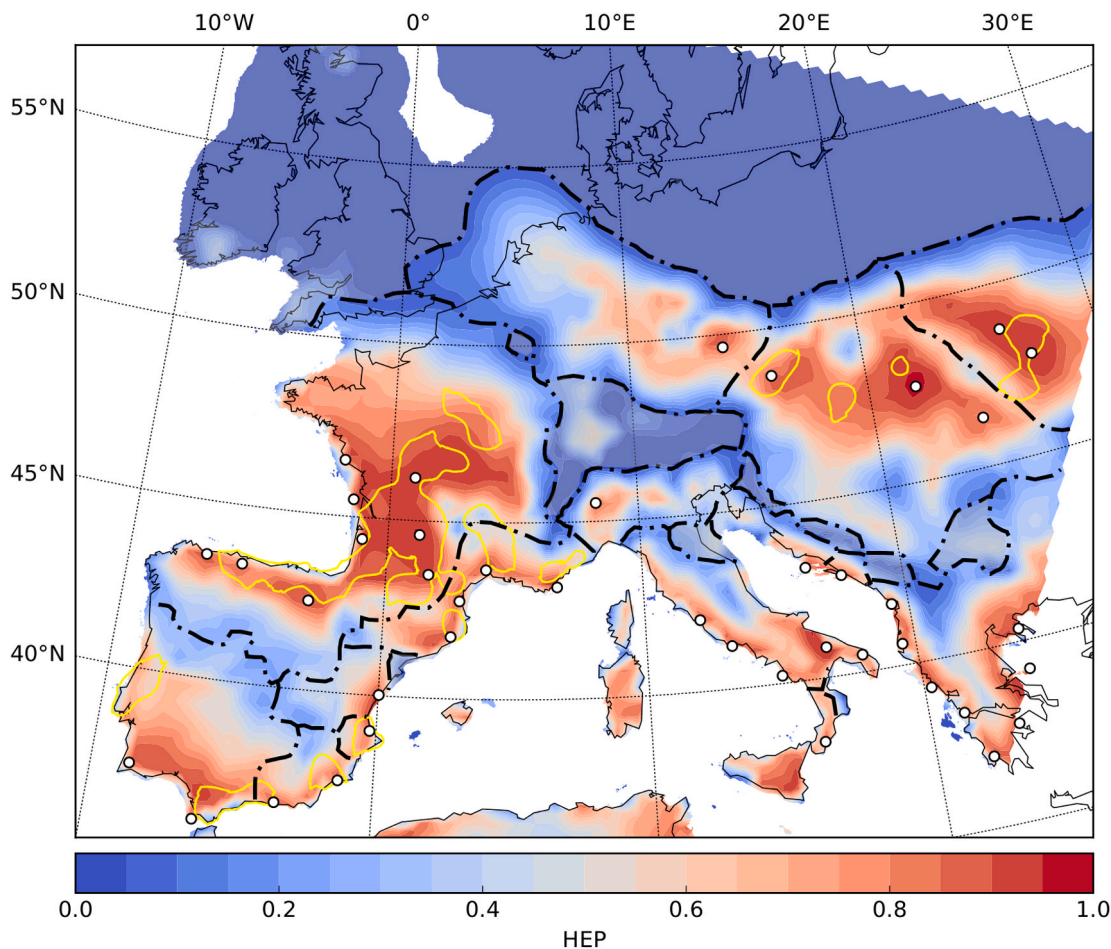


Fig. 10. Human Existence Potential (HEP) for Europe by selecting the largest HEP_{CA} of either the western or the eastern population (Figs. 6b and 7b). Environmental Human Catchments (EHC) are depicted by the black chain line. They are enclosed areas with $HEP > 0.85$ (white dots) and an “upflow” from each grid point to a local maximum. The rules applied to determine EHC are given in Fig. 5. Regions not belonging to an EHC are shaded.

the southeastern part. It is interesting to note that, apart from the high local maximum in Cantabria, all other high local maxima in Iberia are located along the coast. The HEP pattern in Italy and the Balkans is subdivided into a number of small EHCs, with high local maxima along the Mediterranean coast. The relatively sharp boundary dividing the EHC in northern Italy from the south may indicate that hunter-gatherers encountered environmental barriers hindering the southward expansion.

The eastern population considered in this study is divided into three EHCs. The westernmost EHC includes four minor catchments in the Netherlands and Germany, while the maximum, with a HEP of 0.87, is located in the Czech Republic. The maximum of one of the EHCs further east is in Hungary. It extends to the southern regions, bordering with the eastern EHCs associated to the western population. The other EHC covers the northern parts of the high HEP regions with a possible extension to areas further east, which are not included in our dataset.

6. Discussion

The presented HEP results show that the spatial up- and temporal down-scaling of archaeological data provides new insight into the

settlement patterns of hunter-gatherers during the LGM. Mismatches between the archaeological record and the model, or differences between the HEP derived on different datasets (i.e. here DatALL and DatCA) are useful to enrich our understanding of human adaptation. While both, HEP_{CA} and HEP_{ALL} , agree well with the archaeological records for regions of high site density, HEP_{CA} better coincides with the records for regions where none or low presence of hunter-gatherers was expected. For example, while both high HEP_{CA} and HEP_{ALL} regions cover Franco-Cantabria, HEP_{CA} is smaller than HEP_{ALL} in Central Germany and inland Iberian Peninsula, which were sparsely populated based on archaeological evidence.

Fig. 10 shows that 33% of the land area has a HEP_{CA} (eastern and western HEP_{CA} combined) larger than 0.5, and 59% larger than 0.1. These percentages correspond to the minimum and maximum percentages of inhabited land areas estimated by Tallavaara et al. (2015), who investigated human population dynamics from the pre-LGM at 30 ky to the Late Glacial at 13 ky in Europe using modern ethnographic population densities and climate envelope modeling. This outcome indicates that during the LGM high HEP_{CA} regions were inhabited during harsh climate and new territories were explored when the climate became more favorable.

A significant negative ΔHEP is found at the extent of the glacier based on the eastern setup and in the northeastern part of France and northern part of the Balkans for the western setup. This outcome suggests that hunter-gatherers settled continuously in more southern latitudes during the LGM, while intermittent settlements were possible further north. The occurrence of archaeological sites north of the high HEP_{CA} regions can be explained by temporal excursions either under stable conditions or - more likely - during phases of climatic amelioration. Negative ΔHEP also occurs in inland Iberian Peninsula. HEP_{CA} is much lower in the inland than along the coast, indicating that only the coastal areas of the Iberian Peninsula provided stable conditions for viable populations, a long-standing and intensively debated pattern (see Alcaraz-Castaño et al., 2019). ΔHEP suggests that changing climate conditions have increased the probability of hunter-gatherer settlements in the inland in intermittent phases.

The HEP pattern in the Iberian Peninsula is also reflected in the BPP analysis of the Solutrean social network: the cost of the BPP is the lowest along the coast (see Weniger et al., 2019). However, the cost of inland BPPs decreases using HEP_{ALL} , suggesting that changing climate provided intermittent corridors for social networks among hunter-gatherers. These corridors provide plausible explanations to the existence of archaeological sites in inland Spain, such as Peña Capón in the central area and sites of Foz Côa along the north-western route. An improved insight into the social network can be achieved by using higher resolution climate data or by incorporating variables important on smaller time and spatial scales, such as the perceived accessibility and the perception of the landscape.

A striking result of our study is that areas of high HEP_{CA} do not overlap for the eastern and western population. A pattern that is also reflected in the EHCs which are clearly separated for the eastern and western populations. These results suggest that the two population groups inferentially adapted to different environmental conditions and that an environmental barrier may have divided the two groups and prohibited interactions between them. This finding appears to explain the emergence and persistence of the Solutrean and Epigravettian techno-complexes in western and eastern Europe, respectively, throughout the LGM. In comparison to Maier et al. (2016), who came to the same conclusion, our results show a more pronounced difference of environmental adaptations. Possible changes to these observations might emerge when Italy and the Balkans are considered in the training process of the HEP. However, the current reconstructions of the environmental conditions do not support the narrative that close contact between the two populations existed during the LGM. A southward orientation of movement within the Epigravettian is nevertheless possible as suggested by the negative ΔHEP in the Balkan region, which are located to the South of the currently considered eastern European sites.

The EHCs reflect patterns of internal regionalization within the techno-complexes during the LGM. These patterns show a tight correlation with the distribution of regional variants of Solutrean point types on the Iberian Peninsula, which emerged during the Middle and Late Solutrean. These point types, reflecting regional traditions of point manufacture, use, and stylistic - or even idiosyncratic - expressions (Schmidt, 2015a, b), have already been related to ecological niches (Banks et al., 2009). The EHCs underpins the likeliness that these groups would be attracted to the environmental catchments. New studies comparing the extent of EHCs with regional traditions could lead to interesting results.

Exploring the relation between large-scale patterns of human distribution and environmental factors relies heavily on our understanding

and the robustness of the model. Noticeable mismatches between the HEP and the archaeological records exist in some areas. For example, high HEP regions are simulated in central Germany and the Netherlands based on sites of the eastern population, although no archaeological sites have been found there. There are several likely reasons for this mismatch. First, the density of the eastern population was not large enough to trigger dispersal by population pressure. This explanation is supported by the pattern of the EHC. Given the definition of an EHC, preceding external drivers would be required for the eastern population to explore western parts of Germany. As there were no archaeological sites assigned to the LGM in these regions, it is likely that such drivers did not exist. This observation is in accordance with the finding of Maier et al. (2016), that the population density in eastern Europe was extremely low, probably too low to act as a driving force for human emigration out of the catchment into areas further west. It is also likely that since predictors such as flora and fauna, which were only taken indirectly into account in our study by the bioclimatic variables, change the HEP if they are considered. However, adding additional predictors to the model can cause uncertainties on larger scale. Nevertheless, the exclusion of relevant predictors or inclusion of irrelevant predictors is a possible explanation for the mismatches between the modeled HEP and archaeological records. The possibility of archaeological biases, i.e., remains have either not been found or vanished over time, seems rather unlikely, given the current state of knowledge of these regions. Furthermore, as we showed in section 3.3, the HEP model is robust to new archaeological input data.

Another reason for mismatches is probably related to the resolution of the environmental dataset: conspicuously low HEP - despite the presence of several archaeological sites - are observed for the western population at the Massif Central. This area could have been explored and inhabited by hunter-gatherers in intermittent phases of climatic change. Valleys, which are beyond the spatial resolution of our datasets, might have provided niches for temporal or even continuous settlement along the mountains. Better insights of the HEP can be provided in the future by increasing the spatial resolution of the climate data (e.g., Burke et al., 2017; Ludwig et al., 2018).

The 30-year climate simulation which is assumed to represent the average conditions during the LGM from 25 to 20 ky BP, is based on steady state conditions with constant orbital parameters and greenhouse gas concentrations, as evaluated for 21 ky BP, and with a fixed glacier extent and constant surface conditions. This assumption is certainly not the full truth, as changing external forcing must have influenced the climate during the 5000 year period, so that the long-term climate changed. More realistically would be a time dependent $\text{HEP}(t)$ for the LGM based on changing climate conditions. Especially the margins of the high HEP_{CA} regions could have extended northwards during warmer and shifted southwards during colder conditions.

7. Conclusion

In this study, we investigate the human existence potential (HEP) and its implications for human movement and interactions on regional to continental scales in Europe during the LGM. The HEP is evaluated by applying logistic regression of bioclimatic predictors to a dataset of human-presence and -absence based on archaeological sites. The concept of HEP defines the upper limit of the resources available to humans given the technological structure and the social development of the humans. To account for the accessibility, the HEP is computed by applying modification functions, which depend on topography, glaciers, water bodies, and vegetation. By integrating temporal up-scaled

archaeological site data into the HEP model, we could identify regions continuously habitable for humans during the LGM and regions habitable in intermittent phases of climatic improvement. We could thereby explain some of the earlier mismatches between models and archaeological records. We show that, while inland Iberia and regions close to the Scandinavian Ice Sheet were areas unfavorable for continuous settlement in the LGM, those areas had high HEP in intermittent phases, which provided suitable conditions for human settlement, aligning with the sporadic occurrence of archaeological sites.

Due to the harsh climate conditions at the time, most regions in Europe were uninhabitable, only for 33% of the European mainland did the HEP exceed 0.5. This constriction of suitable habitats must have affected the mobility and cultural and demographic developments of humans. Our results support the hypothesis of a human population breakdown in parts of central Europe during the LGM as reflected by the limited inhabitable area, continuing the developments of the final Gravettian. The results also indicate that the western and eastern populations adapted to different environmental conditions, supporting the hypothesis that the emergence and persistence of the Solutrean and Epigravettian techno-complexes in western and eastern Europe, respectively, throughout the LGM were driven by the environment. Moreover, we show that an environmental barrier probably prevented the contact between the two populations.

The BPP and EHC study help to improve our understanding of the dynamics and regionalization of hunter-gatherers, and the social and technological interactions between them. The EHC classification indicates the separation of Solutrean and Epigravettian hunter-gatherers during the LGM. Also, the EHC patterns allow the identification of areas of internal regionalization, as for example on the Iberian Peninsula, where the EHCs correlated well with the distribution of Solutrean point types (Schmidt, 2015a, b). The EHCs give one exploratory scenario

Appendices.

A. Bioclimatic variables

To evaluate the bioclimatic variables, monthly temperature (T) and precipitation (P), and daily maximum temperature (Tx) and minimum temperature (Tn) values on a curvilinear grid with approx. 0.5° resolution of a 30 years time series are used. The calculations are performed for each grid point separately (not shown in the equations).

A.1. Annual Mean Temperature

$$\text{Bio}_1 = \frac{1}{30} \sum_{i=1}^{30} \left(\frac{1}{12} \sum_{j=1}^{12} T((i-1) \cdot 12 + j) \right) \quad (12)$$

A.2. Mean Diurnal Range

$$\text{Bio}_2 = \frac{1}{10958} \sum_{i=1}^{10958} (Tx(i) - Tn(i)) \quad (13)$$

A.3. Isothermality

$$\text{Bio}_3 = \text{Bio}_2 / \text{Bio}_1 \cdot 100 \quad (14)$$

as to why Germany and the Netherlands have so little evidence of human occupation despite the high HEP in these regions. Based on the BPP analysis, we suggest stable contact between Solutrean Core Areas in France and northern Iberia. The dispersal of Solutrean groups into southern Iberia is modeled along the coast, while the inland might have provided corridors during intermittent phases in a changing climate (see also Weniger et al., 2019).

As demonstrated with the BPP method, HEP is a valuable quantity to estimate the likeliness of contact and dispersal processes of hunter-gatherers based on climatic and environmental conditions. In agent-based (Wren and Burke, 2019) or dynamic human dispersion models (e.g., Steele, 2009; Timmermann and Friedrich, 2016), HEP can be used to define the attractiveness of a region for human existence, providing thereby a common ground between HEP-based human dispersion models and agent-based models.

Declaration of competing interest

The authors declare that they have no known competing financial interests or personal relationships that could have appeared to influence the work reported in this paper.

Acknowledgments

The authors thank Andreas Zimmermann (University of Cologne), Andreas Hense (University of Bonn) and two anonymous reviewers for their comments and discussions that helped to improve the paper. This paper was developed within the framework of the CRC 806 (project ID 57444011) and funded by the Deutsche Forschungsgemeinschaft (DFG, German Research Foundation). All simulations were performed at the German Climate Computing Center (DKRZ) within Project 965.

A.4. Temperature Seasonality

$$\text{Bio } 4 = \frac{1}{30} \sum_{i=1}^{30} \sqrt{\frac{1}{12} \sum_{j=1}^{12} (T((i-1) \cdot 12 + j) - \bar{T}_i)^2}, \tag{15}$$

while \bar{T}_i is the mean Temperature of the year i .

A.5. Max Temperature of Warmest Month

T_{xm} is the monthly mean maximum temperature. For $j \in [1, 12]$:

$$\text{Bio } 5 = \max_j \left(\frac{1}{30} \sum_{i=1}^{30} \left(T_{xm} \left((i-1) \cdot 12 + j \right) \right) \right) \tag{16}$$

A.6. Min Temperature of Coldest Month

T_{nm} is the monthly mean minimum temperature. For $j \in [1, 12]$:

$$\text{Bio } 6 = \min_j \left(\frac{1}{30} \sum_{i=1}^{30} (T_{nm}((i-1) \cdot 12 + j)) \right) \tag{17}$$

A.7. Temperature Annual Range

$$\text{Bio } 7 = \text{BIO } 5 - \text{BIO } 6 \tag{18}$$

A.8. Mean Temperature of Wettest Quarter

For each month the precipitation of two consecutive months have been added to get 12 different quarterly precipitations (PQ). For the quarterly precipitation of November and December the precipitation of the following year have been added. In the last year the precipitation of January respectively January and February of the same year is taken. Then, the quarterly precipitation is averaged over the 30 years.

$$PQ_k = \frac{1}{30} \sum_{i=1}^{30} \left(\sum_{j=k}^{k+2} P((i-1) \cdot 12 + j) \right), \text{ with } k \in [1, 12], \tag{19}$$

for $i = 30$ and $k = 11$ and 12 as described in the text.

The quarterly temperature (TQ) is calculated in the same way, but taking the average over 3 month instead of accumulating.

$$TQ_k = \frac{1}{30} \sum_{i=1}^{30} \left(\frac{1}{3} \sum_{j=k}^{k+2} T((i-1) \cdot 12 + j) \right), \text{ with } k \in [1, 12], \tag{20}$$

for $i = 30$ and $k = 11$ and 12 as described in the text.

For $k \in [1, 12]$, where: $PQ_m = \max_k PQ_k$

$$\text{Bio } 8 = TQ_m \tag{21}$$

A.9. Mean Temperature of Driest Quarter

For $k \in [1, 12]$, where: $PQ_m = \min_k PQ_k$

$$\text{Bio } 9 = TQ_m \tag{22}$$

A.10. Mean Temperature of Warmest Quarter

For $k \in [1, 12]$, where: $TQ_m = \max_k TQ_k$

$$\text{Bio } 10 = TQ_m \tag{23}$$

A.11. Mean Temperature of Coldest Quarter

For $k \in [1, 12]$, where: $TQ_m = \min_k TQ_k$

$$\text{Bio } 11 = TQ_m \tag{24}$$

A.12. Annual Precipitation

$$\text{Bio } 12 = \frac{1}{30} \sum_{i=1}^{30} \left(\sum_{j=1}^{12} P((i-1) \cdot 12 + j) \right) \tag{25}$$

A.13. Precipitation of Wettest Month

$$\text{Bio } 13 = \frac{1}{30} \sum_{i=1}^{30} \max_j (P((i-1) \cdot 12 + j)), \text{ with } j \in [1, 12], \tag{26}$$

A.14. Precipitation of Driest Month

$$\text{Bio } 14 = \frac{1}{30} \sum_{i=1}^{30} \min_j (P((i-1) \cdot 12 + j)), \text{ with } j \in [1, 12], \tag{27}$$

A.15. Precipitation Seasonality

$$\text{Bio } 15 = \frac{1}{30} \sum_{i=1}^{30} \left(\frac{\sqrt{\frac{1}{12} \sum_{j=1}^{12} (P((i-1) \cdot 12 + j) - \bar{P}_i)^2}}{\bar{P}_i} \right), \tag{28}$$

while \bar{P}_i is the mean precipitation of the year i .

A.16. Precipitation of Wettest Quarter

For $k \in [1, 12]$, where: $PQ_m = \max_k PQ_k$

$$\text{Bio } 16 = PQ_m \tag{29}$$

A.17. Precipitation of Driest Quarter

For $k \in [1, 12]$, where: $PQ_m = \min_k PQ_k$

$$\text{Bio } 17 = PQ_m \tag{30}$$

A.18. Precipitation of Warmest Quarter

For $k \in [1, 12]$, where: $TQ_m = \max_k TQ_k$

$$\text{Bio } 18 = TQ_m \tag{31}$$

A.19. Precipitation of Coldest Quarter

For $k \in [1, 12]$, where: $TQ_m = \min_k TQ_k$

$$\text{Bio } 19 = TQ_m \tag{32}$$

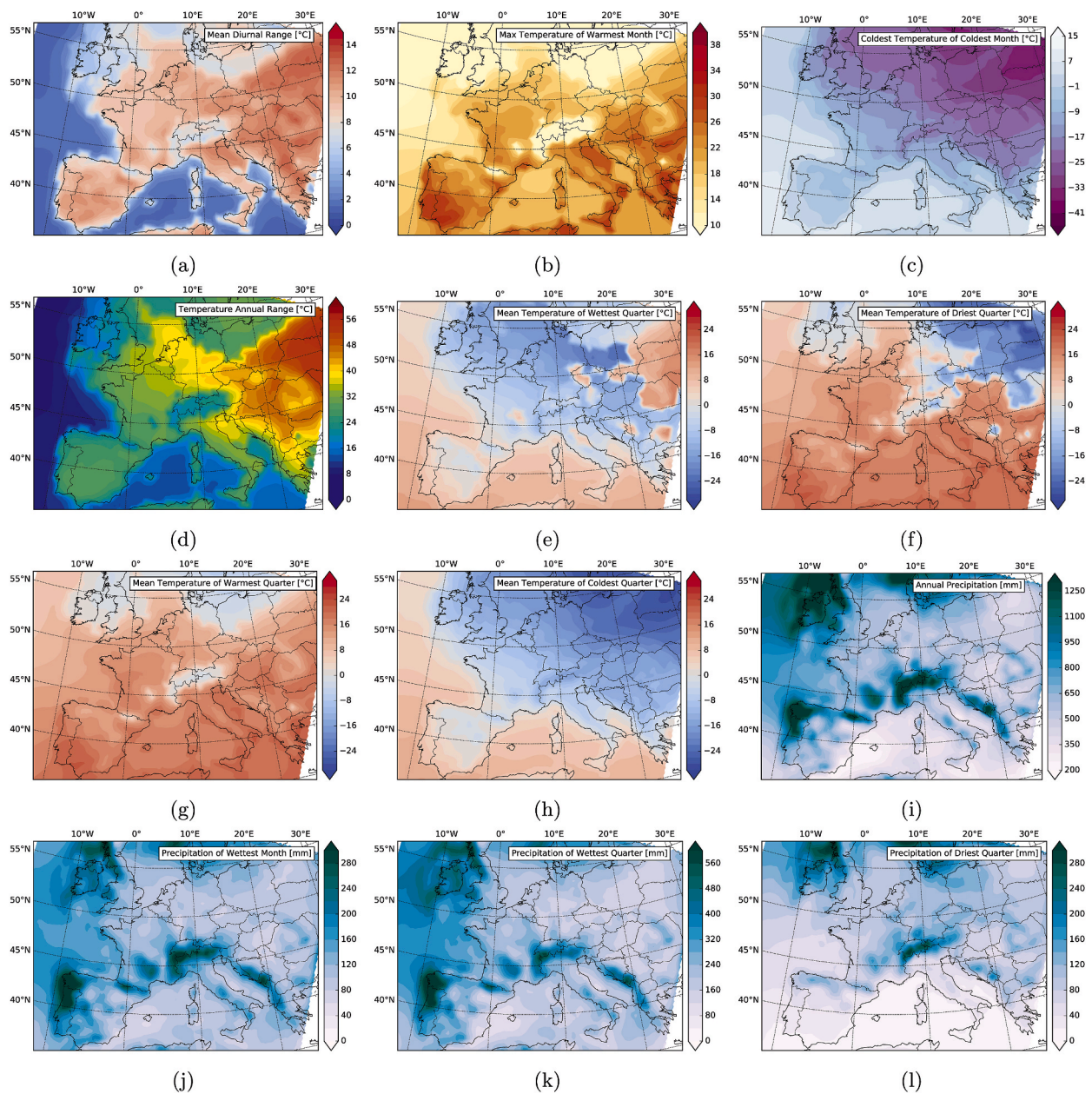


Fig. A.1. Climate maps of the bioclimatic variables not used to calculate the HEP

B. Correlation Clustering

The correlation clustering of the seven predictors remaining after VIF analysis is shown in Fig. B.1. To reduce the amount of predictors, four main branches are defined by choosing a threshold distance score of 0.3. One variable is taken from each branch.

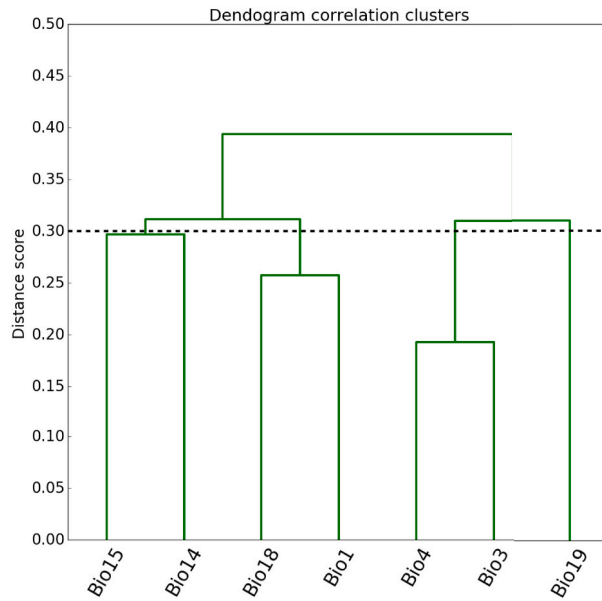


Fig. B.1. Hierarchical dendrogram correlation clustering calculated from the seven bioclim variables determined after VIF analysis

C. Topography around the archaeological sites

We evaluate the average and the standard deviation of the elevation of a 30 s topographic dataset (Shao et al., 2018) by joining them to cells representing a 10 min grid. The elevation and standard deviation of elevation of each archaeological site is taken from the 10 min grid cell it is located in. Fig. C.1 shows the probability of a site to have a specific elevation level. Fig. C.2 shows the probability of a site to feature a specific elevation complexity. The lower and upper limits listed in Table 4 are chosen based on the characteristics of the histograms.

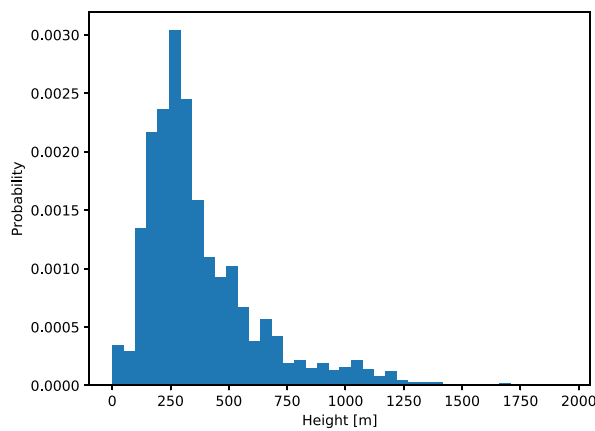


Fig. C.1. Histogram of sites with their elevation.

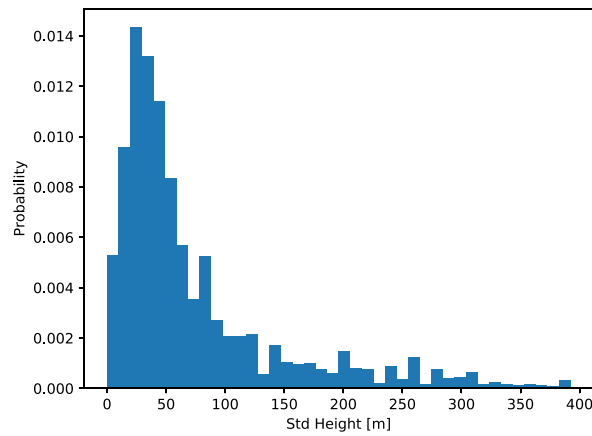


Fig. C.2. Histogram of sites with their complexity (std) of elevation.

D. Sensitivity analysis of the HEP model

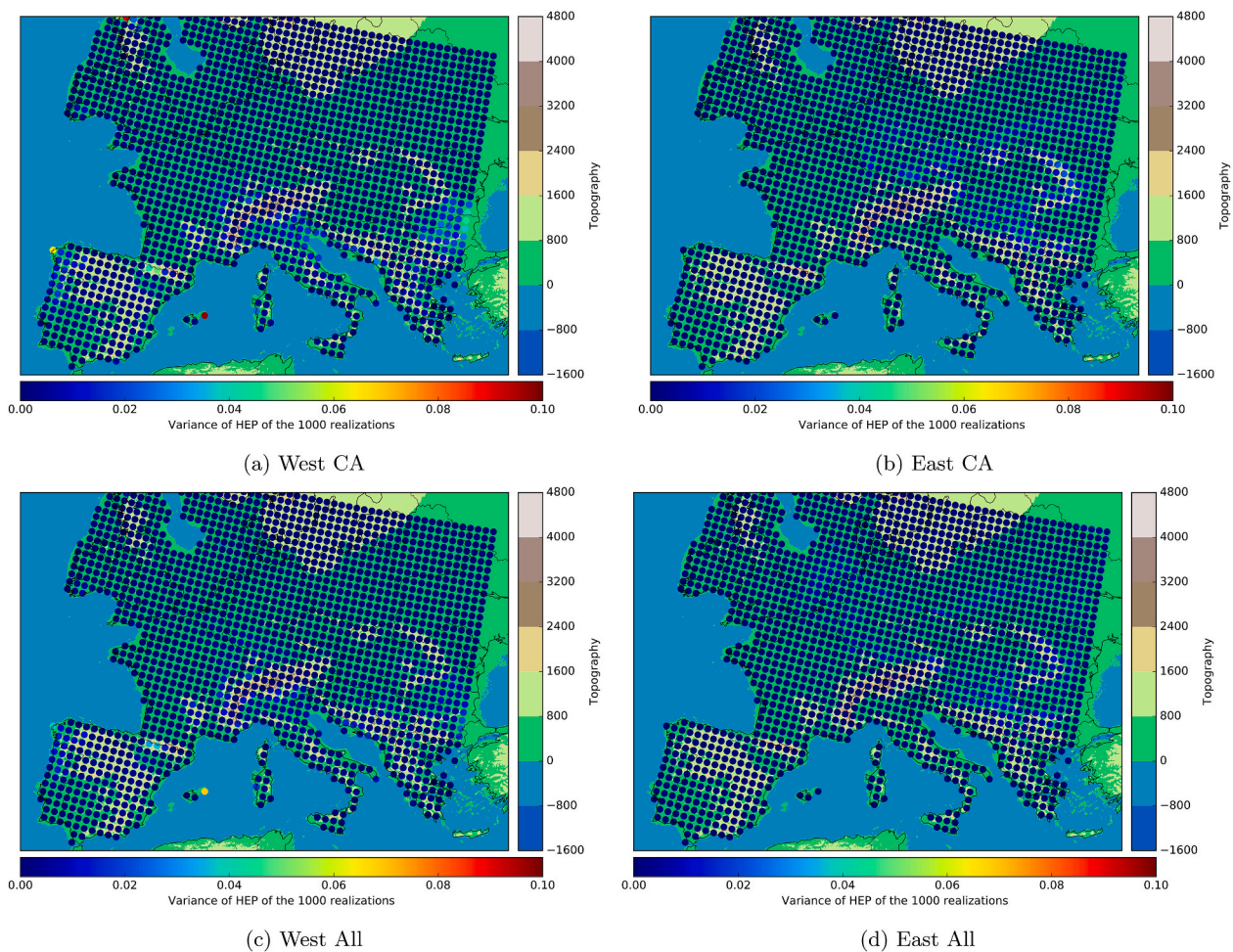


Fig. D.1. Local variance of HEP of the 1000 realizations per grid for a) HEP West CA, b) HEP East Ca, c) HEP West All, and d) HEP East All (depicted topography from Shao et al., 2018).

References

Alcaraz-Castaño, M., Alcolea-González, J.-J., Balbín-Behrmann, R., Kehl, M., Weniger, G.-C., 2019. Recurrent human occupations in central iberia around the last glacial maximum. The solutrean sequence of Peña Capón updated. In: Bicho, N., Cascabeira, J., Schmidt, I. (Eds.), Human Adaptations to the Last Glacial Maximum: The Solutrean and its Neighbors. Cambridge Scholar Publishing, Newcastle upon Tyne, ISBN 978-1-5275-3848-1, pp. 148–170.

- Alin, A., May 2010. Multicollinearity. *Wiley Interdiscip. Rev.: Comput. Stat.* 2 (3), 370–374. <https://doi.org/10.1002/wics.84>.
- Annan, J.D., Hargreaves, J.C., Feb. 2013. A new global reconstruction of temperature changes at the Last Glacial Maximum. *Clim. Past* 9 (1), 367–376. <https://doi.org/10.5194/cp-9-367-2013>.
- Banks, W.E., Zilhão, J., d'Errico, F., Kageyama, M., Sima, A., Ronchitelli, A., 2009. Investigating links between ecology and bifacial tool types in western Europe during the last glacial maximum. *J. Archaeol. Sci.* 36 (12), 2853–2867. <https://doi.org/10.1016/j.jas.2009.09.014>.
- Banks, W.E., d'Errico, F., Zilhão, J., 2013. Human–climate interaction during the early upper paleolithic: testing the hypothesis of an adaptive shift between the proto-aurignacian and the early aurignacian. *J. Hum. Evol.* 64 (1), 39–55. <https://doi.org/10.1016/j.jhevol.2012.10.001>.
- Bartlein, P.J., Harrison, S.P., Brewer, S., Connor, S., Davis, B.A.S., Gajewski, K., Guiot, J., Harrison-Prentice, T.I., Henderson, A., Peyron, O., Prentice, I.C., Scholze, M., Seppä, H., Shuman, B., Sugita, S., Thompson, R.S., Viau, A.E., Williams, J., Wu, H., Aug. 2011. Pollen-based continental climate reconstructions at 6 and 21 ka: a global synthesis. *Clim. Dynam.* 37 (3–4), 775–802. <https://doi.org/10.1007/s00382-010-0904-1>.
- Becker, D., De Andrés-Herrero, M., Willmes, C., Weniger, G.-C., Bareth, G., 2017. Investigating the influence of different DEMs on GIS-based cost distance modeling for site catchment analysis of prehistoric sites in Andalusia. *ISPRS Int. J. Geo-Inf.* 6 (2) <https://doi.org/10.3390/ijgi6020036>.
- Binford, L., 2002. Constructing frames of reference: an analytical method for archaeological theory building using ethnographic and environmental data sets. *J. Anthropol. Res.* 58 (3), 416–419. <https://doi.org/10.1086/jar.58.3.3631188>.
- Bocquet-Appel, J.-P., Demars, P.-Y., Noiret, L., Dobrowsky, D., 2005. Estimates of upper paleolithic meta-population size in Europe from archaeological data. *J. Archaeol. Sci.* 32 (11), 1656–1668. <https://doi.org/10.1016/j.jas.2005.05.006>.
- Braconnot, P., Harrison, S.P., Kageyama, M., Bartlein, P.J., Masson-Delmotte, V., Abe-Ouchi, A., Otto-Bliesner, B., Zhao, Y., June 2012. Evaluation of climate models using paleoclimatic data. *Nat. Clim. Change* 2 (6), 417–424. <https://doi.org/10.1038/nclimate1456>.
- Bradtöller, M., Pastoors, A., Weninger, B., Weniger, G.-C., Jan. 2012. The repeated replacement model – rapid climate change and population dynamics in Late Pleistocene Europe. *Quat. Int.* 247, 38–49. <https://doi.org/10.1016/j.quaint.2010.10.015>.
- Burke, A., Kageyama, M., Latorre, G., Fasel, M., Vrac, M., Ramstein, G., James, P.M., 2017. Risky business: the impact of climate and climate variability on human population dynamics in Western Europe during the Last Glacial Maximum. *Quat. Sci. Rev.* 164, 217–229. <https://doi.org/10.1016/j.quascirev.2017.04.001>.
- Dormann, C.F., Elith, J., Bacher, S., Buchmann, C., Carl, G., Carré, G., Marquéz, J.R.G., Gruber, B., Lafourcade, B., Leitão, P.J., Münkemüller, T., McClean, C., Osborne, P.E., Reineking, B., Schröder, B., Skidmore, A.K., Zurell, D., Lautenbach, S., Jan. 2013. Collinearity: a review of methods to deal with it and a simulation study evaluating their performance. *Ecography* 36 (1), 27–46. <https://doi.org/10.1111/j.1600-0587.2012.07348.x>.
- French, J.C., Collins, C., Mar. 2015. Upper Palaeolithic population histories of Southwestern France: a comparison of the demographic signatures of 14c date distributions and archaeological site counts. *J. Archaeol. Sci.* 55, 122–134. <https://doi.org/10.1016/j.jas.2015.01.001>.
- Grove, M., June 2018. Hunter-gatherers adjust mobility to maintain contact under climatic variation. *J. Archaeol. Sci.: Rep.* 19, 588–595. <https://doi.org/10.1016/j.jasrep.2018.04.003>.
- Hanley, J.A., McNeil, B.J., Apr. 1982. The meaning and use of the area under a receiver operating characteristic (ROC) curve. *Radiology* 143 (1), 29–36. <https://doi.org/10.1148/radiology.143.1.7063747>.
- Hijmans, R.J., Cameron, S.E., Parra, J.L., Jones, P.G., Jarvis, A., Dec. 2005. Very high resolution interpolated climate surfaces for global land areas. *Int. J. Climatol.* 25 (15), 1965–1978. <https://doi.org/10.1002/joc.1276>.
- Kelly, R., 2013. *The Lifeways of Hunter-Gatherers: the Foraging Spectrum*. Cambridge University Press, ISBN 9781107355095.
- Kondo, Y., Sano, K., Omori, T., Abe-Ouchi, A., Chan, W.-L., Kadowaki, S., Naganuma, M., O'ishi, R., Oguchi, T., Nishiaki, Y., Yoneda, M., 2018. Ecological niche and least-cost path analyses to estimate optimal migration routes of initial upper paleolithic populations to Eurasia. In: *The Middle and Upper Paleolithic Archeology of the Levant and beyond, Replacement of Neanderthals by Modern Humans Series*. Springer, Singapore, pp. 199–212. <https://doi.org/10.1007/978-981-10-6826-313>.
- Kretschmer, I., 2015. *Demographische Untersuchungen zu Bevölkerungsdichten, Mobilität und Landnutzungsmustern im späten Jungpaläolithikum*. Kölner Studien zur Prähistorischen Archäologie 6. VML Vlg Marie Leidorf, Rahden.
- Ludwig, P., Pinto, J.G., Raible, C.C., Shao, Y., May 2017. Impacts of surface boundary conditions on regional climate model simulations of European climate during the Last Glacial Maximum: regional European climate during the LGM. *Geophys. Res. Lett.* 44 (10), 5086–5095. <https://doi.org/10.1002/2017GL073622>.
- Ludwig, P., Shao, Y., Kehl, M., Weniger, G.-C., 2018. The Last Glacial Maximum and Heinrich event I on the Iberian Peninsula: a regional climate modelling study for understanding human settlement patterns. *Global Planet. Change* 170, 34–47. <https://doi.org/10.1016/j.gloplacha.2018.08.006>.
- Ludwig, P., Gómez-Navarro, J.J., Pinto, J.G., Raible, C.C., Wagner, S., Zorita, E., 2019. Perspectives of regional paleoclimate modeling. *Ann. N. Y. Acad. Sci.* 1436 (1), 54–69. <https://doi.org/10.1111/nyas.13865>.
- Maier, A., Zimmermann, A., 2015. CRC806-E1 LGM-Sites Database V-20150313.
- Maier, A., Zimmermann, A., 2017. Populations headed south? the gravettian from a palaeodemographic point of view. *Antiquity* 91 (357), 573–588. <https://doi.org/10.15184/aqy.2017.37>.
- Maier, A., Lehmkuhl, F., Ludwig, P., Melles, M., Schmidt, I., Shao, Y., Zeeden, C., Zimmermann, A., 2016. Demographic estimates of hunter-gatherers during the last glacial maximum in Europe against the background of palaeoenvironmental data. *Quat. Int.* 425, 49–61. <https://doi.org/10.1016/j.quaint.2016.04.009>.
- Maier, A., Ludwig, P., Zimmermann, A., Schmidt, I., 2020. The sunny side of the Ice Age: solar insolation as a potential long-term pacemaker for demographic developments in Europe between 43 and 15 ka ago (accepted manuscript). *PaleoAnthropology*.
- Marami Milani, M., Hense, A., Rahmani, E., Ploeger, A., July 2016. Applying least Absolute shrinkage selection operator and akaike information criterion analysis to find the best multiple linear regression models between climate indices and components of cow's milk. *Foods* 5 (4), 52. <https://doi.org/10.3390/foods5030052>.
- Müller, U.C., Pross, J., Tzedakis, P.C., Gamble, C., Kotthoff, U., Schmiel, G., Wulf, S., Christanis, K., 2011. The role of climate in the spread of modern humans into Europe. *Quat. Sci. Rev.* 30 (3), 273–279. <https://doi.org/10.1016/j.quascirev.2010.11.016>.
- Müllner, D., 2013. fastcluster: fast hierarchical, agglomerative clustering routines for R and python. *J. Stat. Softw.* 53 (9), 1–18. <https://doi.org/10.18637/jss.v053.i09>.
- O'Donnell, M.S., Ignizio, D.A., 2012. Bioclimatic predictors for supporting ecological applications in the conterminous United States. *U.S. Geological Survey Data Series* 691, 10.
- Schmidt, I., 2015a. Beyond solutrean point types: technological organization and behavioral implications. *J. Anthropol. Res.* 71 (4), 493–508. <https://doi.org/10.3998/jar.0521004.0071.402>.
- Schmidt, I., 2015b. Solutrean points of the Iberian Peninsula. Tool making and using behaviour of hunter-gatherers during the last glacial maximum. *BAR Int. Ser.* 2778 <https://doi.org/10.30861/9781407314709>.
- Schmidt, I., Bradtöller, M., Kehl, M., Pastoors, A., Tafelmaier, Y., Weninger, B., Weniger, G.-C., 2012. Rapid climate change and variability of settlement patterns in Iberia during the Late Pleistocene. *Quat. Int.* 274, 179–204. <https://doi.org/10.1016/j.quaint.2012.01.018>.
- Schmidt, I., Hilpert, J., Kretschmer, I., Peters, R., Broich, M., Schiesberg, S., Vogles, O., Wendt, K., Zimmermann, A., Maier, A., 2020. Approaching prehistoric demography: proxies, scales and scopes of the Cologne protocol for the European context. In: *Proceedings of the Royal Society Series B, Page to Appear*.
- Shao, Y., Anhäuser, A., Ludwig, P., Schlüter, P., Williams, E., Sept. 2018. Statistical reconstruction of global vegetation for the last glacial maximum. *Global Planet. Change* 168, 67–77. <https://doi.org/10.1016/j.gloplacha.2018.06.002>.
- Skamarock, W., Klemp, J., Dudhia, J., Gill, D., Barker, D., Wang, W., Huang, X.-Y., Duda, M., Jun 2008. *A Description of the Advanced Research WRF Version 3*. Technical Report. UCAR/NCAR.
- Steele, J., Apr. 2009. Human dispersals: mathematical models and the archaeological record. *Hum. Biol.* 81 (2–3), 121–140. <https://doi.org/10.3378/027.081.0302>.
- Stevens, B., Giorgetta, M., Esch, M., Mauritsen, T., Crueger, T., Rast, S., Salzmann, M., Schmidt, H., Bader, J., Block, K., Brokopf, R., Fast, I., Kinne, S., Kornbluh, L., Lohmann, U., Pincus, R., Reichler, T., Roeckner, E., 2013. Atmospheric component of the mpi-m earth system model: echem6. *J. Adv. Model. Earth Syst.* 5 (2), 146–172. <https://doi.org/10.1002/jame.20015>.
- Straus, L.G., 1990a. The last glacial maximum in Cantabrian Spain: the solutrean. In: Soffer, O., Gamble, C. (Eds.), *The World at 18,000 BP: High Latitudes*. Unwin Hyman, London, pp. 88–108.
- Straus, L.G., 1990b. The original arms race: Iberian perspectives on the solutrean phenomenon. In: Kozłowski, J. (Ed.), *Feuilles de Pierre. Les industries à pointes foliacées du paléolithique supérieur européen*. ERAUL, Liège, pp. 425–447. *Actes du Colloque de Cracovie*.
- T, R., Hastie, T., Friedman, J., 2008. *The Elements of Statistical Learning: Data Mining, Inference, and Prediction, second ed.* Springer.
- Tallavaara, M., Luoto, M., Korhonen, N., Järvinen, H., Seppä, H., 2015. Human population dynamics in Europe over the last glacial maximum. *Proc. Natl. Acad. Sci. Unit. States Am.* 112 (27), 8232–8237. <https://doi.org/10.1073/pnas.1503784112>.
- Tibshirani, R., 1996. Regression shrinkage and selection via the lasso. *J. Roy. Stat. Soc. B* 58 (1), 267–288. ISSN 359246.
- Timmermann, A., Friedrich, T., Oct. 2016. Late Pleistocene climate drivers of early human migration. *Nature* 538 (7623), 92–95. <https://doi.org/10.1038/nature19365>.
- Tzedakis, P.C., Hughen, K.A., Cacho, I., Harvati, K., 2007. Placing late Neanderthals in a climatic context. *Nature* 449, 206–208.
- van Andel, T.H., Davies, W. (Eds.), 2003. *Neanderthals and Modern Humans in the European Landscape during the Last Glaciation: Archaeological Results of the Stage 3 Project*. McDonald Institute for Archaeological Research monographs.
- Vita-Finzi, C., Higgs, E.S., Sturdy, D., HARRIS, J., Legge, A.J., Tippett, H., 1970. Prehistoric economy in the mount Carmel area of Palestine: site catchment analysis. *Proc. Prehist. Soc.* 36 (1–37) <https://doi.org/10.1017/S0079497X00013074>.

- Weniger, G.-C., de Andrés-Herrero, M., Bolin, V., Kehl, M., Otto, T., Potl, A., Tafelmaier, Y., 2019. Late glacial rapid climate change and human response in the westernmost mediterranean (iberia and Morocco). *PLoS One* 14 (12), 1–33. <https://doi.org/10.1371/journal.pone.0225049>, 12.
- White, D., Surface-Evans, S., 2012. *Least Cost Analysis of Social Landscapes: Archaeological Case Studies*. University of Utah Press, ISBN 9781607811992.
- Wren, C.D., Burke, A., June 2019. Habitat suitability and the genetic structure of human populations during the last glacial maximum (LGM) in western europe. *PLoS One* 14 (6), e0217996. <https://doi.org/10.1371/journal.pone.0217996>.
- Zimmermann, A., Richter, J., Frank, T., Wendt, K.P., 2004. Landschaftsarchäologie ii: Überlegungen zu prinzipien einer landschaftsarchäologie. *Berichte der Römisch-Germanischen Kommission* 85, 37–95.
- Zimmermann, A., Hilpert, J., Wendt, K.P., 2009. Estimations of population density for selected periods between the neolithic and ad 1800. *Hum. Biol.* 81, 357–380. <https://doi.org/10.3378/027.081.0313>.

Chapter 3

The impact of the Heinrich Event 4 on human populations in Iberia (1): static analysis

Authors

- Konstantin Klein, Institute for Geophysics and Meteorology, Cologne, Germany.
- Patrick Ludwig, Karlsruhe Institute of Technology, Karlsruhe, Germany.
- Yaping Shao, Institute for Geophysics and Meteorology, Cologne, Germany.
- Christian Stepanek, Alfred Wegener Institute, Helmholtz Centre for Polar and Marine Research, Bremerhaven, Germany.
- Xu Zhang, Alfred Wegener Institute, Helmholtz Centre for Polar and Marine Research, Bremerhaven, Germany.
- Gerd-Christian Wegener, Neanderthal Museum, Mettmann, Germany.

Abstract

The Iberian Peninsula is of particular interest for the transition from Neanderthals (NEA) to anatomically modern humans (AMH) due to its geographical position. AMHs arrived here last on their way from Eastern Europe and possible contacts between the two human populations happened here later than elsewhere in Europe. Rapid climate change affected human dispersal and demography during MIS 3. Various studies emphasize the role of Heinrich events in this context. The Heinrich 4 event (HE4) occurred in this transition phase. A precise chronology of the cultural process is missing or highly controversial. We model the Human Existence Potential (HEP) of the HE4 as an example for stadial conditions and of Greenland Intestadial 9 (GI9) as an example for interstadial conditions and examine their influences on the populations in the Iberian Peninsula. Our results show that HE4 had a dramatic impact on both populations. During HE4, large parts of the peninsula were not suitable for settlement. This is especially true for the immigrating AMHs. Resident Neanderthals had to leave the interior of the peninsula. High HEP existed only at isolated hotspots in coastal areas. This indicates a high vulnerability of the social networks. While we cannot conclude definitively whether this instability led to a breakdown of the NEA population, it is plausible to suggest that it was crucial for the demise of NEA. The model results show that even under interstadial conditions only patchy coastal areas were suitable for the settlement of AMH. During HE4 relatively high HEP existed only in a small stretch in Northern Iberia. The influence of AMH on the demise of NEA is found to be insignificant.

3.1 Introduction

Heinrich events are phases in which armadas of icebergs of the Laurentide Ice Sheet drift from the Hudson Strait southwards in the North Atlantic, melt on their way and create fresh water release to the ocean (Heinrich, 1988; Bond et al., 1992). The reduced salinity and lower temperature of the freshwater lead to changes in the thermohaline circulation in the North Atlantic. The climate changes of an Heinrich Event are caused by two factors, the freshwater impulse (Clement and Peterson, 2008) and the topographical changes of the Laurentide Ice Sheet (Ziemen et al., 2019). The freshwater release changes the sea surface temperature gradient of the North Atlantic and thereby shifts the Inter Tropical Convergence Zone to the southeast. In addition, the lower temperature leads to a reduction in evaporation and a subsequent decrease in precipitation. The decrease in the height of the Laurentide Ice Sheet shifts the jet stream to the north, thereby weakening the subpolar gyre and the transport of heat to Europe (Hofer et al., 2012).

In general, humans' evolution is shaped by change and adaptation to new conditions imposed by the environment (Müller et al., 2011; Maier et al., 2016; Timmermann and Friedrich, 2016; Ludwig et al., 2018; Klein et al., 2021). Harsh climate conditions may trigger new adaptations by technological or social innovations or adjustments (Bradt Möller et al., 2012; Schmidt et al., 2012), but also the loss of knowledge due to the breakups of social networks (Banks et al., 2009). Marine isotope stage 3 (MIS 3) was a phase of repeated rapid climate changes on millennial scales. However, low resolution of archaeological site chronology and radiocarbon dating do not allow a precise connection between the climate oscillations such as Heinrich Events to cultural changes (Tzedakis et al., 2007; Schmidt et al., 2012). Nevertheless, abrupt climate changes, as shown in proxy data (Wolf et al., 2018) or climate model simulations (Sepulchre et al., 2007; Ludwig et al., 2018), are often found to correspond well to the time periods of human transition, suggesting their significant impact on the Late Pleistocene hunter-gatherers.

In this study, we investigate the climatic impact of the Heinrich event 4 (HE4) during Greenland Stadial 9 (GI9) at about 40 ka (Roche et al., 2004) on human subsistence in Iberia. Between HE5 and HE4 an important population turnover took place in Europe. Indigenous Neanderthal (NEA) populations with basically Middle Palaeolithic (MP) lithic technology were replaced by immigrating groups of anatomically modern humans (AMHs). In Iberia, these early AMH groups are connected to the Aurignacian (AUR) techno-complex that reached the area from Eastern Europe via Southern France. Even after decades of research, this pan-European transition process is still not well understood and subject of numerous hypotheses, some of which contradict each other (Villa and Roebroeks, 2014). Even if genome sequencing and paleontological analyzes were able to prove that contact and interbreeding took place between NEAs and AMHs (Trinkaus, 2007; Fu et al., 2016), it is still not clear why the NEAs became extinct. Whether the abrupt climate and vegetation changes (Staubwasser et al., 2018), competitive exclusion (Banks et al., 2008), repeated migration by random species drift (Kolodny and Feldman, 2017), inbreeding, allee effects and stochasticity (Vaesen et al., 2019), or the lower efficiency in exploiting resources compared to AMHs (Timmermann, 2020) were decisive. The hypothesis of "cognitive superiority" of the AMH, which was favoured for many decades, is now considered the least probable (Villa and Roebroeks, 2014).

In Iberia, as elsewhere in Europe, the timing of the disappearance of NEAs is highly debated (Wood et al., 2013; Galván et al., 2014; Zilhão et al., 2017; Kehl et al., 2018; Wolf et al., 2018). NEA fossils from El Sidrón are dated directly to 48.4 ± 3.2 ka

BP (Higham et al., 2014). Fragmentary NEA remains from Sima de las Palomas de Cabezo Gordo, likely not preserved in primary deposition, were found together with burnt faunal bones, that provide two radiocarbon dates with age ranging between 42.01 ka cal BP and 38.4 ka cal BP (Walker et al., 2008; Zilhão et al., 2017). But radiocarbon dating of burnt bones is assumed to be less reliable (Wood et al., 2013), and the stratigraphic context of Units A and B does not exclude the possibility that the accumulation of the remains occurred long after NEAs disappeared. While sites with dated NEA fossils are rare, sites with MP technology, representing NEA groups from MIS 3, are abundant in Iberia (Rotgänger et al., 2021). At several of these sites, MP assemblages were dated to younger than 45 ka and gave support to the idea of a late survival of NEAs (Zilhão et al., 2017). In particular, Southern Iberia was assumed as their last refuge and the "Ebro frontier" model was proposed, which suggests that the environmental conditions in the Ebro Valley in northwestern Spain prevented the further southward dispersal of AMHs (Zilhão, 2000). Stratigraphic re-evaluation of several of these sites and new and more reliable radiocarbon dating in combination with independent age control using U/Th or luminescence methods (Maroto et al., 2012; Wood et al., 2013, 2014, 2018; Kehl et al., 2013, 018b,a; Higham et al., 2014; Galván et al., 2014; Cunha et al., 2019; Zilhão et al., 2021) changed the perspective. Late MP layers were thus pushed back by several millennia. Currently, few sites remain which provide indirect evidence for a late survival of NEAs in the South of Iberia, such as Sima de las Palomas de Cabezo Gordo and Cueva Antón in Murcia (Walker et al., 2008; Zilhão et al., 2017). At Gorham's cave in Gibraltar, radiocarbon dating of layers securely linked to the MP levels, yielded ages older than 43.8 ka cal BP (Zilhão, 2006). Recently, the deposition of the uppermost alluvial deposits with MP finds at the open-air site of Cardina/ Salto de Boi in Northern Portugal was luminescence dated to 39.5 ± 1.8 ka (Aubry et al., 2020). Out of nearly 100 MP sites from MIS 3, not more than three might belong to a time frame around 40 ka cal BP. The vast majority of the sites dated to the Late MP in Iberia suggests a much earlier abandonment by NEAs, probably before ca. 45 ka (Higham et al., 2014). This would indicate a bust of the NEA population already with HE5 and the final disappearance at the latest before or during HE4.

Against this very complex chronological background, we model the human existence potential (HEP) of the HE4 and the preceding Greenland Interstadial 9 (GI9) in Iberia and South France to test the impact of rapid climate change on the populations of NEAs and AMHs. The HEP is estimated based on a selection of climatic predictors and archaeological sites (Klein et al., 2021; Shao et al., 2021). We use high-resolution regional climate model simulation and the latest compilation of the AUR and MP excavation sites. The AMHs of the AUR were pioneers and not yet adapted to the conditions in Iberia, so it is necessary to include sites outside Iberia to evaluate their adaptive range. Two different HEP simulations are carried out, one with all sites (AUR All) and the other with only those sites assigned to the first settlement phase of the AUR in the time period before and during the HE4 (AUR P1) (Shao et al., 2021). In contrast, the NEAs had lived in Iberia for tens of thousands of years and were well adapted to the local conditions. For this reason, only the sites within Iberia are included in the HEP calculation, so all sites in Iberia assigned to the MP during MIS 3 are used for the NEA population (Rotgänger et al., 2021). We assume that both the AMH and NEA populations were adapted to the conditions of the GI9. The HEP of the HE4 of both human species is then calculated by applying the fitted coefficients of the logistic regression based on the GI9 conditions to the new climate (for a comparison, see Shao et al. (2021)). By comparing the differences in HEP between

GI9 and HE4, we can estimate the climatic impact of the event on the human populations. We identify refugia, where the human populations could have survived the harsh conditions. Moreover, probable regions of contact between AMHs and NEAs are indicated, giving new impetus to the discussions regarding the transition from the Middle to Upper Paleolithic in Iberia.

3.2 Results

The best HEP regions for the NEAs during the GI9 are the coastal areas of Iberia and parts of the Northern Meseta, where most of the archaeological sites are located (Fig. 3.1a). The highest HEP, with values greater than 0.9, occurs along the northern coast, Mediterranean coast and the western coast of Portugal. With an area of almost zero HEP in the northwest of Iberia and an area of low HEP in southern Meseta, the west coast is largely cut off from the rest of the peninsula. Both these areas correspond with the archaeological site distribution, as no late MP sites have been found there. In contrast, the northern Meseta is an area with high HEP but very low site density, especially in the western part. The NEAs were well adapted to the topographically demanding terrains. The mountain ranges in central Iberia, including the Iberian System (Sistema Ibérico) and Central System (Sistema Central), which appeared to be obstacles for the AMHs to expand into central Iberia (Fig. 3.2a), were potential habitats for the NEAs. In GI9, the NEAs were well adapted to the diverse topographic and local-climatic conditions as seen in the broad frequency distribution of the topographic properties (Fig. 3.3) and local-climatic conditions (Fig. B.2.1) of the MP sites. The diverse local-climatic conditions are reflected in the range of annual mean temperature (Bio1) and precipitation seasonality (Bio15). The distribution of the temperature seasonality (Bio4) quickly approaches zero for temperature variations greater than 6K, which could explain why the HEP is generally lower in inland Iberia, especially in southern Meseta (Fig. B.1.2). Based on the distributions of the precipitation of the wettest (Bio16) and driest (Bio17) quarters, the Neanderthals of Iberia were generally more adapted to drier conditions. However, MP sites are also located in regions with more rainfall (Fig. B.1.4 and B.1.5), such as in northern Iberia, which on the one hand shows the broad adaptive range of the NEA, and on the other hand indicates different ways of life of the NEA in north and south Iberia.

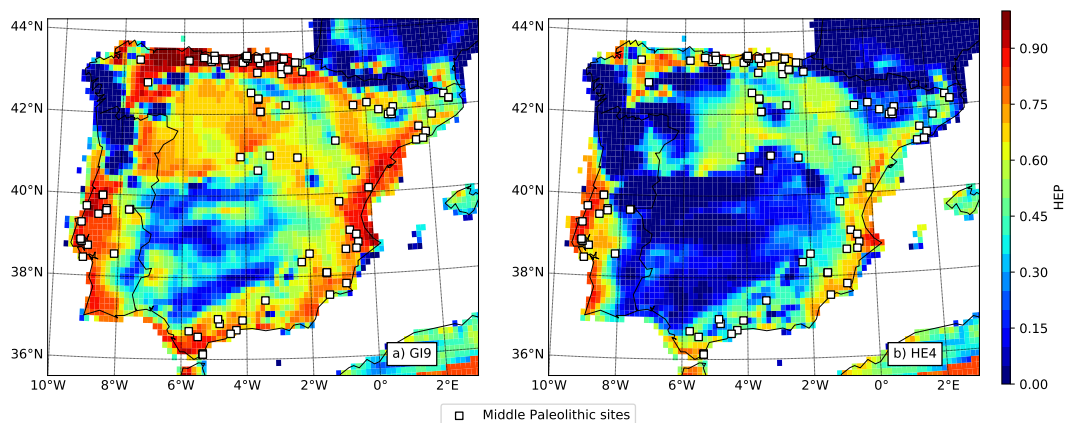


FIGURE 3.1: HEP of the NEA for GI9 (a) and HE4 (b) conditions based on the MP sites (white squares) and the logistic regression coefficients estimated by the GI9 bioclimatic variables.

The HE4 must have affected the NEAs all over Iberia, as the HEP decreases by 0.1

- 0.5 across almost the entire peninsula (Fig. 3.1b). The effects are generally more pronounced in the interior than in the coastal areas where in some places the HEP even increases compared to that for the GI9. The results therefore indicate that the NEA settlements in the interior of the Iberian Peninsula, which were already sparse during GI9, were abandoned at an earlier time than in the coastal areas which served as places of retreat. Areas with high HEP are now limited to the Valencia region, the coast of Portugal, and smaller areas in the Ebro depression, the Central depression and in the north and south of Iberia. At the Portuguese coastal areas, the HEP hardly changes, but the area is now more clearly cut off by low HEP regions.

The HEP for the AMH of the AUR All shows high values in most parts of Franco-Cantabria, which is also reflected in the distribution of archaeological sites (Fig. 3.2a). In northern Iberia, high HEP regions extend to the west coast of Spain, i.e. significantly further than the westernmost site location Arnero in Asturias of the data set. In addition, some areas along the west coast of Portugal are potentially good settlement areas for AMH hunters-gatherers during the GI9. However, these regions are largely cut off from the other settlement areas by low HEP areas. Similar results for Franco-Cantabria and the Iberian west coast occur for AUR P1 (Fig. 3.2c). Interesting differences between the two modeling results can be seen along the Mediterranean coast of the Iberian Peninsula. While the Mediterranean France exhibit favourable HEP in both simulations (AUR All: 0.55 - 0.8, AUR P1: 0.75 - 0.95), the Mediterranean coast of Spain differs significantly. In AUR All, suitable HEP regions with $HEP > 0.5$ occur along the entire coast up to the southernmost site Bajondillo in Andalusia. In contrast, there are no suitable HEP areas south of the Ebro Valley for AUR P1. The small areas with moderate HEP in the interior of the Iberian Peninsula are slightly connected to coastal areas for AUR All, while they are cut off for AUR P1. The topographical range to which the AMHs have adapted is significantly smaller than that of the NEAs. There are only a few sites at altitudes above 600 m and topographical roughness greater than 150 m (Fig. 3.3). The climate distributions of AUR All sites show that AMHs were well adapted to a high range in temperature seasonality and both dry and wet conditions (Fig. B.2.1). In contrast, the range of annual mean temperatures is very narrow. The low HEP conditions in central and southern Iberia are probably related to the high annual mean temperatures there. In addition, the distribution of Bio15 shows that high precipitation seasonality was not present in the adaptive spectrum of the immigrating AMH of the AUR.

As a result of HE4, the HEP drops sharply in large parts of the Western Mediterranean region (Fig. 3.2b). The inland of the Iberian Peninsula, which at least in small parts had favourable settlement areas under GI9 conditions, becomes a completely hostile area with the HE4, in which the HEP largely falls below 0.05. The HEP decreases do not only affect the inland but also the coastal areas of Iberia. The suitable areas in Portugal are disappearing almost completely and settlement areas on the north and east coast are clearly decreasing. Refuges for the AMHs in known environmental conditions are on the Atlantic coast in southwest France and in the north of Spain, and on the eastern Mediterranean coast of Spain. The effects are similar if one only looks at AUR P1 (Fig. 3.2d). However, the Mediterranean coast of Spain, which already had significantly lower HEP at GI9, is not a refuge. Surprisingly, in contrast, favourable HEP areas occur in Portugal and on the Mediterranean coast of France.

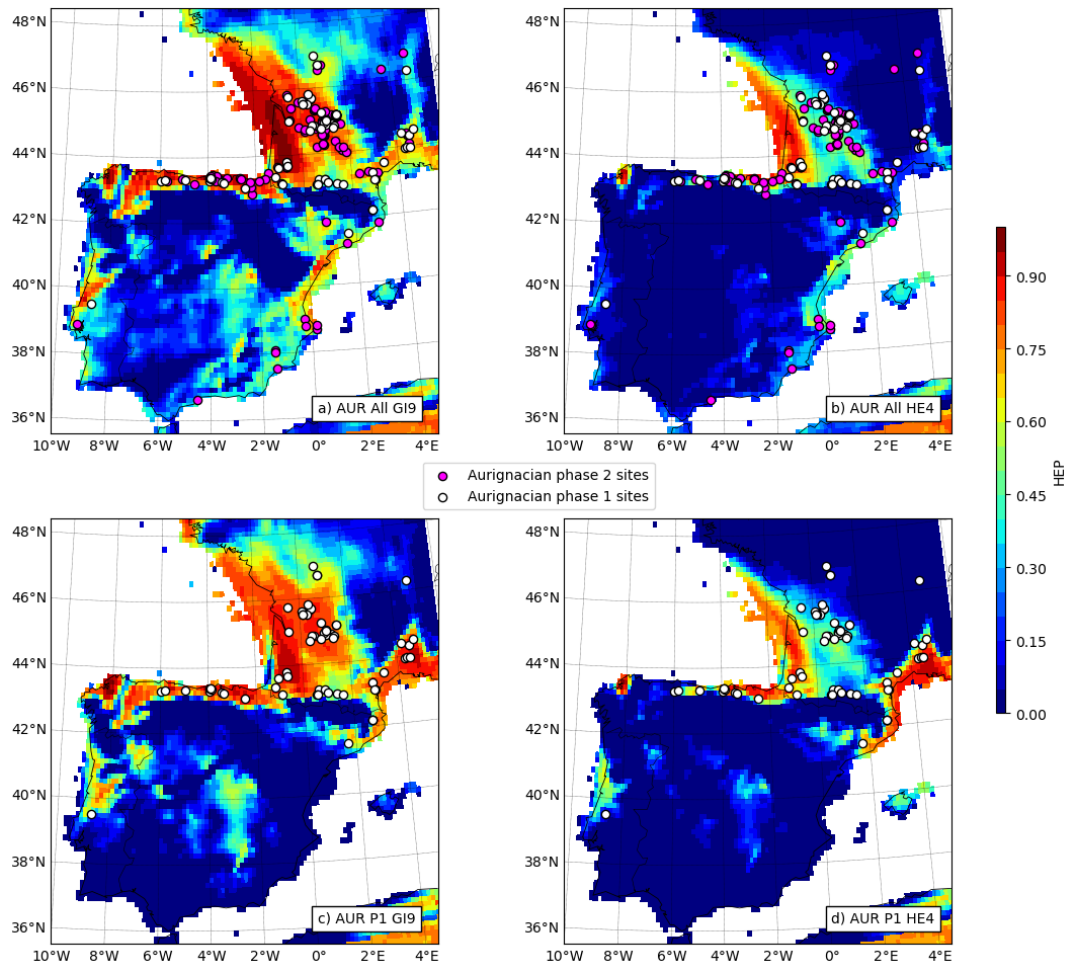


FIGURE 3.2: HEP of the AMHs for GI9 (a, c) and HE4 (b, d) conditions based on all sites of the AUR (AUR All) (a, b) and the sites of the AUR Phase 1 (AUR P1) (c, d) and the logistic regression coefficients estimated by the GI9 bioclimatic variables.

3.3 Discussion

The results shown here are based on the assumption that all sites of the MP in Iberia were potential settlement areas of the NEAs during the GI9. According to current knowledge, at least some, if not the majority of the sites were no longer populated at the time. Gaps in the site stratigraphy at the end of the Middle Palaeolithic support this assumption. However, due to the low resolution of dating it is difficult to differentiate between specific time slices. So all sources are included here for the statistical evaluation of the NEA adaptation on the Iberian environmental conditions. However, the distributions shown should be interpreted with caution, as they represent a kind of maximum spread of the NEAs under the given climate. Nevertheless, the inclusion of all sites offers the advantage that the results can be transferred to earlier time periods. With the assumption that the conditions for GI9 showed similar climatic patterns as during earlier interstadials, the results can be transferred to earlier interstadial phases, such as the GI13 - GI10, where settlement is assumed for significantly more sites. Analogously, one could also assume that earlier Heinrich events, such as HE5, could have had similar effects on the NEA populations. Based on the assumption we can make statements not only about the periods described but also about the settlement

behavior of the NEAs in Iberia in general.

Our modeling results indicate that significantly more areas could potentially be settled by NEAs than previously assumed by the distribution of archaeological sites. These areas extend not only along the coast, but also over large parts of the interior Iberia, such as the upper Meseta. Longterm surveys in the western part of the Northern Meseta, especially the Duero basin indicate that the absence of sites is not a research bias (Sánchez Yustos and Díez Martín, 2015). Our results also indicate low-resource "deserts" or hostile regions in northwest Spain and the lower Meseta. Even if the adaptive range is relatively wide, the maxima of the climatic distribution of the Neanderthal presence are in the dry and warm areas compared to the climatology (Fig. B.2.1), which suggests that the south of Iberia was more populated than the north. In addition, the occurrence of the small local maxima in the wetter climatic conditions indicate different adaptations within the NEA population of Iberia, suggesting differences between the northern and southern populations.

The occurrence of a stadial or a Heinrich event significantly reduced areas that could potentially be settled, with the changes affecting the inland more than the coast. An appropriate response would be a retreat to coastal areas. At the same time hostile areas in the Duero basin in the Northwest and in the Guadiana and Guadalquivir basins in the Southwest cut off settlement areas in Portugal from the rest of Iberia. This is also true to a lesser extent for parts of the southern Mediterranean coast. One can therefore assume that there was a large-scale breakdown of social networks. As a result, unstable populations and local extinctions may have occurred. The assumption that the south of Iberia could serve as the last refuge for the NEAs during the HE4 (Zilhão, 2000; Zilhão et al., 2017), is very questionable in this context. This also agrees with the study (Ludwig et al., 2018) which showed that southern Iberia was severely affected by extreme droughts during the Heinrich events. Suitable regions with HEP well above 0.5 is limited to a small area at the southernmost tip of Spain, which is also largely cut off from the rest of Iberia by low HEP regions. Based on our results, survival is more likely on the Portuguese or eastern Mediterranean coast. But a fragmentation of the settlement area of the Neanderthals becomes very clear with the corresponding negative consequences for the survival of the populations.

Our modeling indicate that even in GI9 only very limited areas were suitable for settlement by AMHs in the AUR and the settlement area was extremely dispersed and therefore highly vulnerable to climate change. A stable and expanded area was mainly the Cantabrian coast. The results show that the settlement of the coast of Portugal and thus Lapo de Picarairo most likely took place along the Duero Drainage System, while the conditions on the coastal region made settlement and migration impossible. During unfavourable conditions of HE4 the Iberian Peninsula turns out to be a hostile area for AMHs of the AUR. Compared to data for the NEAs, the HEP is dramatically reduced for the AMHs, indicating a reduced adaptive range. The AUR can be divided at least into two phase, separated by the HE4 event (Shao et al., 2021). But due to uncertainties in dating and cultural attribution of assemblages this division is uncertain. However to get deeper insight into the dispersal of AMH in Iberia we carried out two experiments using either early AUR sites (AUR P1) or all AUR sites (AUR All). The sites of AUR P1 are supposed to represent the pioneer phase of the AMHs. During this pioneer phase suitable HEP settlement areas get even more reduced. The two HEP runs differ mainly along the Mediterranean coast. From France to the Ebro Valley, the HEP of the AUR P1 is considerably higher than AUR All, which is particularly evident in the HE4. The difference is due to the fact that the proportion of sites in the region is higher for AUR P1 than for AUR All and the logistical function is thus shifted towards the climatic conditions in the region. Below the Ebro Valley,

however, the HEP of AUR P1 is barely greater than zero, while the AUR All has high HEP areas as far as the southern tip of Spain. The Ebro Frontier hypothesis, i.e. the environmental conditions south of the Ebro valley prevented a further expansion of the AMHs before HE4, therefore applies to AUR P1 and not to AUR All. The settlement of the southernmost AUR site in Bajondillo cave (Cortés-Sánchez et al., 2019) could also have taken place at the time of the GI9, considering AUR All. Unfortunately, some information is lost by limiting the included AUR sites to the western Mediterranean region, which could then influence the result. This is however a necessary compromise, as the climate data is limited to the western Mediterranean. The limitation has the advantage for the research question, because the AUR reflects a pioneering cultural event. It is therefore a testing of its home range and its adaptive capacity. The results of AUR P1 are in contrast to the results of the AUR study of (Shao et al., 2021) where the Mediterranean coast of Spain is a high HEP region. The difference could stem from the fact that the sites along the Mediterranean coastlines in Italy are not included here to determine the HEP.

In conclusion, favourable HEP areas of the NEA that do not overlap with those of AMH are located under GI9 conditions in the Upper Meseta, the Iberian system and southern Spain, considering AUR All, and furthermore in the south of Portugal and on the Spanish Mediterranean coast, considering AUR P1. While it is at least questionable whether the southern regions were not settled by AUR hunters-gatherers, one can assume in the central mountain regions that no AMHs were present at the time. However, the central regions deteriorate most clearly with the onset of the HE4. From this we conclude that it was not just the presence of AMHs that triggered the extinction of NEAs, but rather the change in environmental conditions. Presumably this caused social networks to collapse, which led to unstable populations and ultimately to the extinction of the NEAs.

3.4 Materials and methods

The HEP is the resulting score of a logistic regression with second-degree polynomial climatic variables modified by functions defining the accessibility (Klein et al., 2021). To fit the logistic regression, human presence ($y = 1$) and absence ($y = 0$) need to be defined. Human presence is assumed in a radius of 20 km around each archaeological site, a commonly used value to determine archaeological site catchments (e.g., Becker et al., 2017). The HEP (Φ) is then calculated from the mean of 1000 realizations of logistic regression fits (Eq. 3.4), while each realization originates from different training sets, which are random subsets containing 80% of points from the presence and absence records:

$$\Phi = \frac{1}{1000} \sum_{j=1}^{1000} \left\{ 1 + \exp \left[-(\beta_{0,j} + \vec{\beta}_j \cdot \vec{p}) \right] \right\}^{-1} \cdot g_1 \cdot g_2, \quad (3.1)$$

with $\beta_{0,j}$ being the intercept and β_j the fitted coefficients of the realization $j \in [1, 1000]$, and \vec{p} being the standardized second-degree climatic predictors. Each realization is then evaluated by the test set which consists of the remaining 20% of points from the presence and absence records. The functions g_1 and g_2 define the accessibility of regions by varying the Φ based on the topography. For this purpose, a linear function (Eq. 3.2) is fitted to the topographical distribution of the sites (Fig. 3.3), whereby both the topographical height (g_1) and the roughness (g_2), i.e. the standard

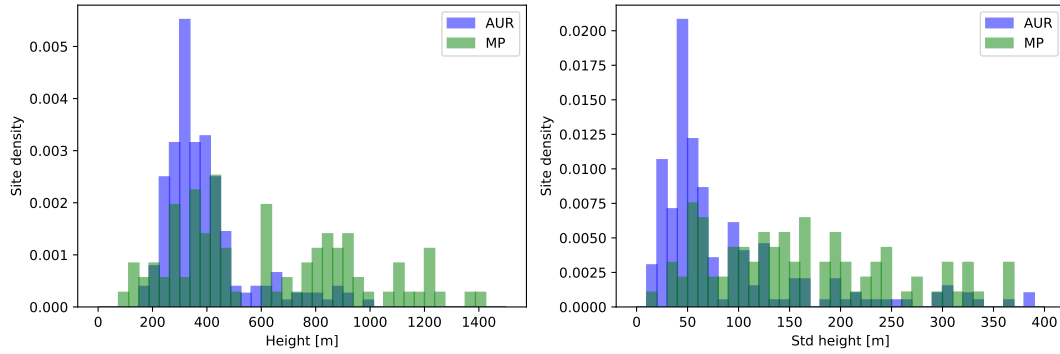


FIGURE 3.3: Topographic distributions of the archaeological sites of the Aurignacian (AUR) and Middle Paleolithic (MP); *left*: topographic height, and *right*: topographic roughness, i.e. the standard deviation of topography around the site.

deviation of the topography around each site, are included.

$$g_{1,2}(x) = \begin{cases} 1.0, & x < x_l \\ 1.0 - (x - x_l) \cdot m, & x_l \leq x < x_u \\ 0.8, & x \geq x_u \end{cases} \quad (3.2)$$

For AUR, the parameters for g_1 are $x_l = 350$ m and $x_u = 2000$ m, and for g_2 $x_l = 70$ m and $x_u = 400$ m. For the MP, $x_l = 450$ m and $x_u = 2000$ m. As the roughness according the MP sites does not show a clear pattern or linear decrease towards higher standard deviations, it is not considered for the accessibility calculation. Furthermore, a sea level of -90 m compared to today is assumed, all grid points that are below this altitude are masked.

3.4.1 Archeological data

The Middle Paleolithic (MP) data set consists of 98 archaeological sites containing proof of NEA existence in Iberia during MIS 3 (white squares in Fig. 3.1). The sites are, for the most part, securely dated and technologically assigned to the Mousterian technocomplex. At some of the sites in northern Iberia both, AUR and NEA evidence, have been found. Moreover, in 8 northerly sites, another technocomplex, the Chatelperronian, occurs in a sublayer of the stratigraphy. This technocomplex is supposed to represent a transition phase of Middle-to-Upper Paleolithic and is associated with Neanderthals. As already discussed, all sites of the MP are listed here for generalization, even if it can be assumed for some of the sites that they were no longer inhabited at the time of GI9.

Since the main focus of the work is on human evolution in Iberia, only the archaeological sites of the Aurignacian that are close to it ($< 47^\circ\text{N}$ and $< 6^\circ\text{E}$) are used, implying that only those humans populated Iberia who have adapted to neighboring environmental conditions. Of the total set of sites that were either technologically assigned to the AUR or dated to the period of about 43-33 kyr calBP, 203 were used that were classified as reliable (dots in Fig. 3.2). Of the sites listed, 66 are assigned to the first settlement phase of the Aurignacian.

3.4.2 Climate data

The global climate simulations were carried out with the global climate model COSMOS (Zhang et al., 2013). Two simulations for the GI9 and the HE4 conditions were carried out with a 30-year run-time, respectively. For both simulations the boundary conditions of the PMIP3 protocol were used (Braconnot et al., 2012). The Heinrich event was implemented by a "hosing" experiment by simulating fresh water flow into the North Atlantic (Kageyama et al., 2013). The freshwater attenuates the thermohaline circulation and leads to a temperature decrease and less evaporation above the North Atlantic.

The regional climate simulations were carried out with the Weather Research and Forecasting (WRF) model (Skamarock et al., 2019). The regional climate model was nested in 5 years of the GCM runs (where the first 5 years are considered for model spin-up and thus are not used for the analysis) of the GI9 and HE4, respectively, to get a high-resolution climate estimate of the western Mediterranean region. The resolution of the WRF model run is 0.15° , which corresponds to around 12.5 km in the middle latitudes and is achieved by a 2-step nesting approach (GCM \rightarrow WRF 50km \rightarrow WRF 12.5 km). While the coarse WRF domain covers entire Europe, the high resolution domain is limited to southwestern Europe. Ice cover was taken over from ICE-6G-C model of the PMIP4 database (Peltier et al., 2015), whereby the ice cover, which arises at a sea level of -72 meters, was used for the GI9 run, and the ice cover at a corresponding sea level of -96 meters was used for the HE4 run. Because there is almost no area-wide information of the vegetation available for GI9/HE4 conditions, the vegetation was set to the potential vegetation of today (Ramankutty et al., 2010). The topography of today was used, while the land-sea -mask was adapted to a reduced sea-level of -72m (GI9) and -96m (HE4). The same topography was used to estimate the accessibility and to create Fig. 3.3. The parameters defining the orbital forcing were set to the values of 40 ky BP, that is the eccentricity = 0.013158, the obliquity = 23.6109° , and the precession = 358.898° . The trace gas concentrations were chosen to be $\text{CO}_2 = 210$ ppm, $\text{CH}_4 = 440$ ppb, and $\text{N}_2\text{O} = 225$ ppb.

3.4.3 Predictor selection

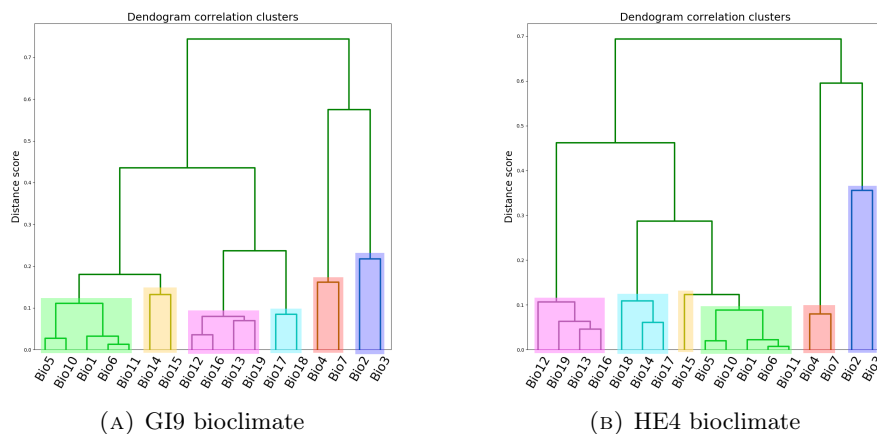


FIGURE 3.4: Dendrogram correlation cluster of the bioclimatic variables for (a) GI9 and (b) HE4, and separation into climate groups: mean temperature (green), temperature variation (red), daily temperature variation (blue), mean precipitation (magenta), precipitation variation (yellow) and mean dryness (cyan)

The 19 bioclimatic predictors are calculated from the regional climate data (for details see Klein et al. (2021)), from which a subset is chosen after statistical analysis to be the climatic predictors to estimate the HEP. The statistical properties thereby must apply to both climate data sets, i.e. for the bioclimatic variables of the GI9 and HE4. Bio8 and Bio9 are excluded in advance because of the discontinuous distribution, as this can lead to problems with the convergence of the regression. For the other variables, the statistical analysis is done by examining the variables for correlation, by applying the dendrogram analysis, and multicollinearity, by estimating the variance inflation factor (VIF). The statistical evaluation is carried out, on the one hand, to reduce the determination of the HEP to variables that contain different information and, on the other hand, to avoid that correlated and collinear variables falsify the result of the regression (Durbin, 1970; Dormann et al., 2013). Finally, of the uncorrelated and non-collinear combinations of variables, the combination that is most important for human existence is used to determine the HEP.

At first, the mutual correlations of the bioclimatic variables are investigated by the dendrogram analysis. Therefore, an hierarchical clustering is applied on the distance matrix (\mathbf{D}), which is defined by the correlation matrix (\mathbf{R}) by: $\mathbf{D} = 1 - \mathbf{R}$, to define a dendrogram. By this method, clusters of variables are hierarchically combined until one cluster remains, which then becomes the root. The distance of the clusters is chosen to be the average distance score of the combined variables. The correlation matrix is calculated only from the climate over land by masking out water grids. The dendrogram subdivides the bioclimatic variables into groups of highly correlated variables (Fig. 3.4). It suggests to divide the variables into six main groups which describe the following (the assignment to different dendrogram groups must apply for both climatic phases, i.e. Fig. 3.4a and 3.4b, since the same set of variables are used for both HEP simulations):

- **Mean temperature:** Bio1, Bio5, Bio6, Bio10, Bio11
- **Temperature variation:** Bio4, Bio7
- **Daily temperature variation:** Bio2, Bio3
- **Mean precipitation:** Bio12, Bio13, Bio16, Bio19
- **Precipitation variation:** Bio14, Bio15
- **Mean dryness:** Bio14, Bio17, Bio18

Bio14 is assigned to both the precipitation variation and the mean dryness group. Only one variable is chosen from each group to minimize the mutual correlations of the predictors.

Permuting over all possible combinations of variables from the six groups gives 400 possibilities, so a further evaluation of the variables is necessary. At first, the group "daily temperature variation", which contains the variables Bio2 and Bio3, is no longer taken into account. The time scale of this group does not correspond to the scale of the HEP. The HEP is supposed to represent the climatic/environmental preference of humans for a period of several hundred years and daily fluctuations are not considered to be of importance in this context. We furthermore assume that the accumulated quarterly rainfall is of greater importance for human existence than monthly values, for either dry or wet conditions. Bio13 and Bio14 are therefore also excluded from further analysis.

TABLE 3.1: Variance inflation factor (VIF) of the bioclimatic variables from the mean temperature (T mean), temperature variation (T var), mean precipitation (P mean), precipitation variation (P var), and mean dryness (D mean) groups. The upper four factors correspond to the GI9 and the lower ones to the HE4 climate.

| | T mean | T var | P mean | P var | D mean |
|--------------|--------|-------|--------------|-------|--------------|
| 1/4/12/15/17 | 5.26 | 1.74 | 10.22 | 6.54 | 13.39 |
| 1/4/12/15/18 | 5.37 | 1.78 | 5.24 | 5.63 | 4.49 |
| 1/4/16/15/17 | 5.19 | 1.75 | 3.85 | 6.42 | 6.49 |
| 1/4/19/15/18 | 5.32 | 1.76 | 2.05 | 5.63 | 2.47 |
| 1/4/12/15/17 | 6.94 | 2.14 | 8.25 | 8.29 | 12.35 |
| 1/4/12/15/18 | 7.4 | 2.16 | 4.63 | 7.56 | 5.29 |
| 1/4/16/15/17 | 6.86 | 2.17 | 2.99 | 8.26 | 6.33 |
| 1/4/19/15/18 | 7.21 | 2.14 | 1.67 | 7.74 | 3.1 |

The first variable to be selected is Bio1 from the mean temperature group. All variables in this group are highly correlated and the annual mean temperature is assumed to be the most important of them for human existence. The standard deviation of temperature and precipitation play an important role for hunter-gatherers as shown in Grove (2018), so Bio4 is selected from the temperature variation group. These considerations confine the combinations of predictors to six possibilities: Bio1, Bio4, Bio12/16/19, Bio15, Bio17/18. For the purpose of a better interpretation of the outcome, the quarterly rainfall quantities are limited to either warm/cold or wet/dry quarters, which leads to an exclusion of the combinations 1/4/16/15/18 and 1/4/19/15/17. The remaining four combinations are tested for multicollinearity by VIF analysis (Tab. 3.1). For a combination of the five variables, a VIF is calculated for each variable from the coefficient of determination of a linear regression where the variable being dependent and the other four variables independent. The combination 1/4/12/15/17 is excluded because it contains variables with a VIF > 10, which is a general used threshold to determine multicollinearity (Alin, 2010). The three remaining combinations 1/4/12/15/18, 1/4/16/15/17 and 1/4/19/15/18 are solid from a statistical point of view, with VIF < 10, and meaningful considering the effect on human existence.

All three combinations are reasonable predictors to estimate the HEP. Since the results of the three regressions differ only slightly from each other, we limit the analysis of the results to the predictor combination 1/4/16/15/17. Deviations are shown in Fig. S2 and S3.

3.4.4 Statistical evaluation

The two quantities that are used for evaluation are the “area under a receiver operating characteristics curve” (AUC) and the Brier skill score (BSS). The AUC measures the

TABLE 3.2: Area under a receiver operating characteristics curve (AUC) and Brier skill score (BSS) for the HEP fits shown in Fig. 3.1 and 3.2.

| | MP GI9 | MP HE4 | AUR All | AUR P1 |
|-----|--------------|-------------|--------------|--------------|
| AUC | 0.89 ± 0.011 | 0.9 ± 0.01 | 0.88 ± 0.013 | 0.9 ± 0.014 |
| BSS | 0.78 ± 0.01 | 0.82 ± 0.01 | 0.78 ± 0.01 | 0.78 ± 0.015 |

accuracy of a binary classification by comparing the true positive and false positive rates (Hanley and McNeil, 1982). The BSS determines the improvement of the fit compared to a comparison model in which only the intercept is considered (Brier, 1950). The values for AUC and BSS for the different fits are shown in Tab. 3.2.

Chapter 4

Constrained Random Walk Model (CRWM)

4.1 Introduction

The Constrained Random Walk Model (CRWM) simulates human dispersal and population dynamics. It is a numerical model based on physical assumptions, and its processes are mainly driven by the human existence potential (HEP), as defined in Chapter 2. The model assumptions are made for hunter-gatherer groups in the Paleolithic. It can, however, be adapted to different mobility and dispersal scenarios by modifying these assumptions and the estimation of the HEP. Here, all assumptions and conclusions are based on the HEP definition for hunter-gatherers, as in [Klein et al. \(2021\)](#). Accordingly, the central assumption of the CRWM is that human dispersal and population dynamics during the Paleolithic are primarily influenced and shaped by climatic and environmental conditions while considering some aspects of social and cultural structure.

In the CRWM, the expansion and dynamics of populations are realized by the mobility and dispersal of individual humans. Based on a given initial population, a trajectory is determined for each human, which is defined by the equations of motion. The two main processes governing human mobility are macroscopic drift and microscopic random motion. Mathematically, these processes can be expressed using a stochastic differential equation, which describes a random walk motion constrained by a drift function. Two constraints of the random walk are included in the drift function: a directional flow based on climate and environment preferences and a diffusion depending on population densities. These constraints are applied because humans migrate towards favorable conditions, cluster to population groups to optimize the conditions of existence and the efficiency of social structures, and avoid overpopulation and over-exploitation of the available resources. In addition to the constrained random walk defining individual human mobility, population size changes are integrated into the model via a birth and death module.

The CRWM has manifold applications. Human migration processes regarding climate preferences or climate change scenarios can be examined by an ensemble average of all individual trajectories. By including population size changes into the modeling framework, extinction events can be simulated or source regions of human populations diagnosed. Moreover, contact or trading networks of different groups and regions can be traced by analyzing migration paths and population flow. The output can include several key quantities defining the migration velocity, random mobility, population sizes, and reproduction. The CRWM is based on three main assumptions, which are elaborated on in the next subsections. Macroscopic and microscopic scales in this context are in the range of 1 - 100 km and 1 - 1000 m, respectively.

- **First assumption:** Dispersal of humans is directed by environmental and climatic factors on the macroscopic level.
- **Second assumption:** Randomness is the dominating factor for human mobility on the microscopic level.
- **Third assumption:** Population dynamics, comprising population size changes and population diffusion, is governed by population densities with respect to the available resources.

4.1.1 Human dispersal driven by climatic and environmental conditions

The first assumption of the CRWM is that the direction and magnitude of human dispersal are driven by the environment and climate on the macroscopic level. As already described and shown in Chapters 2 and 3, the life of hunters-gatherers is largely determined by their environment, which is for the most part shaped by the climate. The hunters-gatherers of the Paleolithic were very flexible and adapted to different conditions. This flexibility made it possible for humans not only to colonize certain biotopes, but also large parts of the Earth. The dispersal of humans out of Africa and into Europe is not a linear process, but rather waves of propagation that are associated with climatic phases (e.g., [Bae et al., 2017](#)). The history of human settlement can be described as an adaptive cycle model with the successive phases of population growth, conservation, distortion and reorganization ([Walker et al., 2006](#)). If climatic instability is introduced as a parameter, the cycle can, depending on its severity, lead to resilience, retreat into refuges, micro and macro extinction or collapse of the system in the populations ([Bradtmöller et al., 2012](#)). This repeated replacement concept is consistent with the climatic and environmentally driven human migration, as simulated in the CRWM.

The modeled migration processes of the CRWM are governed by climate properties. Technically, this feature is implemented as a drift of humans in the direction of favorable climatic regions. The preferences are thereby expressed by means of the human existence potential (HEP). As shown in Chapter 2 and [Klein et al. \(2021\)](#), the HEP is a quantity to assess a region's suitability for human settlement based on the climatic and environmental features. A score is estimated using a set of climate predictors by applying logistic regression with second-degree polynomials on a presence and absence record derived from archaeological site locations. This score is modified by functions depending on topography, vegetation, water bodies and glaciers. As archaeological site data are incorporated in the HEP modeling framework, it contains information about human technological expertise and environmental preferences. As shown in [Klein et al. \(2021\)](#), the preferences of different techno-complexes can differ strongly. The gradient field of the HEP expresses a directional field leading towards more suitable regions, with consideration of the cultural preferences and technological aspects of the society. In the CRWM, the macroscopic part of the human individual mobility is proportional to the gradient of the HEP (see Fig. 4.1). The entire population of a technocomplex experience the macroscopic force towards more favorable regions, defined by the HEP score.

4.1.2 Stochastic mobility of individuals

The second assumption is that randomness determines the human mobility on the microscopic scale. On the macroscopic scale, the migration is described by the general habitation preferences of humans, on the microscopic scale, the human mobility is based on individual behavior. Numerous studies in the anthropological community are concerned with human behavior and mobility of hunter-gatherers (e.g., [Binford \(2002\)](#); [Kelly \(2013\)](#)). Most of the results are based on findings from in situ observations made by today’s hunter-gatherer tribes. Agent-based models often use a modeling setup based on results of those ethnographic field studies (e.g., [Bernabeu Aubán et al., 2015](#); [Cucart-Mora et al., 2018](#)). In contrast to those approaches, I assume that migration is only a deterministic process on macroscopic scale; on microscopic scale, it is supposed to be stochastic. I thereby respect that human behavior cannot be precisely predicted, and, moreover, I avoid incorporating possibly false assumptions into the model from a far-reaching and complex research field that is beyond my knowledge. The mean of the random movement is, however, defined by a certain order of magnitude that is consistent with ethnographic results.

In the CRWM, human microscopic mobility is integrated as a random walk motion based on a given dispersion matrix. Random walk motion can thereby produce fluctuations around a center, which in human groups could occur due to hunting and gathering or social activities. But also small scale movements in random directions can be simulated by the implemented random walk. By assuming the human mobility to be a stochastic process, the trajectory of each human is unique. Technically, the velocity of each human is supposed to be a Markov process in the CRWM, so the velocity of each time step is independent of the velocities of the previous time steps. The stochastic component of the human velocities is thereby integrated as uncorrelated zero mean Gaussian random variables. The individual mobility of each human, in summary, is composed of two components: a macroscopic drift component proportional to the gradient of the HEP and a microscopic stochastic component, as illustrated in [Fig. 4.1](#). A general behaviour of populations can be derived by averaging over the trajectories of the whole population.

4.1.3 Overpopulation and population clustering

In the next step, the presence of other humans and its influence on the migration processes is incorporated in the CRWM, as specified in the third assumption. Accessible resources for human existence in a region, with respect to the particular preferences, are defined by the HEP. However, resource availability is reduced by competition with other humans. On the other hand, the presence of other people offers protection and enables the given resources to be exploited in the first place. Therefore, two aspects of population influences are integrated in the CRWM: first, humans are gregarious animals, so low population numbers in a region are not attractive for human migration; and second, if the population numbers reach or even exceed those possible for the available resources, the attractiveness of a region declines due to overpopulation. The consequences of the first aspect are that humans tend to cluster into groups and that new regions only become attractive for settlement if enough humans are already settled there. The second aspect incorporates the concept of population pressure into the framework of the CRWM. Although it is generally assumed that large-scale migration is not directly triggered by population pressure, it definitely has an effect on local migration movements. If the local resources are insufficient to feed a population, population pressure arises, which leads to a diffusion of people into the surrounding

regions. Regional population pressure can be triggered both by the population exceeding a critical limit and by regional environmental conditions deteriorating due to a changing climate.

The presence of other humans and its influence on human mobility is incorporated into the modeling framework of the CRWM by calculating the population density from the individual positions of each human. Technically, this is done by defining grid cells and dividing the total number of counted humans in the grid cell by the area of the cell. The population density is then compared to the carrying capacity of the region which defines a maximum sustainable population density from the environmental conditions (Kelly, 2013). Since the resources of a region and their accessibility are defined by the HEP, the assumption is made that the carrying capacity is proportional to the HEP. It thus involves technological progress and particular preferences of the cultures. Every human culture therefore has its own *culture carrying capacity* which defines a specific maximum population density depending on the environmental conditions (the exact definition of the cultural carrying capacity can be found in in Sec. 4.4). The ratio of population density to cultural carrying capacity then defines the attractiveness of a region for human settlement and therefore influences the macroscopic dispersal of humans. Both aspects of population influences, as mentioned above, are brought together by the population attractiveness function. This function changes the given HEP to an available HEP which is then used to calculate the macroscopic drift (see Fig. 4.1).

4.1.4 Population growth and decline

Human history shows that the population steadily grew over time. It is assumed that the total population increased steadily with growth rates of 1 – 3 % (Zimmermann et al., 2020). However, this increase was repeatedly accelerated by leaps in growth, probably triggered by the colonization of new areas or technical progress, such as the discovery and use of fire or the agricultural revolution. Nevertheless, as shown by gaps in the stratigraphy of excavation sites and the evolution of human technologies and cultures, there have been periods of population decline and regional extinction. In addition to possible competitive disputes that could have triggered population decline, the climatic and environmental conditions certainly played a decisive role in the population development of the Paleolithic hunters-gatherers (e.g., Bradtmöller et al., 2012). Population size changes also play an important role in migration processes, as local population pressure develops through increasing population sizes, which in turn drives migration. In addition, larger populations increase the likelihood that unpopulated areas will be discovered and colonized. The population changes are therefore a decisive factor that must be taken into account when studying migration processes. In the CRWM it is decided stochastically whether a new human is born or a human dies, but the probability of both processes depends on the environmental and climatic conditions. Arguments similar to those used for defining the population attractiveness function are used to define a birth-death function for the CRWM. Analogously, the two variables determining population size changes are the population density and the cultural carrying capacity. The probability for reproduction is high if a sufficient amount of resources exist in a region with a given population density. The probability for population decline raises when the population density reaches the cultural carrying capacity of a region. Analog to the population attractiveness function, low population densities are adverse, as it is more difficult for humans to survive without nearby humans' support. The so-called allee effect (e.g., Lewis and Kareiva, 1993) is introduced as an additional factor: In areas where the population density falls below

a certain limit value, reproduction can no longer take place and the population will die out with a probability given by the environmental conditions.

4.1.5 Outlook

In the following some mathematical definitions are reflected that are important to understand the CRWM (Sec. A.1). Then, the CRWM and the embedded processes, such as the population attractiveness function and the birth and death module, are mathematically developed. Parameters, which are important for evaluation, are introduced to determine the model output. For the introduced parameters archaeo-physical explanations are provided. Finally, the numerical implementation of the CRWM is illustrated, including the initial state and integrated boundary conditions.

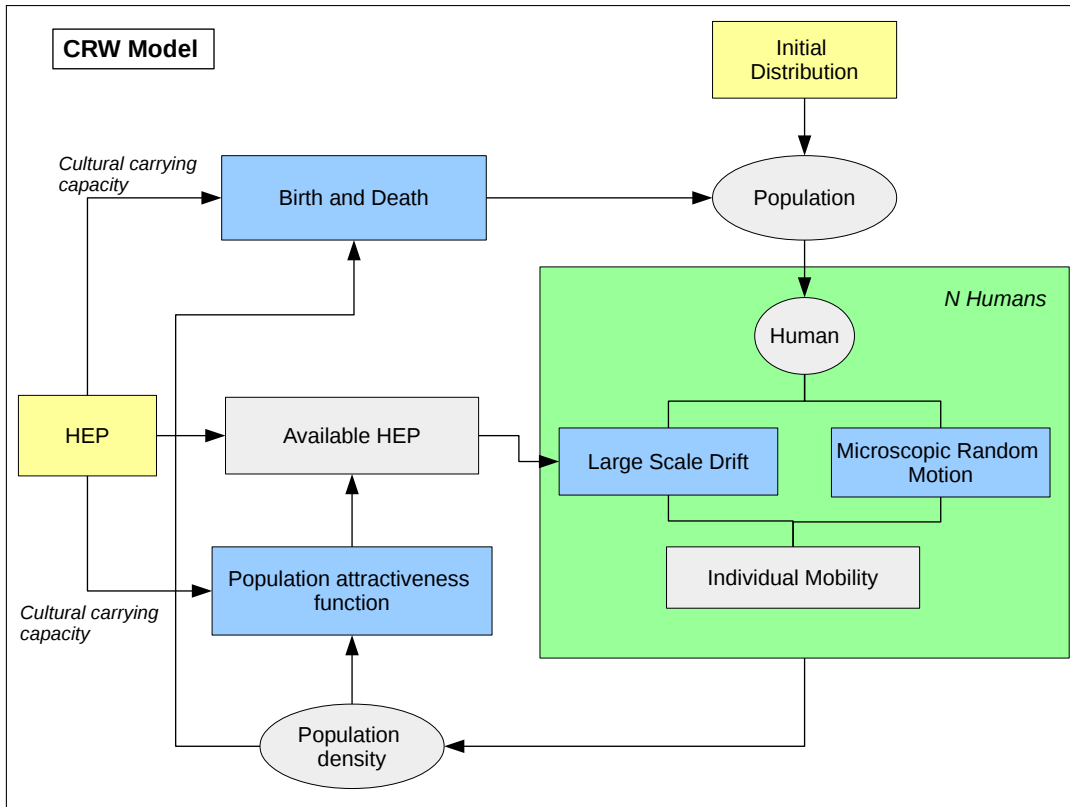


FIGURE 4.1: Schematic description of the Constrained Random Walk Model (CRWM). Blue colored are the main modules of the CRWM and yellow colored is the model input.

4.2 Mathematical description of the CRWM: Main equations

In the CRWM, the dispersal of humans is estimated by simulating the mobility of individuals, while each human's trajectory is described in the Lagrangian specification. This specification means that the model follows the human, leading to a free movement which is not bound to any grid. The Lagrangian specification is in contrast to the Eulerian specification, where the timely change in position and velocity are observed at grid points at specific locations. The Lagrangian trajectory of each human ($h \in N_h$) is thereby defined by his longitudinal (λ_h) and latitudinal (ϕ_h) position on a globe

with constant radius a ($\mathbf{x}_h \in \mathbb{R}^2$):

$$\mathbf{x}_h(t) = \begin{pmatrix} \lambda_h(t) \\ \phi_h(t) \end{pmatrix}, \quad (4.1)$$

and his velocity in eastward (u_h) and northward (v_h) direction ($\mathbf{u}_h \in \mathbb{R}^2$)¹:

$$\mathbf{u}_h(t) = \begin{pmatrix} u_h(t) \\ v_h(t) \end{pmatrix}. \quad (4.2)$$

Humans' velocity is thereby specified in kilometers per year, and the time frame of the simulations will be several 1000 years.

As exemplified in the theoretical introduction of the CRWM (Sec. 4.1), the mobility of each human is supposed to be governed by a drift force on the macroscopic scale, while it corresponds to a random motion on the microscopic scale. As shown in Sec. A.1.3, a mathematical formulation of the two described processes is the Itô stochastic differential equation (SDE, Eq. A.19). In the CRWM, it is assumed that the velocity of a human is defined to be a Markov process (for definition, see Sec. A.1.2) and is formulated as an SDE. Consequently, a human's velocity is the main quantity defining its trajectory. Influences on human mobility can then directly be included as physical forces, making the HEP, which is a physical potential, directly capable of being integrated into the model. The SDE defines the velocity and consists of a drift function ($\mathbf{f}(\mathbf{u}(t), \mathbf{x}(t), t) \in \mathbb{R}^2$), a dispersion matrix ($\mathbf{L}(\mathbf{u}(t), \mathbf{x}(t), t) \in \mathbb{R}^2$) and a stochastic component ($\mathbf{W}(t) \in \mathbb{R}^2$). The longitudinal and latitudinal positions of the humans are then determined deterministically from the simulated velocities. The whole human trajectory is put together as follows:

$$d\mathbf{u}(t) = \mathbf{f}(\mathbf{u}(t), \mathbf{x}(t), t) \cdot dt + \mathbf{L}(\mathbf{u}(t), \mathbf{x}(t), t) \cdot d\mathbf{W}(t), \quad (4.3)$$

$$d\lambda(t) = \frac{1}{a \cos \phi(t)} \cdot u(t) \cdot dt, \quad (4.4)$$

$$d\phi(t) = \frac{1}{a} \cdot v(t) \cdot dt. \quad (4.5)$$

An integral of Eq. 4.3 over time from t and t_0 gives the solution of $\mathbf{u}(t)$:

$$\mathbf{u}(t) = \mathbf{u}(t_0) + \int_{t_0}^t \mathbf{f}(\mathbf{u}(t'), \mathbf{x}(t'), t') dt' + \int_{t_0}^t \mathbf{L}(\mathbf{u}(t'), \mathbf{x}(t'), t') d\mathbf{W}(t'), \quad (4.6)$$

with the second integral on the right-hand side being an Itô stochastic integral. As shown in Sec. A.1.3, a numerical solution can be achieved by using increments of the Wiener process $d\mathbf{W}$ which are Gaussian mean random variables which satisfies $\langle dW_i dW_j \rangle = \delta_{i,j} dt$.

4.2.1 HEP based drift component

As described in the mathematical introduction of the SDE in Sec. A.1.3, the function $\mathbf{f}(\mathbf{u}, \mathbf{x}, t)$ defines a drift function. This drift is the deterministic part of the SDE and constrains the human random walk motion. As shown in the theoretical introduction of the CRWM (Sec. 4.1), two processes are supposed to constrain the random motion, a directional drift based on climate and environment preferences, and population features determined by population densities. The population features are implemented

¹The subscript h is neglected from now on as the equations are equivalent for all humans

into CRWM by the population attractiveness function in a following step, which is introduced in Sec. 4.4. Here, the directional drift by means of the HEP is described. The HEP defines the suitability of a region for human settlement based on specific cultural adaptations to environmental and climatic conditions. Theoretically, humans in the CRWM are supposed to generally migrate towards preferential regions, so regions providing the highest HEP in the macroscopic range the human is located in. Migration in this context is the ensemble and timely average of all human trajectories. The migration is established by a drift function that pushes all humans into the direction of better HEP. In a physical sense, this HEP-induced drift can be interpreted as an timely and ensemble (all humans) averaged acceleration ($\mathbf{a}_{drift} \in \mathbb{R}^2$), which is proportional to the gradient field of the HEP:

$$\left\langle \frac{d\bar{\mathbf{u}}}{dt} \right\rangle = \mathbf{a}_{drift} \propto \nabla \Phi(\mathbf{x}(t), t). \quad (4.7)$$

with Φ being the HEP at position \mathbf{x} and time t , and $\langle \cdot \rangle$ indicating the ensemble and $\bar{\cdot}$ the timely mean.

In addition to the drift \mathbf{a}_{drift} , a second force acting on macroscopic level needs to be introduced to ensure the trajectory to converge to HEP maxima. As schematically shown in the one-dimensional example in Fig. 4.2 (a two-dimensional example for a model without friction can be found in Chapter 5, Sec. 5.1.1), if the gradient force would be the only force on macroscopic level, a human's velocity would be at maximum speed when crossing an HEP maxima while decelerating right after. This acceleration leads to the depicted oscillations across the HEP maximum as shown by the green line in Fig. 4.2. As humans are expected to drift towards high HEP regions, a force must act opposite to the direction of motion and decelerate the motion. This force can be compared to a physical friction force. As shown by the black line in Fig. 4.2, a friction of $\mathbf{a}_{friction} = -0.05 \cdot \mathbf{u}(t)$ leads to the desired effects.

The macroscopic drift $\mathbf{f}(\mathbf{u}(t), \mathbf{x}(t), t)$ is then the compound acceleration from \mathbf{a}_{drift} and $\mathbf{a}_{friction}$ ($\in \mathbb{R}^2$), and by introducing two constants α and γ , it is described as:

$$\mathbf{f}(\mathbf{u}(t), \mathbf{x}(t), t) = \alpha \cdot \nabla \Phi(\mathbf{x}(t), t) - \gamma \cdot \mathbf{u}(t). \quad (4.8)$$

4.2.2 Stochastic component

The random component in Eq. 4.3 is governed by two terms, the Wiener process \mathbf{W} and the dispersion matrix \mathbf{L} . As defined in Sec. A.1.3 and shown in Särkkä and Solin (2019), the increments of the Wiener process are independent of each other and zero mean Gaussian variables with covariances proportional to the time increment Δt and the diffusion matrix \mathbf{Q} . I assume that diffusional processes on microscopic scale are random in magnitude and direction and thereby independent of the location and time. This random diffusion reflects the intended human mobility on microscopic scale, which is defined to be solely based on individual behaviour. The diffusion matrix is therefore assumed to be constant and thus time- and location-independent.

The dispersion matrix \mathbf{L} defines how the random diffusion is influenced by outer conditions and thereby determines the magnitude and direction of the microscopic velocity. Outer conditions here, are the environment, such as rivers, mountains or forests, or the climate/weather, while also timely changes of both can be taken into account. One could think of a microscopic diffusional velocity which is enhanced along rivers or coast lines, or in regions with favorable climatic conditions. On the contrary,

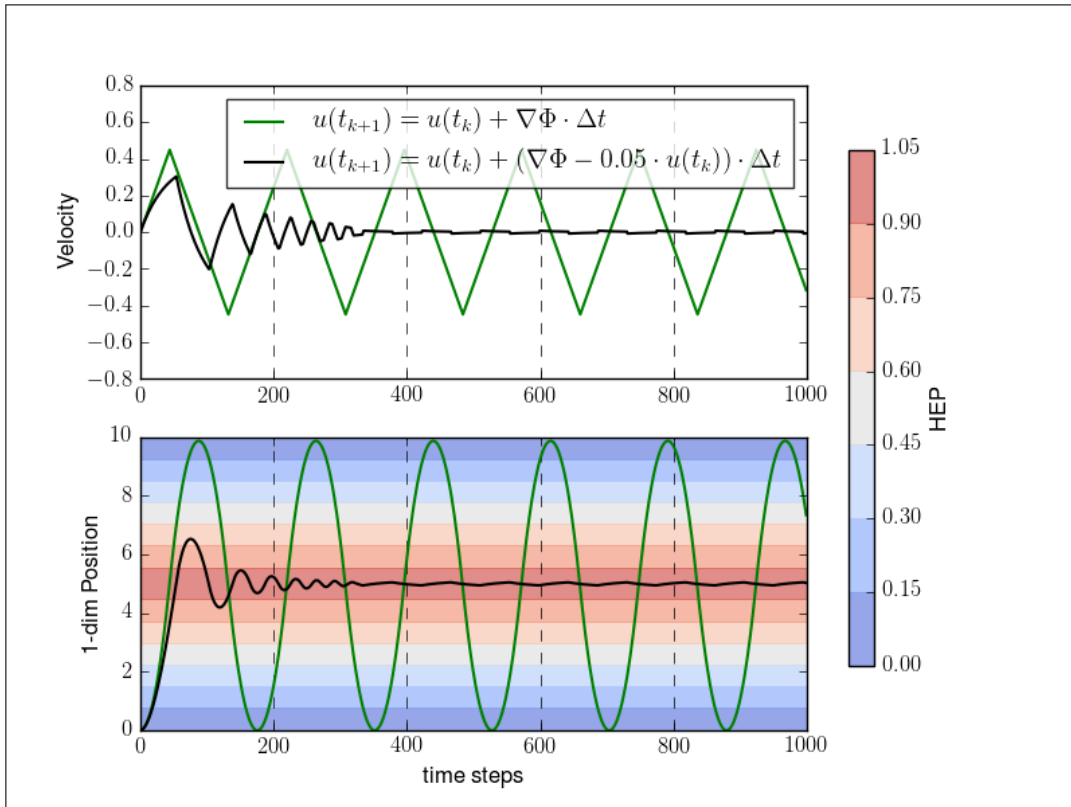


FIGURE 4.2: Schematic illustration of the macroscopic drift in one dimension with friction (black line, $\alpha = 1$ and $\gamma = 0.05$) and without friction (green line, $\alpha = 1$ and $\gamma = 0$); depicted are the velocity (top) and the position (bottom) for a constant HEP for 1000 time steps with $u(t_0) = 0$, $x(t_0) = 0$, and $\Delta t = 0.5$.

it is feasible to assume that the mobility of hunter-gatherers rose in unfavorable climate conditions, because it got more extensive to gather resources. Accordingly, it is not straightforward to define a reasonable dispersion matrix. Furthermore, a directional dispersion process could be captured by the drift part of the differential equation and is then not a stochastic process anymore. As it is not fully clear how to define dispersive processes on microscopic scale, I choose to neglect them in this study and assume homogeneity. The stochastic microscopic diffusion is then solely scaled by a constant (β) defining the magnitude of the stochastic process:

$$\mathbf{L}(\mathbf{u}(t), \mathbf{x}(t), t) = \beta \cdot \mathbb{I}. \quad (4.9)$$

4.2.3 Compound equations

Inserting \mathbf{f} and \mathbf{L} in Eq. 4.3 gives:

$$d\mathbf{u}(t) = [\alpha \cdot \nabla \Phi(\mathbf{x}(t), t) - \gamma \cdot \mathbf{u}(t)] \cdot dt + \beta \cdot d\mathbf{W}(t). \quad (4.10)$$

As the movement is taking place on a sphere, the Eq. 4.10 needs to be formulated in spherical coordinates (for the derivation see Sec. A.2 in the Appendix). The new coordinate system is not stationary but changes over time, which is why curvature

terms have to be added to the equations of motion:

$$du = \left[\frac{uv \tan \phi}{a} + \alpha \cdot \frac{\partial \Phi}{\partial x} - \gamma \cdot u \right] \cdot dt + \beta \cdot dW_x, \quad (4.11)$$

$$dv = \left[-\frac{u^2 \tan \phi}{a} + \alpha \cdot \frac{\partial \Phi}{\partial y} - \gamma \cdot v \right] \cdot dt + \beta \cdot dW_y. \quad (4.12)$$

However, scale analysis shows that the magnitude of the curvature terms in both Equations, 4.11 and 4.12, are much smaller than the magnitudes of the other terms. These terms are included in the numerical model, but are not listed in the following definitions for the sake of clarity.

The SDEs in Eq. 4.10 are nonlinear and there is no analytical solution for \mathbf{u} . It is numerically solved by the Euler-Maruyama method, which is shown in Sec. 4.6. The parameterization of Eq. 4.10, thus the assignment of the constants α , β and γ , is pointed out in Sec. 4.3.

4.3 Parameterization of the main equations

The CRWM is a new type of model for simulating human migration, the parameterization is thus not a straightforward process. Some ideas have already occurred in a similar way in other modeling studies, so that parameters can be adopted from there in an adapted form. Some parameters, however, have to be newly introduced. While it has to be ensured that the physical interpretation of the different terms in the equation 4.10 are correct, I integrate existing concepts from archeology and anthropology when defining the parameters. From a physical perspective, two conditions have to be considered for the three constants α , β and γ in Eq. 4.10:

1. The physical units have to be $[\alpha] = \text{km}^2/\text{yr}^2$, $[\beta] = \text{km}/\text{yr}^{3/2}$ (considering $[dW] = \text{yr}^{1/2}$), and $[\gamma] = 1/\text{yr}$.
2. The parameters have to consist of some scaling factors, so that the different parts of Eq. 4.10 are independent of the model's spatial and timely scale. Meaning that the model delivers similar results for different setups of Δt and resolutions of the HEP.

As will be shown in the following sections, many parameters are necessary to describe the spread and the growth or decline of a population. With each new parameter, the degrees of freedom and thus the complexity of the model increases. Many degrees of freedom can lead to very good modeling results, which should, however, be treated with caution, as these only apply to specific cases and may not be representative due to over-parameterization. To improve the representativeness of the results, I will therefore limit the degrees of freedom insofar as the complexity of the model allows it. The configuration of the modeling experiments is therefore limited to certain key parameters, which are highlighted and explained in more detail in the gray boxes. All other parameters are calibrated in Chapter 5 using idealized experiments.

4.3.1 Drift parameters

First of all, the magnitude of the macroscopic HEP-based drift, which is decelerated by a friction force, needs to be assigned by a velocity term. The velocity that mainly determines the macroscopic migration is the *maximal migration velocity*, defined as follows:

Maximal migration velocity (u_{max})

Human migration was a longsome process. First evidences of anatomical modern humans have been found in Africa and date back to 315,000 years BP and 195,000 years BP (Hublin et al., 2017; Stringer and Galway-Witham, 2017). It took the early humans several thousand years to leave the African continent and to populate Europe, where a large-scale settlement is assumed only from about 43,000 years BP (Higham et al., 2011; Bae et al., 2017). A slow human expansion rate of about one kilometer per year can be assumed for migration processes that occurred in shorter time windows, as the spread of farming in Europe during the Neolithic (Ammerman and Cavalli-Sforza, 1971).

One of my main assumptions is that human migration is driven by a climatic and environmental forced drift on macroscopic scale. The drift force causes the human populations to migrate towards favorable regions on the long term, disregarding the random fluctuations of human mobility. In the CRWM this macroscopic scale migration drift is implemented by the gradient of the HEP. The migration is by definition the ensemble and timely average of all human trajectories from one point to another. One can now define a maximal migration velocity that occurs between two points, and thus determine an upper limit for the migration velocity based on the HEP gradient. Mathematically the maximal migration velocity is described as:

$$u_{max} = \max_t \langle |\mathbf{u}(t)| \rangle. \quad (4.13)$$

Since the migration velocity is defined by the HEP gradient between two points, an idealized case is created in Chapter 5 that generally defines the maximal migration velocity. This maximal velocity governs the large scale migration of populations and is chosen in a way to keep migration velocities in the range of 1 – 20 kilometers per year, to be in agreement with former studies dealing with human migration velocities.

Additionally to the maximal migration velocity, two more parameters have to be defined specifying the length and time scale, so that the physical units of α and γ are correct. The drift is regulated by a drift time scale (D_t) and a gradient distance scale (G_d), which will be calibrated in Chapter 5. The parameters are defined as follows:

- **Drift time scale (D_t):** A time scale is introduced that governs the magnitude of the macroscopic drift. This time scale is called drift time scale (D_t). An archaeological explanation of D_t could be the time period humans needed to adapt to new conditions. While humans migrate to new regions, they encounter unfamiliar environments with different resource occurrences and new dangers. The adaptation to this conditions takes some time and therefore decelerate further migration. All humans need time for adaption, however the expense can depend on the technology and knowledge of different cultures. I suppose a range of 0.1 – 10 years for D_t , which could be assumed to be in the time range that hunter-gatherers would need to adapt to new conditions. If the adaption time D_t is low, humans are able to migrate faster to new regions, while the migration is decelerated when adaption takes more time.
- **Gradient distance scale (G_d):** To satisfy the physical dimensions in Eq. 4.6, the gradient is normalized by a maximal gradient of the HEP which would lead

to a dispersal with maximal migration velocity. This maximal gradient of the HEP is a spatial quantity that defines the velocity of the large scale migration. As the HEP is a score between zero and one, the maximal difference in HEP is one, so that the maximal gradient is defined by a gradient distance scale (G_d) by:

$$|\nabla\Phi|_{max} = \frac{1}{G_d}. \quad (4.14)$$

Small values of G_d mean that only very steep gradients of the HEP lead to velocities close to the maximal migration velocity. Larger values indicate that maximal migration velocity is reached already for rather flat gradients. In accordance to the length scale of the large-scale migration processes, a gradient distance scale of about 100 – 300 km can be assumed as a distance at which the maximal migration velocity can be reached, if the difference in HEP would be maximal.

With u_{max} , D_t and G_d the parameter α is chosen to be:

$$\alpha = \frac{u_{max}}{D_t \cdot |\nabla\Phi|_{max}} = \frac{u_{max} \cdot G_d}{D_t}. \quad (4.15)$$

The friction term in Eq. 4.10 is scaled by the same time scale as the gradient term, for a better interpretation of the deterministic drift. The parameter γ is decided to be:

$$\gamma = \frac{1}{D_t}. \quad (4.16)$$

Even if it initially seems contradictory that a high D_t results in a low friction, I would like to point out that the introduction of the friction has numerical reasons and should not initially be interpreted by anthropological behavior. Section 5.1.1 shows how to calibrate the parameters D_t and G_d in order to simulate realistic human movements.

4.3.2 Stochastic parameters

The random walk of the humans in the CRWM acts on microscopic spatial and timely scale. Two new parameters, the individual mobility and the stochastic time scale, are introduced, to define the scale of the random walk and the time scale of the movement. The individual mobility is the key parameter defining the scale of the microscopic stochastic process, while the stochastic time scale is a calibration parameter determined in Chapter 5. An explanation for both parameters is given in the following:

Individual mobility (σ_u)

The individual mobility expresses, in contrast to the maximal migration velocity, the hourly to daily fluctuations of humans based on their individual behaviour. Presumably, this mobility is connected to hunting and gathering excursions or walks to raw material sources. Moreover, one could assume social aspects such as marriages, propagation, conflicts or religious rituals to induce individual movement of humans. Aside from that, also undirected migration can be expressed by the individual mobility. The individual mobility of each human is included as a random walk in the CRWM, so only the scale of the stochastic process is defined by parameters. As the CRWM operates on yearly time scales, one have to assume in which range the individual mobilities take part during a year. I assume the range to be around 50 – 200 kilometers, leading

to an assumed individual mobility σ_u of around 50 – 200 km/year.

- **Stochastic time scale (τ):** The time scale defining particle trajectories in turbulent flows for Gaussian turbulence is the Lagrangian integral time scale for homogeneous and stationary conditions or the so-called local decorrelation timescale for considerable inhomogeneity or unsteadiness (Thomson, 1987). An equivalent of the Lagrangian time scale for the stochastic diffusion of humans could be the humans' ability to remember. The ability to remember expresses human knowledge and experience and comprises anthropological concepts such as the perceived accessibility and the perception of the landscape. Low numbers indicate a random walk dominated mobility, while high numbers lead to a more deterministic migration. However, the ratio of deterministic to stochastic mobility in the CRWM is determined by the two velocity parameters, the maximal migration velocity, and the individual mobility. So a value is set for the stochastic time scale (τ) after calibration, which is supposed to be in the same magnitude as D_t (0.1 - 10 years), so that both, macroscopic and microscopic features, are resolved by the CRWM.

With both parameters σ_u and τ and by regarding the physical dimensions of β , the parameter is defined as:

$$\beta = \sqrt{\frac{\sigma_u^2}{\tau}}. \quad (4.17)$$

Inserting the definitions of α , β , and γ in Eq. 4.10 gives the parameterized velocity equations of motion:

$$d\mathbf{u}(t) = \frac{1}{D_t} [u_{max} \cdot G_d \cdot \nabla \Phi(\mathbf{x}(t), t) - \mathbf{u}(t)] \cdot dt + \frac{\sigma_u}{\sqrt{\tau}} \cdot d\mathbf{W}(t). \quad (4.18)$$

4.4 Population attractiveness function

The second constraint of a human's random motion in the CRWM comes from population features, as introduced in Sec. 4.1. So the size of the population inhabiting a region influences the mobility of the humans. Two aspects are considered: (1) humans are gregarious; regions with low population sizes are less interesting for immigration. (2) Resources are depleted by other humans; when the population size of a region exceeds a certain threshold, population pressure occurs. Both aspects are combined in the population attractiveness function that defines a region's attractiveness for settlement based on the population and the available resources.

4.4.1 Definition

A common way to describe population sizes is the population density (ρ), the number of humans per area in the units² hms/100 km². The available resources of a region are described by the carrying capacity, which defines a maximal population density that can be sustained in a region. As hunter-gatherers adaptations vary for different cultures or techno-complexes, so does the carrying capacity of a region depending on the human culture. Therefore, an individual cultural carrying capacity (ρ_c) is calculated for each human culture. The available resources of a region gathered by a

²The abbreviation hms is introduced here for humans as a physical unit.

human culture are determined by the environmental conditions, and thus the HEP. It is assumed that the cultural carrying capacity is linear proportional to the HEP, and thus involves technological progress and particular preferences of the cultures:

$$\rho_c(\mathbf{x}(t), t) = \rho_{max} \cdot \Phi(\mathbf{x}(t), t). \quad (4.19)$$

The proportional constant ρ_{max} is the *maximal cultural carrying capacity*, so the cultural carrying capacity that occurs for optimal conditions ($\Phi = 1$). This parameter is a key parameter and regulates the population sizes in the CRWM. It is defined as follows:

Maximal cultural carrying capacity (ρ_{max})

Population sizes during the Paleolithic are usually estimated by projecting results from ethnological studies to the past. The ethnological data is thereby either connected to climatic reconstructions (Binford, 2002; Tallavaara et al., 2015) or put in context with archaeological data (Bocquet-Appel et al., 2005; Maier et al., 2016). Although the outcome of the studies is ambiguous, one could assume the population size to be in the range of about 3,000 - 80,000 individuals in total within Europe during the Paleolithic. Population densities are thereby not uniformly distributed across the European continent. Some areas were inhabitable, and humans adapted to particular environmental conditions. The maximal cultural carrying capacity is defined for regions providing optimal conditions, which is defined by a HEP of one. As humans keep their population numbers below the limit, the maximal cultural carrying capacity is chosen to be higher than the maximal estimated population densities. These densities are in the range of 0.5 – 20 hms/100 km².

The population density of an area combined with the corresponding cultural carrying capacity, defines how much of the HEP is used up by other humans and how much is still available. It is commonly assumed that hunter-gatherer communities never use up all of the available resources (Kelly, 2013). They usually keep the population size at a portion of the carrying capacity (in Kelly (2013) 20-30% are assumed) so that the environment stays in balance. Consequently, population pressure already occurs when population densities reach a certain percentage of the cultural carrying capacity.

A function is introduced to define the attractiveness of a region based on the population density. According to my assumptions, this function is supposed to have the following properties:

$$f_{pa} \rightarrow 0, \text{ if } \rho \rightarrow 0, \text{ and,} \quad (4.20)$$

$$f_{pa} \rightarrow 0, \text{ if } \rho \rightarrow \rho_c, \quad (4.21)$$

and which reaches its maximum in between. The scaled Weibull function, with the variable ρ/ρ_c and two parameters ($\eta > 0$ and $\epsilon > 0$) that define the shape of the function, fulfill the presupposed properties and is chosen as the *population attractiveness function* (exemplary shown for different ρ_c in Fig. 4.3):

$$f_{pa}(\rho/\rho_c) = C_{pa} \cdot \left\{ \left(\frac{\eta}{\epsilon} \right) \cdot \left(\frac{\rho}{\epsilon \cdot \rho_c} \right)^{\eta-1} \cdot \exp \left[- \left(\frac{\rho}{\epsilon \cdot \rho_c} \right)^\eta \right] \right\}. \quad (4.22)$$

C_{pa} scales the population attractiveness function to 1 at its maximum. This is calculated by:

$$\frac{df_{pa}}{d\rho} = 0 \quad (4.23)$$

$$\Leftrightarrow \frac{\rho}{\rho_c} = \epsilon \cdot \left(1 - \frac{1}{\eta}\right)^{1/\eta}. \quad (4.24)$$

By the condition:

$$f_{pa} \left(\epsilon \cdot \left(1 - \frac{1}{\eta}\right)^{1/\eta} \right) = 1, \quad (4.25)$$

C_{pa} is defined by:

$$C_{pa} = \left\{ \left(\frac{\eta}{\epsilon}\right) \cdot \left(1 - \frac{1}{\eta}\right)^{1-\frac{1}{\eta}} \cdot \exp \left[- \left(1 - \frac{1}{\eta}\right) \right] \right\}^{-1}. \quad (4.26)$$

The two parameters η and ϵ are calibrated in Chapter 5.

The population attractiveness function is supposed to affect the macroscopic population dynamics and therefore the deterministic part of the equations of motion (Eq. 4.18). The product of the population attractiveness function and the HEP can be understood as the HEP which is actually available and attractive for harvesting for humans migrating to a region. It is therefore called available HEP (Φ_{av}):

$$\Phi_{av}(\mathbf{x}(t), t) = f_{pa} \left(\frac{\rho(\mathbf{x}(t), t)}{\rho_c(\mathbf{x}(t), t)} \right) \cdot \Phi(\mathbf{x}(t), t). \quad (4.27)$$

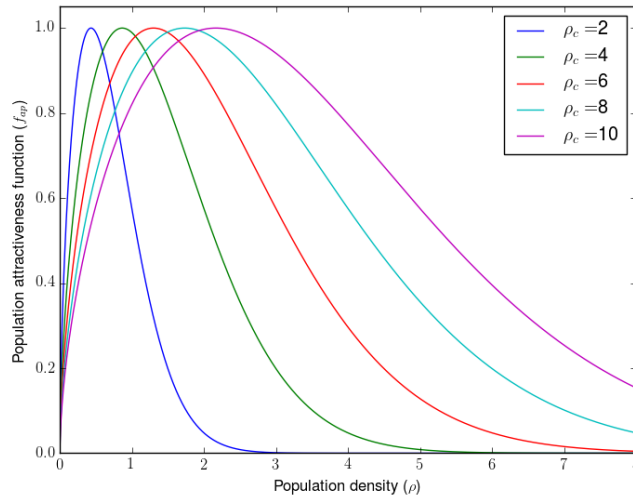


FIGURE 4.3: Population attractiveness function (f_{pa}) defined in Eq. 4.22, based on the population density (ρ) in hms/100 km² for the parameters $\eta = 1.6$ and $\epsilon = 0.4$ and different cultural carrying capacities (ρ_c).

By replacing the HEP with the available HEP in Eq. 4.18 the population attractiveness is integrated in the model as follows:

$$d\mathbf{u}(t) = \frac{1}{D_t} [u_{max} \cdot G_d \cdot \nabla (f_{pa}(\rho/\rho_c) \cdot \Phi(\mathbf{x}(t), t)) - \mathbf{u}(t)] \cdot dt + \frac{\sigma_u}{\sqrt{\tau}} \cdot d\mathbf{W}(t) \quad (4.28)$$

$$\Leftrightarrow d\mathbf{u}(t) = \frac{1}{D_t} [u_{max} \cdot G_d \cdot \nabla \Phi_{av}(\mathbf{x}(t), t) - \mathbf{u}(t)] \cdot dt + \frac{\sigma_u}{\sqrt{\tau}} \cdot d\mathbf{W}(t), \quad (4.29)$$

4.4.2 Example

The effects of the population attractiveness function are shown in Fig. 4.4, which shows the HEP, the population density and the available HEP for a cultural carrying capacity of 6 hms/100 km². This figure is only a theoretical illustration of the influence of the population attractiveness function. In the CRWM, high population densities in low HEP regions are very unlikely to occur. It can be seen that some regions, especially in the south and north of the figure, which actually have high HEP, have a low available HEP due to the population densities and the application of the population attractiveness function. In the northeast and southeast, the combination of low HEP < 0.5 and population densities > 2 hms/100 km² lead to very low available HEP, close to zero. In these regions, the population pressure is already reached for rather low population densities, since there are hardly any resources available. In contrast, the available HEP in the southwest is very low despite high HEP values. This is because there are maximum population densities of up to 4 hms/100 km², so there is also an overpopulation here (this occurs well before the cultural carrying capacity is reached). A macroscopic diffusion can be expected from the over-populated regions to the surroundings, as the gradient force based on the available HEP leads away from over-populated regions to less populated ones. In the CRWM, the humans drift to the less populated regions with high resource occurrences north and northeast of the population density maximum. Regions with very low population densities also lower the available HEP independent of the existing HEP, as shown in the middle of the distribution, at around $x = 30^\circ$ and $y = 30^\circ$. The resulting available HEP in this region is lowered due to the low population density. Those regions raise in attractiveness in the CRWM if the population increases, this could happen by the stochastic microscopic diffusion of humans. The growth of the population density would then lead to higher available HEP, which would then increase the macroscopic drift to this region.

4.5 Birth and death module

The CRWM not only simulates population migration by the individual trajectories of each human, but also growth and decline of the population are integrated into the modeling framework. In accordance with the model's setup and the Lagrangian specification, this is done by implementing a module that determines the birth or death of individual humans. Analog to assumptions made for defining the population attractiveness function, the two variables governing the growth or decline are the available resources, defined by the cultural carrying capacity, and the population density. A consequence of the insufficient availability of resources is starvation. In overcrowded regions, one could expect conflicts to occur within a group of hunter-gatherers or between different groups. The logical consequence of both cases is that the population declines. Contrary, in areas with viable population sizes and a sufficient

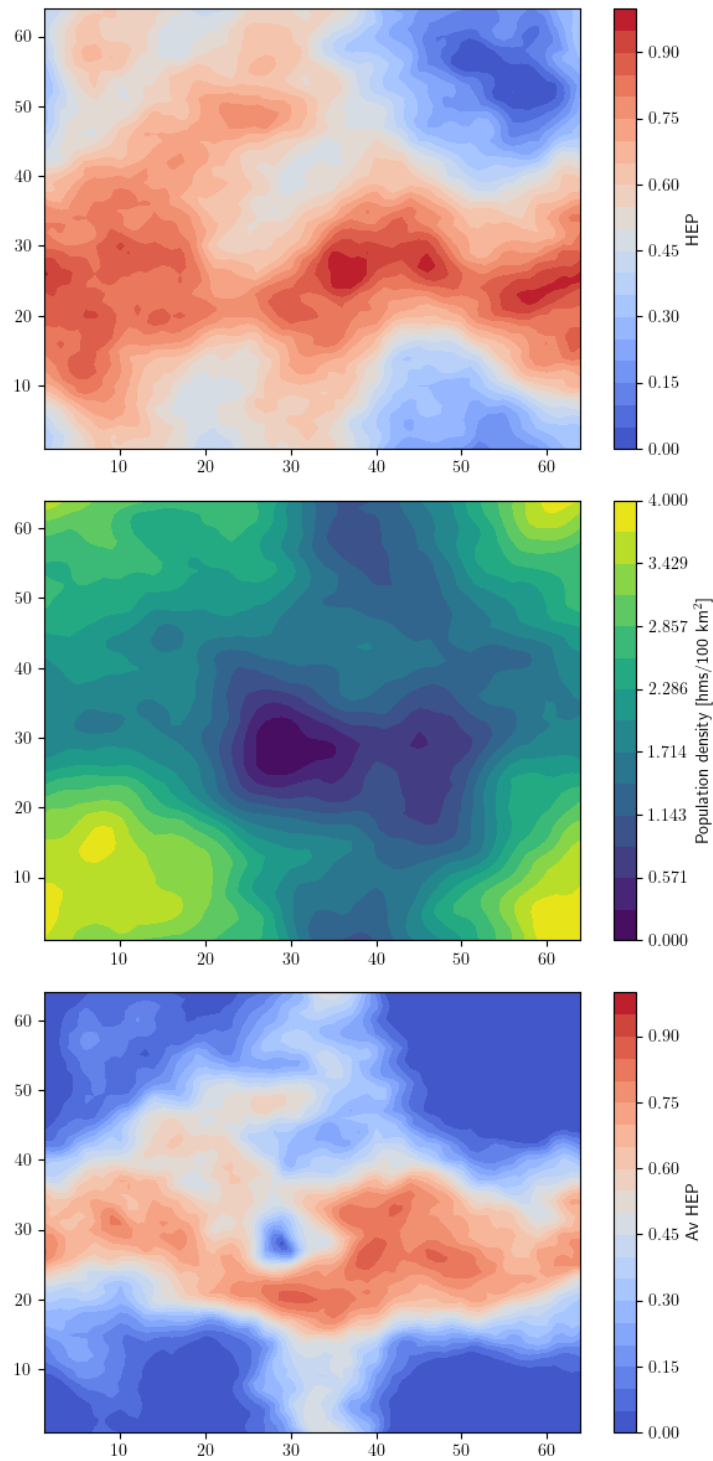


FIGURE 4.4: Theoretical illustration of the effect of the population attractiveness function (f_{pa}) for $\eta = 1.6$, $\epsilon = 0.3$ and $\rho_{max} = 6$ hms/100 km², considering a random HEP distribution Φ (*top*), and a randomly generated population density ρ in [hms/100 km²] (*middle*); depicted is the resulting available HEP calculated by $\Phi_{av} = f_{pa} \cdot \Phi$ (*bottom*).

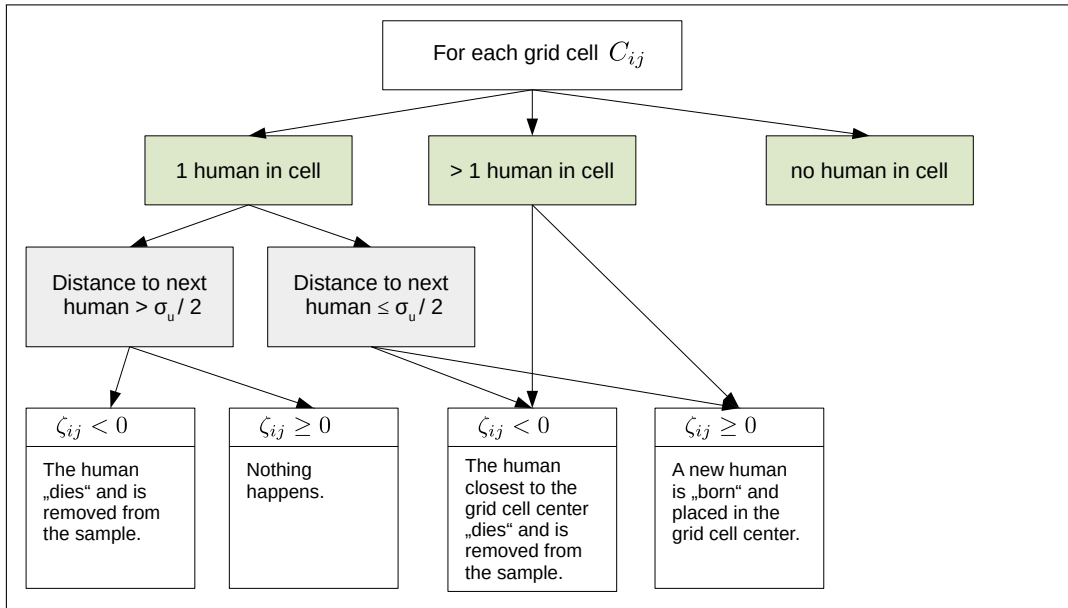


FIGURE 4.5: Framework of the birth and death module. It is determined separately for each grid cell C_{ij} by random variables ζ_{ij} whether a new human is born or a human dies in the CRWM.

amount of resources, the human population is more likely to grow. However, if the population size within an area with sufficient size is smaller than two, no reproduction is possible, despite the volume of available resources.

4.5.1 Definition

Population growth and decline is based on the population density and the cultural carrying capacity of each grid cell. This limitation is clearly a simplification of reality, and one could think of several other reasons that are relevant, such as the age or health of humans. By considering the inaccuracy of our approach and humans' individuality, the decision if a human dies or a new human gets born is chosen to be a stochastic process in the CRWM. For each populated grid cell C_{ij} , the processes are implemented by introducing a random number ζ_{ij} . It is determined by this random number whether the population within the cell increases, if $\zeta_{ij} \geq 0$, or decreases, if $\zeta_{ij} < 0$. So if the specific random number of the cell is positive, a new human is "born" and placed in the grid cell center. If $\zeta_{ij} < 0$, the person in the cell which is in closest distance to the grid cell center "dies" and is removed from the sample. A special case occurs when there is only one person inside the grid cell. Then it is first checked whether the person is within the individual mobility range of other people (specified by $\frac{\sigma_u}{2}$ as defined in Sec. 4.3). If this is the case, then it is possible that a person is born in these grid cells, otherwise only the death of the person in the grid cell is possible (for $\zeta_{ij} \geq 0$ nothing would happen). The procedure of birth and death within grid cells is shown in Fig. 4.5.

All random numbers ζ_{ij} are chosen to be Gaussian distributed with a constant standard deviation ($\sigma_{\zeta_{ij}} = 1$), but a variable mean value ($\mu_{\zeta_{ij}}$). The mean value $\mu_{\zeta_{ij}}$ shifts the Gaussian distribution and therefore influences the probability of ζ_{ij} being either positive or negative. The probability distribution that defines ζ^3 is exemplary shown for an arbitrary μ_ζ in Fig. 4.6a. The probability of $\zeta \geq 0$ (green shaded area in Fig.

³The example applies for all grid cells C_{ij} , so the subscripts are neglected here.

4.6a) for this case is calculated by:

$$P(\zeta \geq 0) = \int_0^{\infty} \frac{1}{\sqrt{2\pi}} \exp\left(-\frac{(x - \mu_\zeta)^2}{2}\right) dx = \frac{1}{2} \left[\operatorname{erf}\left(\frac{\mu_\zeta}{\sqrt{2}}\right) + 1 \right], \quad (4.30)$$

and of $\zeta < 0$ (grey shaded area in Fig. 4.6a) by:

$$P(\zeta < 0) = \int_{-\infty}^0 \frac{1}{\sqrt{2\pi}} \exp\left(-\frac{(x - \mu_\zeta)^2}{2}\right) dx = \frac{1}{2} \operatorname{erfc}\left(\frac{\mu_\zeta}{\sqrt{2}}\right), \quad (4.31)$$

with erf being the error function and erfc the complementary error function:

$$\operatorname{erf}(x) = \frac{1}{\sqrt{2\pi}} \int_0^x e^{-t^2} dt, \quad (4.32)$$

$$\operatorname{erfc}(x) = 1 - \operatorname{erf}(x). \quad (4.33)$$

The integrated probabilities $P(\zeta \geq 0)$ and $P(\zeta < 0)$ are shown in Fig. 4.6b for different values of μ_ζ . One can see that the two probabilities add up to one, as expected, and for $\mu_\zeta = 0$, both probabilities are the same, so $P(\zeta \geq 0) = P(\zeta < 0) = 0.5$. For $\mu_\zeta = 3$, the probabilities approximately reach $P(\zeta \geq 0) \approx 1$ and $P(\zeta < 0) \approx 0$, and for $\mu_\zeta = -3$, they approach $P(\zeta \geq 0) \approx 0$ and $P(\zeta < 0) \approx 1$.

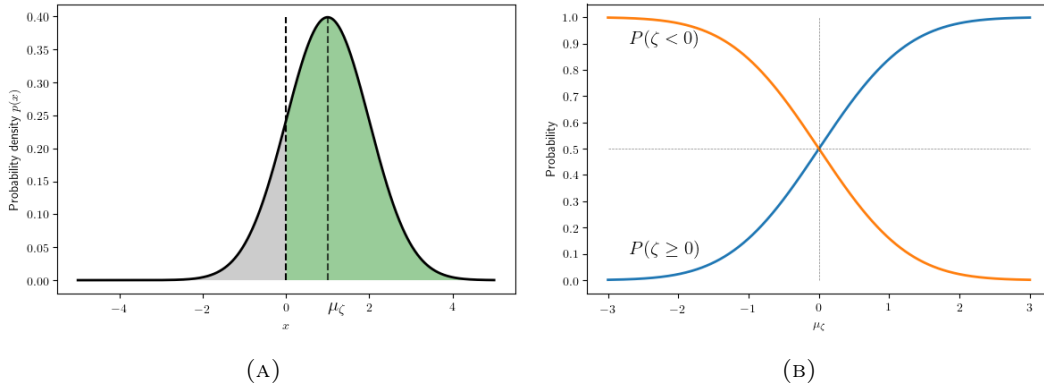


FIGURE 4.6: (A) Gaussian probability density $p_\zeta(x)$ with $\mu_\zeta = 1$ and $\sigma_\zeta = 1$ used to estimate the random variable ζ ; the green and grey shaded areas are the probabilities of ζ being either positive, $P(\zeta \geq 0)$, or negative, $P(\zeta < 0)$, respectively. (B) The probabilities $P(\zeta \geq 0)$ and $P(\zeta < 0)$ for different mean values μ_ζ .

As shown, the probability of ζ is mainly influenced by the mean value of the Gaussian distribution μ_ζ . A function is defined for μ_ζ in a way that it is positive for good conditions, implying growth is more probable than decline, while the opposite occurs for bad conditions. Good or bad conditions are thereby defined separately for each grid cell (C_{ij}) by the particular cultural carrying capacities ($\rho_{c,ij}$) and the population densities (ρ_{ij}). Population growth in ecological studies is usually modelled by a logistic function developed by Verhulst (1838) (Murray, 2002; Steele, 2009):

$$\frac{d\rho}{dt} = \rho r \left(1 - \frac{\rho}{K}\right). \quad (4.34)$$

The population grows until its limit is reached, the carrying capacity K . The strength of the growth is thereby regulated by the population growth rate r . If the carrying capacity is exceeded ($\rho > K$), the population density rate ($\frac{d\rho}{dt}$) is negative and the

population decreases. This formula (Eq. 4.34) is now being adapted to the concepts of the CRWM to define a function for the mean value of the Gaussian distribution (μ_ζ). For each grid cell C_{ij} it is defined by (Fig. 4.7):

$$\mu_{\zeta_{ij}}(\rho_{ij}, \rho_{c,ij}) = \kappa \cdot \rho_{ij} \cdot r \left(1 - \frac{\rho_{ij}}{0.6 \cdot \rho_{c,ij}} \right). \quad (4.35)$$

Here, as with the population attractiveness function, the cultural carrying capacity (ρ_c) is used with the restriction that the population limit is already exceeded at a population density of 60% of ρ_c . This is consistent with the assumption that hunters and gatherers never exhaust all available resources, but deliberately keep their population low (Kelly, 2013). The population growth rate r scales the population growth and is a key parameter of the CRWM and therefore described in more detail. The parameter κ is a scaling parameter calibrated in Chapter 5 so that the modelled population growth rate coincides with r .

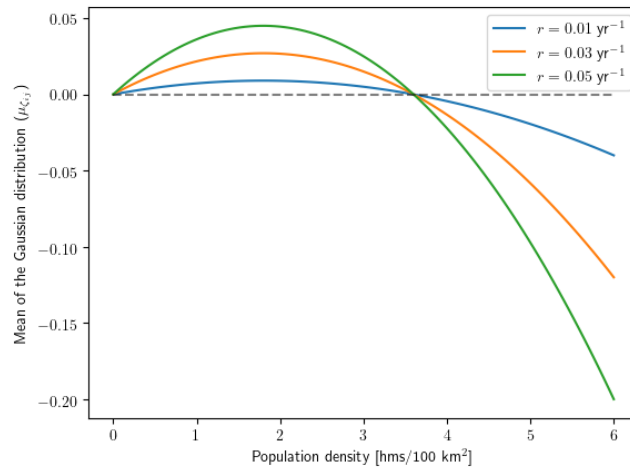


FIGURE 4.7: Mean of the Gaussian distribution $\mu_{\zeta_{ij}}$ (Eq. 4.35) defining the probability density of the random variable ζ_{ij} , determined by the population density (ρ) for a cultural carrying capacity of $\rho_c = 6$ hms/100 km². Shown are different realization according to the growth rate r with $\kappa = 1$.

Population growth rate (r)

The population growth rate is the average amount of offspring per human and is usually defined in the units yr^{-1} or generation^{-1} . For a generation time of 27 years, values of the population growth rates are assumed to be $r = 0.017 - 0.027$ 1/yr, which corresponds to a population growth of 1.7 – 2.7% (Fort et al., 2004). Other studies simulate human expansion processes with slightly lower ($r = 0.004$ 1/yr) (Timmermann and Friedrich, 2016) or higher values ($r = 0.031$ 1/yr) (Campos et al., 2006). Migration in the CRWM is triggered on the one hand by local population pressure and on the other hand by random processes. The former in particular is strongly influenced by population growth. The size of the population growth rate therefore also determines how quickly migration processes take place. In addition, r determines how quickly populations can decrease, for example in the event of changes in external conditions. High r values ensure, on the one hand, greater growth, but also a faster

population decrease, since μ_ζ decreases faster for $\rho > 0.6 \cdot \rho_c$ (Fig. 4.7).

4.6 Numerical Implementation

4.6.1 Main equations

For the numerical solution of the equations of motion, the corrected equations are used by adding the correction terms of the spherical coordinates. Since the movement takes place on earth, a radius of $a = 6371.000785$ km of the sphere is assumed, the ellipsoidal deformation of the earth is neglected in the modeling. The method used to numerically solve Eq. 4.11 and 4.12 is the so-called Euler-Maruyama method. The Eq. 4.4 and 4.5 are solved by the forward Euler method. For a chosen time interval T with a number N of equal time steps $\Delta t = T/N$, and with $k \in [1, \dots, N-1]$ the numerical solution $(\hat{\mathbf{u}}, \hat{\mathbf{x}})$ is:

$$\begin{aligned} \hat{u}^{k+1} = \hat{u}^k + & \left\{ \frac{\hat{u}^k \hat{v}^k \tan \hat{\phi}^k}{a} + \frac{1}{D_t} \left[u_{max} \cdot G_d \cdot \frac{\partial \{ f_{av}(\rho^k / \rho_c^k) \cdot \Phi(\hat{\mathbf{x}}^k, t_k) \}}{\partial x} - \hat{u}^k \right] \right\} \cdot \Delta t \\ & + \frac{\sigma_u}{\sqrt{\tau}} \cdot \Delta W_x^k, \end{aligned} \quad (4.36)$$

$$\begin{aligned} \hat{v}^{k+1} = \hat{v}^k + & \left\{ -\frac{(\hat{u}^k)^2 \tan \hat{\phi}^k}{a} + \frac{1}{D_t} \left[u_{max} \cdot G_d \cdot \frac{\partial \{ f_{av}(\rho^k / \rho_c^k) \cdot \Phi(\hat{\mathbf{x}}^k, t_k) \}}{\partial y} - \hat{v}^k \right] \right\} \cdot \Delta t \\ & + \frac{\sigma_u}{\sqrt{\tau}} \cdot \Delta W_y^k, \end{aligned} \quad (4.37)$$

$$\hat{\lambda}^{k+1} = \hat{\lambda}^k + \frac{1}{a \cos \hat{\phi}^k} \cdot u^{k+1} \cdot \Delta t, \quad (4.38)$$

$$\hat{\phi}^{k+1} = \hat{\phi}^k + \frac{1}{a} \cdot v^{k+1} \cdot \Delta t. \quad (4.39)$$

With given initial conditions at $t = 0$, so u^0 , v^0 , λ^0 , and ϕ^0 the set of equations is solvable with ΔW_x^k and ΔW_y^k being the increments of the Brownian motion as defined in Sec. A.1.3 and 4.2. So all ΔW_x^k and ΔW_y^k are independent for all times, and have an expected value of zero and a variance of Δt . By defining the dispersion matrix to be constant (Eq. 4.9), so by having a constant noise additive, the strong order of convergence:

$$E[|\mathbf{u}(t_k) - \hat{\mathbf{u}}(t_k)|] \leq K \Delta t^p \quad (4.40)$$

is in the order of $p = 1$ for the Euler-Maruyama method (for proof see Särkkä and Solin, 2019).

4.6.2 Gradient

Numerically, Φ is not a continuous function, but a matrix ($\Phi \in \mathbb{R}^{n \times m}$) with discrete values at longitudinal positions $[\tilde{\lambda}_1, \tilde{\lambda}_2, \dots, \tilde{\lambda}_n]$ and latitudinal positions $[\tilde{\phi}_1, \tilde{\phi}_2, \dots, \tilde{\phi}_m]$. The gradients in Eq. 4.36 and 4.37 are numerically calculated by incorporating the 8 HEP values of the grid cells surrounding the cell a human is located in at the time step t_k (see Fig. 4.8). The gradient is calculated separately in u and v direction, whereby the grid cells east and west are included for the u direction, i.e. the grid cells

marked in blue in Fig. 4.8:

$$\Phi_{i+1,j-1}, \Phi_{i+1,j}, \Phi_{i+1,j+1}, \Phi_{i-1,j-1}, \Phi_{i-1,j}, \Phi_{i-1,j+1},$$

and in v direction, the cells north and south are used, yellow marked in Fig. 4.8:

$$\Phi_{i-1,j+1}, \Phi_{i,j+1}, \Phi_{i+1,j+1}, \Phi_{i-1,j-1}, \Phi_{i,j-1}, \Phi_{i+1,j-1}.$$

The gradient the human in the model encounters at the simulated position $(\hat{\lambda}^k, \hat{\phi}^k)$ for time $t = t_k$, as depicted in Fig. 4.8, is calculated by:

$$\frac{\partial}{\partial x} \Phi(\hat{\mathbf{x}}^k, t_k) = \frac{1}{a \cos \hat{\phi}^k} \cdot \frac{\partial}{\partial \lambda} \Phi(\hat{\lambda}^k, \hat{\phi}^k, t_k) \quad (4.41)$$

$$\frac{\partial}{\partial y} \Phi(\hat{\mathbf{x}}^k, t_k) = \frac{1}{a} \cdot \frac{\partial}{\partial \phi} \Phi(\hat{\lambda}^k, \hat{\phi}^k, t_k) \quad (4.42)$$

and solved numerically by averaging over the 6 grid cells:

$$\frac{\partial}{\partial \lambda} \Phi^k = \frac{1}{6} \sum_{m=-1}^1 \left\{ \frac{\Phi_{i+1,j+m}^k - \Phi_{i,j}^k}{\tilde{\lambda}_{i+1} - \hat{\lambda}^k} + \frac{\Phi_{i-1,j+m}^k - \Phi_{i,j}^k}{\tilde{\lambda}_{i-1} - \hat{\lambda}^k} \right\}, \quad (4.43)$$

$$\frac{\partial}{\partial \phi} \Phi^k = \frac{1}{6} \sum_{n=-1}^1 \left\{ \frac{\Phi_{i+n,j+1}^k - \Phi_{i,j}^k}{\tilde{\phi}_{j+1} - \hat{\phi}^k} + \frac{\Phi_{i+n,j-1}^k - \Phi_{i,j}^k}{\tilde{\phi}_{j-1} - \hat{\phi}^k} \right\}. \quad (4.44)$$

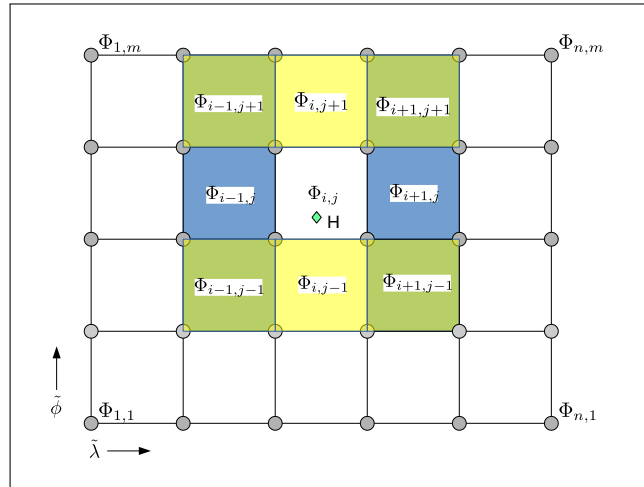


FIGURE 4.8: Illustration of the grid of the HEP (Φ) based on the longitude ($\tilde{\lambda}$) and latitude ($\tilde{\phi}$) to better understand the numerical calculation of the gradient used to estimate the drift determining the macroscopic mobility of a human H (green diamond).

The outer edge of the grid is already defined as the outer limit, so if a human is at $i = 1$, $i = n$, $j = 1$ or $j = m$, they will be removed from the sample.

4.6.3 Population attractiveness

The cultural carrying capacity is, according to the HEP, defined at longitudinal positions $[\tilde{\lambda}_1, \tilde{\lambda}_2, \dots, \tilde{\lambda}_n]$ and latitudinal positions $[\tilde{\phi}_1, \tilde{\phi}_2, \dots, \tilde{\phi}_m]$, and therefore also a matrix ($\rho_{\mathbf{c}} \in \mathbb{R}^{n \times m}$):

$$\rho_{\mathbf{c}} = \rho_{max} \cdot \Phi \quad (4.45)$$

To compare the density with the cultural carrying capacity, the same grid is applied to define grid cells with particular population densities $\rho_{i,j}$ with $\boldsymbol{\rho} \in \mathbb{R}^{n \times m}$. The density in each cell is calculated by counting the individuals, and dividing by the area of the cell $A_{i,j}$ with $\mathbf{A} \in \mathbb{R}^{n \times m}$. The four edges of each cell are defined by the positions $[\tilde{\lambda}_{i+k}, \tilde{\phi}_{j+l}]$ for $k, l \in [-\frac{1}{2}, \frac{1}{2}]$, with:

$$\begin{aligned}\tilde{\lambda}_{i+\frac{1}{2}} &= (\tilde{\lambda}_{i+1} + \tilde{\lambda}_i)/2 \\ \tilde{\lambda}_{i-\frac{1}{2}} &= (\tilde{\lambda}_{i-1} + \tilde{\lambda}_i)/2 \\ \tilde{\phi}_{j+\frac{1}{2}} &= (\tilde{\phi}_{j+1} + \tilde{\phi}_j)/2 \\ \tilde{\phi}_{j-\frac{1}{2}} &= (\tilde{\phi}_{j-1} + \tilde{\phi}_j)/2.\end{aligned}\tag{4.46}$$

Apparently, different rules have to be applied at the boundaries of the grid. The edges of the grid cells are there defined by:

- for $i = 1$: $[\lambda_1, \phi_{j-\frac{1}{2}}]$, $[\lambda_1, \phi_{j+\frac{1}{2}}]$, $[\lambda_{\frac{3}{2}}, \phi_{j-\frac{1}{2}}]$, and $[\lambda_{\frac{3}{2}}, \phi_{j+\frac{1}{2}}]$
- for $i = n$: $[\lambda_{n-\frac{1}{2}}, \phi_{j-\frac{1}{2}}]$, $[\lambda_{n-\frac{1}{2}}, \phi_{j+\frac{1}{2}}]$, $[\lambda_n, \phi_{j-\frac{1}{2}}]$, and $[\lambda_n, \phi_{j+\frac{1}{2}}]$
- for $j = 1$: $[\lambda_{i-\frac{1}{2}}, \phi_1]$, $[\lambda_{i-\frac{1}{2}}, \phi_{\frac{3}{2}}]$, $[\lambda_{i+\frac{1}{2}}, \phi_1]$, and $[\lambda_{i+\frac{1}{2}}, \phi_{\frac{3}{2}}]$
- for $j = m$: $[\lambda_{i-\frac{1}{2}}, \phi_{m-\frac{1}{2}}]$, $[\lambda_{i-\frac{1}{2}}, \phi_m]$, $[\lambda_{i+\frac{1}{2}}, \phi_{m-\frac{1}{2}}]$, and $[\lambda_{i+\frac{1}{2}}, \phi_m]$

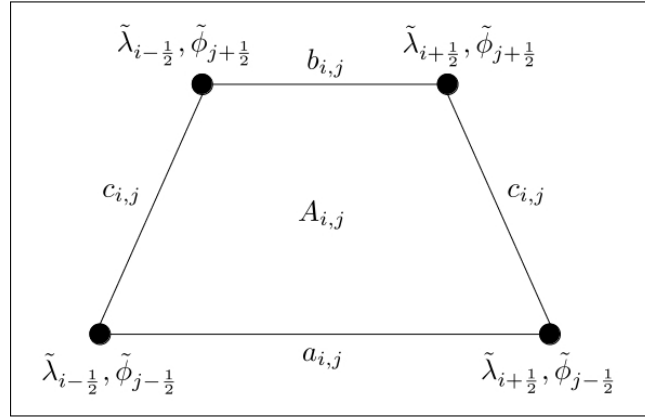


FIGURE 4.9: Definition of the area $A_{i,j}$ of a grid cell used to calculate the population density.

The area of each grid cell $A_{i,j}$ is due to the curvature of the Earth approximately shaped as a trapezoid, as shown in Fig. 4.9, with two equal wing lengths $c_{i,j}$, a bottom length $a_{i,j}$, and a top length $b_{i,j}$. The different lengths between the grid points on a globe are calculated by:

$$a_{i,j} = a \cdot \cos(\phi_{j-\frac{1}{2}}) \cdot [\lambda_{i+\frac{1}{2}} - \lambda_{i-\frac{1}{2}}],\tag{4.47}$$

$$b_{i,j} = a \cdot \cos(\phi_{j+\frac{1}{2}}) \cdot [\lambda_{i+\frac{1}{2}} - \lambda_{i-\frac{1}{2}}],\tag{4.48}$$

$$c_{i,j} = a \cdot [\phi_{j+\frac{1}{2}} - \phi_{j-\frac{1}{2}}].\tag{4.49}$$

With the area formula of a trapezoid, the area of a grid cell $A_{i,j}$ is then calculated by:

$$A_{i,j} = \frac{(a_{i,j} + b_{i,j})}{2} \cdot \sqrt{c_{i,j}^2 - \left(\frac{a_{i,j} - b_{i,j}}{2}\right)^2}. \quad (4.50)$$

With the amount of humans in a cell ($N_{i,j}$), the density of a cell ($\rho_{i,j}$), which is calculated in the units hms/100 km², to be comparable to values from the archaeological literature, is:

$$\rho_{i,j} = \frac{N_{i,j}}{A_{i,j}} = \frac{N_{i,j} \cdot \frac{100 \text{ km}^2}{A_{i,j}}}{100 \text{ km}^2}. \quad (4.51)$$

The population pressure function and the available potential are then calculated per grid cell:

$$\Phi_{i,j}^{av}(t_k) = f_{pp} \left(\frac{\rho_{i,j}(t_k)}{\rho_{i,j}^c(t_k)} \right) \cdot \Phi_{i,j}(t_k) \quad (4.52)$$

Replacing the HEP in Eq. 4.43 and 4.44 with the available HEP in Eq. 4.52 gives the numerical solution of the gradient including the population attractiveness function.

To save computational costs, and to enable some random motion without a changing drift, the population density and the available HEP are only calculated and changed every tenth time step in the CRWM.

4.6.4 Initial conditions

For initialization a starting number of humans (h_0) is chosen. All humans start with zero velocity, the positions are randomly appointed around a fixed centre with a Gaussian distributed random number with a chosen standard deviation. An identification number is assigned to every human, to keep track of the dispersal. At the first time step, all humans outside of the chosen research area and above water are counted as outside and drowned, respectively (for definitions see 4.6.5). The population densities, carrying capacities and clusters are calculated, which define the population dynamics of the first time steps.

4.6.5 Boundary conditions

The Lagrangian model is not bound to any area, but the HEP is. The HEP is defined on the grid $(\tilde{\lambda}, \tilde{\phi})$, and will eventually reach its limits if it is not defined on a global scale. To avoid the humans to reach areas without HEP information, and to confine the research to a certain area, a minimal and maximal longitude, and a minimal and maximal latitude are defined (black lines on Fig. 4.10). Those values indicate the outer boundaries of the research area, which is implemented as an open boundary in one direction, indicating that humans can leave the research area but not come back. All humans leaving the research area are counted and the positions and velocities are masked.

Another natural boundary for human expansion are water bodies. With a given land-sea-dataset the HEP over sea-grids are set to negative values (exemplary shown in Fig. 4.10). Humans approaching water bodies are driven away by a drift directing away from the water. Water bodies are thus implemented as reflective boundaries, while the direction of the reflection depends on the incident angle. If a human should be above a water surface, i.e. the HEP of the grid cell in which he is located is negative, the human is counted as drowned and the position and velocity are masked.

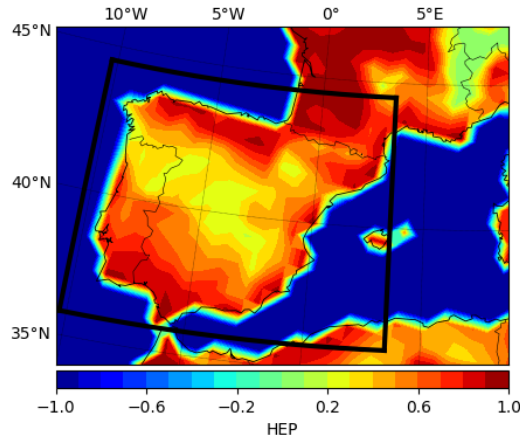


FIGURE 4.10: Representation of the boundary conditions used in the CRW model; the black lines show the outer boundary of the research area, HEP values are set to -1 for water bodies.

This case can only occur, disregarding the initialization, if the stochastic part of the velocity in Eq. 4.10 exceeds the maximal drift velocity. This shouldn't be the case. The model needs to be tuned in a way that the drowned counter stays constant after initialization. This can be implemented by adjusting the parameters or by reducing the HEP value assigned to the water grid cells.

4.7 Summary

The CRWM simulates population dispersal by determining individual trajectories of humans and population growth and decline. In principal, each trajectory is a random motion constrained by environmental and population features. The main quantity determining these constraints is the HEP. The environmental influences are included as a macroscopic drift proportional to the gradient of the HEP. The incorporation of the population features is done by the available HEP, which is calculated by multiplying the HEP with the population attractiveness function. This function takes the population density and the cultural carrying capacity of a region to calculate a score defining the attractiveness of a region by the resource availability and the existence of other humans. Additionally, population size changes are part of the CRWM by including birth and death of humans. It is determined stochastically whether a new human is born or a human dies, while the probability of either of both processes depends on the population density and the cultural carrying capacity. The modeling framework is described in Fig. 4.1.

With the velocity in east/west (u) and north/south (v) direction, the latitudinal (λ) and longitudinal (ϕ) position, the HEP (Φ), the Wiener process in east/west (W_x) and north/south (W_y) direction, the population density (ρ), and the random variable (ζ) defining birth or death, the equations governing the CRWM are listed in the grey box. The constant a is the mean Earth radius and C_{pa} the maximum of the population attractiveness function as defined in Eq. 4.26. The key parameters of the CRWM are listed in Tab. 4.1. The key parameters together with the numerical parameters, such as the simulation period (T) and the starting amount (N_0) and starting distribution of humans, govern the output of the CRWM. Further parameters of the CRWM are the drift time scale (D_t), the gradient distance scale (G_d), the stochastic time scale (τ), the shape parameters of the population attractiveness function (ϵ and η), and

the scale parameter of the growth parameter (κ). Those parameters are calibrated in Chapter 5, so that the CRWM delivers reasonable results from a physical and archaeological perspective.

Equations of motion:

$$du(t) = \left\{ \frac{u(t)v(t) \tan \phi(t)}{a} + \frac{1}{D_t} \left[u_{max} \cdot G_d \cdot \frac{\partial \Phi_{av}(\mathbf{x}(t), t)}{\partial x} - u(t) \right] \right\} \cdot dt + \frac{\sigma_u}{\sqrt{\tau}} \cdot dW_x(t)$$

$$dv(t) = \left\{ -\frac{u(t)^2 \tan \phi(t)}{a} + \frac{1}{D_t} \left[u_{max} \cdot G_d \cdot \frac{\partial \Phi_{av}(\mathbf{x}(t), t)}{\partial y} - v(t) \right] \right\} \cdot dt + \frac{\sigma_u}{\sqrt{\tau}} \cdot dW_y(t)$$

$$d\lambda(t) = \frac{1}{a \cos \phi} \cdot u(t) \cdot dt$$

$$d\phi(t) = \frac{1}{a} \cdot v(t) \cdot dt$$

Population attractiveness:

$$\rho_c(\mathbf{x}(t), t) = \rho_{max} \cdot \Phi(\mathbf{x}(t), t)$$

$$\Phi_{av}(\mathbf{x}(t), t) = C_{pa} \cdot \left\{ \left(\frac{\eta}{\epsilon} \right) \cdot \left(\frac{\rho}{\epsilon \cdot \rho_c} \right)^{\eta-1} \cdot \exp \left[- \left(\frac{\rho}{\epsilon \cdot \rho_c} \right)^\eta \right] \right\} \cdot \Phi(\mathbf{x}(t), t)$$

Birth or death in a grid cell C_{ij} :

$$p_{\zeta_{ij}}(x) = \frac{1}{\sqrt{2\pi}} \cdot e^{-(x-\mu_{\zeta_{ij}})^2/2}$$

$$\mu_{\zeta_{ij}}(\rho_{ij}, \rho_{c,ij}) = \kappa \cdot \rho_{ij} \cdot r \left(1 - \frac{\rho_{ij}}{0.6 \cdot \rho_{c,ij}} \right)$$

TABLE 4.1: Key parameters of the CRWM.

| Parameter name | Parameter |
|------------------------------------|--------------|
| Maximal migration velocity | u_{max} |
| Individual mobility | σ_u |
| Maximal cultural carrying capacity | ρ_{max} |
| Population growth parameter | r |

Chapter 5

Calibration and evaluation of the CRWM

The theoretical and numerical description of the CRWM was completed in Chapter 4. Before the model can be applied to a case study, (1) the parameters that have not been declared as key parameters must be calibrated, and (2) the individual model components must be validated and tested using idealized experiments. The parameters are chosen in such a way that the population dynamics, i.e. both the spread and the growth or decrease, are simulated on a realistic scale. Furthermore, the model should react sensitively to changes in the key parameters. In order to be able to meet both points, the CRWM is calibrated using a Gaussian HEP distribution, with separate experiments being carried out for each of the components (Sec. 5.1). The calibrated model is then validated for dynamic and numerical properties (Sec. 5.2).

5.1 Calibration

A set of parameters has been introduced in Chapter 4 defining the CRWM. As pointed out in Sec. 4.3, the model results are determined by the key parameters. The other parameters are calibrated in a way that the model works as intended, which means that the processes within the CRWM run on a scale that is feasible from a archeophysical perspective and comparable to archaeology and anthropology studies. To determine the parameters, the CRWM is calibrated on a predetermined distribution. Therefore, I use a two-dimensional Gaussian HEP distribution with a maximum in the center at $(5^\circ, 5^\circ)$ and a resolution of 0.25° in longitude and latitude (Fig. 5.1). The Gaussian HEP is a representation of an HEP maximum which can occur in a similar way for the modelled HEP computed by logistic regression and based on climate data.

5.1.1 Calibration of the drift component

In a first step, the deterministic drift, which is determined by the gradient of the HEP, is calibrated by the HEP in Fig. 5.1. To calibrate the drift, the stochastic parts in Eq. A.40 and A.41 are eliminated, so that the horizontal velocities in eastward (u) and northward direction (v) are determined by:

$$du(t) = \left\{ \frac{u(t)v(t) \tan \phi(t)}{a} + \frac{1}{D_t} \left[u_{max} \cdot G_d \cdot \frac{\partial \Phi(\lambda, \phi, t)}{\partial x} - u(t) \right] \right\} \cdot dt, \quad (5.1)$$

$$dv(t) = \left\{ -\frac{u(t)^2 \tan \phi(t)}{a} + \frac{1}{D_t} \left[u_{max} \cdot G_d \cdot \frac{\partial \Phi(\lambda, \phi, t)}{\partial y} - v(t) \right] \right\} \cdot dt. \quad (5.2)$$

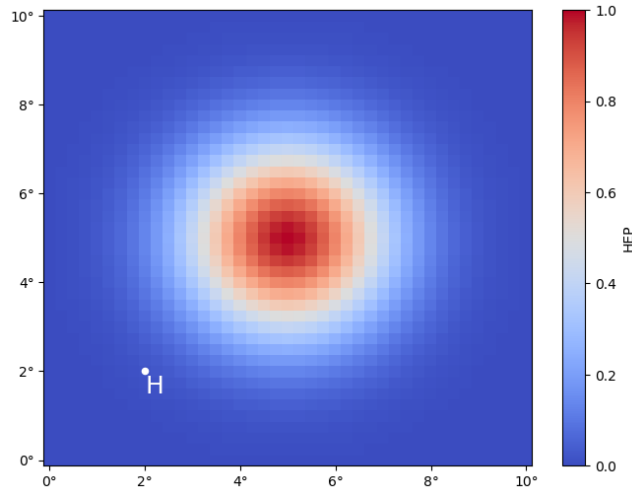


FIGURE 5.1: Input Gaussian HEP and initial position of the human (H) used for calibration and validation of the constrained random walk model.

With the velocities, the longitudinal and latitudinal positions are then calculated by:

$$d\lambda(t) = \frac{1}{a \cos \phi} \cdot u(t) \cdot dt, \quad (5.3)$$

$$d\phi(t) = \frac{1}{a} \cdot v(t) \cdot dt. \quad (5.4)$$

The drift is determined by two components that act in opposition to each other, the gradient of the HEP and the frictional force. Since the drift is defined by the key parameter u_{max} , the two parameters D_t and G_d must be calibrated in such a way that the trajectory and the speed of movement correspond to the specifications, which are explained in detail in the corresponding sections. The equations of motion are calibrated by the drift induced movement of a single human H with initial conditions $\lambda_0 = 2^\circ$, $\phi_0 = 2^\circ$, $u_0 = 0$ km/yr, and $v_0 = 0$ km/yr (H in Fig. 5.1).

Sensitivity of the friction according to D_t

The drift time scale D_t , which is the time period humans need to adapt to new conditions, influences the human movement in the CRWM in two ways, first, by decelerating the gradient induced movement, and second, by defining the magnitude of the friction. The friction is a numerical component introduced to ensure the human movement to converge at the HEP maxima. While minor overshooting of the maxima always occur due to the timely resolution of the CRWM, large scale overshooting is supposed to be eliminated by calibrating the model with fitting parameters. As the friction is determined by the drift time scale D_t (Eq. 4.16), an appropriate model based on the friction is accomplished by adjusting this parameter.

First, the sensitivity of the frictional force according to D_t is tested based on the movement of the human H in Fig. 5.1, who drifts into the center of the distribution of the Gaussian HEP. Different experiments are therefore carried out for different values of D_t . Because D_t not only determines the friction, but also the gradient induced movement speed, G_d has to be adapted in the experiments, so that the human reaches the center of the HEP distribution in an appropriate run time even for high values of D_t . The experimental setup for D_t and G_d is shown in Tab. 5.1, while the maximal

TABLE 5.1: Experimental setup of Fig. 5.3 to test the friction component of the CRWM.

| | D_t [yr] | G_D [km] |
|---|-----------------------|------------|
| A | 2 (but $\gamma = 0$) | 200 |
| B | 500 | 2000 |
| C | 50 | 275 |
| D | 2 | 275 |

migration velocity in the experiments is $u_{max} = 10$ km/year and the simulation period is 500 years.

In Fig. 5.2, the results of the different friction setups in Tab. 5.1 are shown. The friction models (A), (B), and (C) are all falsely parameterized. For the model without friction (Fig. 5.2a) the parameter γ in Eq. 4.11 and 4.12 is set to zero. As expected, because it was already shown for an one-dimensional model in Sec. 4.2, without friction, the human is accelerated towards the maximum of the Gaussian HEP and reaches maximum velocity at the center of the distribution. It then overshoots the centre and decelerates afterwards until it reaches zero velocity close to the mirror point of the initial position of an axis perpendicular to the direction of motion going through the center of the HEP. The oscillations take place until the end of the time

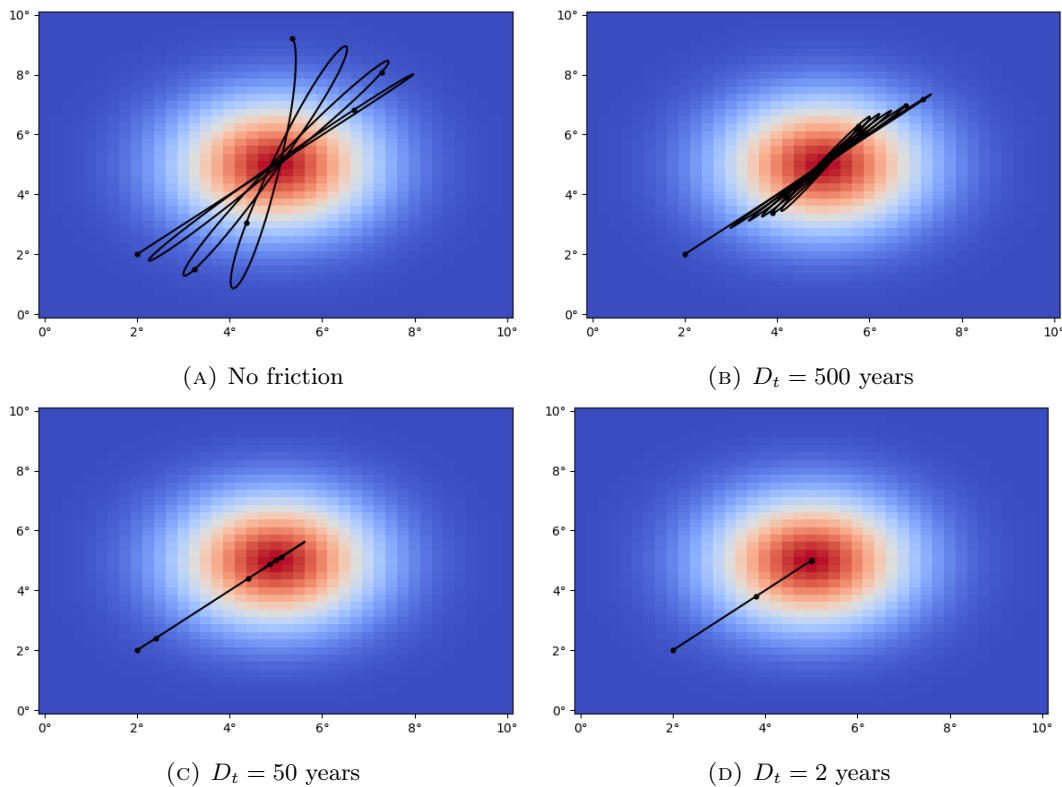


FIGURE 5.2: Examples for the trajectory of human H with initial condition $(\lambda_0, \phi_0) = (2^\circ, 2^\circ)$ and $(u_0, v_0) = (0, 0)$ km/year determined by the drift of the CRWM (Eq. 5.1 and 5.2) for different setups determining the friction of the model as defined in Tab. 5.1 with $u_{max} = 10$ km/yr. Black dots indicate the position of the human in 100 year time steps. Setup (D) delivers the desired results, a calibrated model without large-scale overshooting.

series, while the position slightly changes due to the curvature of the Earth. Two other examples of models are shown in Fig. 5.2b, with $D_t = 500$ years, and 5.2c, with $D_t = 50$ years, where the friction is not working appropriately due to overshooting. Although the position approaches the center of the HEP distribution, the overshooting takes place on an order of magnitude that does not correspond to the assumptions of the model.

An example for a well calibrated model is shown in Fig. 5.2d, with a drift time scale of $D_t = 2$ years. The human reaches the center after less than 200 years and then stays there (only three black dots can be seen as the others overlap in the center). Of course, one can assume that different parameter combinations will produce similar results. The calibration of D_t can therefore only be carried out in connection with G_d . However, one can see from the examples that D_t must be sufficiently small, so that the friction is strong enough to prevent large scale overshooting. This result, after all, corresponds to the definition of D_t from Sec. 4.3, in which the range was set at 0.1 - 10 years.

Calibration of G_d and D_t

The setup in Fig. 5.1 is now used to calibrate the parameters G_d and D_t and define the maximal migration velocity u_{max} . As pointed out in Section 4.3, migration is the ensemble averaged trajectory between two points. In the CRWM, this quantity is mainly determined by the drift and therefore the HEP distribution. Consequently, different starting or ending points lead to different maximal migration velocities. Here, the Gaussian HEP distribution is used to calibrate the magnitude of the drift. The maximum speed that is achieved by the HEP gradient acceleration is, due to the Gaussian distribution, the same for all positions that are at a certain distance from the center. The maximum ensemble speed therefore corresponds to the maximum speed of the human H in Fig. 5.1, whose trajectory is now used for calibration.

The calibration of D_t and G_d can only be done by considering both parameters together. Since a D_t of 2 years has been shown to work (Fig. 5.2d), the parameter is kept constant while different values of G_d are tested in the following experiments. To evaluate the movement of H , the absolute velocity is calculated by:

$$|\mathbf{u}(t)| = \sqrt{u(t)^2 + v(t)^2}, \quad (5.5)$$

with the definitions of u and v from Eq. 5.1 and 5.2. The speed of H is first accelerated to a maximum and then slowed down by the friction force so that the speed is approximately 0 km/yr when it reaches the center (see, e.g., Fig. 5.4). The absolute velocity maximum (M) of the time period, based on u_{max} and G_d :

$$M(u_{max}, G_d) = \max_t |\mathbf{u}(t, u_{max}, G_d)| \quad (5.6)$$

is now examined to configure G_d , which is chosen in a way that the maximum of the absolute velocity of H coincides with u_{max} .

For four configurations of maximal migration velocities u_{max} (2.5, 5, 7.5 and 10 km/yr), the maximum of the absolute velocity of H is determined for G_d values from 220 to 260 km (Fig. 5.3 left). The maximal absolute velocity increases with increasing G_d for all four configurations. For low G_d , all straight lines have maximal absolute velocities that are smaller than the maximum migration velocity; these then increase with increasing G_d until they exceed u_{max} . However, the intersection occurs at different G_d for each u_{max} . The optimal G_d is determined from the combination of the four u_{max} configurations. This is done by the minimal deviation (D) of the maximal absolute

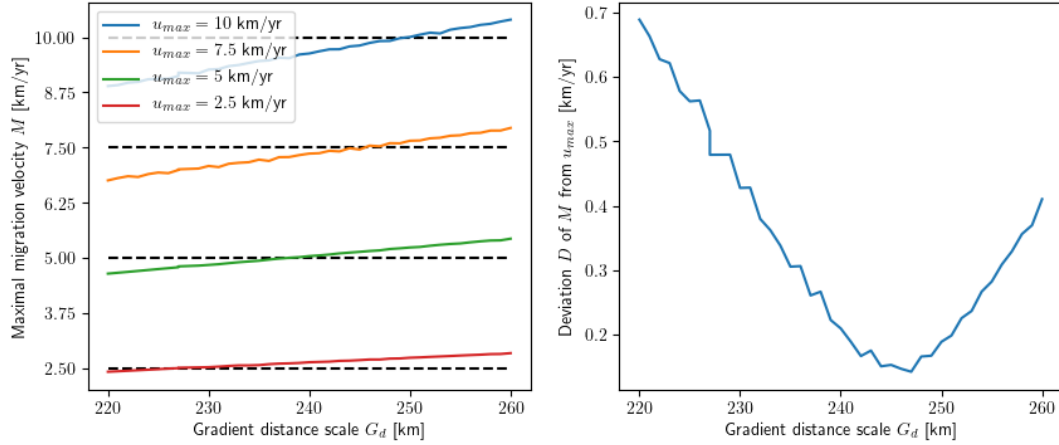


FIGURE 5.3: *Left*: Maximal absolute velocity M as defined in Eq. 5.6 of human H in Fig. 5.1 for different configurations of u_{max} with $D_t = 2$ years. *Right*: Combined deviation of M from u_{max} for the different u_{max} configurations (2.5, 5, 7.5, and 10 km/yr) as defined in Eq. 5.7.

velocity M from u_{max} based on the four configurations. The deviation D is calculated by:

$$D(G_d) = \frac{1}{2} \cdot \left\{ [M(u_{max} = 2.5, G_d) - 2.5]^2 + [M(u_{max} = 5, G_d) - 5]^2 + [M(u_{max} = 7.5, G_d) - 7.5]^2 + [M(u_{max} = 10, G_d) - 10]^2 \right\}^{\frac{1}{2}}, \quad (5.7)$$

and shown in Fig. 5.3 right. The curve of D shows a clear minimum at $G_d = 247$ km and increases for larger and smaller values of G_d . The respective deviations of the maximum absolute velocity from u_{max} are for 2.5 km/yr: 0.21 km/yr; for 5 km/yr: 0.175 km/yr; for 7.5 km/yr: 0.031 km/yr; and for 10 km/yr: -0.087 km/yr.

The configuration $G_d = 247$ km is therefore the best choice for a parameterization of the CRWM as the maximal absolute velocities generally come closest to the maximal migration velocities. For $G_d = 247$ km, and $u_{max} = 10$ km/yr, $u_{max} = 7.5$ km/yr, $u_{max} = 5$ km/yr, and $u_{max} = 2.5$ km/yr the modelled maximal absolute velocities are $M = 9.86$ km/yr, $M = 7.53$ km/yr, $M = 5.17$ km/yr, and $M = 2.71$ km/yr respectively (shown in Fig. 5.4).

In summary, the results of the calibration of the drift component by the Gaussian HEP for the two parameters drift time scale (D_t) and gradient length scale (G_d) are shown in Tab. 5.2. This parameter setup is used in all further experiments of the CRWM. Changes in the deterministic drift magnitude in the CRWM are then solely determined by the maximal migration velocity (u_{max}).

TABLE 5.2: Calibrated parameters D_t and G_d .

| Drift time scale (D_t) | Gradient length scale (G_d) |
|----------------------------|---------------------------------|
| 2 years | 247 km |

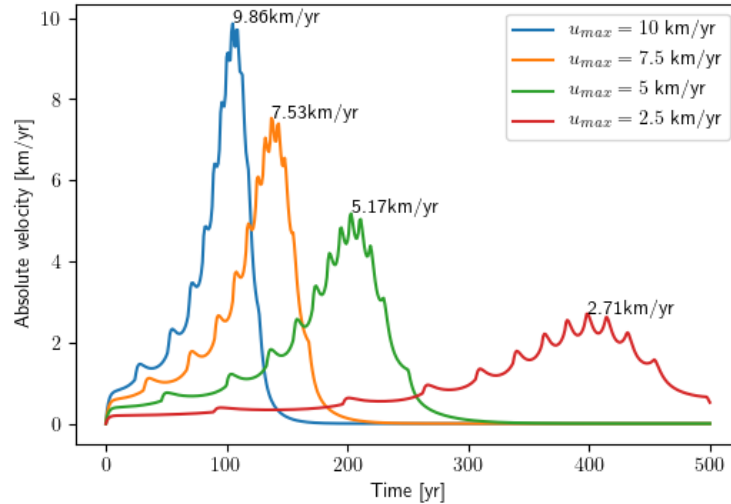


FIGURE 5.4: Absolute velocities for the human H in Fig. 5.1 for different u_{max} with $G_d = 247$ km/yr, $D_t = 2$ yr, and a time period of 500 years. The maximal absolute velocity M for each configuration is specified.

5.1.2 Calibration of the stochastic component

To evaluate the random movement, the random walk is now considered in addition to the deterministic drift. So the main equations 4.18 are used without population attractiveness or birth and death. The validation of the stochastic component of the model takes place through the spatial evaluation of the random movements. In addition to human H in Fig. 5.1, 999 other people are randomly distributed between $0 - 10^\circ$ East and $0 - 10^\circ$ North. As a result of the drift, all people are accelerated towards the center of the HEP distribution, so that in the long term, despite the random movement, all people move towards the center. So after an initialization period (here 500 years are assumed), the position of the people can be used to determine at what distance around the center the random movements take place. For this purpose, circles are drawn around the HEP center with increasing radii and the number of people within the circles compared to the total population is determined. This is shown as an example in Figure 5.5, in which 35% of the population are in a 50 km circle, 76% in a 100 km circle, 94% in a 150 km circle and 99% in a 200 km circle around the center.

To calibrate the parameter *stochastic time scale* (τ), runs for different values of the *individual mobility* (σ_u) are now being examined for the randomly distributed starting population of 1000 people (experiments for $\tau \in [1, 2, 3, 4, 5, 6, 7, 8]$ yr and $\sigma_u \in [50, 100, 150, 200]$ km/yr). The parameter σ_u defines the size of the random walk in the model and determines the random movements of a human that can occur within a year. This mobility can also result in migrations, but the random walk is intended to model the annual fluctuation around a "settlement center". Since in Gaussian HEP this population settlement center is in the maximum of the distribution, a large part of the random movements should also take place within a certain distance from this center; σ_u accordingly defines a radius in which the random movements take place around the settlement center. For $\sigma_u = 150$ km/yr, e.g., the maximum radius corresponds to 75 km because of the way there and back. A large part of the random movements should therefore take place within 75 km from the center. The parameter τ can then be calibrated in such a way that most humans are located within the

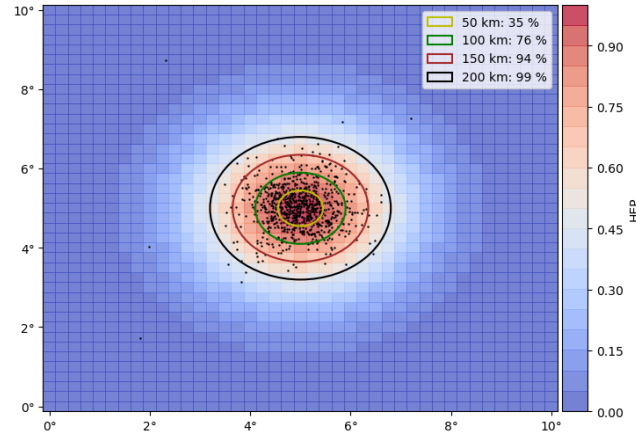


FIGURE 5.5: Example of how the stochastic component is validated in the CRWM: 1000 people are randomly distributed around the Gaussian HEP; after an initialization period of 500 years, the distance from the center of the population is evaluated. 34% of the population is located within a 50 km radius from the center, 76% within a 100 km radius, 94% within a 150 km radius and 99% within a 200 km radius.

certain radius.

Since drift and random walk act simultaneously, the size of the random walk is also determined by u_{max} . The calibration is carried out here with $u_{max} = 5$ km/yr and afterwards it is shown that the result can also be transferred to other u_{max} . The distance of each human from the center is calculated for each time step and assigned to the circles with the respective radius. Then, the percentage of humans within the circles are compared to the total population. In Fig. 5.6, the averaged percentages

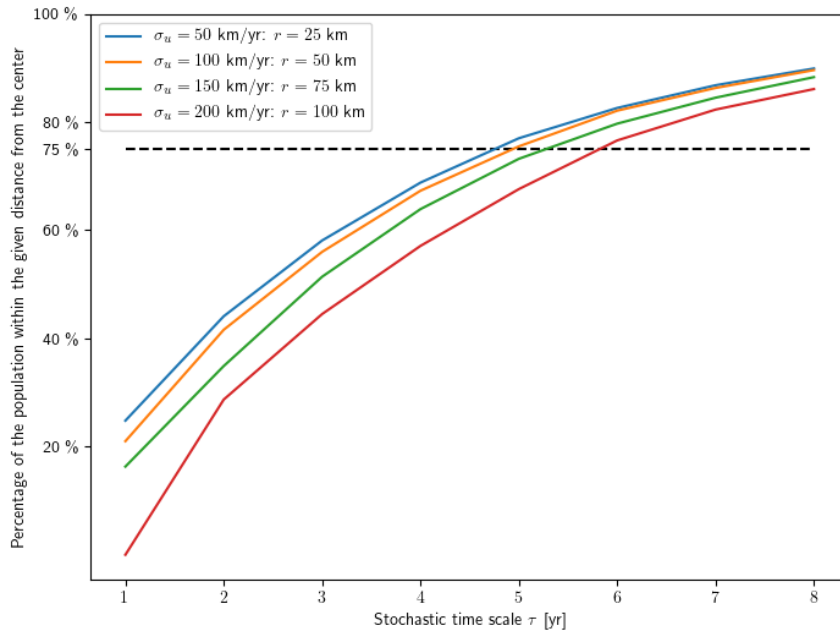


FIGURE 5.6: Percentage of the population which are located inside circles around the center with different radii defined by the individual mobility σ_u of the CRWM run, with $u_{max} = 5$ km/yr. For $\tau = 6$ yr, all four curves exceed the 75% threshold line.

from the years 500 to 1000 (after the initialization phase) are shown for the radii $r = 25$ km for $\sigma_u = 50$ km/yr, $r = 50$ km for $\sigma_u = 100$ km/yr, $r = 75$ km for $\sigma_u = 150$ km/yr, and $r = 100$ km for $\sigma_u = 200$ km/yr. So that random migration is not completely suppressed, a threshold of 75% of the total population is set, which on average must be within the circles. The optimal τ is then the minimum value at which all four curves in Fig. 5.6 have exceeded the 75% curve, which is the case for $\tau = 6$ years.

The results for different values of u_{max} and σ_u for $\tau = 6$ are shown in Tab. 5.3. As expected, the random movement is strongly linked to the size of the migration speed. At a u_{max} of 10 km/yr, almost the entire movement takes place around the settlement center (PiC > 96%), while at $u_{max} = 2.5$ km/yr, significantly more people leave the settlement center (PiC < 57%). While in the first case random migration is almost completely suppressed, in the second case it occurs very frequently. The choice of the two velocities should therefore always be coordinated with one another and chosen differently depending on the research question. The stochastic time scale, however, is set to $\tau = 6$ yr in all further experiments.

TABLE 5.3: Percentage of the population (averaged from years 500 to 1000) that is located within the circle (PiC) with radius r around the HEP center in Fig. 5.1, with a starting population of 1000 humans that are randomly distributed around the center with a Gaussian probability and a standard deviation of 2° . In the CRWM, the parameters u_{max} and σ_u are specified in the table, and $\tau = 6$ yr.

| u_{max} | σ_u | r | PiC |
|-----------|------------|--------|-----|
| 2.5 km/yr | 50 km/yr | 25 km | 57% |
| | 100 km/yr | 50 km | 56% |
| | 150 km/yr | 75 km | 52% |
| | 200 km/yr | 100 km | 44% |
| 5 km/yr | 50 km/yr | 25 km | 83% |
| | 100 km/yr | 50 km | 82% |
| | 150 km/yr | 75 km | 78% |
| | 200 km/yr | 100 km | 77% |
| 7.5 km/yr | 50 km/yr | 25 km | 93% |
| | 100 km/yr | 50 km | 93% |
| | 150 km/yr | 75 km | 92% |
| | 200 km/yr | 100 km | 90% |
| 10 km/yr | 50 km/yr | 25 km | 97% |
| | 100 km/yr | 50 km | 97% |
| | 150 km/yr | 75 km | 96% |
| | 200 km/yr | 100 km | 96% |

5.1.3 Calibration of the population attractiveness function

The population attractiveness function (f_{pa} , Eq. 4.22) is defined in such a way that, on the one hand, migration leads away from regions that are overpopulated and, on the other hand, migration to unpopulated regions is unattractive. It takes as arguments the population density, derived by the individual position of each human and the area of grid cells, and the cultural carrying capacity (ρ_c). This capacity is a quantity proportional to the HEP with the parameter "maximal cultural carrying capacity" (ρ_{max}) being the constant of proportionality (Eq. 4.19). The cultural carrying

capacity defines an upper limit of sustainability for populations in a region depending on the culture, while it corresponds to the maximal cultural carrying capacity for optimal conditions, i.e., $\text{HEP} = 1$. The population attractiveness function is a Weibull function taking the variables population density and cultural carrying capacity and returning a value between 0 and 1 (Eq. 4.22). The shape of the Weibull distribution is thereby defined by ρ_c and the parameters η and ϵ (see Fig. 4.3).

Calibration of η and ϵ

The calibration of the population attractiveness function is done by diagnosing the parameters η and ϵ . The parameter η shifts the distribution and scales the Weibull function, while the parameter ϵ mainly defines the shape of the function. In the following, fixed values for both parameters are determined to define a certain shape and a standard scale. Shifts of the population attractiveness function then solely depend on the parameter maximal cultural carrying capacity ρ_{max} . The choice of the parameters η and ϵ are done in a way that, on the one hand, the presupposed properties defined in Eq. 4.20 and 4.21 are fulfilled, and, on the other hand, the resulting human trajectories lead to population densities that smoothly adapt to the given HEP distribution. In the case of the Gaussian HEP the second precondition would lead to Gaussian distributed population densities.

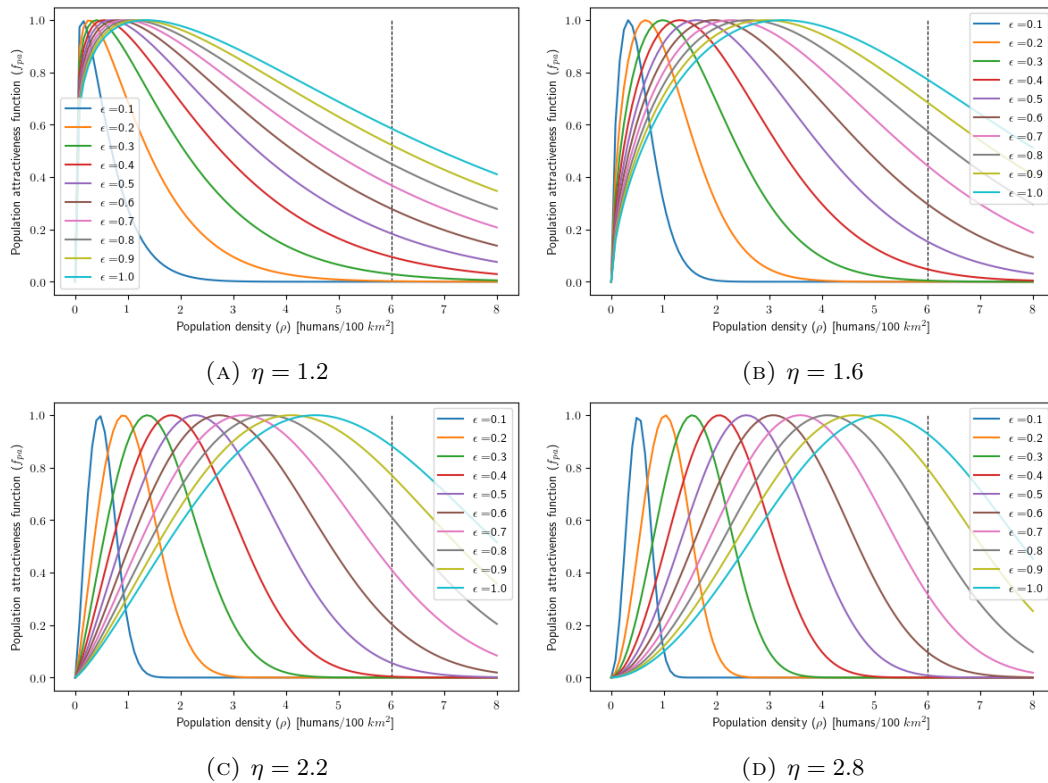


FIGURE 5.7: Shape of the population attractiveness function for different values of the parameters η and ϵ , for $\rho_c = \rho_{max} = 6$ humans/100 km².

The constraints defined in Eq. 4.20 and 4.21 determine a certain range for the parameters η and ϵ at which the Weibull function fulfills the properties. As shown for different values of η and ϵ in Fig. 5.7 with $\rho_c = \rho_{max}$, the Weibull function takes the required shape for $\eta \in [1.1, 3.0]$ and $\epsilon \in [0.1, 1.0]$. For $\eta \leq 1$, the population

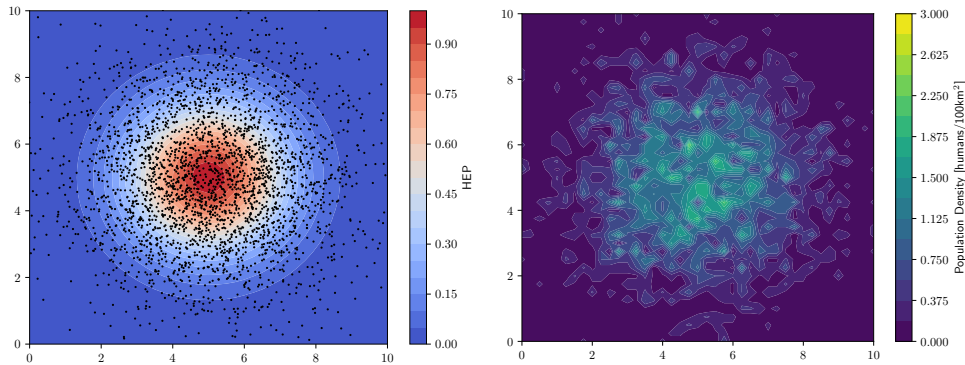


FIGURE 5.8: Initial positions of the 3000 humans (left) and initial population density (right) of the experiments used to calibrate the parameter η and ϵ of the population attractiveness function.

attractiveness function would not go to zero for $\rho \rightarrow 0$. Higher values of η or ϵ would shift the maximum of the curve to higher ρ , so that the second presupposed property, $f_{ap} \rightarrow 0$ for $\rho \rightarrow \rho_c$, would not be fulfilled anymore.

To further confine the parameters and to test whether the second precondition is fulfilled, meaning that the population density adapts to the HEP, experiments are done for different setups of η and ϵ within the identified ranges. Again, the Gaussian HEP in Fig. 5.1 is used for the calibration with 3000 humans. The initial position of the 3000 humans are thereby randomly determined by a two-dimensional Gaussian random distribution with a fixed center at 5°N and 5°E and a standard deviation of 2° . All humans that are outside of the HEP distribution are removed from the dataset. All humans have a zero initial velocity. The initial positions and the resulting initial population density are shown in Fig. 5.8. The parameters for each of the experiments are listed in table 5.4.

TABLE 5.4: Experimental setup to calibrate the population attractiveness function (f_{pa}). Further parameters are defined as: $D_t = 2$ yrs, $G_d = 247$ km, and $\tau = 6$ yrs.

| N | T | u_{max} | σ_u | ρ_{max} |
|-------------|---------|-----------|------------|------------------------------|
| 3000 humans | 100 yrs | 10 km/yr | 200 km/yr | 6 humans/100 km ² |

Shown in Fig. 5.9 are the population densities averaged over the 100 years simulation time for different setups of η and ϵ . Three examples are shown where the averaged population densities are not Gaussian distributed (Fig. 5.9a, 5.9d, and 5.9f), and three that are Gaussian distributed (Fig. 5.9b, 5.9c and 5.9e).

The population attractiveness function with $\eta = 1.2$ and $\epsilon = 0.1$ (Fig. 5.9a) is an example of a Weibull function that is too narrow for my application. The density is roughly Gaussian distributed, but there are several maxima in the distribution. This shape comes from the narrow Weibull function (Fig. 5.7) that strongly restricts the drift of the humans when the population exceeds a comparatively low density. The available HEP is then only for certain population densities unequal to zero.

For the population attractiveness function with $\eta = 2.2$ and $\epsilon = 0.6$ (Fig. 5.9d), there are gaps in the population density around the center of the Gaussian HEP. As shown in Fig. 5.7, the maximum of f_{pa} for these parameters lies at around $\rho = 3$ humans/100 km² for $\rho_c = \rho_{max}$, while $f_{pa} < 0.4$ for $\rho \leq 1$. Due to this course of the curve, low population densities decisively lower the available HEP, which leads to a

more pronounced clustering of populations with population densities around the maximum of the population attractiveness function. Random mobility of some individuals will eventually lead to a Gaussian distributed population density. This procedure takes, due to the restricted available HEP for low population densities, more time and has not occurred after the chosen time interval of 100 years. The setup can be used if a stronger clustering of humans is intended. In this study, different parameters will be used for the population attractiveness function, so that the individual mobility is not that much decelerated for low population densities.

In the next setup with $\eta = 2.8$ and $\epsilon = 1.0$ (Fig. 5.9f), the mobility is even more suppressed, so that clusters occur with population densities exceeding the cultural carrying capacity of $\rho_{max} = 6$. The position of the clusters only depend on the initial population density and not on the HEP distribution. Moreover, they do not vanish for longer time intervals. This setup is an extreme example of a falsly parameterized model.

Also shown in Fig. 5.9 are three examples, the ones in Fig. 5.9b, 5.9c, and 5.9e, where the shape of the 100 yearly mean of the population densities are Gaussian distributed and therefore correspond to the HEP distribution. These setups are therefore possible parameter candidates for the population attractiveness function. As a lot of the tested functions have a similar shape, there are a lot of parameter combinations where the chosen preconditions are fulfilled. However, it can be seen, that the maximum of the mean population density and the width of the Gaussian distribution differs for the three setups. In Fig. 5.10 is shown the timely mean of the maximum population density per time step for the different setups of η and ϵ . It is intended, that the maximal population density is, even for best environmental conditions, significantly smaller than the maximal cultural carrying capacity (ρ_{max}). This condition is in accordance with the anthropological research (Kelly, 2013), humans always keep the population below the capacity to keep the environment in balance. It can be seen, that the maximal population density rises for increasing ϵ . As the center of the Gaussian distribution is not settled at the end of the time interval for some of the models, the optimal conditions ($\rho_c = \rho_{max}$) are not reached yet. One could expect that the maximal density of those models is higher for larger time intervals.

For my modelling purposes it is feasible when the maximal density for optimal conditions is in the range of $\rho \leq 0.8 \cdot \rho_{max}$. I choose the setup $\eta = 1.6$ and $\epsilon = 0.4$ to be the standard of my further studies. The mean maximal density of 3.82 humans/100 km² is in the accepted range for the calibration experiment and the population density adapts well to the Gaussian HEP as shown in Fig. 5.9c.

5.1.4 Calibration of the birth and death module

The birth and death module is designed in such a way that it is decided separately for each grid cell of the HEP grid whether a human is born or a human who is inside the grid cell dies. The decision is made at random, with the probability of whether a human will be born or die is determined by the mean value of the probability distribution in Eq. 4.35, which depends on the cultural carrying capacity and population density:

$$\mu_{\zeta_{ij}}(\rho_{ij}, \rho_{c,ij}) = \kappa \cdot \rho_{ij} \cdot r \left(1 - \frac{\rho_{ij}}{0.6 \cdot \rho_{c,ij}} \right). \quad (5.8)$$

Since the CRWM calculates with humans and thus discrete numbers, the birth and death module must be calibrated so that the population growth is comparable to the fundamental logistic growth population model (Eq. 4.34) that calculates with population densities. Therefore the parameter κ was introduced, which is to be calibrated

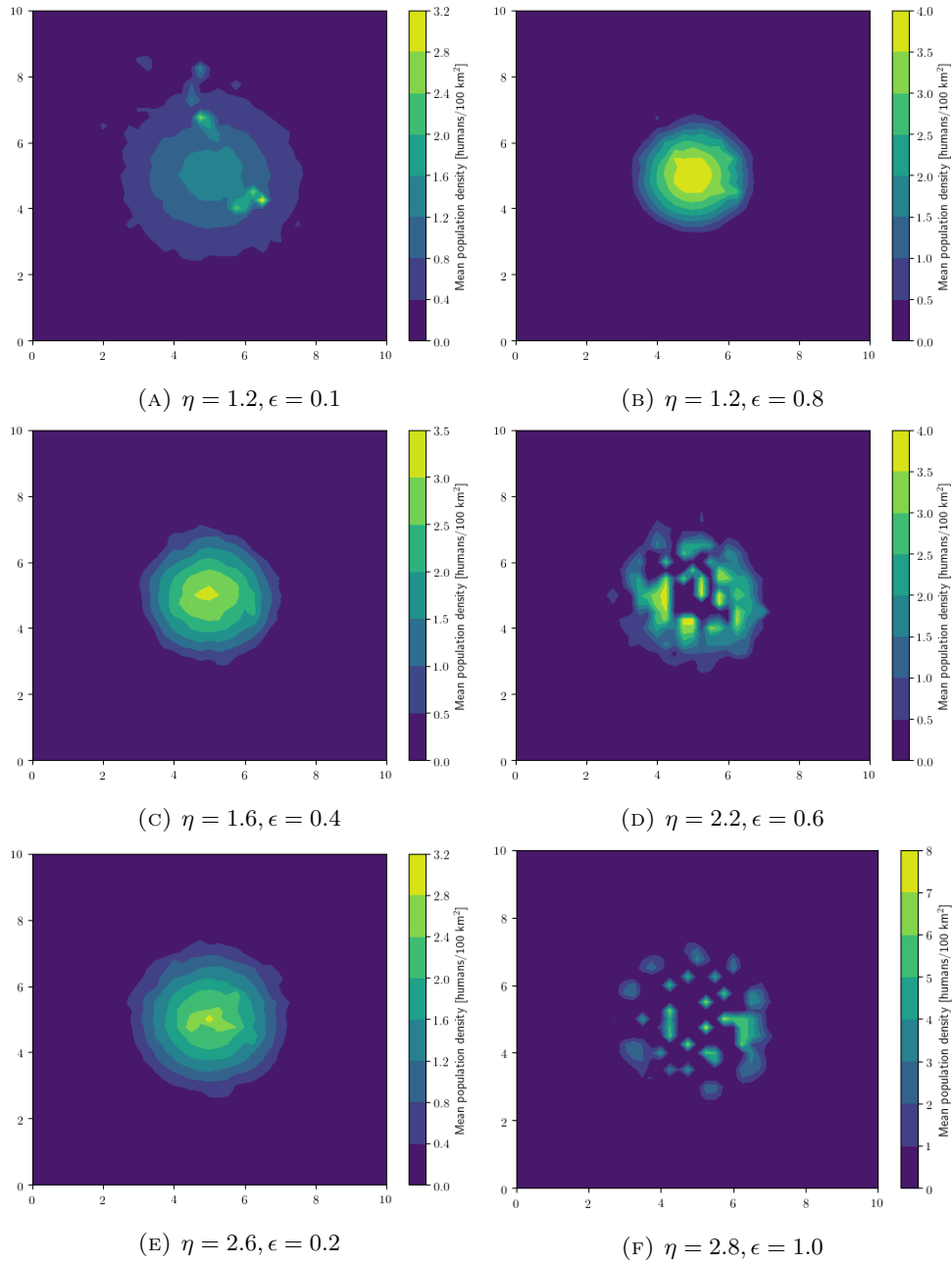


FIGURE 5.9: Population density averaged over the 100 years of the simulation for the initial setup shown in Fig. 5.8 for different values of the parameters η and ϵ .

in the following.

First of all, however, it must be noted that due to the cell-by-cell determination of births and deaths, the resolution of the grid has a strong influence on population growth in the CRWM. With a high-resolution HEP grid, significantly more people can be born, but also die, than with a less-resolved grid. An additional component must therefore be integrated into the birth and death module in order to take the grid size into account in the calculation. Since the birth-death module is decoupled from the equations of motion, a grid size-dependent time interval Δt^{bd} can be introduced at which changes in population size take place. The different population increases or decreases depending on the size of the grid are then compensated for by separate time

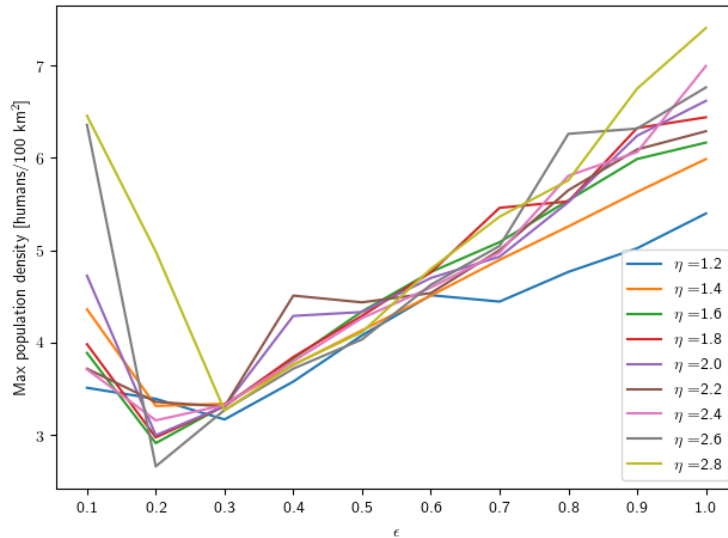


FIGURE 5.10: Timely mean of the maximal population density per time step based on the population attractiveness function for different setups of η and ϵ .

intervals Δt^{bd} , so that the same growth rates are achieved in the long term.

Determination of Δt^{bd}

First of all, different values for Δt^{bd} are tested for a fixed grid size of 0.25° in order to be able to estimate how the model produces realistic numbers. To do this, the model is evaluated based on the death rate (r_d), i.e. the number of humans who have died per year. For the experiment, 500 humans are randomly distributed around the Gaussian HEP in Fig. 5.1. The parameter setup of the experiment is shown in Tab. 5.5. As with the other experiments, humans migrate to the center of the Gaussian HEP distribution and are driven to HEP outer areas by the population attractiveness function and random movement. In addition, the birth and death module leads to a sporadic population growth after an initial population decline, which is triggered by the random distribution and thus the positioning of humans in poor HEP areas. As a result of the population growth, more and more HEP areas are populated until a steady state is reached. The death rate of the CRWM that occurs after the initialization phase is now evaluated in order to determine Δt^{bd} for the grid resolution of 0.25° . To calculate the death rate (r_d), the number of people who have died, interpolated over a year, is determined and divided by the total population (Fig. 5.11a). As expected, the number of deaths per year and thus the death rate decrease if Δt^{bd} is increased, i.e. the time interval at which the birth and death module is applied. The averaged death rates decrease almost linearly from $r_d = 0.05 \text{ yr}^{-1}$ for $\Delta t^{bd} = 1 \text{ yr}$ to $r_d = 0.004 \text{ yr}^{-1}$ for $\Delta t^{bd} = 12 \text{ yr}$, which corresponds to a life expectancy (calculated by the inverse of the death rate $1/r_d$) that takes place in the time interval of 20 to 250 yrs. The life expectancy of Paleolithic hunters and gatherers is not known, but like

TABLE 5.5: Experimental setup to calibrate Δt^{bd} in the the birth and death module.

| N_0 | T | u_{max} | σ_u | ρ_{max} | $\kappa \cdot r$ |
|---------|----------|-----------|------------|---------------------------|-----------------------|
| 500 hms | 3000 yrs | 5 km/yr | 150 km/yr | 4 hms/100 km ² | 0.15 yr ⁻¹ |

other parameters, it can be estimated using ethnological data. I am orienting myself here on the study by [Gurven and Kaplan \(2007\)](#), which determined a life expectancy of 70 yrs. For this experiment, this would be the case for $\Delta t^{bd} = 4$ yr with a death rate of $r_d = 0.0131$ and a life expectancy of 76 yrs. However, the result can only be transferred to other experiments with caution, since other HEP distributions can lead to different death rates. It is always advisable to evaluate the death rate separately for each experiment and to adjust Δt^{bd} accordingly.

The result is now used to find a law between the birth and death rate and the grid size of the HEP distribution. To determine Δt^{bd} as a function of the grid size, the CRWM is run for differently resolved Gaussian HEP. In addition to the 0.25° resolved grid from Fig. 5.1, the calculation is also made for a 0.125° and a 0.5° grid in order to find a connection between the grid resolution and population growth. By adjusting the three time intervals ($\Delta t_{0.125}^{bd}$, $\Delta t_{0.25}^{bd}$, $\Delta t_{0.5}^{bd}$), an attempt is made to bring the growth rates closer together. The same setup as in Tab. 5.5 is used, with ρ_{max} being set to 10 hms/100 km², because otherwise the high-resolution 0.125° model would not produce stable results (see the discussion in Chapter 6, Sec. 6.2.6). Fig. 5.11b shows the number of modeled people as a function of time for the 0.5° HEP (blue lines), the 0.25° HEP (green line) and the 0.125° HEP (red lines) for different Δt^{bd} . You can see that the resolution has a striking influence on the growth rate. In the experiment, a maximum number of 6000 humans was set, which is achieved in all 0.125° runs, while with a resolution of 0.5° this maximum value is only achieved for $\Delta t_{0.5}^{bd} = 1$ yr. Even if it were theoretically possible to find a mathematical law that connects the resolution and the growth rate in order to find the optimal Δt^{bd} , which is not entirely trivial due to the stochastic approach to the birth and death module, I see it as sufficient for this determining to use the best fits, i.e. the curves that come closest to the 0.25° curve. For the 0.125° resolution this corresponds to a $\Delta t_{0.125}^{bd}$ of 12 years and for the 0.5° resolution a $\Delta t_{0.5}^{bd}$ of 1 year. This is of course only a rough estimate, but should be sufficient for the purposes of the CRWM. Otherwise, it should again be pointed out that each time the CRWM is used, the death rate should be taken into account and Δt^{bd} should be adjusted accordingly.

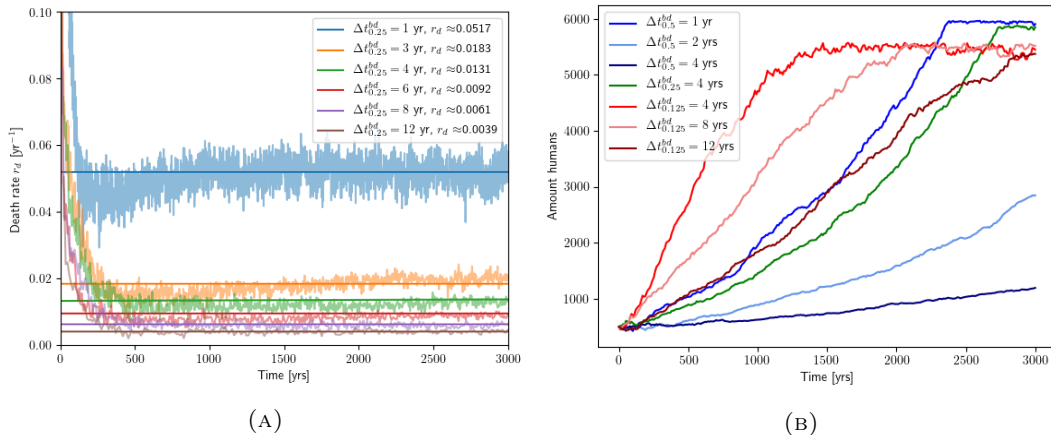


FIGURE 5.11: Calibration of the time interval of the birth and death module (Δt^{bd}). (A) Amount of deaths compared to the total population per year for different Δt^{bd} for the setup as specified in Tab. 5.5 and the Gaussian HEP in Fig. 5.1. The straight line is the mean of the death rate (r_d), disregarding the spinup time. (B) Amount of humans modelled for differently resolved HEP distributions with 0.125° , 0.25° and 0.5° , for different Δt^{bd} , with the setup of Tab. 5.5 by changing ρ_{max} to 10 hms/100 km².

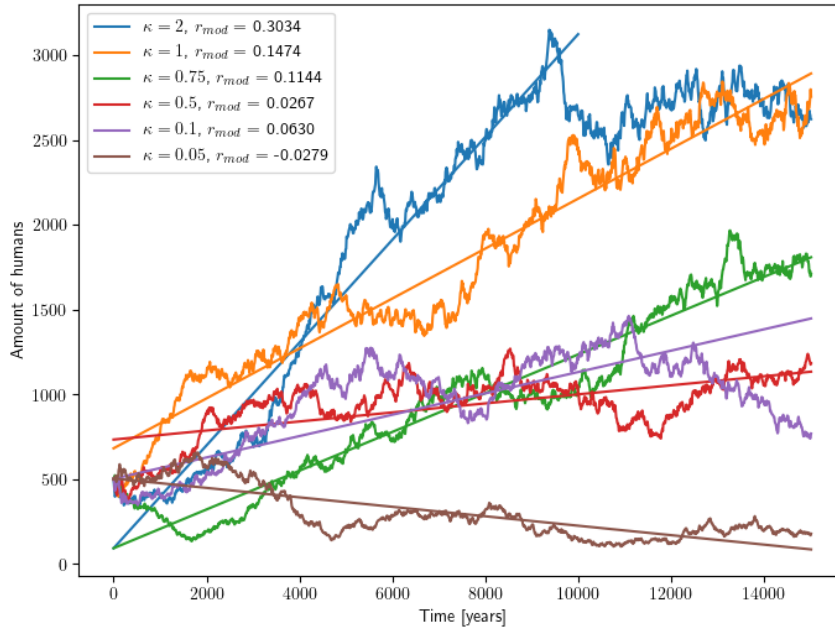


FIGURE 5.12: Modelled population growth rate r_{mod} for different κ for a chosen growth rate of $r = 0.03 \text{ yr}^{-1}$; the setup of the experiment is taken from Tab. 5.7 for the Gaussian HEP on Fig. 5.1.

Determination of κ

After the death rate runs on the correct scale, the next step is to try to calibrate the growth rate of the model. This is done by adapting the specially introduced parameter κ in Eq. 5.8 so that the modeled growth rate (r_{mod}) roughly corresponds to the chosen growth rate (r). The setup of the experiment is shown in Tab. 5.7 and the results of r_{mod} for different κ are shown in Fig. 5.12. Even if there are strong fluctuations in the population change due to randomness, with the exception of $\kappa = 0.1$, it can be seen that r_{mod} also increases for increasing κ . For this experiment, $\kappa = 0.5$ is the best choice, since there $r_{mod} = 0.0267$ roughly corresponds to the value of $r = 0.03$. Unfortunately, it cannot be completely ruled out whether this value arises by chance or is a statistical property of the CRWM. This is because for very small values of κ the mean value of the Gaussian distribution (Eq. 5.8) approaches zero, whereby the decision whether a person is born or dies becomes independent of the external conditions. As a result, the population growth is purely random, which probably explains the increased growth rate for $\kappa = 0.1$: at the end of the time series, the population decreases sharply, which would suggest that the initial increase was more of a random nature. For $\kappa = 0.05$, a population decrease is even modeled.

Furthermore, the relationship between modeled growth rate (r_{mod}) and κ is not linear. A more complex approach would have to be chosen to adjust r_{mod} to r , which could not be implemented in this work. Nevertheless, one can deduce from the experiment that the growth rate r , with a chosen κ of 0.5, should be between 0.03 and 0.06. For

TABLE 5.6: Experimental setup to calibrate κ in the the birth and death module.

| N_0 | T | u_{max} | σ_u | ρ_{max} | Δt^{bd} | r |
|---------|------------|-----------|------------|---------------------------|-----------------|-----------------------|
| 500 hms | 15,000 yrs | 5 km/yr | 150 km/yr | 4 hms/100 km ² | 4 yrs | 0.03 yr ⁻¹ |

smaller values the model becomes unstable and at 0.06 the modeled growth rate is already very high. However, it cannot be assumed that the selected growth rate also corresponds to the modeled one, which is why the growth rate is also evaluated for each experiment and adapted to the results.

5.2 Test and numerical evaluation of the equations of motion

Some tests will now be carried out using a Gaussian HEP, but to clarify the results, the area will be enlarged compared to the HEP that was used for calibration (Fig. 5.13). This HEP distribution is chosen because it is from a physical sense very clear how the deterministic part of the model should behave for the HEP based gradient. The distribution is therefore suitable to test model performance for different setups. As shown in Fig. 5.13, the HEP maximum is chosen to be in the center of the pattern at $(\text{lon}, \text{lat}) = (25^\circ, 25^\circ)$. At the boundaries, for $\text{lon} < 2.5^\circ$, $\text{lon} > 47.5^\circ$, $\text{lat} < 2.5^\circ$, and $\text{lat} > 47.5^\circ$, the HEP is set to -1 to simulate a reflective water boundary. The resolution of the HEP is 1.25° in longitude and latitude. The set of experiments which are carried out for the Gaussian HEP can be seen in Tab. 5.8.

5.2.1 Experiment G1

In this experiment, only the deterministic part of Eq. 4.18 is evaluated, therefore σ_u is set to 0. The velocity is therefore determined numerically by Eq. 5.1 and 5.2. In a first run, two humans are simulated, which are positioned at t_0 at the corners: $\mathbf{x}_1(t_0) = (10^\circ, 10^\circ)$, and $\mathbf{x}_2(t_0) = (10^\circ, 40^\circ)$ with velocities $\mathbf{u}_1(t_0) = \mathbf{u}_2(t_0) = (0, 0)$ (see Fig 5.14). The model set up is $u_{max} = 3.2$ km/yr, with $\Delta t = 0.01$ years, and $T_n = 180,000$. The migration of the two humans is simulated for a total of 1800 years. Obviously, a human is not able to survive that long, in later simulations the birth and death module will prevent such migration processes by single humans. This setup is used as a first test to check whether the deterministic model works and to evaluate the curvature terms in the equations of motion.

Both, human 1 (H1, black lines) and human 2 (H2, yellow lines), migrate towards the

TABLE 5.7: Experimental setup to calibrate κ in the the birth and death module.

| N_0 | T | u_{max} | σ_u | ρ_{max} | Δt^{bd} | r |
|---------|------------|-----------|------------|---------------------------|-----------------|-----------------------|
| 500 hms | 15,000 yrs | 5 km/yr | 150 km/yr | 4 hms/100 km ² | 4 yrs | 0.03 yr ⁻¹ |

TABLE 5.8: Experiments with different model setups based on different HEP distributions to evaluate and test the equations of motion.

| Exp | Model setup | Purpose |
|-----|---|---|
| EG1 | Only drift | Test of the curvature terms of the deterministic model |
| EG2 | Only drift, different Δt | Evaluation of numerical convergence, error in position and runtime based on time increment Δt |
| EG3 | Only drift, two similar HEP patterns with different resolutions | Evaluation of the impact of the HEP resolution on the movement |

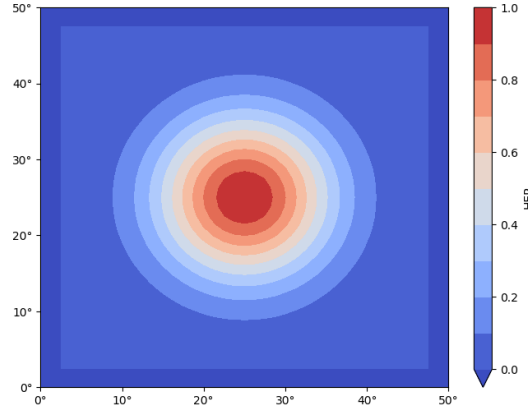


FIGURE 5.13: 2d Gaussian HEP distribution with 1.25° resolution used for CRWM evaluation, encompassed by a rectangle of simulated water with $\text{HEP} = -1$.

maximum of the HEP distribution in the center at longitude and latitude $(25^\circ, 25^\circ)$, shown in the upper figure in Fig. 5.14. As both humans are accelerated by the same gradient force, they experience the same macroscopic drift. This migration is therefore as expected. Due to the curvature of the earth, the human in the south (H1) has a longer path to the center than the one in the north (H2), he therefore needs more time. Shown in the lower figure is the great circle distance to the center of the distribution (d_c), calculated by the Haversine formula by:

$$\Delta\varphi(t_k) = \frac{25^\circ - \hat{x}_\varphi(t_k)}{2}, \quad (5.9)$$

$$\Delta\theta(t_k) = \frac{25^\circ - \hat{x}_\theta(t_k)}{2}, \quad (5.10)$$

$$d_c(t_k) = 2a \cdot \arcsin \left[\sqrt{\sin^2[\Delta\varphi(t_k)] + \cos[25^\circ] \cos[\hat{x}_\theta(t_k)] \sin^2[\Delta\theta(t_k)]} \right]. \quad (5.11)$$

Moreover, the absolute velocity is calculated and shown in the lower figure:

$$|\hat{\mathbf{u}}(t_k)| = \sqrt{u^2 + v^2}. \quad (5.12)$$

Shown by the continuous lines on the lower figure in Fig. 5.14, H2 accelerates earlier and reaches his maximum velocity after around 836 years, while H1 is fastest after 1034 years. This progression is as expected as H2 experiences the gradient force before H1 does due to the lower distance to the center of the HEP. The progression of the absolute velocities of H1 and H2 is then very similar with a time delay of about 150 years. The maximum absolute velocities are in the same range: $|\hat{\mathbf{u}}_1| \approx 4.82$ km/year, and $|\hat{\mathbf{u}}_2| \approx 4.93$ km/year. The maximum velocity achieved is different than the assumed maximal migration speed. This was to be expected because the Gaussian HEP in the experiment was distributed over a larger area than the one used for calibration. H2 attains the center of the distribution, with $d_c < 10$ km, after 1238 years, which is earlier than H1, who arrives there after 1420 years. Both trajectories converge to the center of the distribution without large scale overshooting, while the absolute velocities approximately go to zero. This progression indicates that the friction force works as intended for this model setup.

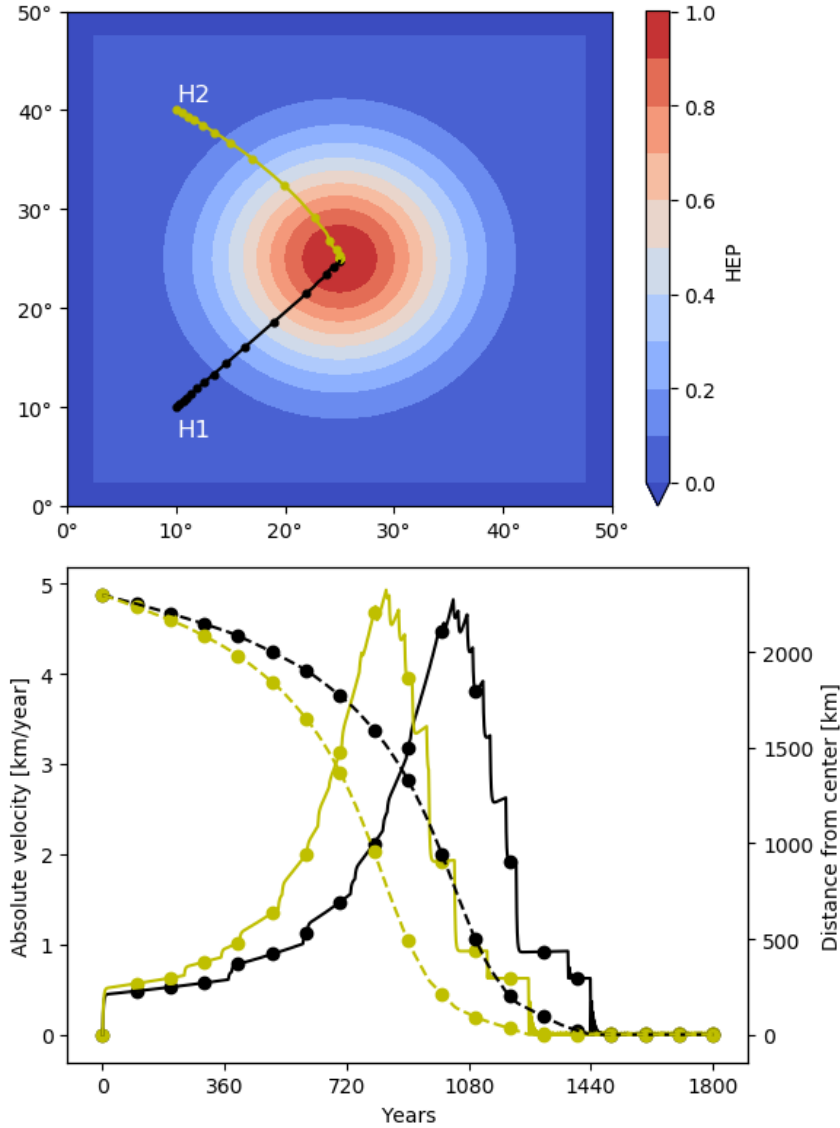


FIGURE 5.14: **Experiment G1:** Test of the macroscopic forces for two humans, H1 (black lines) with initial conditions $\mathbf{x}_1(t_0) = (10^\circ, 10^\circ)$ and $\mathbf{u}_1(t_0) = (0, 0)$, and H2 (yellow lines) with initial conditions $\mathbf{x}_2(t_0) = (10^\circ, 40^\circ)$ and $\mathbf{u}_2(t_0) = (0, 0)$ for 1800 years with $\Delta t = 0.01$, and a Gaussian HEP by switching of the random part of the CRW model. The maximal migration velocity is chosen to be $u_{max} = 3.2$ km/year. Shown on the upper figure is the migration trajectory in space. Depicted on the bottom figure is the absolute velocity of both humans (Eq. 5.5) in continuous lines, and the distance from the center at $(25^\circ, 25^\circ)$ (Eq. 5.11) in dashed lines. On both figures the dots indicate 100-yearly time steps.

5.2.2 Experiment G2

Now, the sensitivity of the deterministic model is tested based on the numerical properties. First of all, numerical convergence and stability are tested by means of the time increment Δt . The same model setup as for EG1 is used with $u_{max} = 3.2$ years, while only human H1 is simulated with $\mathbf{x}(t_0) = (10, 10)$ and $\mathbf{u}(t_0) = (0, 0)$. To test model convergence, the migration is simulated for different time increments Δt . The

human is supposed to migrate to the center of the HEP and stay there, so the distance from the centre (d_c) should converge to zero for rising t . The same is expected for the absolute velocity as the mobility goes to zero in the center of the HEP with zero gradient. Model convergence of the differential equations 5.1 and 5.2 is therefore evaluated by the order η of:

$$\lim_{t \rightarrow \infty} |\hat{\mathbf{u}}(t)| = c \cdot \eta, \quad (5.13)$$

with a constant c .

In Fig. 5.15a the progression of the absolute velocity of H1 is depicted, modelled for different values of Δt for a total of 3000 years. As we have shown in EG1, the human reaches the center of the HEP distribution with $d_c < 10$ after 1420 years, so his absolute velocity should converge to zero afterwards. As can be seen in Fig. 5.15a, the absolute velocity roughly coincide for all models with different time increments Δt on the path to the center of the HEP distribution. This concordance in simulated velocities lead to a similar migration of H1 from the edge of the Gaussian distribution to the center for all Δt , as depicted by the matching distance to the center in Fig. 5.15b. In the center of the HEP, the absolute velocity is supposed to converge to zero. As can be seen in Fig. 5.15a, this is not the case. The absolute velocities oscillate around a constant value depending on the time increment Δt . As the oscillations of all models stay the same until the end of the simulation, I assume that they would

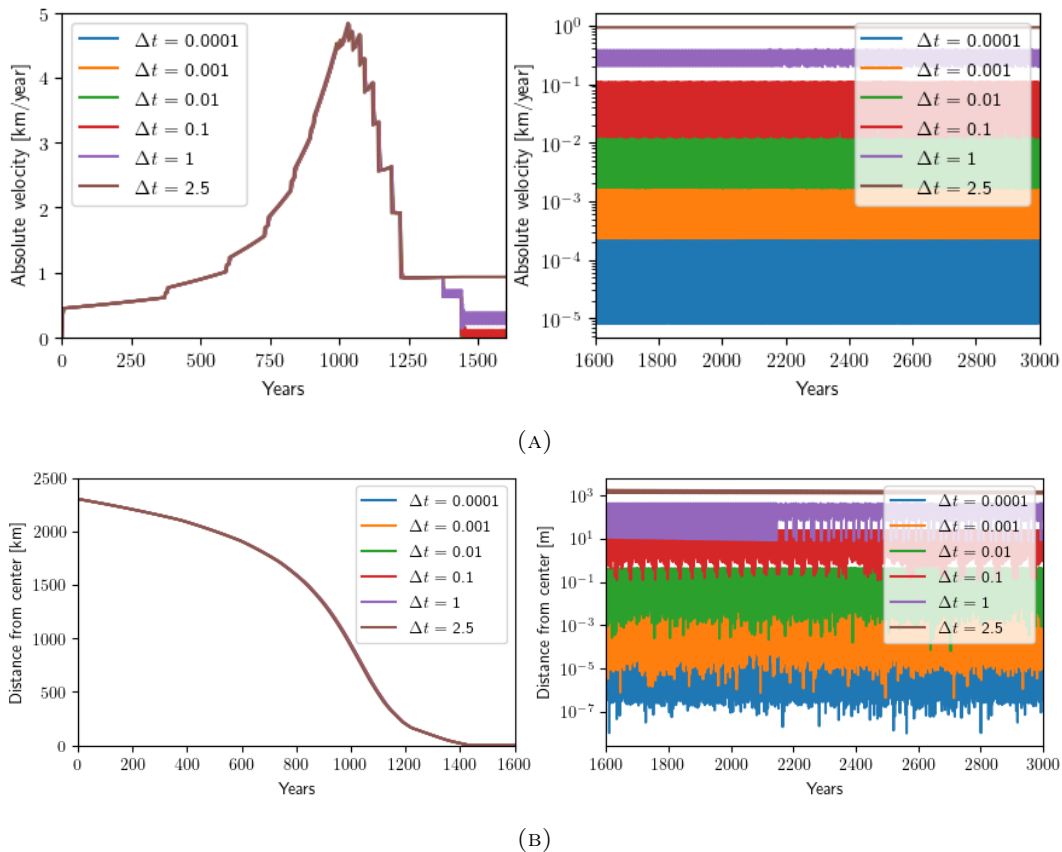


FIGURE 5.15: **Experiment G2:** Test of the numerical stability of the CRWM for different time increments Δt with $u_{max} = 3.2$ km/year for human H1 of EG1; (A): absolute velocity $|\mathbf{u}|$ and (B): distance from center; from 0 – 1500 yr (left) and from 1500 – 3000 yr (right). The right figures illustrate the oscillations around the center of the HEP distribution for different Δt , they are displayed in logarithmic scale.

continue if $t \rightarrow \infty$. The order of the mean value of the oscillations is therefore assumed to be the order of convergence η of the different models. The oscillating velocities lead to an oscillating migration of the human around the center of the HEP distribution (Fig. 5.15b). The mean value of the oscillating distance from the center can be seen as an general error in position (Δx) of the model, because the human is supposed to stay in the center with $d_c = 0$.

Both, the order of convergence and the error in position, as well as the runtime of the models, are listed for different values of Δt in Tab. 5.9. The results of the convergence analysis are as expected, for $\Delta t \rightarrow 0$ the order of convergence $\eta \rightarrow 0$, and the error in position $\Delta x \rightarrow 0$. However, the computing time rises significantly with decreasing Δt . It is therefore important to find a Δt which is sufficiently small without exaggerating the computing time. For this setup, $\Delta t = 0.01$ would be sufficiently small for model convergence, which is in the order of $\eta = 10^{-3}$, while also the computing time of a few seconds is not exaggerating compared to larger time increments Δt . The error in position for $\Delta t = 0.01$ is in the range of 10^{-1} m, which would be neglectable for the purpose of my studies. The computing time for the model with $\Delta t = 0.0001$ for this simple setup takes 30 minutes, this time increment is therefore unusable for large-scale studies about human populations. For $\Delta t \geq 0.1$, $\eta \geq 10^{-2}$ and $\Delta x \geq 10$ m, thus the errors would get significant. This result is as expected, as Δt is then maximal an order smaller than the drift time scale D_t . In summary, a time increment in the range of 10^{-3} or 10^{-2} years is suitable for my modeling purposes.

TABLE 5.9: Order of convergence, error in position and runtime of the CRWM based on the time increment Δt for $u_{max} = 3.2$ km/year.

| Time increment (Δt) | Order of convergence (η) | Error in position (Δx) | Runtime |
|-------------------------------|---------------------------------|----------------------------------|---------|
| 0.0001 | 10^{-4} | 10^{-5} m | 30 min |
| 0.001 | 10^{-4} | 10^{-3} m | 3 min |
| 0.01 | 10^{-3} | 0.14 m | 18 s |
| 0.1 | 10^{-2} | 10.2 m | 2 s |
| 1 | 10^{-1} | 228 m | < 1 s |
| 2.5 | 10^0 | 1447 m | < 1 s |

5.2.3 Experiment G3

In this experiment, the sensitivity of the velocity according to the resolution of the HEP is tested. Therefore, the distribution of the Gaussian HEP is interpolated to a grid with 0.25° resolution. The model is set up equivalently as in experiment EG1, while this time the high resolution 0.25° HEP is used to estimate the velocity. The absolute velocity of H1 from EG3 and the absolute velocity of H1 estimated in EG1 are shown in Fig. 5.16. It can be seen that the velocities approximately coincide for both HEP resolutions. However, the stepwise changes in absolute velocity caused by the HEP resolution are smaller for the high resolution run, which locally leads to a variance of both velocities. These variances result in differences in position. The difference of the distances to the center (d_{diff}) for HEP 1.25° and HEP 0.25° is shown in Fig. 5.16 as well, calculated by:

$$d_{diff}(t_k) = d_c^{1.25^\circ}(t_k) - d_c^{0.25^\circ}(t_k). \quad (5.14)$$

The absolute velocity from the 1.25° HEP run is higher than the absolute velocity of the 0.25° HEP until the maximum of the velocity distribution is reached, leading to a d_{diff} that accumulates to a maximal difference of 50 km at the velocity maximum. Afterwards, the velocity of the 0.25° HEP run is slightly higher, so that d_{diff} approaches zero.

Although the general progression of the absolute velocities coincide for both HEP distributions, the stepwise acceleration based on the grid of the HEP leads to differences in the trajectories of the human. One can therefore suppose that the resolution of the HEP influences the large scale drift. In the experiment this led to a delayed arrival of the human in the centre of the HEP distribution with $d_c < 10$ of about 110 years when using the HEP with 0.25° resolution. In addition to the birth and death module (see Sec. 5.1.4), the drift also changes due to differently resolved HEP. Subsequent results have to be evaluated in terms of the resolution of the HEP distribution.

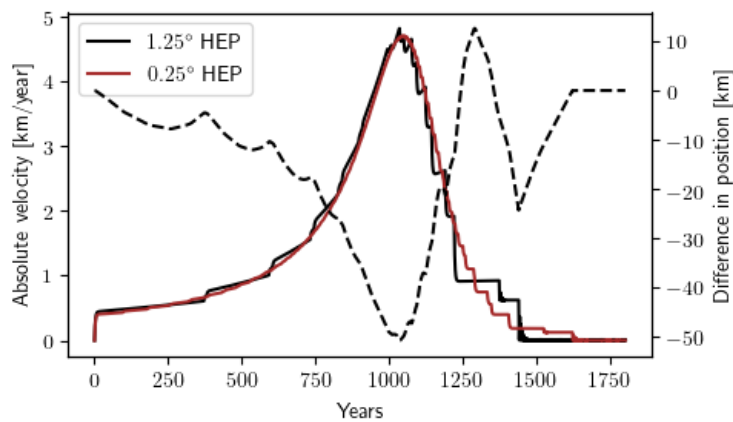


FIGURE 5.16: **Experiment G3:** Test of CRWM with the model setup as in EG1 for human H1 for similar HEP distributions with different resolutions: in brown, absolute velocity for an HEP with 0.25° resolution; in black, absolute velocity for an HEP with 1.25° resolution, in black dashed, difference of the distance from center of model with HEP 0.25° and HEP 1.25° (eq. 5.14).

5.3 Summary

In this chapter it was shown that the simulated movement of humans and the spread of populations works the appropriate way as it was defined in Chapter 4, that the individual modules deliver reasonable results and that the numerical error is in the size range, which is irrelevant for studies of the CRWM. In order to ensure the correct functioning, parameters have been defined that were introduced in Chapter 4. The parameters "drift time scale" and "gradient distance scale" were calibrated to $D_t = 2$ yrs and $G_d = 247$ km so that the drift and the friction, i.e. the deterministic part of the equations of motion, lead to a motion that ends in the maxima of the HEP distribution, without large-scale over-shooting, and runs at a speed that is comparable to the key parameter "maximal migration velocity" (u_{max}). The "stochastic time scale" was calibrated to $\tau = 6$ yrs so that most of the random movement takes place within a radius around the settlement centers, which is determined by the key parameter "individual mobility" (σ_u). It was shown here that when evaluating the results, the deterministic and stochastic velocity components must always be considered in combination, which will also be confirmed in the case study in Chapter 6. The two

parameters that determine the shape of the population attractiveness function and thus control both the clustering of humans and the population pressure in the CRWM were calibrated to $\eta = 1.6$ and $\epsilon = 0.4$. In order to achieve realistic population growth rates through the birth and death module, the free parameter was set to $\kappa = 0.5$. It has been shown that the birth and death rate is strongly dependent on the grid size of the HEP. Therefore, a timescale Δt^{bd} was introduced on which the birth and death module operates. However, the results of the idealized experiment on Δt^{bd} can only to a limited extent be transferred to other cases, which is why it is recommended to fit Δt^{bd} for each new experiment so that the death rate or the life expectancy corresponds to the expected value.

Three more experiments were performed to test the correct functioning and numerical convergence and stability of the CRWM. First, a test run was carried out with two humans in order to prove that the migration process is proceeding on a reasonable scale and that the conversion into spherical coordinates, which is necessary due to the earth's surface, delivers correct results. Next, the order of convergence and error in position were evaluated for different time increments dt , by taking the model run time into account. It has been shown that a $dt = 0.01$ years provides reasonable results for the studies carried out here with a comparatively short run time. Finally, the influence of the grid size on the simulated movement was evaluated. Even if the general course of movement is similar for the different grid sizes, the two runs deviate strongly from one another in between, with a maximum deviation of approx. 50 km. The arrival of humans at the center of the HEP distribution occurs 110 years later in the higher-resolution case. Even if the differences appear to be relevant here, they only become important when two differently resolved HEPs are compared. Otherwise, the migration is an interplay of many factors, so that deviations that appear due to the grid resolution can be ignored. Nevertheless, as has been seen with the birth and death module, the CRWM output is influenced by the grid resolution, which is why results should always be discussed in this regard. In general, it can be assumed that a higher resolution HEP leads to more precise results.

The influence of the key parameters on the result was not further evaluated here, but will be assessed on the basis of a case study in Chapter 6. On the one hand, the parameters must be of a magnitude that corresponds to archaeo-physical values, as defined in Chapter 4, and, on the other hand, lead to stable model results. The parameter limits for which the model becomes unstable must, however, be determined anew for each case study.

Chapter 6

The impact of the Heinrich Event 4 on human populations in Iberia (2): dynamic analysis

6.1 Introduction

Building on the results of the HEP study in Chapter 3, the study on human populations on the Iberian Peninsula is expanded by applying the CRWM. In this way, many questions can be investigated that could not be answered by the static approach, such as:

- How fast and along which routes did the migration process of modern humans take place?
- Which areas on the Iberian Peninsula were settled by Neanderthals under interstadial conditions and between which regions was contact?
- Where was the mobility particularly high and were there regions in which more humans were born than died, i.e. so-called source regions?
- How devastating was the impact of the Heinrich Event 4? How extensive was the collapse of social networks and under what conditions did unstable population sizes and thus local extinction occur?
- Where on the Iberian Peninsula did Neanderthals and modern humans come into contact? What effects could this contact have had?

Special experiments are set up to answer these questions and are dealt with in the different sections of this chapter. The HEP results from Chapter 3 are used as the input for all experiments, i.e. the HEP from Fig. 3.1 for the Neanderthals of the Middle Paleolithic during MIS 3 and the HEP from Fig. 3.2 for the anatomically modern humans (AMHs) of the Aurignacian. Finally, the advantages and disadvantages of the CRWM results are discussed and the limits of the modeling are shown.

6.2 Migration of the Aurignacian to the Iberian Peninsula

The Aurignacian (AUR) is the techno-complex of the first AMHs in Europe, which, starting from eastern Europe, spread over a large part of the European continent. The expansion is often divided into 2 to 3 phases in the literature, whereby the first phase applies to the period before and during Heinrich Event 4 (HE4) (in some studies this phase is divided) and the second phase to the period afterwards (Banks et al., 2013;

Schmidt and Zimmermann, 2019). The occurrence of the HE4 is therefore given an important role in the history of the AUR. It can be assumed that the onset of the cold phase led to a collapse in the population and a retreat into environmental refugia.

It is assumed here that the dispersal or migration took place mainly during warm periods, the interstadials. As shown in Shao et al. (2021), the HEP and thus the spread of hunters-gatherers decreased significantly during the cold phases. I therefore assume that mobility and thus expansion also decreased. Migration also occurred under stadial conditions, but it is assumed that the dispersal was more pronounced under interstadial conditions. The three warm phases that come into question for the AUR dispersal are the Greenland Interstadials (GI) 11 to 9. The immigration of modern humans to the Iberian Peninsula is exemplarily simulated for the HEP under GI9 conditions, based on the HEP in Fig. 3.2.

Since it can be assumed that modern humans immigrated from the east, a starting population of 500 humans is assumed in the experiments, who arrive at the southeastern edge of the HEP area in France (center of the Gaussian distribution: lon = 4°, lat = 44°), with a narrow starting distribution (standard deviation of the Gaussian distribution: 0.5°). The population number is possibly a little too high, but must be assumed here for numerical reasons, as many humans leave the area due to the spatial limitation of the HEP and therefore disappear from the calculation (outer boundary condition: lon_{min} = -10°, lon_{max} = 5°, lat_{min} = 35°, lat_{max} = 48°).

In order to evaluate the effects of the HE4 on the populations, the external conditions are then changed, i.e. the HEP is adjusted to the conditions of the HE4. Since HEs change the climatic conditions relatively abruptly but not instantaneously, the HEP of the GI9 is sporadically changed to the HEP of the HE4 within 100 years. For this purpose, the conditions between GI9 and HE4 are interpolated and the HEP is changed every 10 years, so that after 100 years the conditions of HE4 prevail. This enables the populations to somewhat adapt to the changing conditions, so that the impact of HE4 on the populations is weakened. As the next sections will show, the effect is nonetheless very serious. The impact of the HE4 conditions on the population is then calculated for 3000 years.

6.2.1 Calibration of Δt^{bd}

First, as described in Chapter 5, the birth and death module must be adapted to the HEP distribution by choosing a suitable Δt^{bd} . For this purpose, a first run is carried out with the setup listed in Tab. 6.1 and the death rate of the population is evaluated (all other parameters, i.e. D_t , G_d , ϵ , η and κ have the values calibrated in Chapter 5). Since the population would otherwise become unstable, high values must be assumed for both ρ_{max} and r .

The model is tested for different Δt^{bd} and the death rate and the life expectancy of a person is determined for evaluation. The results for $\Delta t^{bd} = 4, 6, 7$ and 8 yrs are shown in Fig. 6.1. Although the HEP has a resolution of 0.15°, a Δt^{bd} of 12 yrs, as described in Chapter 5, would not lead to meaningful results here. The results suggest that the best modeling results are achieved for $\Delta t^{bd} = 7$ yrs, since there the average lifetime of 68 yrs comes closest to the assumed time for hunters-gatherers of 70 yrs. For $\Delta t^{bd} = 6$ yrs the average lifetime is 59 yrs, which is too low, and for $\Delta t^{bd} = 8$ yrs the lifetime is 76 yrs, which is a little too high. $\Delta t^{bd} = 7$ yrs is used for all of the following experiments.

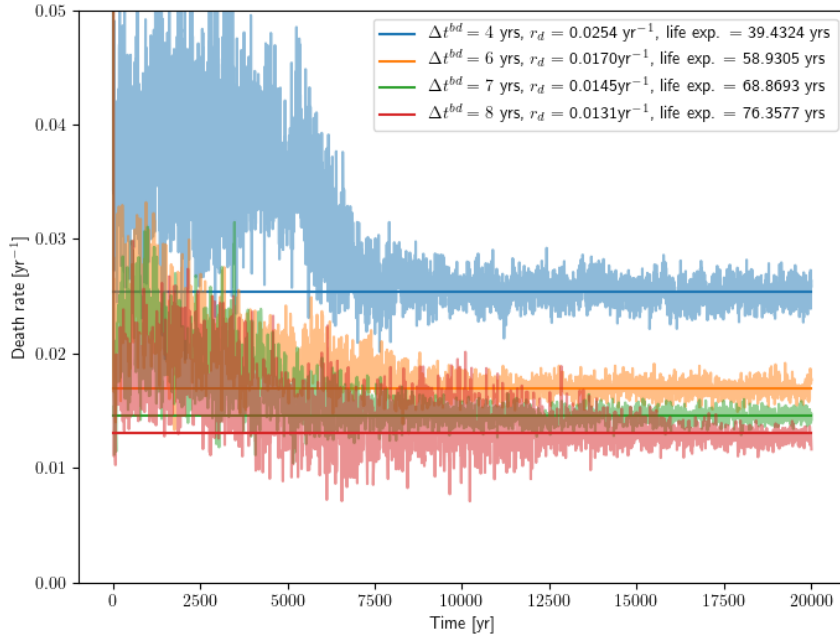


FIGURE 6.1: Calibration of Δt^{bd} by the death rate (number of deaths in relation to the total population per year) for the AUR migration defined by the setup in Tab. 6.1. r_d is the average death rate, disregarding the initial phase.

TABLE 6.1: Experimental setup to calibrate Δt^{bd} for the simulation of the AUR dispersal.

| N_0 | T | u_{max} | σ_u | ρ_{max} | r |
|---------|------------|-----------|------------|---------------------------|-----------------------|
| 500 hms | 20,000 yrs | 5 km/yr | 150 km/yr | 7 hms/100 km ² | 0.06 yr ⁻¹ |

6.2.2 First experiment: the standard configuration

As was shown in Chapter 5 and which is also entirely in the sense of the modeling, the results of the CRWM strongly depend on the selected parameters of the model. These key parameters, which were introduced in Chapter 4, i.e. the maximal migration velocity (u_{max}), the individual mobility (σ_u), the maximal cultural carrying capacity (ρ_{max}) and the population growth rate (r), decisively determine how movement and births and deaths are modeled in the CRWM. So there is not one solution to simulate the migration of the AUR, but a large ensemble of solutions. Nevertheless, a standard configuration must first be used and evaluated in order to understand how the dispersal is simulated. In the next step, this configuration can then be changed in order to be able to make statements about the influence of the parameters on the simulated migration processes. The default configuration is shown in Tab. 6.2.

TABLE 6.2: Parameter of the standard configuration to model the Aurignacian dispersal.

| N_0 | T | u_{max} | σ_u | ρ_{max} | r |
|---------|-------------|-----------|------------|---------------------------|-----------------------|
| 500 hms | 100,000 yrs | 5 km/yr | 150 km/yr | 7 hms/100 km ² | 0.06 yr ⁻¹ |

Since the CRWM is a stochastic model, no conclusions can be drawn from a single simulation that roughly covers the expected time period of the dispersal. There are two ways of minimizing the randomness that is inherent in the migration process within the

CRWM: firstly, one conducts an ensemble of simulations with different random seed numbers, or secondly, one chooses the time period long enough to simulate as many random fluctuations as possible. For practical reasons, I choose the latter method as it allows me to significantly minimize both the simulation effort and the memory used. A time period T of 100k yrs was therefore set for the experiment. This method can be used to determine probabilities for the settlement of areas. However, no statements can be made about the times at which areas were populated.

Migration over time

The results of the simulation are shown in Fig. 6.2. The number of humans initially drops from the starting amount of 500 humans to a minimum of 161 humans after 1100 years. This is because, on the one hand, some humans walk out of the area due to the close proximity to the border of the examined area and, on the other hand, due to the random distribution at the beginning. Many humans are located in HEP-poor areas or are away from other humans and thus the probability for them to die is very high. In addition, 16 humans were distributed over the water through the random distribution and thus excluded from the calculation by the algorithm. After the initial decline, there is a sharp increase in the population, with the number increasing to around 4500 humans within 16k yrs. Thereafter, there are irregular fluctuations in the population size up to the end of the time series. The population maximum is reached after 94k yrs with a population size of 6458 individuals.

In order to better understand the simulated migration process, the population densities averaged over the depicted time periods are also shown in Fig. 6.2. The cyan color depicts the initial phase of the dispersal from 0 to 1000 yrs: a density maximum forms on the Mediterranean coast of France, near the center of the initial distribution (lon = 4°, lat = 44°). Smaller groups of humans move around the center with one group moving towards the large HEP area in south west France. It is not shown here, but the group settles in Franco-Cantabria and reproduces strongly, so that the strong population growth occurs. While the population in Franco-Cantabria continues to increase, more groups immigrate from the Mediterranean coast until the population on the Mediterranean coast disappears completely. However, the Franco-Cantabria population continues to expand with increasing numbers, so that the Mediterranean coast is also repopulated. This can be seen from the averaged population density of the blue time period from 16k yrs to 20k yrs, that the whole of southwest France and the Mediterranean coast are populated.

The population continues to grow in the further course, but there are constant fluctuations in the population size. The averaged population densities of four further time periods are shown, which depict the maxima and minima of the population size. The red period, from 22k to 24k yrs, shows a maximum within the fluctuation. There is a rapid increase in population due to the settlement of the Iberian Mediterranean east coast and parts of central Iberia, with populations that have now expanded into the south of Spain. However, as can be seen from the population minimum during the yellow time period of 40k - 41k yrs, the southern settlements are unstable and dissipated. In addition, there is a break in contact between the populations of the north and east coast of Spain. There are also declines in the population on the Mediterranean coast of France. After the population minimum, the number of humans increases again and areas in central Iberia are repopulated. Even at the time of the green period from 66.5k - 71k yrs, these are still populated despite the population decline. At the population maximum in the magenta phase, from 87k - 100k yrs, the areas in northwestern Spain are settled for the first time.

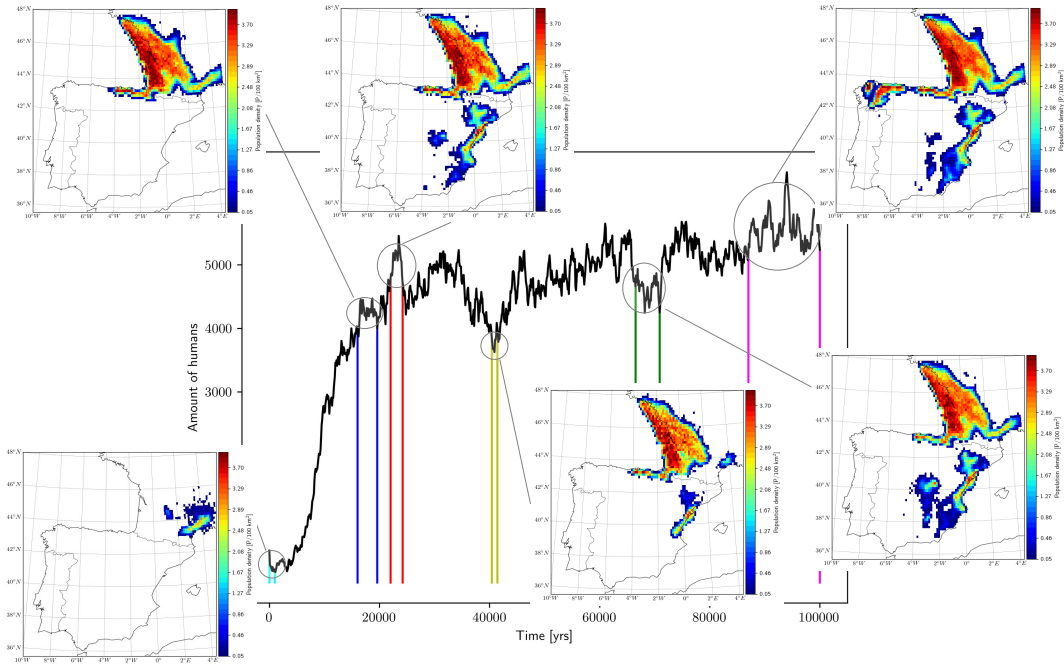


FIGURE 6.2: Dispersal of the humans of the Aurignacian based on the standard configuration (Tab. 6.2). It shows the total number of humans and the population density averaged over the color-coded time periods. The marked periods are in cyan 0 - 1k yrs, in blue 16k - 20k yrs, in red 22k-24k yrs, in yellow 40k - 41k yrs, in green 66.5k - 71k yrs, and in magenta 87k - 100k yrs.

Settlement statistics

In the next analysis, the percentage of the time an area was populated is evaluated (Fig. 6.3). For this purpose, the time steps at which the population density $\rho_{ij} > 0$ are determined for each grid cell C_{ij} and divided by the total number of time steps. The initial growth phase is thereby not taken into account, the settlement is evaluated from the point in time at which the statistical fluctuations begin, i.e. from 16k yrs on. Percentages below 5% are not shown in the evaluation.

The Franco-Cantabria region, as well as the Mediterranean coast of France and large parts of the Mediterranean coast of Spain south of the Pyrenees were populated almost 100% of the time. In addition, the region in the Ebro Valley is densely populated for over 90% of the time. The results indicate that humans migrated to Iberia west of the Pyrenees and not along the Mediterranean coast. The Mediterranean coast of Spain was then settled through immigration along the Ebro Valley. However, there is no continuous settlement connection between north and east Iberia, so it can be assumed that there was no permanent contact between the populations. Rather, the results indicate that groups from northern Spain have reached the Ebro Valley and continued to migrate towards the Mediterranean coast, but no return migration took place.

Starting from the settlement center at the Mediterranean coast of Spain, areas in the center of Iberia were then populated. However, these settlements were never stable and broke up after a few centuries, which is why the areas there were only populated to 5 - 30% of the time. Even if it is difficult to identify from the HEP distribution, the hurdle for immigration to northwestern Spain seems to be very high. These areas were only populated at the end of the time series, which is why the percentage is so low (5 - 20%). It is not possible to fully estimate how stable this population is. However,

since settlement came so late, it can be assumed that the probability that humans of the AUR colonized these areas is to be assessed as low. This result would also agree with the distribution of archaeological sites. In addition, there are some areas that have not been populated during the entire 100k yrs despite high HEP, such as some areas in the center of the Iberia and on the coast of Portugal. This is because these areas are cut off by low HEP areas.

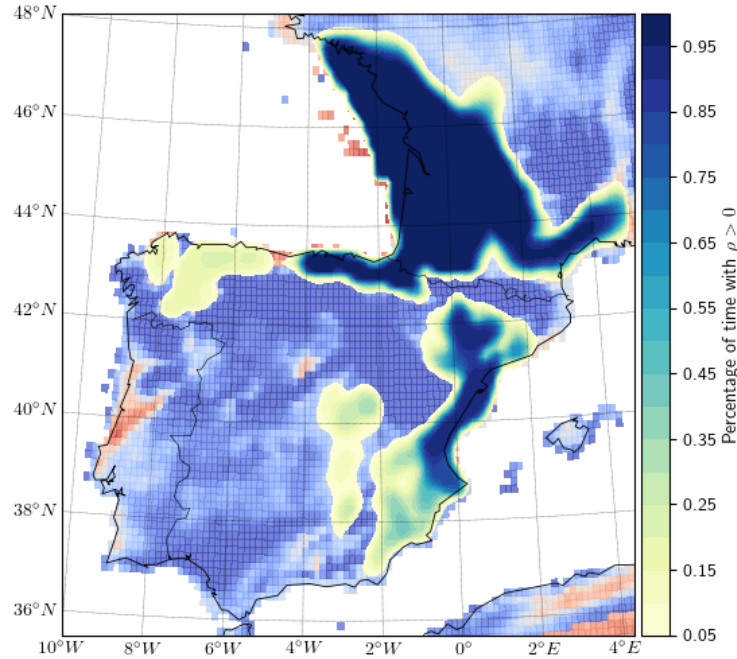


FIGURE 6.3: Percentage of time steps (from 16k - 100k) at which the grid points were populated ($\rho_{ij} > 0$) based on the experiment from Tab. 6.2. Grid cells that were populated less than 5% of the time are not shown.

Source and sink regions

Next, the births and deaths are evaluated in order to determine the source and sink regions, i.e., regions in which noticeably more humans are born than die, and vice versa. For this purpose, the sum of all births minus the sum of all deaths that occurred within a grid cell is calculated for each time step. Since the calculated time period was very long, not every time step could be saved for storage reasons, but only every hundred years¹. Since the position of humans changed within 100 years, the results presented here do not fully reflect the simulated results. Especially at the border of the study area, this can lead to higher death rates as humans who leave the area are also counted as dead. Nevertheless, I assume that the statistical evaluation delivers meaningful results due to the low movement speed and the direction-independent random movement. In Fig. 6.4, the number of births minus deaths averaged over the 100k yrs simulation time is shown, while only time steps with population densities greater than zero are used. Based on the distribution, source regions with a positive growth rate (red circles) and sink regions with a negative growth rate (blue circles)

¹Even here, a memory of 800 MB is required for a simulation of 100k years. With the large number of simulations that were carried out for the doctoral thesis, it was necessary to minimize the stored time steps as far as possible. As has been shown, the modeled migration takes place over thousands of years, so hardly any information is lost in the statistical analysis.

are determined.

The most pronounced source regions are in southwest France and Cantabria, so significantly more humans are born than die in these areas. This in turn drives migration through local population pressure. One can therefore assume that the population surplus that occurs here will migrate to the neighboring regions. In the case of southwest France, the source regions occur inland, while on the Atlantic coast there are sink regions, i.e. more humans die than are born. The sink regions are particularly pronounced on the Bay of Biscay, which may be related to somewhat lower HEP in the region compared to the surrounding area. The results show that the coastal region is constantly being repopulated, but the conditions there are significantly more unstable than inland. From the source region in Cantabria, first the Ebro Valley, and finally the Iberian Mediterranean coast, and the areas in northwestern Spain are settled. In the Ebro Valley there are no distinct source or sink areas, which confirms the hypothesis that this area was more likely to be walked through than settled in the long term. On the Iberian Mediterranean coast there is a weak source region around Valencia. The center and south of Iberia were probably settled from there, with a weak sink region directly south of it. On the Mediterranean coast of France there is another source region, which indicates a settlement connection from Franco-Cantabria to the Mediterranean coast. However, the local population pressure there was obviously not great enough to trigger migration along the Mediterranean coast east of the Pyrenees. At the eastern edge of the study area, on the Mediterranean coast of France, a sink region forms, which is probably mainly related to the fact that humans leave the study area and are therefore counted as dead.

Population flow

Finally, the modeled movement dynamics of the population are evaluated. For this purpose, the population flow is calculated at each point in time for each grid cell, i.e. the velocity of each person in the grid cell is added up and divided by the area of the grid cell (scaled to $\text{km} / (\text{yr} \cdot 100 \text{ km}^2)$). Fig. 6.5 shows the time-averaged population flow over the 100k years. In this way, areas can be determined in which the population has a high level of movement dynamics and migration flows can be identified. Due to the randomness that is inherent in the modeled movement in the CRWM, however, the migration flows are not straight and are difficult to identify in some places.

Four regions can be identified that have increased movement dynamics, the Bay of Biscay, Cantabrian, the eastern Mediterranean coast of Iberia and the coast of the Gulf of Lion. It is noticeable that all these regions are close to the coast, which suggests that the main population movements, and thus also the migration, took place along the coasts. The flow of movement in the Bay of Biscay is mostly directed to the north, this is caused by the high population in southwest France that expands into northern areas. In the interior of the country, however, there is backward migration towards the south, which can be explained by the fact that the humans who spread to the north encounter poor HEP areas in Brittany, which divert them inland and then drive them south. In Cantabria, no directed migration flow can be seen, but the high dynamic of movement indicates that the surrounding areas were migrated from here. The high population flow in the Gulf of Lion represents the constant exchange between the populations in southwest France and on the Mediterranean coast. On the eastern Iberian Mediterranean coast, the population flow runs largely parallel to the coast, both north and south.

In the interior of the country, the population flow is significantly lower. Here, however, one has to distinguish between regions that were permanently and very densely

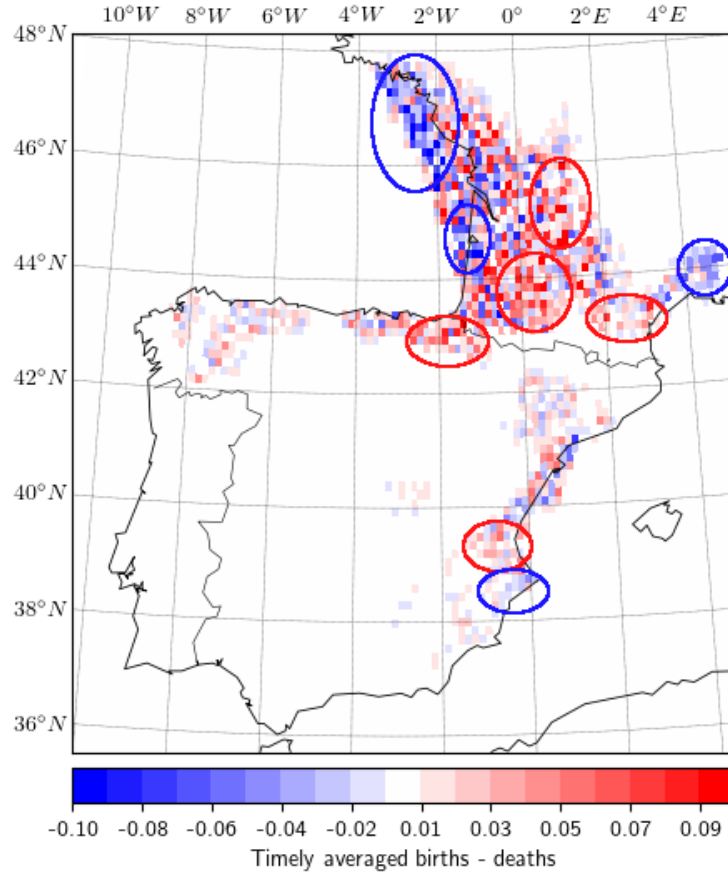


FIGURE 6.4: Timely averaged births minus deaths in each grid cell (C_{ij}), while only those time steps are considered at which $\rho_{ij} > 0$. The source and sink regions are indicated by red and blue circles, respectively.

populated, such as south-west France, and regions that were only temporarily and less densely populated, such as the Ebro Valley (Fig. 6.2 and 6.3). In the permanently populated regions with a low population flow, the population has reached a stable population size, so that there are neither large immigration nor emigration movements. In the less dense and only temporary populated regions, several reasons can be responsible for the low population flow: (1) the low population density, (2) the short period of settlement, or (3) the slow speed of the humans migrating through. In the Ebro Valley, the low population density is probably responsible, as the low HEP area was probably only crossed / settled by small groups of humans. In north-western Spain, the low population flow is more likely due to the short period of settlement.

6.2.3 Parameter testing

In the following, one of the parameters u_{max} , σ_u , r and ρ_{max} is changed in comparison to the standard configuration in Tab. 6.2 in order to evaluate its effects on the modeling results. The simulation is carried out analogously to the first experiment for 100k years and with the same random initial distribution of 500 humans. The statistics of the spread (Fig. 6.6) and growth of the population (Fig. 6.7) are analyzed.

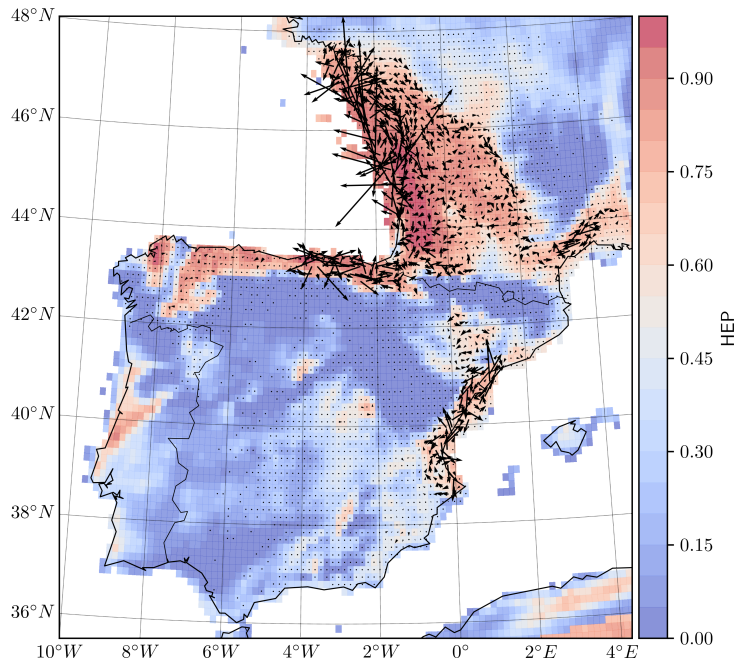


FIGURE 6.5: Population flow calculated by the sum of the velocities of all humans within a grid cell in $\text{km}/(\text{yr} \cdot 100 \text{ km}^2)$, averaged over the 100k year time period (black arrows); and the HEP of AUR All.

Growth rate r

Fig. 6.6a, 6.6b and 6.6c show the influence of the *growth rate* (r) on the statistical distribution of the population. In Fig. 6.6a and 6.6b, a lower growth rate of $r = 0.04 \text{ yr}^{-1}$ and $r = 0.05 \text{ yr}^{-1}$ is assumed than in the standard configuration, respectively. This decreases the likelihood that offspring will be produced and increases the likelihood that humans will die, so that the population does not grow as much, which in turn slows down the migration process. At a lower growth rate (tested for $r = 0.03 \text{ yr}^{-1}$, not shown), no stable population emerges and the population dies out after a while. Fig. 6.6a shows therefore the spread of the population for the minimum growth rate that can be assumed. However, a stable population only develops in the region in southwest France with HEP close to 1, which was settled more than 95% of the time. The rest of Franco Cantabria is also sporadically settled, but not for the entire duration of the 84k yrs. Humans permanently emigrated from the high HEP areas in southwest France, but due to the increased probability of death, the spread quickly came to an end. The areas on the Mediterranean coast of Iberia and northwestern Spain were not populated as a result. The strong growth phase occurs with a delay compared to the standard configuration, after approx. 20k years, and the total population is smaller, which is due to the fact that fewer areas have been populated (Fig. 6.7a).

The areas in southwest France and Cantabria are populated for $r = 0.05 \text{ yr}^{-1}$ for more than 95% of the time (Fig. 6.6b), which is also the case for the standard configuration (Fig. 6.3). The spread at the beginning and the population growth is analogous to that of the standard configuration, which can also be seen in the growth curves, which roughly coincide in the first 20,000 yrs (Fig. 6.7a). Thereafter, the population fluctuates at generally lower values compared to the standard configuration. There are short-term settlements on the Mediterranean coast of Iberia (less than 25% of the time), while the northwest coast of Spain remains unpopulated.

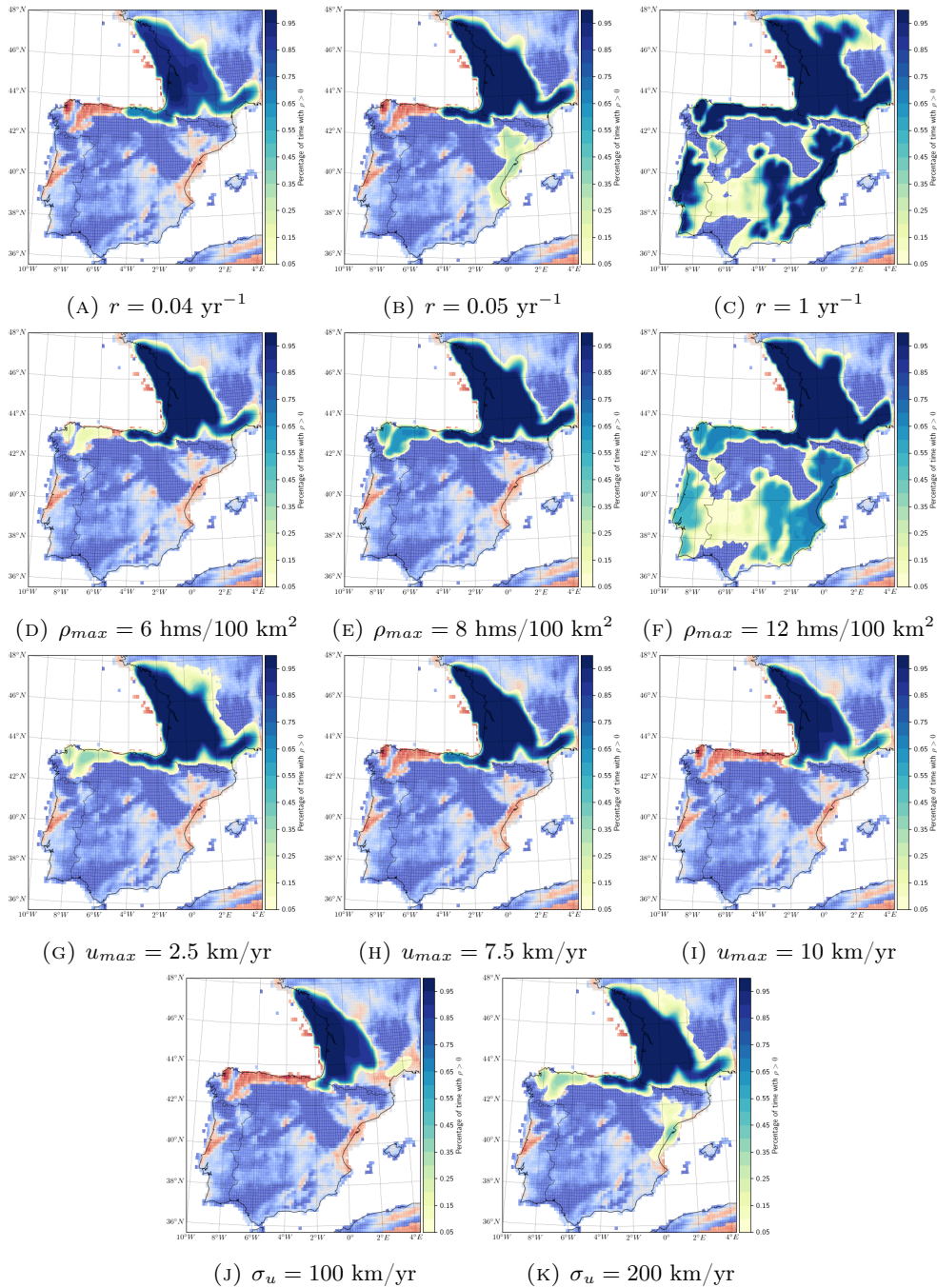


FIGURE 6.6: Percentage of time from 16k - 100k yrs in which the regions were populated by humans of the Aurignacian ($\rho > 0$), based on slightly modified experiments of the CRWM to the standard configuration of the 1st experiment (Tab. 6.2) for testing the parameter influence, with the modified parameter is shown in the caption.

Next, a simulation with a very high $r = 1 \text{ yr}^{-1}$ was carried out to test the sensitivity of the model. The initial fluctuations in the population size due to the Gaussian distribution of the initial population hardly occur here; instead, there is a population boost right from the start (Fig. 6.7a). The growth continues for about 3600 years until all regions with a sufficiently high HEP are populated, including the coast of Portugal, northwestern Spain, central Spain and the Mediterranean coast (Fig. 6.6c). The population size remains at approx. 8600 humans, apart from minor fluctuations

which occur due to random movements after the steady state has been reached, but which are considerably smaller than in the standard configuration. This example illustrates how much the migration is driven by population growth.

It is noticeable that all of the modeled growth rates ($r_{mod} = 0.23 \text{ yr}^{-1}$ for $r = 0.04 \text{ yr}^{-1}$, $r_{mod} = 0.25 \text{ yr}^{-1}$ for $r = 0.05 \text{ yr}^{-1}$, $r_{mod} = 0.29 \text{ yr}^{-1}$ for $r = 0.06 \text{ yr}^{-1}$, $r_{mod} = 2.24 \text{ yr}^{-1}$ for $r = 1 \text{ yr}^{-1}$) clearly exceed the selected growth rates r at the time of the population boom that occurs when settling in southwestern France. The discovery of unpopulated regions with very high HEP results in a population boost in the model that significantly exceeds the assumed growth rates. However, a short-term boost may not be so unrealistic, as many resources were available and thus many offspring could grow up in a secure environment. Even if the growth rates appear to be very high, short-term phases with a high growth boost are consistent with the results from the Cologne Protocol (Schmidt et al., 2020; Zimmermann et al., 2020). Of course, the CRWM operates on a resolution that does not reflect all environmental conditions and only incorporates the interactions between hunter-gatherer to a limited extent. These sub-scale processes could significantly reduce the rate of growth at the local level. In addition, the model completely ignores the fact that some regions were likely populated by Neanderthals at the time of the arrival of the modern humans, whose presence could have both slowed down migration and limited population growth.

Maximal cultural carrying capacity ρ_{max}

The next step is to test to what extent changes in the *maximal cultural carrying capacity* (ρ_{max}) influence the simulated migration of the humans of the AUR. This parameter determines the maximum number of humans allowed to settle in an area and thus determines both the strength of the population pressure and the size of the population growth at the local level. In the standard configuration a $\rho_{max} = 7 \text{ hms}/100 \text{ km}^2$ was used, in the experiments here, a simulation with lower $\rho_{max} = 6 \text{ hms}/100 \text{ km}^2$ (Fig. 6.6d), higher $\rho_{max} = 8 \text{ hms}/100 \text{ km}^2$ (Fig. 6.6e) and an extreme example with very high $\rho_{max} = 12 \text{ hms}/100 \text{ km}^2$ (Fig. 6.6f) is carried out.

The populated areas for $\rho_{max} = 6 \text{ hms}/100 \text{ km}^2$ and $\rho_{max} = 8 \text{ hms}/100 \text{ km}^2$ are roughly the same, Franco-Cantabria and the Mediterranean coast of France are populated over 95% of the time, and northwestern Spain in 10% of the time (Fig. 6.6d) or 50% of the time (Fig. 6.6e). It is noticeable that despite the increased $\rho_{max} = 8 \text{ hms}/100 \text{ km}^2$ compared to the standard configuration, the Mediterranean coast of Iberia was not populated in the 100k year simulation period. Actually, by shifting the population attractiveness function in the direction of higher population densities, regions with poorer HEP conditions should increase in attractiveness to be settled. The barrier that prevented humans from crossing the Ebro Valley should therefore be lower for $\rho_{max} = 8 \text{ hms}/100 \text{ km}^2$ than in the standard configuration. This suggests that the simulated settlement of the Mediterranean coast of Iberia in the standard configuration occurred by chance. In order to be able to estimate the probability, an ensemble analysis with different random seed numbers, the Monte Carlo experiment, is carried out in the next step.

The shift in attractiveness can be observed well in the extreme example $\rho_{max} = 12 \text{ hms}/100 \text{ km}^2$ (Fig. 6.6f), in that all regions with sufficiently good HEP conditions are populated for more than 5% of the time. This population distribution corresponds to the population distribution modeled by the extreme growth rate $r = 1 \text{ yr}^{-1}$ (compare with Figure 6.6c), although the time of settlement occurs later in most regions. Two phases with intensive population growth can be seen (Fig. 6.7b), which is probably due to the fact that it takes some time for the model to fill all regions in southwest

France and Cantabria. In the second growth phase, north-west Spain and the Iberian Mediterranean coast are populated and immediately afterwards the coast of Portugal and parts of central Iberia. Most of the areas are populated about 50% of the time (Fig. 6.6f), which corresponds to the timing of the second growth phase. If one were to increase ρ_{max} further, all regions would gradually be colonized and the population would grow to an exorbitant size. However, $\rho_{max} = 12$ hms/100 km² is already an extreme example, since the modeled population size of over 14,000 humans at the end of the simulation time (Fig. 6.7b) can be assumed to be clearly too high.

Overall, we see that ρ_{max} has a major impact on the total number of humans in the CRWM (Fig. 6.7b). The population size for $\rho_{max} = 8$ hms/100 km² towards the end of the simulation roughly agrees with the population size of the standard configuration, but this is due to the fact that more areas were populated in the simulation of the standard configuration. All of the population sizes modeled here are, however, somewhat higher than the sizes assumed in archeology, e.g. the Cologne Protocol (Schmidt et al., 2020). However, further reducing ρ_{max} is only possible to a limited extent, because due to the grid size of the climate simulations (here 0.125°, which corresponds to about 12 - 15 km) and thus of the HEP, a smaller ρ_{max} would lead to a discretization of the population attractiveness function and thus to instability of the equations of motion. More precisely, the grid cells used here have an area of 175 - 225 km². If, for example, one sets $\rho_{max} = 1$ hms/100 km², the population attractiveness function drops to 0 even for optimal conditions (HEP = 1) if there are more than 2 humans within the grid cell. So there can be no population growth in the model and extinction occurs. Tests have revealed that with this grid size a ρ_{max} of at least 4 hms/100 km² must be used (not shown). As with the increased growth rate, it can be assumed that sub-scale processes influence the number of humans at a very local level and thus lead to different overall population sizes. Nevertheless, for the somewhat larger-scale simulations here, the modelled population sizes (for $\rho_{max} = 6 - 8$ hms/100 km²) are within the scope of what can be assumed (cf. Bocquet-Appel et al., 2005).

Maximal migration velocity u_{max} and individual mobility σ_u

Finally, the influence of the velocity components on the simulated migration and population dynamics is evaluated. In the equations of motion, the velocity is subdivided into a deterministic part, which is determined by the gradient of the HEP, and a stochastic part. The parameter that determines the size of the first component is the *maximal migration velocity* (u_{max}), the latter component is determined by the parameter *individual mobility* (σ_u). Since both components do not act independently of each other, both parameters must always be considered in combination, whereby the ratio of deterministic to stochastic velocity is decisive. In the following, one velocity parameter of the standard configuration is changed in each experiment and the effects on the distribution and population growth are evaluated.

If σ_u remains the same, more areas are populated when u_{max} is reduced (Fig. 6.6g), and fewer areas are populated when u_{max} is increased (Figs. 6.6h and 6.6i). This is counter-intuitive if you look at the definition of u_{max} , which should actually accelerate the migration when it is increased and thus also increase the populated area. However, one has to consider that targeted migration only takes place very locally in the CRWM, so humans are only driven to a local maximum of the available HEP. The results clarify how the expansion takes place in the CRWM, humans migrate to a local maximum, scatter in all directions due to local population pressure, then new regions are discovered through random motion, so that local migratory movements occur again. Since the random motion is proportionally more pronounced at a low

u_{max} , more areas are discovered and populated as a result. At a high u_{max} , however, the drift in the direction of the local maxima dominates, the random motion is suppressed so that fewer areas are discovered.

In the case study, lower u_{max} means that southwest France is discovered more quickly and therefore the population boom begins at an earlier point in time (Fig. 6.7c). The mean population size after the population boom is for both smaller and larger u_{max} smaller than that of the standard configuration. For small u_{max} , humans spread more widely due to the increased random motion, so that fewer births can take place and the death rate rises. For larger u_{max} , the populated areas are very densely populated, but the suppressed random motion leads to an overpopulation that does not spread to new areas but dies. Due to these two effects, the population dies out if u_{max} is chosen to be even smaller (tested for $u_{max} = 1$ km/yr, not shown) or larger (tested for $u_{max} = 15$ km/yr, not shown).

The same results arise from the variation of σ_u . For smaller σ_u , the deterministic part becomes more important, so that fewer areas are populated (Fig. 6.6j) and the population boom occurs at a later point in time (Fig. 6.7d). For larger σ_u it is the opposite, more areas are settled (Fig. 6.6k) and the population boom occurs earlier (Fig. 6.7d). For $\sigma_u = 50$ km/yr and $\sigma_u = 250$ km/yr the population dies out (not shown).

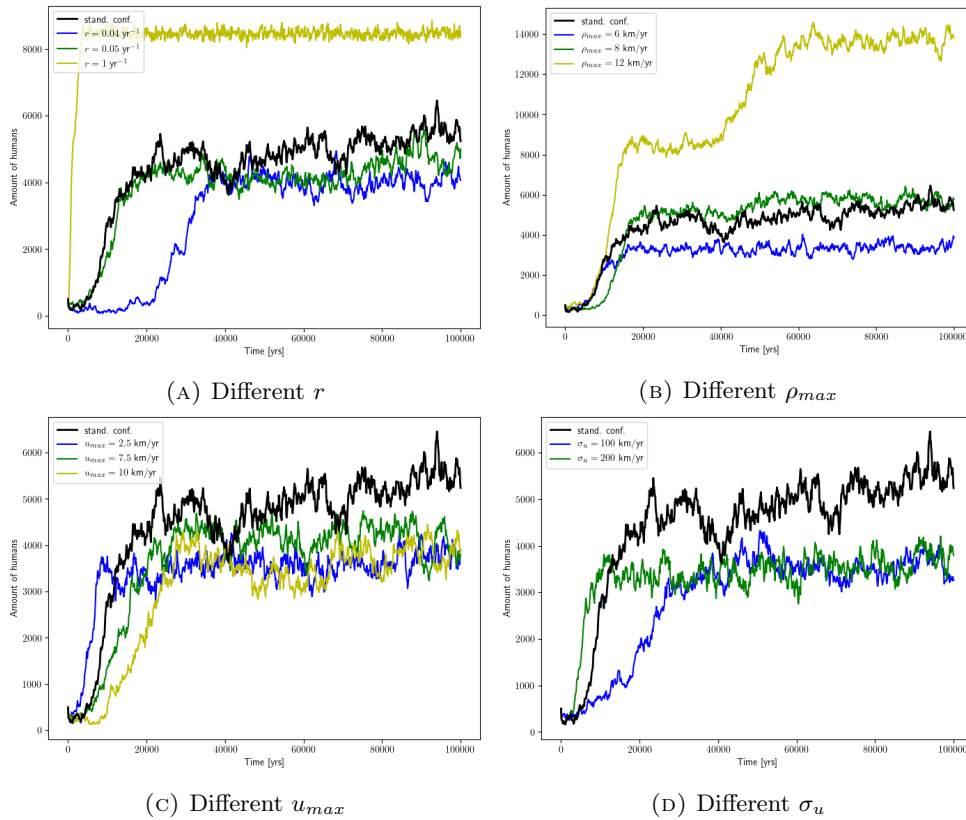


FIGURE 6.7: Number of humans in the 100k yrs CRWM simulation of the dispersal of the humans of the AUR, for modified experiments to the standard configuration (Tab. 6.2), with the modified parameters being listed in the legends.

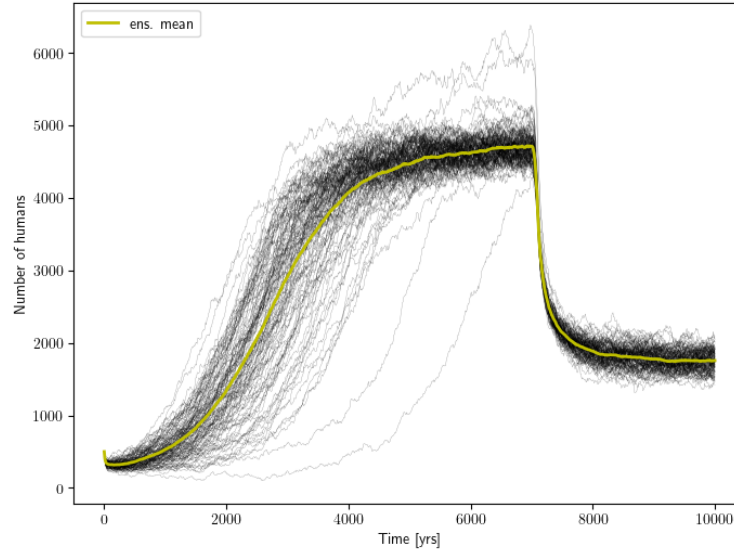


FIGURE 6.8: Number of humans of the 120 CRWM runs of the Monte Carlo experiment (with different random numbers) based on the setup in Tab. 6.3 (black lines), and the ensemble mean of the 120 runs (yellow line). After 7000 years the HEP changes to the conditions of HE4.

6.2.4 Monte Carlo experiment

While we have already shown how changes in the parameters affect the result when the experiments remain the same, we now test how the randomness inherent in the CRWM influences the result. A so-called Monte Carlo experiment is carried out for this, i.e. the same experiment with identical input parameters is repeated as often as possible for different random numbers. The more repetitions, the more meaningful the averaged result of all runs becomes due to the law of large numbers. Here I use a total of 120 runs, which means that a large ensemble is covered and the computational effort remains within reasonable limits². The calculated time that the AMH of the AUR needed to migrate to Iberia is too long in the simulation of the standard configuration, they need about 20k years to populate Iberia, although one can assume a maximum of a few 1000 years. Therefore the growth rate in the Monte Carlo experiment is increased to $r = 0.2 \text{ yr}^{-1}$ and the simulation time is reduced to $T = 7000 \text{ yrs}$. The other parameters remain identical to the standard configuration (Tab. 6.3). As a result of the different random numbers, not only the dynamic component but also the starting distribution of the population changes. After the 7000 years, HE4 begins. The HEP will therefore be changed from the GI9 conditions to the conditions of the HE4 within 100 years. The simulation is carried out for another 3000 years under HE4 conditions.

TABLE 6.3: Parameters of the Monte Carlo experiment to model the Aurignacian dispersal.

| N_0 | T | u_{max} | σ_u | ρ_{max} | r |
|---------|----------|-----------|------------|---------------------------|----------------------|
| 500 hms | 7000 yrs | 5 km/yr | 150 km/yr | 7 hms/100 km ² | 0.2 yr ⁻¹ |

²Each run takes about half an hour

Migration to Iberia

Fig. 6.8 shows the changing population size with the time of the individual runs and the ensemble mean. After the initial population decline, both in the ensemble mean and in the individual runs one can see the typical growth curve of the logistic function: the population size initially increases exponentially, then there is a strong growth phase with a linear course, which then subsides until the total population levels off at a certain size. The growth phase has a very similar course with a similar growth rate in all simulations, only the times at which the growth occurs differ considerably. In the ensemble mean, the linear growth happens after about 2000 years, but in many runs it occurs up to 1000 years earlier or later. The total population averages 4700 humans with a standard deviation of 260 humans at the end of the 7000 years.

Fig. 6.9 shows the migration of the AUR for the Monte Carlo experiment at 1000 year intervals, starting from the Mediterranean coast of France. Shown are the averaged population density, whereby only those runs are taken into account in which the population density is unequal zero, and the percentage of runs that have simulated the respective spread of AMH. The latter can therefore be viewed as a modeled probability of propagation.

After 10 years, all runs (> 95%) model a stable population on the coast of France with population densities in the range of 3 hms / 100 km². While only in a few runs (< 25%) the population spreads north to central France, in most cases (> 50%) there are groups on the way towards southwest France west of the settlement center. After 1000 years, the AMH have reached the large HEP area in southwestern France in more than 75% of the runs, but have barely spread. In none of the runs did the humans reach what was then the Atlantic coast. The northern spread to central France came to a standstill in all model runs and was therefore only related to the random distribution at the beginning. After 2000 years the AMH have built a stable population in southwestern France in more than 75% of the runs with mean population densities of more than 3 hms / 100 km². In some cases (25 - 50%) a large contiguous settlement area forms that extends north along the coast and west to the starting position on the Mediterranean coast. However, in some of the model runs (< 5%) the humans have not yet arrived in southwest France, but are still on the Mediterranean coast. The fact that the southwest of France is settled at different times in the model runs can also be seen in the beginning times of the strong population growth phases (Fig. 6.8), which occur as soon as a stable population has formed there.

After 3000 years, the AMH have settled in all runs in southwest France (> 95%) and almost all runs at the Atlantic coast (> 75%). While the AMH have set foot on the Iberian Peninsula in 25 - 50% of the model runs, Cantabria is fully populated in 1 - 5% of the model runs. The fact that non-zero population densities occur on the Iberian Mediterranean coast shows that there are model runs in which the areas were populated, but this occurs in less than 1% of the runs. After 4000 years, the settlement area in almost all model runs (> 95%) extends over a wide area in southwest France and along the Mediterranean coast of France. In 25 - 50% of the model runs, the population expanded westward along the north coast of Iberia. At this point in time, 1 - 5% of the runs simulate a settlement of AMH in the Ebro Valley. After 5000 years, AMH have arrived in Iberia even for the model runs that simulated slower expansion (> 95%). In addition, in 1 - 5% of the model runs, AMH spread to the Mediterranean coast of Iberia. After 6000 years, the population in the runs in which the Mediterranean east coast of Iberia was reached has spread further south. Also, AMH migrated to northwestern Spain in up to 25% of the runs. The large settlement area in Franco-Cantabria is now fully populated for more than 95% of the runs. After

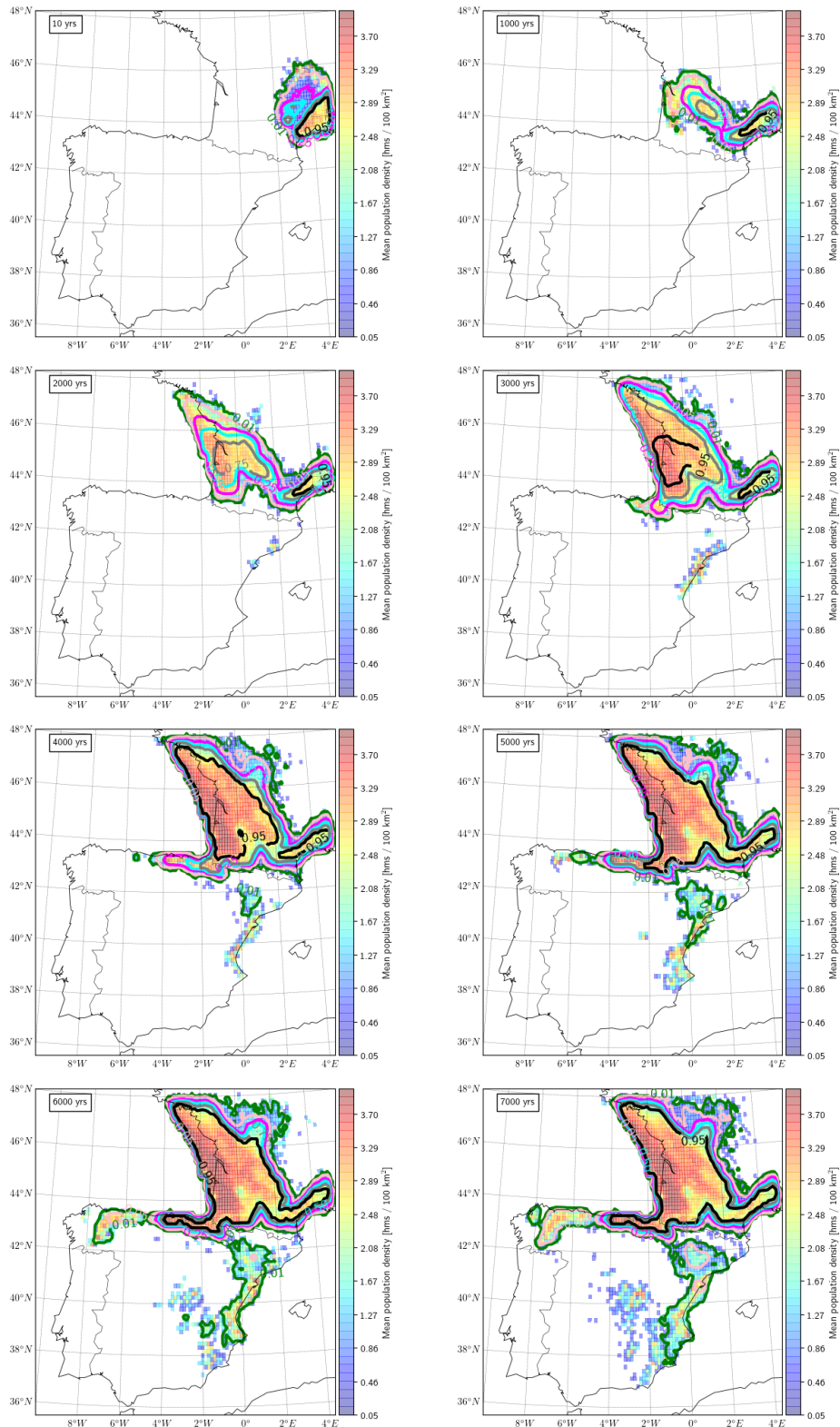


FIGURE 6.9: Different time steps of the simulated migration of the AMH to Iberia based on the Monte Carlo experiment with 120 runs and the setup in Tab. 6.3. Shown are the averaged population density at that point in time for all model runs in which the population density of the cells are unequal zero (colored grid cells), and the population spread in percentages of model runs, in black $> 95\%$, in grey $> 75\%$, in cyan $> 50\%$, in magenta $> 25\%$, in pink $> 5\%$ and in green $> 1\%$ (contour lines).

7000 years, the population in northwestern Spain, which occurs in less than 25% of the runs, has continued to expand, but none of the runs reach the west coast of Iberia. The population on the east coast, which occurs in 1 - 5% of the model runs, spreads further south. The Ebro Valley and a small part of the east coast is now also settled in 5 - 25% of the model runs. The center and the south Mediterranean coast of Iberia, which are populated from the east coast, are only reached in less than 1% of the runs.

Impact of the Heinrich Event 4

In the 120 ensemble runs that simulated the migration of the Aurignacian to Iberia, HE4 now occurs after 7000 years of simulation time. The HEP is now changed from the conditions of GI9 to the conditions of HE4 within 100 years. In Fig. 6.8 one can see that this leads to a dramatic drop in population size in all runs. Although the climatic changes took place over a period of 100 years, so that the model is provided with a certain spin-up time (in reality, one can assume that the environmental changes caused by the HE4 occurred more quickly), the population breaks within 100 - 200 years by more than half. This shows how quickly the effects of the HE4 hit the hunter-gatherers of AMHs and how devastating the climatic and environmental changes have been. After the strong population decline, the population stabilizes again in all runs and remains approximately constant until the end of the simulation period, after 10k years. The fluctuations within and between the runs are smaller than during GI9 conditions because the few refugia with high HEP in which the remaining AMHs could live are cut off from each other by areas with low HEP. As a result, there are no major expansion or migration movements in any of the runs. The ensemble mean results in 1750 humans with a standard deviation of 140 humans at the end of the simulation time.

Next, the population distribution is calculated by determining the average population density and the percentage of runs that simulated a non-zero population density in the respective area at the time (Fig. 6.10). 50 years after the onset of the HE4, after 7050 years of simulation time, not much has changed in the spread of the population. In parts of France and south-west Spain, however, the average population density is falling significantly. After 7100 years, the effects of the HE4 can be seen much more clearly. In many parts of France the population density is falling rapidly, only on the Atlantic coast it remains stable and, in some places, even increases. The same occurs in Iberia, where $\rho > 3$ hms/100 km² occur only in the coastal area of Cantabria and a few places on the eastern Mediterranean coast. Interestingly, the 0.95 and 0.75 isolines contract while the other isolines expand. There are also significantly more grid points with $\rho > 0$ than before HE4. Taken together, this shows that the onset of worse HEP conditions leads to an increase in mobility. However, this does not occur in a targeted, but a diffusive manner, so humans are streaming apart in all directions from the deteriorating areas. This can be explained in the CRWM by the population attractiveness function: due to the worsening HEP conditions, many areas are overpopulated ($\rho > \rho_c$) so that population pressure occurs that acts in all directions. Because there are hardly any good HEP areas available, the drift velocity decreases, so that the propagation is then mainly determined by the random motion. As a result, in many model runs (up to 50%) there are now AMHs in the east of the Pyrenees, and they are also advancing further into central France.

The population spread is already decreasing after 7200 years, which can be explained by the fact that many of the AMHs who have not found refuges with high HEP are dying. This also explains the large population decline in Fig. 6.8. This development continues until the population is in steady state after approx. 7500 years (not shown),

in which it remains until the end of the time series. After 10k years, all model runs (> 95%) agree that there is a population in southwest France along the Atlantic coast and in the lower reaches of the Garonne. In addition, settlements in Cantabria occur in more than 75% of the model runs. The settlement at the Mediterranean coast of France is very unlikely and only occurs in less than 5% of the cases. In the northwest of Spain there is a small spot that is populated in up to 25% of the model runs. The same applies to the eastern Iberian Mediterranean coast, which is populated in up to 25% of the model runs. Since both areas were populated in fewer model runs under GI9 conditions (especially the southern region on the eastern Iberian Mediterranean coast), they were probably mainly reached by AMHs due to the increased mobility with the onset of the HE4.

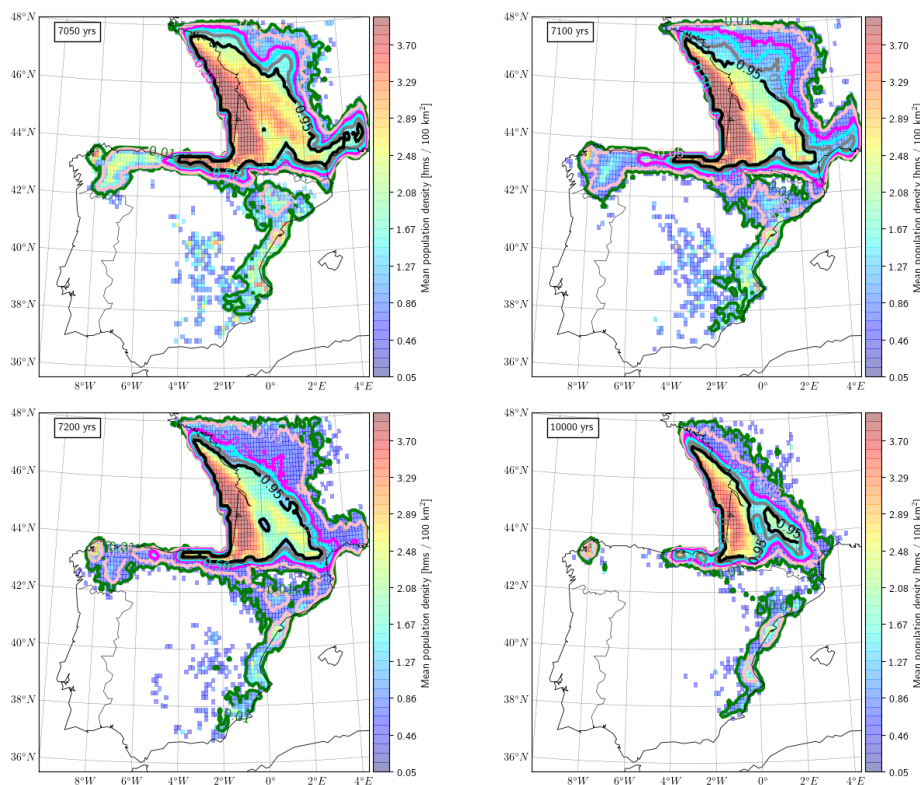


FIGURE 6.10: Same as in Fig. 6.9 with times after the HE4. It occurs after 7k years and within 100 years and remains until the end of the 10k year time series.

6.2.5 Summary

The AMHs of the AUR probably set foot in Europe 43k years ago and then settled most of the continent within a very short period of time. The Iberian Peninsula is a special hotspot in the history of settlement. There, the distribution of archaeological sites indicates that the initial expansion in the north came to a standstill and that the southern parts of the peninsula were settled much later, in the second settlement phase, after HE4. A possible explanation for this is offered by the Ebro Frontier Hypothesis, which states that the dry environmental conditions in the Ebro Valley during that time could have stopped modern humans from advancing southwards (Zilhão, 2000). New findings from Lapo de Picareiro in central Portugal which suggest that this region was populated by AMH as early as the first AUR settlement phase,

change the settlement history in western Iberia (Haws et al., 2020). Furthermore, the spread of the AUR is relevant in the context of the extinction of the Neanderthals, i.e. in the transition from the Middle to the Upper Paleolithic. Both species probably inhabited the Iberian Peninsula at the same time and contact or interaction was possible.

To test these hypotheses, the AUR spread was simulated with the CRWM. Two different experiments were carried out for this purpose. In the first experiment, the propagation was simulated for different input parameters over a long period of time (100k years) in order to cover as many random fluctuations as possible. In the second experiment, a Monte Carlo experiment was carried out. There, due to the randomness of the movement, the simulation of the propagation was repeated 120 times with the same input parameters in order to be able to estimate the propagation probabilities. In the Monte Carlo experiment, the influence of HE4 on the migration of AMHs was evaluated.

The CRWM results show that it took the AMHs of the AUR a few thousand years to reach the settlement center in southwest France. As soon as a group of humans has settled there, there is a population boost in all model configurations. This is because the AMHs encounter an unpopulated area with a large number of resources. With increasing population size, additional regions on the north coast of Iberia and further north along the Atlantic Ocean are populated starting from this main settlement region. As a result, settlement areas with a high population flow and positive birth balance, i.e., source areas, continue to develop in Cantabria and further north. In some model runs or parameter configurations, the AMHs spread further towards northwestern Spain and along the Ebro valley to the eastern Mediterranean coast of Iberia. However, the spread in these two areas can be classified as unlikely by the Monte Carlo experiment. If the eastern Mediterranean coast was settled, a settlement center with a source region developed there from which regions further south and in the center of Iberia were settled. The high HEP region in Portugal was only populated in extreme cases, for very high growth rate or very high maximal cultural carrying capacity. Taking the results of all experiments together and ignoring the extreme cases, a population size of 2500 - 5500 AMH of the AUR in the Western Mediterranean region can be assumed for GI9 conditions.

With onset of the HE4, mobility initially increases as the AMHs are driven out of settlement areas due to the deteriorating conditions. As a result, new areas are discovered and populated. However, many AMHs are now in HEP poor areas, leading to large-scale extinction. The remaining population withdraws to refuges, which are mainly located in southwest France and in some model runs on the eastern Mediterranean coast of Iberia. There the population stabilizes to a population size of 1600 - 1900 humans.

The parameter analysis has shown that the growth rate has a decisive influence on migration, both on the speed and on the spread of humans. With a high growth rate, all potentially colonizable areas are colonized within a short time and an equilibrium is established. At growth rates below $r = 0.03 \text{ yr}^{-1}$, the population dies out. Another decisive factor is the maximal cultural carrying capacity. In addition to the size of the population, this parameter also determines the spread. Since with increasing ρ_{max} the population attractiveness function shifts towards higher population densities and thus regions with lower HEP can be colonized and, as in the case of the Ebro Valley, be overcome. The two velocity components do not influence the spread and speed as decisively as the other two parameters. Both quantities should be in a relationship to one another so that a migration to HEP maxima takes place and random movements are not suppressed.

6.2.6 Discussion

The modeled AMH settlement of the AUR of the western Mediterranean region results in a large settlement center in southwest France and in northern Iberia that extends to Cantabria in the southwest, to the Mediterranean coast of France in the southeast and to Brittany in the north. Based on the modeling results, it is very likely that this area was populated by the AUR over a period of several thousand years. Settlement did not collapse at the HE4 either, but the AMHs withdrew to refuges on the Atlantic coast. The situation is different on the Iberian Mediterranean coast or further west along the Atlantic coast of Iberia. Settlement cannot be assumed with certainty there. In the Monte Carlo experiment, it occurred in less than 25% of the runs. In fact, the Ebro Valley seems to form a barrier to the good settlement area on the Iberian Mediterranean coast, which speaks in favor of the hypothesis of Zilhão (2000). This is particularly astonishing here, since the results are based on the HEP that was calculated for all AUR sites. So sites on the Iberian Mediterranean coast were also included. If one only sites from the first settlement phase of the AUR were included, settlement of the Iberian Mediterranean coast would be even less likely, as no good HEP conditions were simulated there (Fig. 3.2). This calls into question the settlement of Bajondillo Cave during the first settlement phase of the AUR, based on the results of Cortés-Sánchez et al. (2019). The settlement of this region after the HE4 could be related to a changed way of life of the AMH of the AUR or to changing environmental / climatic conditions in the GI8. Based on my results, the colonization of Lapo de Picareiro (Haws et al., 2020) during the first phase of the AUR is very unlikely. Here one can ask oneself whether the model or the observation is wrong.

The modeled speed of propagation of AMH in the Monte Carlo experiment is very slow. It is questionable whether it took AMH 2000 years to reach the Atlantic coast from the Mediterranean coast of France, as the Monte Carlo experiment has modeled in the ensemble of runs. The growth rate has turned out to be the parameter that significantly influences the spread. The speed components also contribute to this, but since they quickly lead to unstable models for values that are too large or too small, their influence is limited. Now one could argue that higher growth rates have to be selected in order to achieve modeled migration speeds that are more in line with archaeological history. Growth rates that are too high though lead to a modeled population growth during the population boost that far exceeds what can be considered realistic. For instance, $r = 1 \text{ yr}^{-1}$ resulted in a modelled growth rate of $r = 2.24 \text{ yr}^{-1}$, so the population size more than doubled every 7 years (because of $\Delta t^{bd} = 7 \text{ yr}$) during the linear growth phase. However, due to the type of modeling in the CRWM, if there is no local population pressure to drive migration, there is no reason for humans to leave familiar surroundings. Migration is then only triggered by population growth, which is a slow process, as described. If one can assume that the AUR migration was faster and the assumptions made in the CRWM are correct, one can conclude that external factors were responsible for this. These factors can be either short-term environmental changes or subscale processes, such as social interactions, that are not included in the models.

As has been shown, the simulated population densities are largely determined by the parameter *maximal cultural carrying capacity* and, for the AMH of the AUR, are in the range of 1 to 5 hms/100 km² in most experiments. These population densities are somewhat higher than estimates of the Cologne Protocol which are in the range of about 1 hms/100 km² (Schmidt et al., 2020) and which are based on the density of sites and ethnological data. However, the determination of a density largely depends on the spatial scale. On a small scale (e.g. Cologne) there are significantly higher densities

(extrapolated to 100 km²) than on a large scale (e.g. North Rhine-Westphalia). This can be transferred to hunters-gatherers of the Paleolithic. In the presented case study, the population density is calculated on a grid size of 0.15° x 0.15°, determined by the resolution of the climate model. In the western Mediterranean region, this grid size corresponds approximately to a grid cell with a total area of 150 – 225 km². In order to deliver stable results, the maximal cultural carrying capacity in the CRWM must be set corresponding to the scale, so higher than estimates from the Cologne Protocol. As it has been shown it must be at least 4 hms/100 km². A $\rho_{max} = 7$ hms/100 km² was chosen in the Monte Carlo experiment because it simulated a more meaningful expansion of modern humans. The population numbers determined are slightly higher than in the Cologne Protocol, but on the same scale. However, this is not directly due to the higher population densities, but rather to the fact that the populated area is significantly larger. This is because, due to the climatic approach, populations also occur in regions for which there is no archaeological evidence.

Processes in the CRWM are driven by the HEP, so another HEP leads to different results in addition to the randomness and the parameters. As illustrated in Chapter 3 a different set of predictors lead to slight changes in the HEP. This has hardly any effect on the general distribution, but it can lead to decisive differences locally. If the HEP differs in certain key regions, the entire simulated settlement history can change. One such key region could be the northern Mediterranean coast in Iberia. The two HEP simulations based on the predictor combinations Bio 1/4/15/18/19 and Bio 1/4/12/15/18 have significantly higher values in this region (Fig. B.2.3). The coastal route east of the Pyrenees, which was not taken by humans in any experiment, would be more likely for those HEP reconstructions. This would also increase the likelihood that AMH would settle more southerly areas of the Iberian Mediterranean coast.

6.3 Neanderthals in Iberia during MIS 3 and the effects of an Heinrich Event

While many studies on population sizes or behavior of modern humans of the Paleolithic base their results on ethnographic data from today's hunter-gatherer groups, this is obviously not possible for Neanderthals. That alone shows that it is much more difficult to model the spread and behavior of the Neanderthals. The complexity leads to different modeling approaches which answer the question why the Neanderthals became extinct differently (Banks et al., 2008; Kolodny and Feldman, 2017; Vaesen et al., 2019; Timmermann, 2020). Possibly the sole reason that the Neanderthal population was smaller than that of modern humans is responsible for the fact that the latter survived while the former became extinct (Bocquet-Appel and Degioanni, 2013). Models such as the CRWM are particularly suitable for testing such hypotheses. Of course there are a variety of hypotheses that can be tested by the CRWM by assuming different parameters or starting configurations. An evaluation of all possibilities would go far beyond the scope of this work. I have therefore limited my work to the effects of different population sizes on the population development of the Neanderthals and the effects of the HE4. The decisive parameter here is therefore the maximal cultural carrying capacity ρ_{max} , which largely determines the size of the population. Pre-simulations (not shown) have yielded that the modeled settlement behavior of the Neanderthals reacted particularly sensitively to changes in ρ_{max} and thus led to different effects of the Heinrich event. The effects of changes in the other parameters on the CRWM have already been evaluated for the AUR (Sec. 6.2.3) and can be transferred. They are therefore not discussed further for the Neanderthals.

In the following, a control run is first carried out in which the standard configuration of the Aurignacian experiment with $\rho_{max} = 7$ hms/100 km² (Tab. 6.2) is used to simulate the population dynamics of the Neanderthals. Since the population size reached very high values in this experiment and the Iberian Peninsula was populated over a large area, this is called the "large population experiment". In the next experiment, ρ_{max} is reduced to 5 hms/100 km²; I call this run the "moderate population experiment". Finally, an experiment with 4 hms/100 km² is carried out, called the "small population experiment". In the experiments, 750 humans are randomly distributed at each of the four starting points in the north (3.93°W, 42.3°N), east (0.72°W, 40.03°N), south (5.54°W, 36.66°N) and west (8.6°W, 39.2°N) of the peninsula with a Gaussian probability with a standard deviation of 2°. A 20,000-year simulation is then carried out under GI9 conditions to evaluate the adaptation of the Neanderthals and the settlement statistics. Then, as with the AUR, within 100 years, the HEP is changed in 10-year time steps to the HE4 conditions. The adaptation of the Neanderthal to the new conditions is then calculated for 10,000 years.

TABLE 6.4: Setup of the three Neanderthal experiments, the moderate population experiment (M), the small population experiment (S) and the large population experiment (L), with T_I being the time frame of the interstadial and T_H the time frame of the Heinrich event, and the other parameters as in Tab. 6.2

| | N_0 | T_I | T_H | ρ_{max} | runs |
|---|----------|---------|---------|---------------------------|------|
| M | 3000 hms | 20k yrs | 10k yrs | 5 hms/100 km ² | 100 |
| S | 3000 hms | 20k yrs | 10k yrs | 4 hms/100 km ² | 100 |
| L | 3000 hms | 20k yrs | 10k yrs | 7 hms/100 km ² | 1 |

6.3.1 Moderate population experiment

Interstadial conditions

For the moderate population run, 100 ensemble runs were carried out, with each run varying both the starting positions and the random motion. Fig. 6.11 shows the population development of the individual runs and the ensemble mean. As can be seen from the mean of the ensemble, a steady state sets in after about 9k years, at which the population size of the Neanderthals changes only slightly. The first growth phase can be seen as a kind of initialization phase in which the population adapts to the given conditions and populates all possible areas. After reaching steady state, fluctuations still occur in the individual runs, but it can be assumed that the main settlement centers are now populated in all runs, regardless of the random distribution at the beginning. After 20k years, 5200 Neanderthals live in the ensemble mean on the Iberian Peninsula with a standard deviation of 500 humans.

Fig. 6.12 shows certain time slices of the spatial expansion of the Neanderthals. After 1k years there are Neanderthals in all main settlement areas, i.e. on the Mediterranean east coast, on the southern tip, on the Portuguese coast, on the north coast and in the central upper Meseta, but these are concentrated in small areas. After 20,000 years, the populated areas in the main settlement centers have expanded in all parts and are settled in all model runs (> 95%). In addition, the population density is increasing there, and in many parts is over 3 hms/100 km². In all model runs a settlement connection stretches from the north coast to the Mediterranean east coast along the Ebro valley. Settlement connections between the Mediterranean east coast and the central upper Meseta or the southern tip exist in more than 75% of the runs. The

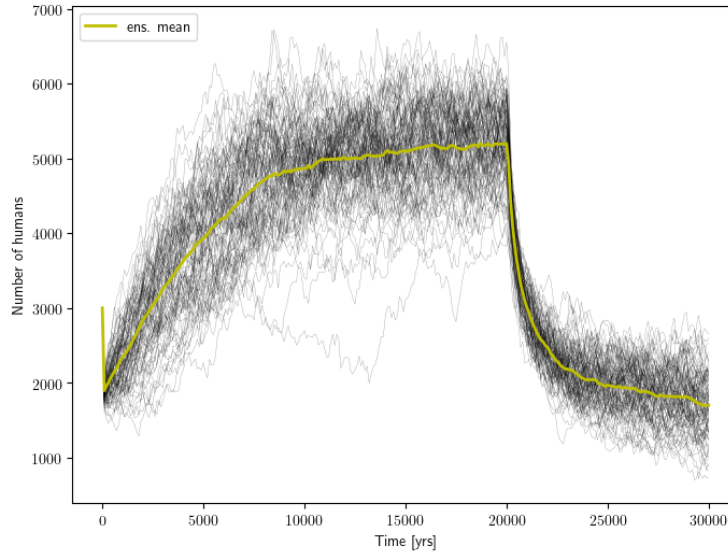


FIGURE 6.11: Number of Neanderthals for the 100 runs of the moderate population experiment, i.e. $\rho_{max} = 5$ hms/100 km² (Tab. 6.4), and the ensemble mean (yellow). The interstadial HEP conditions apply for the first 20k years, these are then changed within 100 years to the HEP conditions of the Heinrich event and simulated for a further 10k years.

Portuguese settlement area is only connected to other settlement areas in up to 25% of the runs at this time and the population density in the intermediate areas is very low. Nevertheless, one can assume that due to the large-scale expansion, there was an exchange of individual humans between the areas in most of the runs. The southern part of the Meseta is largely unpopulated, as is the northwest of Iberia.

Fig. 6.13a shows the population flow and the coefficient of variation (CoV) of the population density, averaged after the steady state has been established, i.e. from 10k to 20k years, and averaged over all runs. The main settlement centers all have a very low CoVs, since the population density there is not subject to great fluctuations compared to the mean. However, the main settlement areas on the coasts are also the regions with the highest population flow. This can be explained by the fact that there is population pressure there due to births or immigration, so that migration flows into the surroundings take place, even if the population density itself stays constant. Therefore, adjacent to the main settlement areas, there are areas with a high CoV, since humans are driven there and settle temporarily. Because the HEP conditions in these areas are not favorable, humans either die out or continue to migrate towards higher HEP areas. This leads to high population density fluctuations while the mean population density remains constant and thus to high CoVs. This creates contact and exchange between humans from different settlement centers. Continuous areas with a high CoV, such as those between the central upper Meseta and the Mediterranean east coast or between the Mediterranean east and south coast, can therefore be declared as contact zones. Contact zones also occur between the Portuguese settlement areas and the Central Meseta and the south of Iberia, albeit somewhat weaker there. The upper central Meseta shows a considerably lower population flow than the main settlement areas on the coast. Neanderthals were rarely driven towards Portugal from there and thus the contact between these settlement areas was modeled as rather low.

The ensemble and time-averaged (from 10k to 20k years) births minus deaths of the

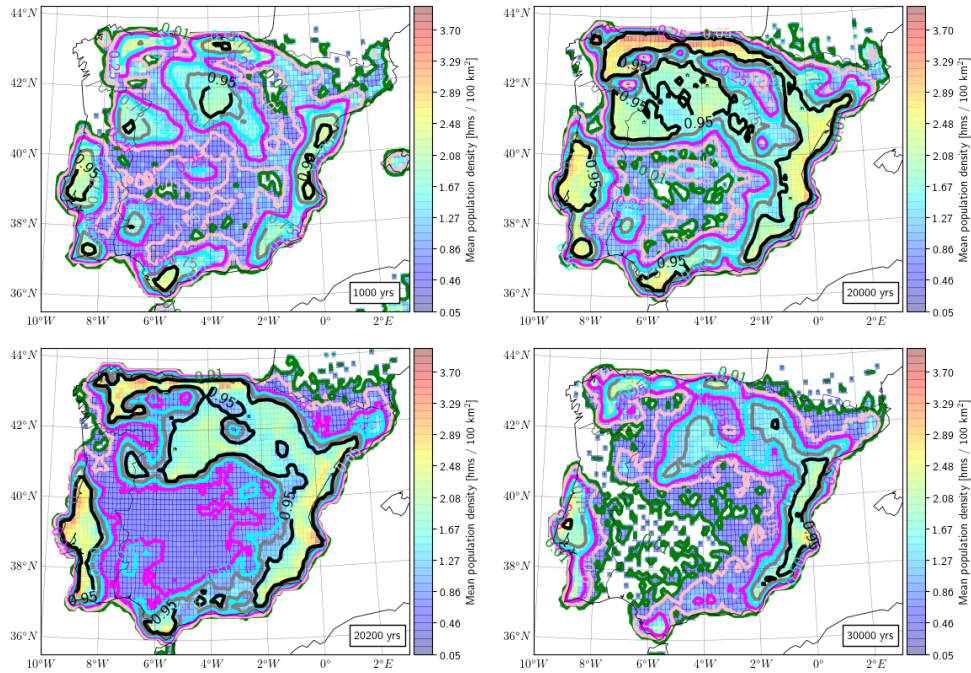


FIGURE 6.12: Settlement probability and population density of the Neanderthals in Iberia during MIS 3 depending on the 100 runs of the moderate population experiment with the same coloring as in Fig. 6.9. Shown are time segments at the beginning of the experiment, after 1k years, at the steady state of the interglacial conditions, after 20k years, immediately after the onset of the Heinrich event, after 20.2k years, and at the end of the time series, after 30k years.

interstadial conditions in Fig. 6.14a show that source regions, i.e. areas in which significantly more humans are born than die, are mainly located on the coast and in the main settlement centers. Since these are also the areas with the highest contiguous HEP, the result is as expected. Areas in which clearly more Neanderthals died than were born, i.e. so-called sink regions, are more inland in the immediate vicinity of large settlement centers, in northwestern Spain, in the central upper Meseta, on the eastern Mediterranean coast, in the Lisbon region in Portugal and on the southern tip of Spain. Interestingly, all of these areas are populated in more than 75% of the model runs after 20k years. So there was a permanent influx of Neanderthals from areas with a positive birth balance. There are also some areas in which births and deaths largely balance each other out, such as the Mediterranean east coast, the Ebro valley and parts of the northern coast. It can be assumed that the population size in these areas remained constant over the time period. Some small-scale or less relevant source or sink regions can be identified that I have not marked and will not discuss here.

Heinrich event conditions

With the Heinrich event occurring, the population decreased dramatically within 100 years and reduces to about a third of the previous size (Fig. 6.11). After 30k years of simulation time, this leads to an ensemble mean of a population size of 1700 Neanderthals with a standard deviation of 400 Neanderthals. Even if the population keeps decreasing in almost all runs until the end of the simulation time, this happens relatively slowly and it cannot be assumed that the population size will become unstable

for longer simulation times. In conclusion, it can be stated that the Neanderthals survived the effects of the Heinrich event in all runs for this CRWM configuration and it can be assumed that they would also survive for a longer simulation period, due to the slow population decline.

The stable population can also be seen in the spatial distribution of the Neanderthals in Iberia after the Heinrich event in Fig. 6.12. After 30,000 years, the Mediterranean east coast is still largely populated with relatively high population densities in all model runs ($> 95\%$). There is also a small area north of Lisbon on the Portuguese coast that is still populated in all model runs. At first, however, the mobility increases with the onset of the environmental changes of the Heinrich event, as with the humans of the Aurignacian. This can be seen in the distribution after 20.2k years, i.e. 200 years after the onset of the Heinrich Event, where Neanderthals spread over large areas, even in previously uninhabited areas, such as the southern Meseta. Since the refuges are very limited so that many humans are in areas with rather poor HEP conditions, there is a mass extinction in many areas of Iberia. After a few centuries, large parts of Central Iberia are uninhabited in all model runs, which remains so until the end of the time series. Because of the "white areas" in Central Iberia, i.e. areas in which not one human was simulated in any of the model runs, Portugal is now clearly cut off from the rest of Iberia. In addition, many runs lead to extinction of the population in southern Iberia, with Neanderthals surviving in a small area in only 50% of the runs. The same occurs on the north coast and in the upper central Meseta, which are still populated in a few regions in over 75% of the runs, but the settlement area is significantly more fragmented, which indicates a collapse of the populations in many model runs.

The averaged population flow and CoV from 25k - 30k years of the simulation time also shows a clearly changed picture compared to interstadial conditions (Fig. 6.13b). The stable settlement centers with a very low CoV are now only on the eastern Mediterranean coast, in the Ebro Valley and on the coast of Portugal in the Lisbon area. The fact that the CoV in many areas of Central Iberia has fallen sharply, especially in Central Iberia, shows that many areas of contact have collapsed. Interestingly, southern Spain, the southern part of the Portuguese coast and parts of the north coast and the central upper Meseta are now areas of high CoV. Large population changes took place

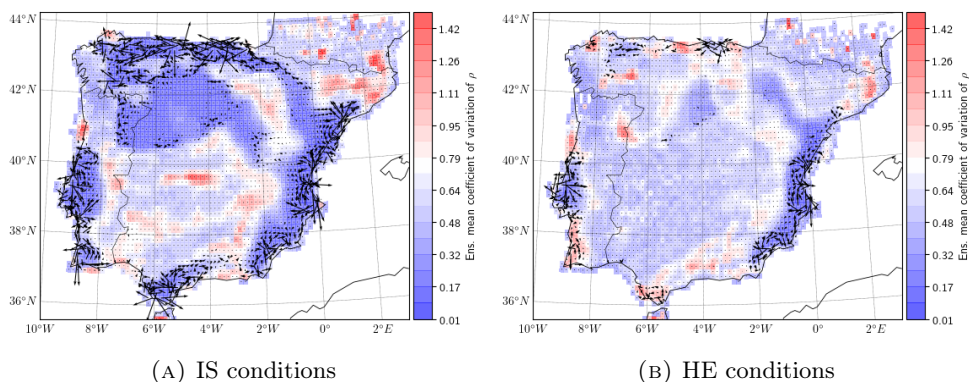


FIGURE 6.13: Settlement dynamics of the Neanderthals represented by the population flow (black arrows) and the coefficient of variation (CoV) of the population density (colored grid cells) averaged over the 100 runs of the moderate population experiment and over the time period (A) of 10k - 20k years (interstadial steady state) and (B) of 25k - 30k years ago (Heinrich event steady state).

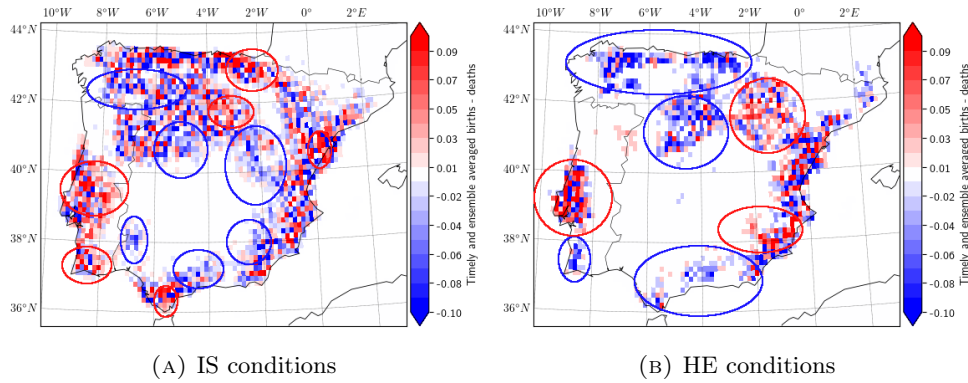


FIGURE 6.14: Time-averaged births minus deaths per grid cell for the time period of (A) 10,000 - 20,000 years (interstadial steady state) and (B) 25k - 30k years (Heinrich event steady state), averaged over the 100 runs of the moderate population experiment. Pronounced or noticeable source and sink regions are marked with red and blue circles, respectively.

here in the ensemble mean, which shows the instability of these areas, so there was emigration or extinction. Areas of high population flow are in the main settlement areas at the time and on the north coast.

With the conditions of the Heinrich event, the distribution of source and sink regions changes dramatically. Many former source regions are now sink regions, e.g. the entire north coast, the central upper Meseta, the southern Mediterranean coast and the south of Portugal. However, the population is also stabilizing in some regions, and the eastern Mediterranean coast continues to be an area in which births and deaths largely balance each other out. There are also a few source regions, e.g. in the central Portuguese coast and in the Ebro valley. Outside of these areas, however, there are hardly any grid cells with a positive birth balance. This supports the previous findings that, the Neanderthals were unable to build stable populations outside the main settlement areas on the east and west coast, but died out there after a short time.

6.3.2 Small population experiment

Interstadial conditions

In the case of a small population experiment, there is initially a population growth in the ensemble mean in the first approx. 7k years (Fig. 6.15). After that, the size of the population in the ensemble mean remains roughly constant until the Heinrich event occurs. The spread of the runs and the fluctuations within the runs are, however, greater than in the moderate population experiment. This indicates significantly stronger variations in the settlement history, both between runs and temporarily within a run. After 20k years, an average of 2600 Neanderthals populated Iberia with a standard deviation of 580 Neanderthals.

The settlement distribution after 1000 years is very similar to that of the moderate population experiment; in all main settlement areas, i.e., at the Mediterranean east coast, at the southern tip, at the Portuguese coast, at the north coast and in the central upper Meseta, small settlement centers have formed in all model runs (Fig. 6.16). After 20k years, the same areas are populated as in the moderate population experiment, but there are clearer variations between the runs, so that the settlement area is significantly more fragmented. Areas that show a population density greater

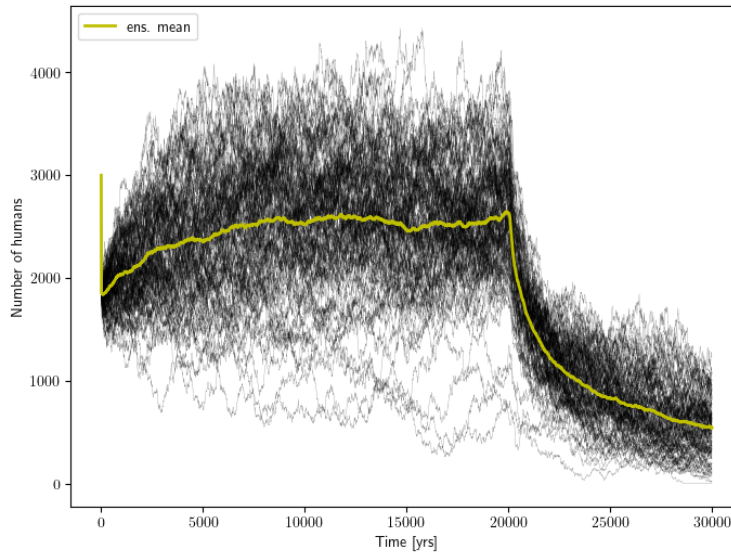


FIGURE 6.15: Same as in Fig. 6.11 but for the small population experiment ($\rho_{max} = 4$ hms/100 km²).

than zero in all courses ($> 95\%$) are only found on the Mediterranean east coast, on the north coast and in a few areas in the central upper Meseta. Starting from the Mediterranean east coast, there is only a continuous settlement connection along the Ebro valley in up to 50% of the runs and contact with the south coast has completely collapsed. In the south and west of the Iberian Peninsula, the populations are much more unstable. On the Portuguese west coast the population goes extinct after 20k years in up to 25% of the model runs and on the southern tip of Spain in up to 50% of the model runs.

The fact that the main settlement centers are smaller and less connected can also be seen in the low CoV areas in Fig. 6.17a. These are limited to the Portuguese west coast, the Mediterranean east coast, the north coast and the central upper Meseta. Some areas in inland Iberia, such as in the Ebro Valley, which were low CoV areas in the moderate experiment, are high CoV areas here, i.e. there were strong population density fluctuations there. Since these areas extend from the east coast to the north coast and into the central Meseta, there was contact of humans between these areas. The south is also a large area with high CoV. However, since there was no settlement center in most of the runs, emigrating groups of Neanderthals could not build up long-term stable populations here. The same is true for southern Portugal. The overall population flow (black arrows in Fig. 6.17a) is lower than in the moderate experiment, which is related to the lower total population and less to the mobility. In the small population experiment there are areas with a high population flow on the coasts. So Neanderthals were driven from there to the inland by local population pressure.

A similar picture emerges if one looks at the births minus deaths averaged over time and ensemble (Fig. 6.18a). The main settlement centers on the north coast, Mediterranean east coast and central upper Meseta, which also have low CoV values, are areas in which births and deaths largely balance each other out. On the central Portuguese coast, births even predominate slightly, which is why this area is marked as a source region. The Ebro Valley is an area with balanced births and deaths and high CoV, i.e. high population fluctuations. Consequently the fluctuations were caused by immigration and emigration rather than population growth or decrease, which shows

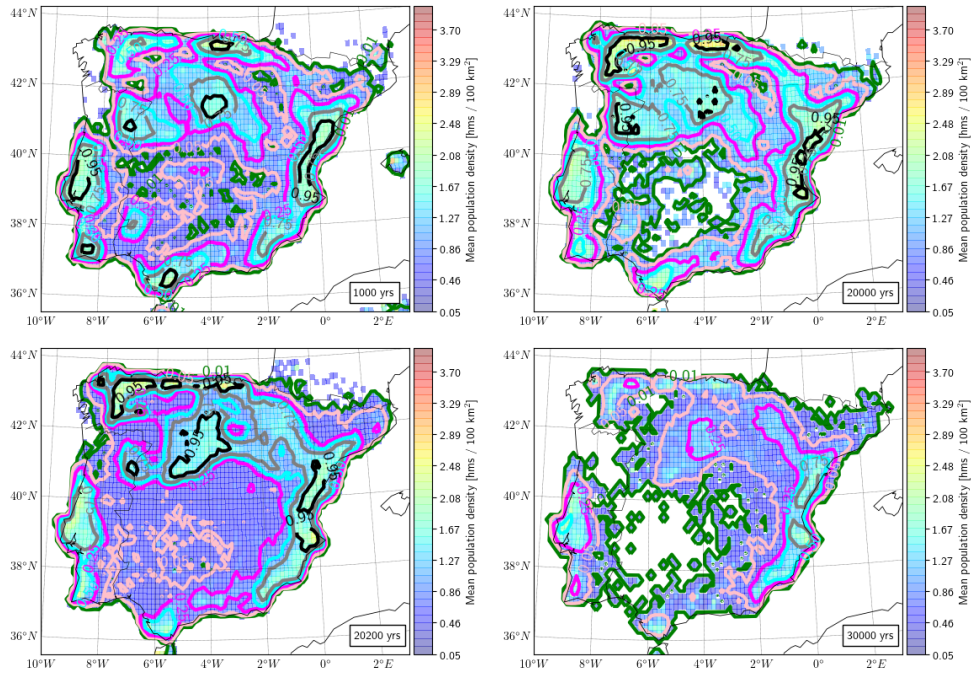


FIGURE 6.16: Same as in Fig. 6.12 but for the small population experiment ($\rho_{max} = 4 \text{ hms}/100 \text{ km}^2$)

that this region was permanently traversed by Neanderthal groups in the model runs. Outside of the settlement areas, predominantly sink regions occur. These are located in north-western Spain, the southern tip, in southern Portugal and in inland regions. In these regions, there is also high CoV everywhere, i.e. the high population fluctuations were not only caused by immigration and emigration but also by increased population mortality.

Heinrich event conditions

The effects of the Heinrich event are even more serious on the smaller population (Fig. 6.15). Of the 2600 Neanderthals that exist under interstadial conditions, 540 are still living after 30k years in the ensemble mean. With a standard deviation of 280 humans, the runs vary significantly from one another and in one run even an extinction of the Neanderthals was simulated. The population continues to decrease in some runs and also in the ensemble mean until the end of the simulation. Due to the low population size, it can be assumed that the population is unstable in many of the runs and would also become extinct with a longer simulation time.

With the beginning of the Heinrich event, one can also see in this experiment that the mobility of the Neanderthals increases after 20,200 years and that many areas are populated that offer very poor HEP conditions (Fig. 6.16). In these areas the Neanderthals die out after a short time, so that after 30,000 years large white areas appear in the center and northwest of Iberia. There is no longer any area that is populated in all (i.e. more than 95%) of the model runs after 30,000 years. In addition, in the south and north there are Neanderthals in less than 25% of the runs and in the central upper Meseta in less than 50% of the runs. On the west coast of Portugal, which is cut off from the rest of the peninsula, there are Neanderthals in less than 75% of the runs. The eastern Mediterranean coast is inhabited the longest in almost all runs and there are Neanderthals still present in more than 75% of the

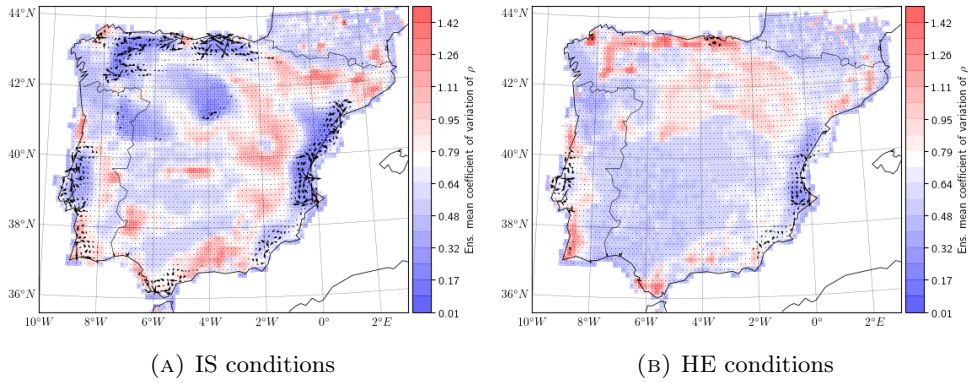


FIGURE 6.17: Same as in Fig. 6.13 for the small population experiment ($\rho_{max} = 4$ hms/100 km²) for the time period (A) 10,000 - 20,000 years (interstadial steady state) and (B) of 25k - 30k years ago (Heinrich event steady state).

runs after 30,000 years.

The same picture emerges if you look at the population flow and the CoV (Fig. 6.17b). The only remaining settlement center with low CoV is on the east coast. In the center and in the north there are some areas with high CoV, but these reflect the instability of the population (due to local extinction) and not the contact between settlement zones, which no longer exist in most runs. The entire lower Meseta is an area with low CoV, which shows that almost no more humans appear here. Due to the small population size, the population flow comes to a standstill almost completely.

The evaluation of the birth and death statistics clearly shows that after the onset of the Heinrich event, a stable population has not formed anywhere in Iberia (Fig. 6.18b). I have changed the time range over which was averaged here slightly compared to the previous experiment in order to show that the sink regions occur throughout Iberia. Averaged over 25k - 30k years, these areas only exist on the east and west coasts (see Fig. B.3.1). This in turn shows that in most of the runs the Neanderthals are extinct in almost all areas after 5000 years. The fact that only very isolated red grid cells appear and the blue grid cells clearly predominate everywhere shows the instability of the Neanderthal population at Heinrich event conditions for this experiment. This solidifies the assumption that the population would have become extinct in the majority of the runs with a longer simulation time.

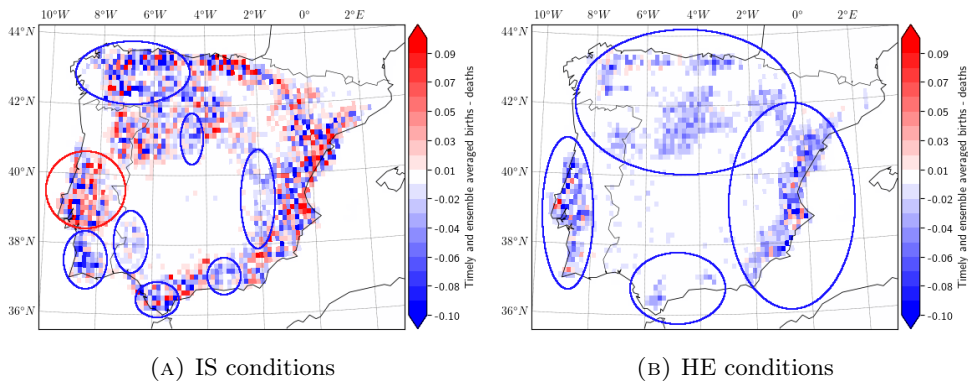


FIGURE 6.18: Same as in Fig. 6.14 but for the small population experiment ($\rho_{max} = 4$ hms/100 km²) for (A) 10k - 20k years (interstadial steady state) and (B) 20.2k - 30k years (Heinrich event steady state).

6.3.3 Large population experiment

Interstadial conditions

In the large population experiment, I refrained from performing a Monte Carlo experiment because the computational effort would be too extensive for the added value. As can be seen in Fig. 6.19, the fluctuations after the initial population growth are very small. This suggests that almost all colonizable areas in Iberia were permanently colonized in this experiment after the initialization phase. It is foreseeable that this development would also have shown in further model runs. In this steady state during interstadial conditions there are 8,800 Neanderthals on the Iberian Peninsula, with the population size fluctuating by around 200 Neanderthals (standard deviation over the years 10,000 to 20,000).

In Fig. 6.20, unlike in the previous experiments, the time-averaged population density for interstadial and Heinrich event conditions is shown. The large population experiment represents the maximum settlement of the Neanderthals in Iberia. An even denser settlement can probably be ruled out due to the low density of archaeological sites (both temporally and spatially). Settlement centers under interstadial conditions with high population densities of well over 3 hms / 100 km² are located on the coasts. The upper central Meseta, which has often appeared as a settlement center, is considerably less densely populated here. One can see a settlement connection along the Serra da Estrela to Portugal and along the Ebro Valley to the north coast. The southern Meseta is largely uninhabited, with the exception of small areas. There is a continuous settlement with stable population densities along the Mediterranean coast.

The maximum spread of colonization in the large population experiment is also illustrated by the CoV in Fig. 6.21. All main settlement centers are interconnected by large-scale low CoV areas. These areas are permanently populated without any significant population fluctuations. High CoV areas occur in the lower Meseta, these are areas of expansion. Due to the higher total population, the population flow is significantly greater than in the other experiments. The highest population flow occurs analog to the other experiments in the coastal areas, while the population flow are significantly smaller in the inland.

If one considers the births minus deaths averaged over time under IS conditions (from 10k to 20k years), it can be seen that these largely offset each other in the main settlement regions (Fig. 6.22a). Source and sink regions still occur locally, but these are usually in the immediate vicinity of each other. For example on the Portuguese coast is a sink region in the Lisbon region and a source region further north. The sink regions inland, which predominate in the moderate population experiment, are permanently populated here with a stable birth / death balance. As a result, the total population remains roughly constant over the entire period.

Heinrich event conditions

As a result of the Heinrich event, the population decreased by about half to 3900 Neanderthals with a standard deviation of 200 Neanderthals, determined over the years 25,000 to 30,000 (Fig. 6.19). The fluctuations in population size are somewhat larger at the beginning of the Heinrich event, which suggests that there would have been differences between model runs. However, since the population stabilizes at the end of the simulation time, I assume that the differences would be insignificant.

The averaged population density in Fig. 6.20 shows that there is a population decline in all settlement centers. This decline is most serious in the interior of Iberia, e.g. in

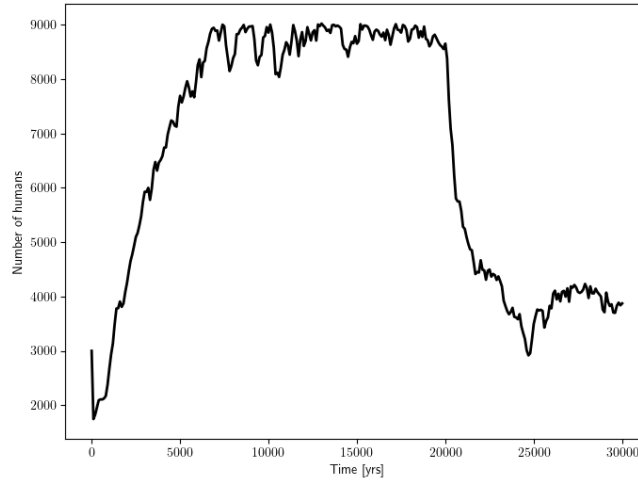


FIGURE 6.19: Same as in Fig. 6.11 but only one run and for the large population experiment ($\rho_{max} = 7$ hms/100 km²)

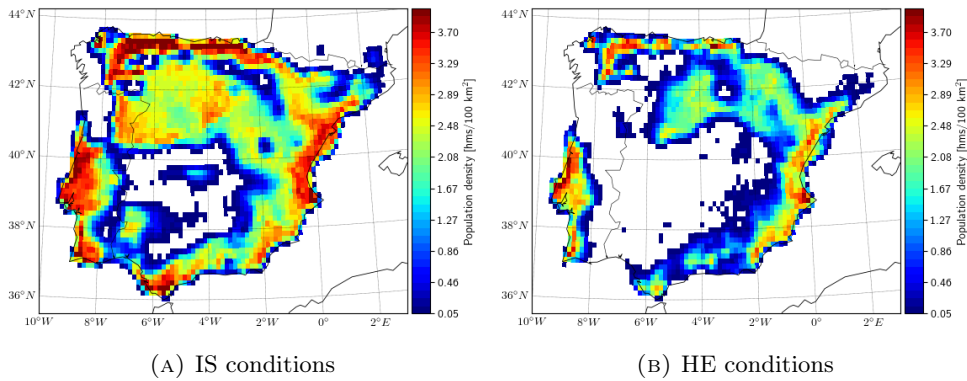


FIGURE 6.20: Timely averaged population density of the large population experiment ($\rho_{max} = 7$ hms/100 km²) for (A) interstadial conditions, from 10k - 20k years, and (B) Heinrich event conditions, from 25k - 30k years.

the central upper Meseta where some areas are no longer populated. As a result, the region on the coast of Portugal, which is still largely populated, is cut off from the rest of the peninsula. Main settlement centers with population densities greater than 3 hms/100 km² are located on the Mediterranean east coast, on the north coast and on the west coast. Stable populations are also forming in the Ebro Valley, in the central upper Meseta and at the southern tip of Spain.

Fig. 6.21 shows that the main settlement areas and areas with stable populations during Heinrich event conditions are also areas with low CoV. A large settlement center stretches from the southern tip along the Mediterranean coast and the Ebro valley to the north coast. Overall, there are few areas with high CoV, so the dynamics and contact between settlement centers that are not directly connected to each other are decreasing. This also shows that there was no contact between Neanderthals on the west coast and Neanderthals in the rest of Iberia.

In the long contiguous settlement area from the north coast and the central upper Meseta along the Ebro valley and the Mediterranean coast to the southern tip of

Iberia, births and deaths balance each other out (Fig. 6.18b). Here, however, unlike under interstadial conditions, sink regions occur at the border areas, in the south of the Central Meseta and south of northwestern Spain. While the south of Spain was connected to the east coast by a source region under interstadial conditions, there is a sink region between the two areas under Heinrich event conditions. So the contact between the areas became unstable. The southern tip itself has meanwhile changed from a sink to a source region. There is still a sink region in the Lisbon region, while the source region to the north has decreased somewhat. Nevertheless, enough humans are born in the entire Portuguese coast region to guarantee a stable population.

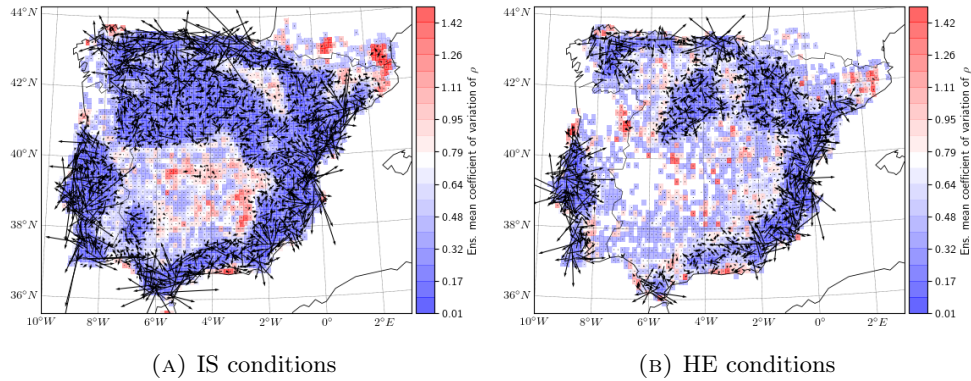


FIGURE 6.21: Same as in Fig. 6.13 but for only one run and the large population experiment ($\rho_{max} = 7$ hms/100 km²) and over the time period (A) of 10k - 20k years (interstadial steady state) and (B) of 25k - 30k years ago (Heinrich event steady state).

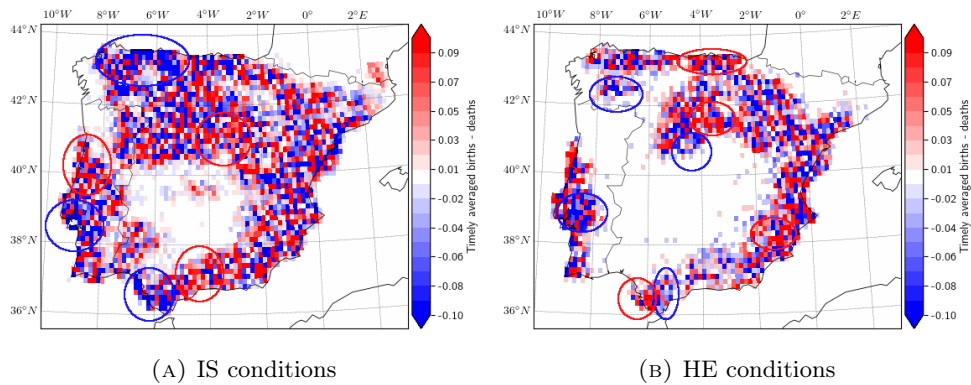


FIGURE 6.22: Same as in Fig. 6.14 but for only one run and the large population experiment ($\rho_{max} = 7$ hms/100 km²) for (A) 10k - 20k years (interstadial steady state) and (B) 25k - 30k years (Heinrich event steady state).

6.3.4 Summary

To investigate the settlement behavior of the Neanderthals during MIS 3 and their adaptation to the conditions on the Iberian Peninsula, three Monte Carlo experiments were carried out with the CRWM, with a large (L), moderate (M) and small (S) population being simulated. The HEP for interstadial and Heinrich event conditions determined in Chapter 3 served as the basis for the simulation. Based on a randomly distributed initial population of 3000 individuals, the adaptation of the Neanderthals

under interstadial conditions was calculated for 20k years followed by the effects of the Heinrich event for a further 10k years. The population dynamics of the Neanderthals were evaluated for each experiment, i.e. the change in population size, the probability of distribution of the population, mobility and contact areas and the source and sink regions. The differences between the experiments are based on the parameter ρ_{max} (Tab. 6.4), while the other parameters are the same in each experiments.

The experiments led to significantly different results, with on average 8800 Neanderthals in the L experiment, 5200 Neanderthals in the M experiment and 2600 Neanderthals in the S experiment simulated under interstadial conditions. The experiments reveal five main settlement areas, the north coast of Spain (NC), the central upper Meseta (UM), the Mediterranean east coast (EC), the southern tip of Spain (ST) and the Portuguese coast (PC). Contact areas between settlement areas arise: between NC and EC along the Ebro Valley (EV), between UM and EC along the southern foothills of the Iberian Mountains (IM), between EC and ST along the southern Mediterranean coast (SC), between ST and PC along the Gulf of Cadiz (GC) and between UM and PC along the Serra da Estrela (SE).

In the L experiment, all main settlement areas and all contact areas are permanently settled under interstadial conditions. In most areas, this results in a balanced birth / death balance. In the M experiment, all main colonization areas and EV and IM are colonized. SC, GC and SE are contact zones here, with high population fluctuations. Source regions occur mainly on the coasts and sink regions in the interior. In the S experiment, stable populations appear in NC, EC, PC and UM; overall, the populated areas are significantly smaller and more fragmented. ST is not populated here for most of the runs. EV, IM and SE are contact zones. SC and GC also have a high fluctuation, but this is mainly due to local extinction. Sink regions are also here inland, but also in the south of PC, in the east of NC, in ST and SC. The only source region is in PC north.

Under Heinrich event conditions, the settlement behavior changes significantly in all experiments. The population sizes decrease in the L experiment to 3900 Neanderthals, in the M experiment to 1700 Neanderthals and in the S experiment to 540 Neanderthals. In the L experiment, NC, PC, EC, ST, the east of UM, EV, parts of IM, and SC are populated. Due to population declines in UM and ST, contact to PC has collapsed. In the populated areas, births and deaths are balanced, at the borders of which sink regions form. In the M experiment, the population collapses in large parts of NC and UM. In ST and PC south there is a complete collapse of the population in most of the model runs. MS, ST, NC, UM east and PC south are also sink regions. Stable populations with source regions are only found in EC, EV and PC north. In the S experiment, the consequences are even more serious. The populations in NC and CU, as well as the contact zones EV, IM and SE collapse in all model runs. In some runs humans still exist in EC and PC north, but these continue to decrease over time. There are only sink regions in Iberia. The extinction of the Neanderthals was simulated in one model run. Due to the instability of the populations, it can be assumed that this would have occurred in most runs with a longer simulation time.

6.3.5 Discussion

As it turned out, the choice of the parameter *cultural carrying capacity* (ρ_{max}) has a decisive influence on the simulated settlement behavior of the Neanderthals during MIS 3 in Iberia. In this way, it determines the extent of settlement, mobility and contact between regions, and the birth and death balance. In the L experiment there is a maximum spread under interstadial conditions in which all regions are colonized

with an HEP greater than 0.5, so that the population increases to 8800 humans. Since population estimates of the Neanderthals turn out to be difficult or even impossible, it is hardly possible to justify which of the modeled results are most likely to apply. Nevertheless, I make the claim that the M and S experiment produce more meaningful results than the L experiment. In the L experiment, ρ_{max} was set equal to the standard configuration for modern humans. This leads to extensive and very dense settlement of large parts of Iberia. However, this does not agree with the distribution of the Neanderthals' sites. Compared to sites that are assigned to modern humans, Neanderthal sites occur in a lower density, both spatially and temporally. Even if various reasons, such as age or preservation, can be invoked, one possible reason is that the Neanderthal population was less dense (Bocquet-Appel and Degioanni, 2013). The fact that many areas were settled in the L experiment in which no Middle Paleolithic site was found confirms the assumption.

The Neanderthals have adapted well to the interstadial conditions in the 20k year long simulation and colonized large areas and different isotopes of Iberia in all experiments. These areas are located both on the coasts (north coast, Mediterranean east coast, southern tips and Portuguese coast), as well as inland (Ebro Valley, Central Upper Meseta). It turns out that mountains played a major role for the Neanderthals. They have spread along mountains (Iberian system, along the Ebro valley, betic cordillera, Serra da Estrela), or they have delimited settlement areas (Central System). This was also shown by the topographical distribution of the sites of the Middle Palaeolithic (Fig. 3.3), that the Neanderthals were well adapted to topographically demanding terrain. Mountain can be bridges due to ecological diversity, water availability, animals in the valley and shelter in the mountains (e.g., Hauck et al., 2018). With the occurrence of the Heinrich event, many settlement centers dissolve and the contact between settlement centers and social networks in Iberia collapse. These consequences are most evident in the center and in the north and south of the peninsula. The last refuges are mainly on the west and east coast, but are also cut off from each other. The Neanderthals could therefore have died out in northern Iberia before the immigration of modern humans, as the results suggest if one assumes that the environmental conditions for Heinrich Event 5 were like that. As the simulated expansion of modern humans has shown, the Ebro Valley was only overcome in a few cases. If one now assumes that this area was settled by Neanderthals at the time, the difficulty of reaching the Mediterranean coast of Iberia for modern humans even increased. The results suggest that there was no contact between modern humans and Neanderthals in Iberia.

Whether the Neanderthals on the Iberian Peninsula became extinct due to the conditions of a Heinrich event cannot be conclusively answered from the modeling results. The results of the S experiment suggest, however, that the case could have occurred. The population became unstable in the experiment and would probably have become extinct with a longer simulation time. The collapse of many population centers and the sharp decline in population numbers in all experiment show that the effects were very serious. Of course, these results depend on many unknowns, which can only be partially explained here. First, the results depend on the determined HEP, and thus on climatic and archaeological site data. Climate model simulations of the Greenland Interstadial 9 and the Heinrich Event 4 were used to calculate the HEP. To what extent these climatic conditions can be transferred to earlier climatic phases, such as the Heinrich event 5, which is more likely to be associated with the extinction of the Neanderthals, cannot be answered here. The assumption that all sites from the Middle Paleolithic associated to MIS 3 are included in the HEP calculation is

error-prone. It is likely that some of the sites were only temporarily inhabited, so possibly not under climatic conditions that were used here to determine the adaptation. Second, the assumption that the Neanderthals became extinct is based on the fact that they did not adapt to the climatic changes. Possible adaptations, i.e. a change in the HEP, could have enabled the Neanderthals to cope with the conditions or to settle in new areas after the onset of the crisis. Third, the time period of 10k years set for the Heinrich event is too long. In climate history there were quicker changes between stadial and interstadial conditions, these events happened within hundreds to a few thousands of years. It is possible that a small population of Neanderthals survived by the onset of better climatic conditions. However, the simulation time was intentionally set high because the model's response time has not yet been validated. Hopefully further research on the birth and death module and more experiments can provide information here in the future.

Chapter 7

Discussion

The main assumption on which the HEP and the CRWM are based is that the climatic and environmental conditions largely determined the life of hunters-gatherers of the Paleolithic. That climate, i.e. mainly temperature and precipitation, has a decisive influence on the environment and thus also all living beings within the environment is obvious. That climate and environment determined human existence and drove human migration at the time is in line with many other studies (e.g., [Bocquet-Appel et al., 2005](#); [Tzedakis et al., 2007](#); [Müller et al., 2011](#); [Schmidt et al., 2012](#); [Banks et al., 2013](#); [Ludwig et al., 2018](#); [Wren and Burke, 2019](#); [Timmermann, 2020](#)). However, nature, with all living beings it contains, especially the human species, is a highly complex and chaotic system in which causal relationships can hardly be established. Especially for the hunter-gatherers of the Paleolithic many reasons, such as religious or spiritual reasons, animal migrations, raw material deposits, topographical occurrences or for reasons completely unknown to us, can lead to deviations from the deterministic climate-human relationship. As shown in the climate-driven dispersal study by [Timmermann and Friedrich \(2016\)](#), modeling results that were initially assumed to be reasonable can quickly be revealed as false by new archaeological discoveries (see [Hublin et al., 2017](#)). So, with all the unknowns and the unpredictability of nature and human behavior, does it even make sense to describe this system using physical equations and to practice human dispersal modeling?

A statistical approach is chosen for the HEP, the value is determined by including different climatic predictors and a large selection of archaeological sites of a techno-complex. Using logistic regression, connections between climate and human settlement are created that would not have been found by a causal approach. By considering the accessible HEP, adaptations to environmental conditions and technological progress of cultures are integrated. In addition, by repeatedly calculating the HEP, taking into account different presence / absence points, an error estimate can be made and a regional forecast accuracy can be achieved. However, there are some pitfalls and problems that need to be considered and that can lead to modeling variations:

- The HEP depends on the pre-selection of the predictors. The predictors are divided into correlation groups, and one predictor from each group is used for the calculation. An exchange of predictors within a group changes the large-scale distribution of HEP only slightly, but can be relevant at the local level. As the Aurignacian case study has shown, a change in HEP in certain key regions (here the Mediterranean coast) can change the entire modeled settlement history.
- The HEP depends on the pre-selection of the archaeological sites. Presence points are defined by a circle around archaeological sites. The climatic conditions of presence points are only used once in the calculation, even if they are located in the vicinity of several sites. Outlying archaeological sites are therefore stronger weighted than sites in clusters. The LGM case study showed how much the

HEP for clustered sites from Core Areas deviates from the HEP in which all sites were used. As settlement of outlying sites is often considered to be less likely, these can lead to false results.

- Although the HEP integrates seasonal climate changes, it remains constant. A seasonal change in HEP would be of interest for regional analyzes.
- The accessibility of HEP is integrated by lowering the calculated logistic regression value. A linear relationship between topography and accessibility is assumed for this. This is clearly a simplification of reality and the complex human-environment interaction (e.g., [Hauck et al., 2018](#)) and is therefore prone to errors, at least on a local scale.

In the CRWM, the available HEP is also estimated and changes due to the presence of other humans. Too little number of humans are unfavorable as this makes survival difficult, leading to population clustering. Too high number of humans for the available resources, i.e. overpopulation, is avoided and creates population pressure and diffusion. As a result, the deterministic component of the CRWM is significantly more complex than a purely climate-driven approach. In addition, the CRWM counteracts the unpredictability by adding a stochastic component to the deterministic one and thus integrating a random factor into the modelled human dispersal. In the model, movement as well as births and deaths are generated by random processes. By repeating the same experiment several times or by performing a dispersal calculation over a long period of time, all possible scenarios can be simulated. Here the problem of such a modeling approach becomes clear, since one obviously cannot find out which of the scenarios is the right one. The problem becomes even greater if one takes into account that the simulated result is parameter controlled and one does not know which parameter combination is the right one. As shown in [R. Vahdati et al. \(2019\)](#), there are two problems in archaeological modeling in general that also apply to the CRWM: the contingency problem, stating that the same setups or parameter combinations cause different results due to the randomness, and the equifinality problem, stating that different setups or combinations lead to the same results.

The equifinality problem is less critical in the modeling studies presented here. As shown in the parameter analysis in the Aurignacian study, the results are similar for different combinations of parameters. However, it is not possible to determine in advance which parameters are correct, and it was also not relevant for my study to specify certain values for the parameters. Similar results from different combinations were interpreted here as a higher probability of the distribution. The contingency problem is more crucial and becomes clear in the Monte Carlo experiments. The individual runs using the same parameters can vary greatly and lead to population sizes from 3000 to 7000 Neanderthals in Iberia, simulated in the moderate population experiment, and to different settlements. Unfortunately, we will never be able to find out whether any of the scenarios even reflect what happened in the past. However, on the basis of the assumptions made, the probabilities of scenarios can be estimated. The probability of dispersal can then be obtained by overlapping the modeling results. In many cases, the ensemble mean is the most likely forecast. It is therefore important to repeat experiments as often as possible in order to obtain the most accurate probability estimate.

Finally, two cases should be discussed in which the modeling likely led to incorrect results. However, these cases are essential in model development and, conversely, can be used to expand and improve the model:

- As discussed in the LGM study, a high HEP is simulated for the eastern population in central Germany and the Netherlands. Since this region has been extensively archaeologically investigated, it can be assumed with a high degree of probability that no humans were present in the area at this time. Even if other reasons, such as a low population density, may be responsible, it cannot be ruled out that the modeled HEP in the region is incorrect. This allows the conclusion that predictors, which were important for hunters-gatherers at the time, were not taken into account in the calculation. For example, permafrost or vegetation could have created unpleasant conditions. In future studies, one could integrate these parameters into the calculation to test this hypothesis and improve the model.
- The Aurignacian's modeled migration for realistic growth rates appears to be too slow. A lack of external factors, such as a HEP that changes with the seasons, or sub-scale processes could be responsible for this. Both could lead to interesting model expansions, whereby possible sub-scale expansions are briefly presented. An extension of the CRWM could be to integrate group formation instead of determining population densities on a grid. With such an approach, of course, the population pressure and birth and death would have to be reinterpreted. The expansion possibilities that this approach offers are enormous. In this way, an age and gender distribution could be determined within the group and births and deaths adjusted accordingly. In addition, group dynamic analyzes can be carried out and conflicts within or with other groups can be simulated. However, there are also disadvantages with this sub-scale approach. The integration of further processes and factors increases the degree of freedom and introduces new imponderables into the CRWM, which make the interpretation of the results even more difficult. In addition, such a model would be based on assumptions that cannot be proven and are therefore questionable. How the integration of groups can be integrated into the CRWM remains to be seen in the future.

It has been shown that many factors influence the outcome when modeling the dispersal of humans. The choice of predictors and sites for HEP, as well as the parameters and randomness for CRWM, must be taken into account in the probability estimate. However, not all modeling results are realistic either, so a good compromise must be found between ensemble means and weighing up the quality of the modeling results. The modeling gives good results at the macroscopic level, but is more difficult at the microscopic level. Local differences in relevant regions can change the whole settlement history. This is a fundamental problem in modeling and is also known from other specialist areas, e.g. microscopic processes frequently lead to mismatches between the numerical weather prediction and the actual weather. An improvement can be made through better, higher-resolution models and through a better description of microscopic processes. The former, however, has numerical limits. The latter is difficult in migration modeling, because human behavior can only to a limited extent be described by physical equations. One has to keep in mind that models are only a reflection of reality, which is why one should refrain from making absolute statements or direct conclusions.

Nonetheless, human dispersal models, including the HEP and CRWM, are a very useful tool for estimating probabilities and testing hypotheses. In addition, they allow analyzes in a spatial and temporal scope that are otherwise not possible. Studies can be carried out in areas and time periods for which no observation data is available. Of course, one has to be very careful with the interpretation of the results and these

must always be discussed in the context of the assumptions. Nevertheless, correctly interpreted and used, they provide immense added value in prehistoric research. That is why I would like to answer the question I asked myself earlier, whether one should model the dispersal of humans, with a resounding "yes".

Chapter 8

Conclusions and outlook

In my doctoral thesis, models were developed and applied to quantify paleolithic human migration and adaptation to the environment. The two models that were developed within the CRC 806: "Our Way to Europe" and within the project "Our Way Model" are the Human Existence Potential (HEP) and the Constrained Random Walk Model (CRWM). The HEP determines a location-based suitability score by including climate, environmental and archaeological data, which defines the potential human settlement. As a result, human's climate and environmental adaptations as well as technological progress and cultural characteristics are included in the calculation. The HEP allows a static analysis of the spread of humans and an initial assessment of contact (best potential path) and group formation (environmental human catchment). In a further step, the impact of climatological changes on humans who have been adapted to certain climatic conditions can be estimated.

The CRWM calculates the spread of a population from the movements of individual people. The movement of a person is described by a stochastic differential equation, i.e. it is a random walk that is constrained by a drift component. In addition, births and deaths are integrated into the CRWM as random processes, with the probability of the processes being determined by the size of the population and the environmental conditions. The main assumptions of the model are (1) dispersal of humans is directed by environmental and climatic factors on the macroscopic level, (2) randomness is the dominating factor for human mobility on the microscopic level, and (3) population dynamics, comprising population size changes and population diffusion, is governed by population densities with respect to the available resources. The external conditions are integrated through the HEP. The CRWM result is controlled by parameters, by the *maximal cultural carrying capacity*, determining the population size, the *growth rate*, defining the population growth and migration speed, and the *maximal migration velocity* and *individual mobility*, balancing movement dynamics, i.e. the ratio of stochastic mobility to deterministic drift, which is directed towards favored conditions. With the CRWM, a dynamic analysis of the spread and migration of humans is possible. The model also allows to quantify contact between settlement areas and to determine source and sink regions. Since the model is based on random processes, the results are always probability estimates based on a large ensemble of runs.

The models were used for various case studies to investigate specific time periods and regions along the human journey from Africa to Europe. The main conclusions of the case studies are summarized below:

- The two cultures resident in Europe at the Last Glacial Maximum, i.e. the Solutrean in the west and the Epigravettian in the east, were adapted to different environmental conditions and an environmental barrier suppressed an exchange between the cultures. By integrating clustered sites (core areas), regions could be identified that could be colonized for a long time or that could only be colonized

at times when the climate was more favorable. In Iberia, for example, the expansion and contact between settlement centers took place mainly along the coast. When the climate was more favorable, however, corridors opened up through the inland, which made contact and expansion possible. Furthermore, an internal regionalization of cultures could be shown by the environmental human catchments, which correlates with archaeological findings (Schmidt, 2015a,b).

- In the study of the HEP in the western Mediterranean region about the modern humans of the Aurignacian and the Neanderthals of the Middle Paleolithic, it was shown that overlapping habitats only appeared in the north of Iberia. The modern humans of the Aurignacian did not colonize either the Mediterranean coast of Iberia or central regions during the first settlement phase, i.e. before the occurrence of Heinrich Event 4. The HEP results confirm the Ebro Frontier hypothesis by Zilhão (2000), i.e. that the environmental conditions in the Ebro Valley prevented the further spread of modern humans to Iberia. In the second settlement phase, however, regions with high HEP also appear south of the Ebro Valley. The effects of the Heinrich event resulted in considerable HEP declines for the Neanderthals that affected inland Iberia more than the coasts. As a result, social networks collapsed. In the north of the Iberian Peninsula, the overall decline and fragmentation of habitable areas may have led to an extinction of the Neanderthals. For regions south of the Ebro Valley, this could not be answered with certainty, as there are still contiguous settlement areas in the west and east of Iberia. Overall, the influence of modern humans on the extinction of the Neanderthals in Iberia could be assessed as minor.
- The CRWM analysis of the immigration of modern humans to the western Mediterranean region shows that southwest France and the north of Iberia were the main Aurignacian main settlement center in this region. From the source regions there, humans spread to areas in the north and south, which is also reflected in an increased population flow. The Ebro Valley represents a barrier to migration that is seldom overcome by groups, but not populated. The probability that the Mediterranean coast of Iberia was settled by modern humans of the Aurignacian can be assessed as low. If the settlement took place, a settlement center was formed there from which areas in central Iberia were settled. 2500 - 5500 humans are modeled under interstadial conditions. With the occurrence of Heinrich Event 4, the population size drops to 1,600 - 1,900 humans. As the conditions deteriorate, the mobility increases at first and humans spread out. This spread subsides after a few hundred years as humans die out locally or retreat to refugia, which are mainly located on the coasts.
- In the CRWM Neanderthal study, the north coast, the Portuguese coast, the eastern Mediterranean coast, the central upper Meseta and the southern tip of Iberia were the main settlement zones for interstadial conditions. Contact zones with high population changes developed between the regions. It is noticeable that mountainous regions, to which the Neanderthals were evidently well adapted, not only played a role as settlement areas, but also as regions of expansion. Contact zones stretch along the Iberian Mountains and the Ebro Valley, and the Serra da Estrela. The southern Meseta separated from the north by the Central System was an unfavorable habitat for Neanderthals. With occurrence of an Heinrich event, the population sank from 2600 - 8000 to 500 - 3900 Neanderthals. The probability is high that the Neanderthals became extinct in the north and south of Iberia. In the west and east of Iberia, populations may

have survived the conditions, but contact zones largely collapsed and the Neanderthals retreated to few areas. The east and west were also separated from each other. It is also possible, if Neanderthals only lived in small population densities, that the conditions of the Heinrich event led to the total extinction of the Neanderthal population in Iberia.

The developed models can, however, be listed as the main result of the doctoral thesis. Hopefully these will be used in case studies in the future to test further hypotheses or to simulate migration scenarios. In addition to the already discussed sub-scale processes that could be integrated into the models (see Chapter 7) there are other interesting model extensions. It might be possible to determine the parameters inversely, by fitting the model to certain archaeological features, as archaeological site distributions with accurate time assignments. It could also be interesting to study more closely the parameters that have been calibrated here to simplify and reduce the degrees of freedom, such as the drift time scale or the stochastic time scale, for which archaeo-physical meanings have also been suggested. The more effective use of the CRWM requires the parallelization to be improved and the model to run on supercomputers, which unfortunately could not be implemented in my doctoral thesis. Even more extensive studies on parameter dependencies could be carried out if the computing time were reduced and the available memory space increased.

In my doctoral thesis I was able to develop the HEP and the CRWM that will be available and hopefully used and improved in further studies in the future. I could provide answers for certain time period and regions of the migration path from Africa to Europe. The increasing collaboration between scientists and interdisciplinary research in the field of prehistory has produced many great ideas and results, and without them this work would not have been possible. With a broader database containing archaeological data and environmental reconstructions, bridges can be built that were previously not possible. In addition, the progress of paleoclimatic modeling provides information on time periods and regions for which no information was previously available. There are exciting times ahead of us in prehistoric research and I am curious about further developments and which answers will be found for "Our Way to Europe".

Bibliography

- Alin, A. (2010, May). Multicollinearity. *Wiley Interdisciplinary Reviews: Computational Statistics* 2(3), 370–374.
- Ammerman, A. J. and L. L. Cavalli-Sforza (1971, December). Measuring the Rate of Spread of Early Farming in Europe. *Man* 6(4), 674.
- Ammermann, A. J. and L. Cavalli-Sforza (1979). 12 - the wave of advance model for the spread of agriculture in europe. In C. RENFREW and K. L. COOKE (Eds.), *Transformations*, pp. 275–293. Academic Press.
- Araujo, M. and M. New (2007, January). Ensemble forecasting of species distributions. *Trends in Ecology & Evolution* 22(1), 42–47.
- Aubry, T., L. A. Dimuccio, A. F. Barbosa, L. Luís, A. T. Santos, M. Silvestre, K. J. Thomsen, E. Rades, M. Autzen, and A. S. Murray (2020, November). Timing of the Middle-to-Upper Palaeolithic transition in the Iberian inland (Cardina-Salto do Boi, Côa Valley, Portugal). *Quaternary Research* 98, 81–101.
- Bae, C. J., K. Douka, and M. D. Petraglia (2017, December). On the origin of modern humans: Asian perspectives. *Science* 358(6368), eaai9067.
- Banks, W. E., F. d’Errico, H. L. Dibble, L. Krishtalka, D. West, D. I. Olszewski, A. T. Peterson, D. G. Anderson, J. C. Gilliam, A. Montet-White, M. Crucifix, C. W. Marean, M.-F. Sánchez-Goñi, B. Wohlfarth, and M. Vanhaeren (2006). Eco-Cultural Niche Modeling: New Tools for Reconstructing the Geography and Ecology of Past Human Populations. *PaleoAnthropology* 2006, 68–83.
- Banks, W. E., F. d’Errico, A. T. Peterson, M. Kageyama, A. Sima, and M.-F. Sánchez-Goñi (2008, December). Neanderthal Extinction by Competitive Exclusion. *PLoS ONE* 3(12), e3972.
- Banks, W. E., F. d’Errico, A. T. Peterson, M. Vanhaeren, M. Kageyama, P. Sepulchre, G. Ramstein, A. Jost, and D. Lunt (2008, February). Human ecological niches and ranges during the LGM in Europe derived from an application of eco-cultural niche modeling. *Journal of Archaeological Science* 35(2), 481–491.
- Banks, W. E., F. d’Errico, and J. Zilhão (2013). Human–climate interaction during the early upper paleolithic: testing the hypothesis of an adaptive shift between the proto-aurignacian and the early aurignacian. *Journal of Human Evolution* 64(1), 39 – 55.
- Banks, W. E., J. Zilhão, F. d’Errico, M. Kageyama, A. Sima, and A. Ronchitelli (2009). Investigating links between ecology and bifacial tool types in western europe during the last glacial maximum. *Journal of Archaeological Science* 36(12), 2853 – 2867.

- Becker, D., M. De Andrés-Herrero, C. Willmes, G.-C. Weniger, and G. Bareth (2017). Investigating the influence of different dems on gis-based cost distance modeling for site catchment analysis of prehistoric sites in andalusia. *ISPRS International Journal of Geo-Information* 6(2).
- Benito, B. M., J.-C. Svenning, T. Kellberg-Nielsen, F. Riede, G. Gil-Romera, T. Mailund, P. C. Kjaergaard, and B. S. Sandel (2017, January). The ecological niche and distribution of Neanderthals during the Last Interglacial. *Journal of Biogeography* 44(1), 51–61.
- Berger, A. (1988, November). Milankovitch Theory and climate. *Reviews of Geophysics* 26(4), 624–657.
- Bernabeu Aubán, J., C. Michael Barton, S. Pardo Gordó, and S. M. Bergin (2015, July). Modeling initial Neolithic dispersal. The first agricultural groups in West Mediterranean. *Ecological Modelling* 307, 22–31.
- Binford, L. (2002). Constructing frames of reference: An analytical method for archaeological theory building using ethnographic and environmental data sets. *Journal of Anthropological Research* 58(3), 416–419.
- Bocquet-Appel, J.-P. and A. Degioanni (2013). Neanderthal demographic estimates. *Current Anthropology* 54(S8), S202–S213.
- Bocquet-Appel, J.-P., P.-Y. Demars, L. Noiret, and D. Dobrowsky (2005, November). Estimates of Upper Palaeolithic meta-population size in Europe from archaeological data. *Journal of Archaeological Science* 32(11), 1656–1668.
- Bond, G., H. Heinrich, W. Broecker, L. Labeyrie, J. McManus, J. Andrews, S. Huon, R. Jantschik, S. Clasen, C. Simet, K. Tedesco, M. Klas, G. Bonani, and S. Ivy (1992, November). Evidence for massive discharges of icebergs into the North Atlantic ocean during the last glacial period. *Nature* 360(6401), 245–249.
- Boria, R. A., L. E. Olson, S. M. Goodman, and R. P. Anderson (2014, March). Spatial filtering to reduce sampling bias can improve the performance of ecological niche models. *Ecological Modelling* 275, 73–77.
- Braconnot, P., S. P. Harrison, M. Kageyama, P. J. Bartlein, V. Masson-Delmotte, A. Abe-Ouchi, B. Otto-Bliesner, and Y. Zhao (2012, June). Evaluation of climate models using palaeoclimatic data. *Nature Climate Change* 2(6), 417–424.
- Bradtmöller, M., A. Pastoors, B. Weninger, and G.-C. Weniger (2012, January). The repeated replacement model – Rapid climate change and population dynamics in Late Pleistocene Europe. *Quaternary International* 247, 38–49.
- Braunisch, V., J. Coppes, R. Arlettaz, R. Suchant, H. Schmid, and K. Bollmann (2013, September). Selecting from correlated climate variables: a major source of uncertainty for predicting species distributions under climate change. *Ecography* 36(9), 971–983.
- Brier, G. W. (1950, January). Verification of Forecasts expressed in terms of Probability. *Monthly Weather Review* 78(1), 1–3.
- Burke, A., M. Kageyama, G. Latombe, M. Fasel, M. Vrac, G. Ramstein, and P. M. James (2017). Risky business: The impact of climate and climate variability on human population dynamics in Western Europe during the Last Glacial Maximum. *Quaternary Science Reviews* 164, 217 – 229.

- Burke, A., G. Levavasseur, P. M. James, D. Guiducci, M. A. Izquierdo, L. Bourgeon, M. Kageyama, G. Ramstein, and M. Vrac (2014, August). Exploring the impact of climate variability during the Last Glacial Maximum on the pattern of human occupation of Iberia. *Journal of Human Evolution* 73, 35–46.
- Campos, D., J. Fort, and V. Méndez (2006, February). Transport on fractal river networks: Application to migration fronts. *Theoretical Population Biology* 69(1), 88–93.
- Clement, A. C. and L. C. Peterson (2008, October). Mechanisms of abrupt climate change of the last glacial period. *Reviews of Geophysics* 46(4), RG4002.
- Cortés-Sánchez, M., F. J. Jiménez-Espejo, M. D. Simón-Vallejo, C. Stringer, M. C. Lozano Francisco, A. García-Alix, J. L. Vera Peláez, C. P. Odriozola, J. A. Riquelme-Cantal, R. Parrilla Giráldez, A. Maestro González, N. Ohkouchi, and A. Morales-Muñiz (2019, February). An early Aurignacian arrival in southwestern Europe. *Nature Ecology & Evolution* 3(2), 207–212.
- Cucart-Mora, C., S. Lozano, and J. Fernández-López de Pablo (2018, January). Bio-cultural interactions and demography during the Middle to Upper Palaeolithic transition in Iberia: An agent-based modelling approach. *Journal of Archaeological Science* 89, 14–24.
- Cunha, P., A. Martins, J.-P. Buylaert, A. Murray, M. Gouveia, E. Font, T. Pereira, S. Figueiredo, C. Ferreira, D. Bridgland, P. Yang, J. Stevaux, and R. Mota (2019, January). The Lowermost Tejo River Terrace at Foz do Enxarrique, Portugal: A Palaeoenvironmental Archive from c. 60–35 ka and Its Implications for the Last Neanderthals in Westernmost Iberia. *Quaternary* 2(1), 3.
- Dansgaard, W., S. J. Johnsen, H. B. Clausen, D. Dahl-Jensen, N. S. Gundestrup, C. U. Hammer, C. S. Hvidberg, J. P. Steffensen, A. E. Sveinbjörnsdottir, J. Jouzel, and G. Bond (1993, July). Evidence for general instability of past climate from a 250-kyr ice-core record. *Nature* 364(6434), 218–220.
- Davison, K., P. Dolukhanov, G. R. Sarson, and A. Shukurov (2006). The role of waterways in the spread of the neolithic. *Journal of Archaeological Science* 33(5), 641–652.
- Dormann, C. F., J. Elith, S. Bacher, C. Buchmann, G. Carl, G. Carré, J. R. G. Marquéz, B. Gruber, B. Lafourcade, P. J. Leitão, T. Münkemüller, C. McClean, P. E. Osborne, B. Reineking, B. Schröder, A. K. Skidmore, D. Zurell, and S. Lautenbach (2013, January). Collinearity: a review of methods to deal with it and a simulation study evaluating their performance. *Ecography* 36(1), 27–46.
- Durbin, J. (1970, May). Testing for Serial Correlation in Least-Squares Regression When Some of the Regressors are Lagged Dependent Variables. *Econometrica* 38(3), 410.
- Elith, J., C. H. Graham*, R. P. Anderson, M. Dudík, S. Ferrier, A. Guisan, R. J. Hijmans, F. Huettmann, J. R. Leathwick, A. Lehmann, J. Li, L. G. Lohmann, B. A. Loiselle, G. Manion, C. Moritz, M. Nakamura, Y. Nakazawa, J. McC. M. Overton, A. Townsend Peterson, S. J. Phillips, K. Richardson, R. Scachetti-Pereira, R. E. Schapire, J. Soberón, S. Williams, M. S. Wisz, and N. E. Zimmermann (2006). Novel methods improve prediction of species’ distributions from occurrence data. *Ecography* 29(2), 129–151.

- Elith, J. and J. R. Leathwick (2009, December). Species Distribution Models: Ecological Explanation and Prediction Across Space and Time. *Annual Review of Ecology, Evolution, and Systematics* 40(1), 677–697.
- Fort, J., T. Pujol, and L. L. Cavalli-Sforza (2004, April). Palaeolithic Populations and Waves of Advance. *Cambridge Archaeological Journal* 14(1), 53–61.
- Fort, J., J. Pérez-Losada, J. J. Suñol, L. Escoda, and J. M. Massaneda (2008, April). Integro-difference equations for interacting species and the Neolithic transition. *New Journal of Physics* 10(4), 043045.
- Fu, Q., C. Posth, M. Hajdinjak, M. Petr, S. Mallick, D. Fernandes, A. Furtwängler, W. Haak, M. Meyer, A. Mittnik, B. Nickel, A. Peltzer, N. Rohland, V. Slon, S. Talamo, I. Lazaridis, M. Lipson, I. Mathieson, S. Schiffels, P. Skoglund, A. P. Derevianko, N. Drozdov, V. Slavinsky, A. Tsybankov, R. G. Cremonesi, F. Mallegni, B. Gély, E. Vacca, M. R. G. Morales, L. G. Straus, C. Neugebauer-Maresch, M. Teschler-Nicola, S. Constantin, O. T. Moldovan, S. Benazzi, M. Persani, D. Coppola, M. Lari, S. Ricci, A. Ronchitelli, F. Valentin, C. Thevenet, K. Wehrberger, D. Grigorescu, H. Rougier, I. Crevecoeur, D. Flas, P. Semal, M. A. Mannino, C. Cupillard, H. Bocherens, N. J. Conard, K. Harvati, V. Moiseyev, D. G. Drucker, J. Svoboda, M. P. Richards, D. Caramelli, R. Pinhasi, J. Kelso, N. Patterson, J. Krause, S. Pääbo, and D. Reich (2016, June). The genetic history of Ice Age Europe. *Nature* 534(7606), 200–205.
- Galván, B., C. M. Hernández, C. Mallol, N. Mercier, A. Sistiaga, and V. Soler (2014, October). New evidence of early Neanderthal disappearance in the Iberian Peninsula. *Journal of Human Evolution* 75, 16–27.
- Gardiner, C. (1994). *Handbook of stochastic methods for physics, chemistry, and the natural sciences*. Springer series in synergetics. Springer.
- Giampoudakis, K., K. A. Marske, M. K. Borregaard, A. Ugan, J. S. Singarayer, P. J. Valdes, C. Rahbek, and D. Nogués-Bravo (2017, March). Niche dynamics of Palaeolithic modern humans during the settlement of the Palaearctic: Climatic niche dynamics of Palaeolithic modern humans. *Global Ecology and Biogeography* 26(3), 359–370.
- Grove, M. (2018, June). Hunter-gatherers adjust mobility to maintain contact under climatic variation. *Journal of Archaeological Science: Reports* 19, 588–595.
- Gurven, M. and H. Kaplan (2007, June). Longevity Among Hunter- Gatherers: A Cross-Cultural Examination. *Population and Development Review* 33(2), 321–365.
- Hamilton, M. J., J. Lobo, E. Rupley, H. Youn, and G. B. West (2016, May). The ecological and evolutionary energetics of hunter-gatherer residential mobility. *Evolutionary Anthropology: Issues, News, and Reviews* 25(3), 124–132.
- Hanley, J. A. and B. J. McNeil (1982, April). The meaning and use of the area under a receiver operating characteristic (ROC) curve. *Radiology* 143(1), 29–36.
- Harvati, K., C. Röding, A. M. Bosman, F. A. Karakostis, R. Grün, C. Stringer, P. Karkanas, N. C. Thompson, V. Koutoulidis, L. A. Moulopoulos, V. G. Gorgoulis, and M. Kouloukoussa (2019, July). Apidima Cave fossils provide earliest evidence of *Homo sapiens* in Eurasia. *Nature* 571(7766), 500–504.

- Hauck, T. C., F. Lehmkuhl, C. Zeeden, J. Bösken, A. Thiemann, and J. Richter (2018, August). The Aurignacian way of life: Contextualizing early modern human adaptation in the Carpathian Basin. *Quaternary International* 485, 150–166.
- Haws, J. A., M. M. Benedetti, S. Talamo, N. Bicho, J. Cascalheira, M. G. Ellis, M. M. Carvalho, L. Friedl, T. Pereira, and B. K. Zinsious (2020, October). The early Aurignacian dispersal of modern humans into westernmost Eurasia. *Proceedings of the National Academy of Sciences* 117(41), 25414–25422.
- Heinrich, H. (1988, March). Origin and consequences of cyclic ice rafting in the North-east Atlantic Ocean during the past 130,000 years. *Quaternary Research* 29(2), 142–152.
- Henn, B. M., C. R. Gignoux, M. Jobin, J. M. Granka, J. M. Macpherson, J. M. Kidd, L. Rodriguez-Botigue, S. Ramachandran, L. Hon, A. Brisbin, A. A. Lin, P. A. Underhill, D. Comas, K. K. Kidd, P. J. Norman, P. Parham, C. D. Bustamante, J. L. Mountain, and M. W. Feldman (2011, March). Hunter-gatherer genomic diversity suggests a southern African origin for modern humans. *Proceedings of the National Academy of Sciences* 108(13), 5154–5162.
- Hershkovitz, I., G. W. Weber, R. Quam, M. Duval, R. Grün, L. Kinsley, A. Ayalon, M. Bar-Matthews, H. Valladas, N. Mercier, J. L. Arsuaga, M. Martín-Torres, J. M. Bermúdez de Castro, C. Fornai, L. Martín-Francés, R. Sarig, H. May, V. A. Krenn, V. Slon, L. Rodríguez, R. García, C. Lorenzo, J. M. Carretero, A. Frumkin, R. Shahack-Gross, D. E. Bar-Yosef Mayer, Y. Cui, X. Wu, N. Peled, I. Groman-Yaroslavski, L. Weissbrod, R. Yeshurun, A. Tsatskin, Y. Zaidner, and M. Weinstein-Evron (2018, January). The earliest modern humans outside Africa. *Science* 359(6374), 456–459.
- Higham, T., T. Compton, C. Stringer, R. Jacobi, B. Shapiro, E. Trinkaus, B. Chandler, F. Gröning, C. Collins, S. Hillson, P. O’Higgins, C. FitzGerald, and M. Fagan (2011, November). The earliest evidence for anatomically modern humans in northwestern Europe. *Nature* 479(7374), 521–524.
- Higham, T., K. Douka, R. Wood, C. B. Ramsey, F. Brock, L. Basell, M. Camps, A. Arizabalaga, J. Baena, C. Barroso-Ruiz, C. Bergman, C. Boitard, P. Boscato, M. Capparrós, N. J. Conard, C. Draily, A. Froment, B. Galván, P. Gambassini, A. Garcia-Moreno, S. Grimaldi, P. Haesaerts, B. Holt, M.-J. Iriarte-Chiapusso, A. Jelinek, J. F. Jordá Pardo, J.-M. Maíllo-Fernández, A. Marom, J. Maroto, M. Menéndez, L. Metz, E. Morin, A. Moroni, F. Negrino, E. Panagopoulou, M. Peresani, S. Pirson, M. de la Rasilla, J. Riel-Salvatore, A. Ronchitelli, D. Santamaria, P. Semal, L. Slimak, J. Soler, N. Soler, A. Villaluenga, R. Pinhasi, and R. Jacobi (2014, August). The timing and spatiotemporal patterning of Neanderthal disappearance. *Nature* 512(7514), 306–309.
- Hofer, D., C. C. Raible, A. Dehnert, and J. Kuhlemann (2012, May). The impact of different glacial boundary conditions on atmospheric dynamics and precipitation in the North Atlantic region. *Climate of the Past* 8(3), 935–949.
- Holton, J. and G. Hakim (2013). *An Introduction to Dynamic Meteorology*. Academic Press. Elsevier Science.
- Hublin, J.-J., A. Ben-Ncer, S. E. Bailey, S. E. Freidline, S. Neubauer, M. M. Skinner, I. Bergmann, A. Le Cabec, S. Benazzi, K. Harvati, and P. Gunz (2017, June). New

- fossils from Jebel Irhoud, Morocco and the pan-African origin of *Homo sapiens*. *Nature* 546(7657), 289–292.
- Hublin, J.-J. and W. Roebroeks (2009, July). Ebb and flow or regional extinctions? On the character of Neandertal occupation of northern environments. *Comptes Rendus Palevol* 8(5), 503–509.
- Kageyama, M., P. Braconnot, S. P. Harrison, A. M. Haywood, J. H. Jungclauss, B. L. Otto-Bliesner, J.-Y. Peterschmitt, A. Abe-Ouchi, S. Albani, P. J. Bartlein, C. Brierley, M. Crucifix, A. Dolan, L. Fernandez-Donado, H. Fischer, P. O. Hopcroft, R. F. Ivanovic, F. Lambert, D. J. Lunt, N. M. Mahowald, W. R. Peltier, S. J. Phipps, D. M. Roche, G. A. Schmidt, L. Tarasov, P. J. Valdes, Q. Zhang, and T. Zhou (2018, March). The PMIP4 contribution to CMIP6 – Part 1: Overview and over-arching analysis plan. *Geoscientific Model Development* 11(3), 1033–1057.
- Kageyama, M., U. Merkel, B. Otto-Bliesner, M. Prange, A. Abe-Ouchi, G. Lohmann, R. Ohgaito, D. M. Roche, J. Singarayer, D. Swingedouw, and X Zhang (2013, April). Climatic impacts of fresh water hosing under Last Glacial Maximum conditions: a multi-model study. *Climate of the Past* 9(2), 935–953.
- Kehl, M., C. Burow, A. Hilgers, M. Navazo, A. Pastoors, G.-C. Weniger, R. Wood, and J. F. Jordá Pardo (2013). Late Neanderthals at Jarama VI (central Iberia)? *Quaternary Research* 80(2), 218–234.
- Kehl, M., D. Álvarez Alonso, M. de Andrés-Herrero, P. Carral González, E. García, J. Jordá Pardo, M. Menéndez, J. Quesada, J. Rethemeyer, J. Rojo, Y. Tafelmaier, and G.-C. Weniger (2018a). Towards a revised stratigraphy for the Middle to Upper Palaeolithic boundary at La Güelga (Narciandi, Asturias, Spain). Soil micromorphology and new radiocarbon data. *Boletín Geológico y Minero* 1129(1-2), 183–206.
- Kehl, M., D. Álvarez Alonso, M. de Andrés-Herrero, A. Díez-Herrero, N. Klasen, J. Rethemeyer, and G.-C. Weniger (2018b). The rock shelter abrigo del molino (segovia, Spain) and the timing of the late middle paleolithic in central Iberia. *Quaternary Research* 90(1), 180–200.
- Kelly, R. (2013). *The Lifeways of Hunter-Gatherers: The Foraging Spectrum*. Cambridge University Press.
- Klein, D., J. Marx, and K. Fischbach (2018). Agent-Based Modeling in Social Science, History, and Philosophy. An Introduction. *Historical Social Research / Historische Sozialforschung* Vol. 43 No. 1. Publisher: GESIS - Leibniz-Institut für Sozialwissenschaften Version Number: 1.
- Klein, K., C. Wegener, I. Schmidt, M. Rostami, P. Ludwig, S. Ulbrich, J. Richter, G.-C. Weniger, and Y. Shao (2021). Human existence potential in Europe during the last glacial maximum. *Quaternary International* 581-582, 7–27. The Last Glacial Maximum in Europe – State of the Art in Geoscience and Archaeology.
- Kolodny, O. and M. W. Feldman (2017, December). A parsimonious neutral model suggests Neanderthal replacement was determined by migration and random species drift. *Nature Communications* 8(1), 1040.
- Kondo, Y., K. Sano, T. Omori, A. Abe-Ouchi, W.-L. Chan, S. Kadowaki, M. Naganuma, R. O’ishi, T. Oguchi, Y. Nishiaki, and M. Yoneda (2018). Ecological

- Niche and Least-Cost Path Analyses to Estimate Optimal Migration Routes of Initial Upper Palaeolithic Populations to Eurasia. In *The Middle and Upper Paleolithic Archeology of the Levant and Beyond*, Replacement of Neanderthals by Modern Humans Series, pp. 199–212. Springer, Singapore.
- Larrasoana, J. C., A. P. Roberts, and E. J. Rohling (2013, October). Dynamics of Green Sahara Periods and Their Role in Hominin Evolution. *PLoS ONE* 8(10), e76514.
- Lewis, M. and P. Kareiva (1993). Allee dynamics and the spread of invading organisms. *Theoretical Population Biology* 43(2), 141–158.
- Ludwig, P., J. J. Gómez-Navarro, J. G. Pinto, C. C. Raible, S. Wagner, and E. Zorita (2019). Perspectives of regional paleoclimate modeling. *Annals of the New York Academy of Sciences* 1436(1), 54–69.
- Ludwig, P., J. G. Pinto, C. C. Raible, and Y. Shao (2017, May). Impacts of surface boundary conditions on regional climate model simulations of European climate during the Last Glacial Maximum: Regional European Climate During the LGM. *Geophysical Research Letters* 44(10), 5086–5095.
- Ludwig, P., E. J. Schaffernicht, Y. Shao, and J. G. Pinto (2016, March). Regional atmospheric circulation over Europe during the Last Glacial Maximum and its links to precipitation: LGM ATMOSPHERIC CIRCULATION OVER EUROPE. *Journal of Geophysical Research: Atmospheres* 121(5), 2130–2145.
- Ludwig, P., Y. Shao, M. Kehl, and G.-C. Weniger (2018). The Last Glacial Maximum and Heinrich event I on the Iberian Peninsula: A regional climate modelling study for understanding human settlement patterns. *Global and Planetary Change* 170, 34 – 47.
- Macal, C. M. and M. J. North (2006). Tutorial on agent-based modeling and simulation part 2: How to model with agents. In *Proceedings of the 2006 Winter Simulation Conference*, pp. 73–83.
- Maier, A., F. Lehmkuhl, P. Ludwig, M. Melles, I. Schmidt, Y. Shao, C. Zeeden, and A. Zimmermann (2016). Demographic estimates of hunter–gatherers during the last glacial maximum in Europe against the background of palaeoenvironmental data. *Quaternary International* 425, 49 – 61.
- Maroto, J., M. Vaquero, Arrizabalaga, J. Baena, E. Baquedano, J. Jordá, R. Julià, R. Montes, J. Van Der Plicht, P. Rasines, and R. Wood (2012). Current issues in late Middle Palaeolithic chronology: New assessments from Northern Iberia. *Quaternary International* 247, 15–25.
- Martino, L. A., A. Osella, C. Dorso, and J. L. Lanata (2007, Sep). Fisher equation for anisotropic diffusion: Simulating South American human dispersals. *Phys. Rev. E* 76, 031923.
- Mellars, P. (2006). A new radiocarbon revolution and the dispersal of modern humans in Eurasia. *Nature International journal of science* 439, 931–935.
- Miebach, A., S. Stolzenberger, L. Wacker, A. Hense, and T. Litt (2019, June). A new Dead Sea pollen record reveals the last glacial paleoenvironment of the southern Levant. *Quaternary Science Reviews* 214, 98–116.

- Morgan, C. (2009, December). Climate change, uncertainty and prehistoric hunter–gatherer mobility. *Journal of Anthropological Archaeology* 28(4), 382–396.
- Murray, J. D. (2002). *Mathematical biology* (3rd ed ed.). Interdisciplinary applied mathematics. New York: Springer.
- Müller, U. C., J. Pross, P. C. Tzedakis, C. Gamble, U. Kotthoff, G. Schmiedl, S. Wulf, and K. Christanis (2011). The role of climate in the spread of modern humans into europe. *Quaternary Science Reviews* 30(3), 273 – 279.
- Nett, J. J. B., F. Lehmkuhl, E. J. Schaffernicht, S. Pötter, P. Schulte, P. Ludwig, T. Sprafke, and U. Hambach (2021, March). Comparing a new paleomap of European loess landscapes to an atmospheric dust circulation model. other, pico.
- Peltier, W. R., D. F. Argus, and R. Drummond (2015, January). Space geodesy constrains ice age terminal deglaciation: The global ICE-6G_c (VM5a) model: Global Glacial Isostatic Adjustment. *Journal of Geophysical Research: Solid Earth* 120(1), 450–487.
- R. Vahdati, A., J. D. Weissmann, A. Timmermann, M. S. Ponce de León, and C. P. Zollikofer (2019, October). Drivers of Late Pleistocene human survival and dispersal: an agent-based modeling and machine learning approach. *Quaternary Science Reviews* 221, 105867.
- Raia, P., A. Mondanaro, M. Melchionna, M. Di Febbraro, J. A. Diniz-Filho, T. F. Rangel, P. B. Holden, F. Carotenuto, N. R. Edwards, M. S. Lima-Ribeiro, A. Profico, L. Maiorano, S. Castiglione, C. Serio, and L. Rook (2020, October). Past Extinctions of Homo Species Coincided with Increased Vulnerability to Climatic Change. *One Earth* 3(4), 480–490.
- Ramachandran, S., O. Deshpande, C. C. Roseman, N. A. Rosenberg, M. W. Feldman, and L. L. Cavalli-Sforza (2005, November). Support from the relationship of genetic and geographic distance in human populations for a serial founder effect originating in Africa. *Proceedings of the National Academy of Sciences* 102(44), 15942–15947.
- Ramankutty, N., J. A. Foley, F. G. Hall, G. J. Collatz, B. W. Meeson, S. O. Los, E. Brown De Colstoun, and D. R. Landis (2010, February). ISLSCP II Potential Natural Vegetation Cover. *ORNL DAAC*.
- Roche, D., D. Paillard, and E. Cortijo (2004, November). Constraints on the duration and freshwater release of Heinrich event 4 through isotope modelling. *Nature* 432(7015), 379–382.
- Rotgänger, M., J. Blumenröther, M. Bradtmöller, M. Kehl, T. Otto, A. Pastoors, I. Schmidt, Y. Tafelmaier, and G.-C. Weniger (2021). Crc806 c1 database iberia late middle palaeolithic to magdalenian.
- Schaffernicht, E. J., P. Ludwig, and Y. Shao (2019, October). Linkage between Dust Cycle and Loess of the Last Glacial Maximum in Europe. preprint, Aerosols/Atmospheric Modelling/Troposphere/Physics (physical properties and processes).
- Schmidt, I. (2015a). Beyond solutrean point types: technological organization and behavioral implications. *Journal of Anthropological Research* 71(4), 493–508.

- Schmidt, I. (2015b). *Solutrean Points of the Iberian Peninsula. Tool making and using behaviour of hunter-gatherers during the Last Glacial Maximum*. BAR International Series 2778.
- Schmidt, I., M. Bradtmöller, M. Kehl, A. Pastoors, Y. Tafelmaier, B. Weninger, and G.-C. Weniger (2012). Rapid climate change and variability of settlement patterns in Iberia during the Late Pleistocene. *Quaternary International* 274, 179–204.
- Schmidt, I., J. Hilpert, I. Kretschmer, R. Peters, M. Broich, S. Schiesberg, O. Vogles, K. Wendt, A. Zimmermann, and A. Maier (2020). Approaching Prehistoric Demography: Proxies, Scales and Scopes of the Cologne Protocol for the European context. *Proceedings of the Royal Society Series B*, to appear.
- Schmidt, I. and A. Zimmermann (2019, February). Population dynamics and socio-spatial organization of the Aurignacian: Scalable quantitative demographic data for western and central Europe. *PLOS ONE* 14(2), e0211562.
- Sepulchre, P., G. Ramstein, M. Kageyama, M. Vanhaeren, G. Krinner, M.-F. Sánchez-Goñi, and F. d’Errico (2007, June). H4 abrupt event and late Neanderthal presence in Iberia. *Earth and Planetary Science Letters* 258(1-2), 283–292.
- Shao, Y., A. Anhäuser, P. Ludwig, P. Schlüter, and E. Williams (2018, September). Statistical reconstruction of global vegetation for the last glacial maximum. *Global and Planetary Change* 168, 67–77.
- Shao, Y., H. Limberg, K. Klein, C. Wegener, I. Schmidt, G.-C. Weniger, A. Hense, and M. Rostami (in review 2021). Human-Existence Probability of the Aurignacian techno-complex under extreme climate conditions. *Quaternary Science Reviews*.
- Skamarock, W. C., J. B. Klemp, J. Dudhia, D. O. Gill, Z. Liu, J. Berner, W. Wang, J. G. Powers, M. G. Duda, D. M. Barker, and X.-Y. Huang (2019, March). A Description of the Advanced Research WRF Model Version 4. Technical report, UCAR/NCAR.
- Staubwasser, M., V. Drăgușin, B. P. Onac, S. Assonov, V. Ersek, D. L. Hoffmann, and D. Veres (2018, September). Impact of climate change on the transition of Neanderthals to modern humans in Europe. *Proceedings of the National Academy of Sciences* 115(37), 9116–9121.
- Steele, J. (2009, April). Human Dispersals: Mathematical Models and the Archaeological Record. *Human Biology* 81(2-3), 121–140.
- Steele, J., J. Adams, and T. Sluckin (1998). Modelling paleoindian dispersals. *World Archaeology* 30(2), 286–305.
- Stringer, C. and J. Galway-Witham (2017). On the origin of our species. *Nature* (546), 212–214.
- Sánchez Yustos, P. and F. Diez Martín (2015, August). Dancing to the rhythms of the Pleistocene? Early Middle Paleolithic population dynamics in NW Iberia (Duero Basin and Cantabrian Region). *Quaternary Science Reviews* 121, 75–88.
- Särkkä, S. and A. Solin (2019). *Itô Calculus and Stochastic Differential Equations*, pp. 42–58. Institute of Mathematical Statistics Textbooks. Cambridge University Press.

- Tallavaara, M., M. Luoto, N. Korhonen, H. Järvinen, and H. Seppä (2015). Human population dynamics in Europe over the last glacial maximum. *Proceedings of the National Academy of Sciences* 112(27), 8232–8237.
- Thomson, D. J. (1987, July). Criteria for the selection of stochastic models of particle trajectories in turbulent flows. *Journal of Fluid Mechanics* 180(-1), 529.
- Timmermann, A. (2020, June). Quantifying the potential causes of Neanderthal extinction: Abrupt climate change versus competition and interbreeding. *Quaternary Science Reviews* 238, 106331.
- Timmermann, A. and T. Friedrich (2016, October). Late Pleistocene climate drivers of early human migration. *Nature* 538(7623), 92–95.
- Trinkaus, E. (2007). European early modern humans and the fate of the Neandertals. *Proceedings of the National Academy of Sciences* 104(18), 7367–7372.
- Tzedakis, P. C., K. A. Hughen, I. Cacho, and K. Harvati (2007). Placing late Neandertals in a climatic context. *Nature* 449, 206–208.
- Vaesen, K., F. Scherjon, L. Hemerik, and A. Verpoorte (2019, November). Inbreeding, Allee effects and stochasticity might be sufficient to account for Neanderthal extinction. *PLOS ONE* 14(11), e0225117.
- Verhulst, P.-F. (1838). Notice sur la loi que la population poursuit dans son accroissement. *Corresp. Math. Phys.* (10), 113–121.
- Villa, P. and W. Roebroeks (2014, 04). Neanderthal demise: An archaeological analysis of the modern human superiority complex. *PLOS ONE* 9(4), 1–10.
- Voelker, A. H. (2002, May). Global distribution of centennial-scale records for Marine Isotope Stage (MIS) 3: a database. *Quaternary Science Reviews* 21(10), 1185–1212.
- Walker, B., L. Gunderson, A. Kinzig, C. Folke, S. Carpenter, and L. Schultz (2006). A Handful of Heuristics and Some Propositions for Understanding Resilience in Social-Ecological Systems. *Ecology and Society* 11(1), art13.
- Walker, M. J., J. Gibert, M. V. Lopez, A. V. Lombardi, A. Perez-Perez, J. Zapata, J. Ortega, T. Higham, A. Pike, J.-L. Schwenninger, J. Zilhao, and E. Trinkaus (2008). Late Neandertals in Southeastern Iberia: Sima de las Palomas del Cabezo Gordo, Murcia, Spain. *Proceedings of the National Academy of Sciences* 105(52), 20631–20636.
- Weitzel, N., A. Hense, and C. Ohlwein (2019, July). Combining a pollen and macrofossil synthesis with climate simulations for spatial reconstructions of European climate using Bayesian filtering. *Climate of the Past* 15(4), 1275–1301.
- Wolf, D., T. Kolb, M. Alcaraz-Castaño, S. Heinrich, P. Baumgart, R. Calvo, J. Sánchez, K. Ryborz, I. Schäfer, M. Bliedtner, R. Zech, L. Zöller, and D. Faust (2018, December). Climate deteriorations and Neanderthal demise in interior Iberia. *Scientific Reports* 8(1), 7048.
- Wood, R., A. Arrizabalaga, M. Camps, S. Fallon, M.-J. Iriarte-Chiapusso, R. Jones, J. Maroto, M. de la Rasilla, D. Santamaría, J. Soler, N. Soler, A. Villaluenga, and T. Higham (2014). The chronology of the earliest Upper Palaeolithic in northern Iberia: New insights from L'Arbreda, Labeko Koba and La Viña. *Journal of Human Evolution* 69, 91–109.

- Wood, R., F. Bernaldo de Quirós, J.-M. Maíllo-Fernández, J.-M. Tejero, A. Neira, and T. Higham (2018). El Castillo (Cantabria, northern Iberia) and the Transitional Aurignacian: Using radiocarbon dating to assess site taphonomy. *Quaternary International* 474, 56–70.
- Wood, R. E., C. Barroso-Ruiz, M. Caparros, J. F. Jorda Pardo, B. Galvan Santos, and T. F. G. Higham (2013, February). Radiocarbon dating casts doubt on the late chronology of the Middle to Upper Palaeolithic transition in southern Iberia. *Proceedings of the National Academy of Sciences* 110(8), 2781–2786.
- Wren, C. D. and A. Burke (2019, June). Habitat suitability and the genetic structure of human populations during the Last Glacial Maximum (LGM) in Western Europe. *PLOS ONE* 14(6), e0217996.
- Wurzer, G., K. Kowarik, and H. Reschreiter (Eds.) (2015). *Agent-based Modeling and Simulation in Archaeology*. Advances in Geographic Information Science. Cham: Springer International Publishing.
- Young, D. A. and R. L. Bettinger (1995). Simulating the global human expansion in the latepleistocene. *Journal of Archaeological Science* 22(1), 89–92.
- Zhang, X., G. Lohmann, G. Knorr, and X. Xu (2013, October). Different ocean states and transient characteristics in Last Glacial Maximum simulations and implications for deglaciation. *Climate of the Past* 9(5), 2319–2333.
- Ziemen, F. A., M.-L. Kapsch, M. Klockmann, and U. Mikolajewicz (2019, January). Heinrich events show two-stage climate response in transient glacial simulations. *Climate of the Past* 15(1), 153–168. Publisher: Copernicus GmbH.
- Zilhao, J. (2006, ene.). Chronostratigraphy of the middle-to-upper paleolithic transition in the iberian peninsula. *Pyrenae* (37), 7–84.
- Zilhão, J. (2000). The Ebro Frontier: a model for the late extinction of Iberian Neanderthals. In *Neanderthals on the edge: 150th Anniversary Conference of the Forbes' Quarry discovery*, pp. 111–121. Oxford: Oxbow Books.
- Zilhão, J., D. Anesin, T. Aubry, E. Badal, D. Cabanes, M. Kehl, N. Klasen, A. Lucena, I. Martín-Lerma, S. Martínez, H. Matias, D. Susini, P. Steier, E. M. Wild, D. E. Angelucci, V. Villaverde, and J. Zapata (2017, November). Precise dating of the Middle-to-Upper Paleolithic transition in Murcia (Spain) supports late Neandertal persistence in Iberia. *Heliyon* 3(11), e00435.
- Zilhão, J., D. E. Angelucci, L. J. Arnold, M. Demuro, D. L. Hoffmann, and A. W. Pike (2021). A revised, Last Interglacial chronology for the Middle Palaeolithic sequence of Gruta da Oliveira (Almonda karst system, Torres Novas, Portugal). *Quaternary Science Reviews* 258, 106885.
- Zimmermann, A., S. Scharl, and I. Schmidt (2020). Demographic transitions—cycles and mobility in the Neolithic of Western Germany. In *Demography and migration. Population trajectories from the Neolithic to the Iron Age*, pp. 94–106. Archaeopress.

Appendices

Appendix A

Constrained random walk model

A.1 Mathematical definitions

In the following, a short introduction into mathematical concepts is given that are important to define the Itô stochastic differential equation, which forms the basis of the CRWM. Thereby important, are the definition and characteristics of random variables and the theoretical concept of a Markov process. Here are only rough mathematical definitions provided, for a more extensive explanation of the concepts the reader is referred to [Gardiner \(1994\)](#).

A.1.1 Probability theory

A probabilistic experiment consists of a non-empty set Ω and a transformation $p : \Omega \rightarrow [0, 1]$ with:

- (i) $p(\omega) \geq 0$ for all $\omega \in \Omega$,
- (ii) $\sum_{\omega \in \Omega} p(\omega) = 1$.

Ω is then called the *sample space* that consists of all possible outcomes of the stochastic experiment. p is the probability and $p(\omega)$ gives the probability for ω .

For the defined probabilistic experiment, a *random event* is defined by $A \subset \Omega$, and the probability of A is:

$$P(A) = \sum_{\omega \in A} p(\omega) \quad (\text{A.1})$$

The following probability axioms apply for A and $P(A)$:

- (i) $P(A) \geq 0$ for all A ,
- (ii) $P(\emptyset) = 0$, $P(\Omega) = 1$,
- (iii) $A \cap B = \emptyset \Rightarrow P(A \cup B) = P(A) + P(B)$.

Two random events $A, B \subset \Omega$ are *independent*, given that their joint probability is:

$$P(A \cap B) = P(A) \cdot P(B). \quad (\text{A.2})$$

The *conditional probability* of A given B is defined by:

$$P(A|B) = \frac{P(A \cap B)}{P(B)}. \quad (\text{A.3})$$

A *random variable* is a function $F(A)$ that takes certain values $\in \mathbb{R}$ for each random event A . A particular random variable is the identity function $X(x)$, which is defined

for a probability space with random events x by:

$$X(x) = x. \quad (\text{A.4})$$

A concept that is used frequently throughout the thesis is the Gaussian distributed random variable, defined by:

$$p(x) = \frac{1}{\sqrt{2\pi\sigma^2}} \exp\left(-\frac{(x-\mu)^2}{2\sigma^2}\right). \quad (\text{A.5})$$

μ is the mean value and σ the standard deviation of the distribution.

A.1.2 Markov process

Considering a stochastic process with a time-dependent random variable $X(t)$ that takes certain values (x_1, x_2, x_3, \dots) at times (t_1, t_2, t_3, \dots) . This probabilistic system of the time evolution of X can be described by the joint probability density:

$$p(x_1, t_1; x_2, t_2; x_3, t_3; \dots). \quad (\text{A.6})$$

Based on this joint probability density one can also define conditional probability densities:

$$p(x_1, t_1; x_2, t_2; \dots | y_1, \tau_1, y_2, \tau_2, \dots) = \frac{p(x_1, t_1; x_2, t_2; \dots; y_1, \tau_1; y_2, \tau_2; \dots)}{p(y_1, \tau_1; y_2, \tau_2, \dots)}. \quad (\text{A.7})$$

By assuming a time ordering:

$$t_1 \geq t_2 \geq t_3 \geq \dots \geq \tau_1 \geq \tau_2 \geq \tau_3 \geq \dots, \quad (\text{A.8})$$

the conditional probability density can then be seen as a prediction of future values (x_1, x_2, \dots) at times (t_1, t_2, \dots) under the condition of past values (y_1, y_2, \dots) at times (τ_1, τ_2, \dots) .

The Markov assumption now indicates that the prediction of the future for all time steps t_k depends only on the condition of the most recent time step t_{k-1} . Mathematically, this can be expressed, assuming the time ordering of Eq. A.8, by changing the conditional probability in Eq. A.7 to:

$$p(x_1, t_1; x_2, t_2; \dots | y_1, \tau_1, y_2, t_2, \dots) = p(x_1, t_1; x_2, t_2; \dots | y_1, \tau_1). \quad (\text{A.9})$$

The Markov assumption applies for all time steps in the chain, moreover the conditional probabilities for different time steps are independent. For a Markov process and a time ordering:

$$t_1 \geq t_2 \geq t_3 \geq \dots \geq t_{n-1} \geq t_n \quad (\text{A.10})$$

the conditional joint probability density of the probabilistic system is defined by:

$$p(x_1, t_1; x_2, t_2; \dots; x_n, t_n) = p(x_1, t_1 | x_2, t_2) \cdot p(x_2, t_2 | x_3, t_3) \dots p(x_{n-1}, t_{n-1} | x_n, t_n) \cdot p(x_n, t_n). \quad (\text{A.11})$$

A.1.3 Itô stochastic differential equation

An heuristic definition of a stochastic differential equation can be done by considering two functions $a(x, t)$ and $b(x, t)$, and a stochastic component $\xi(t)$:

$$\frac{dx}{dt} = a(x, t) + b(x, t) \cdot \xi(t). \quad (\text{A.12})$$

$a(x, t)$ is the drift function of the SDE, representing the deterministic processes, and $b(x, t)$ is the dispersion matrix, that defines how the stochastic component $\xi(t)$ is embedded in the system. $\xi(t)$ is thereby assumed to be a zero mean Gaussian random variable and white noise, a commonly-used theoretical random process. The term "white" noise comes from the corresponding "white" light, that expresses a constant power spectral density over all frequencies. White noise is uncorrelated, meaning that $\xi(t)$ and $\xi(t')$ are independent if $t \neq t'$. A further property is that the sample path $t \mapsto \xi(t)$ is discontinuous almost everywhere. Considering the definition of white noise, it gets obvious that Eq. A.12 can not be treated as a differential equation in the traditional sense, as discontinuous functions are not allowed in ordinal differential equations, as uniqueness and existence of a solution would not be provable based on the Picard-Lindelöf theorem (see e.g., Särkkä and Solin, 2019).

The problem needs to be formulated in a different way. By expecting the differential equation A.12 to be integrable, one can formally integrate it from an initial time t_0 to t :

$$x(t) - x(t_0) = \int_{t_0}^t a(x, t') dt' + \int_{t_0}^t b(x, t') \xi(t') dt'. \quad (\text{A.13})$$

The first integral on the right-hand side can be simply solved by a Riemann integral. For the second integral one have to take a closer look at:

$$v(t) = \int_{t_0}^t \xi(t') dt'. \quad (\text{A.14})$$

Assuming that $v(t)$ exists and it is a continuous function of t due to integral properties, it can be shown that $v(t)$ is a Markov process. As shown in Gardiner (1994) and Särkkä and Solin (2019), a suitable process satisfying the presumed conditions for $v(t)$, so being continuous and a Markov process, is the Wiener process $W(t)$, which is also known as Brownian motion:

$$v(t) = \int_{t_0}^t \xi(t') dt' = W(t), \quad (\text{A.15})$$

so $dW(t) = \xi(t) dt$. The Wiener process is a continuous Gaussian stochastic process with the properties:

1. $\langle W(t) \rangle = w_0$
2. $\langle [W(t) - w_0]^2 \rangle = t - t_0$

with $\langle \cdot \rangle$ being the ensemble mean. Hence, the variance of $W(t)$ goes to infinity with $t \rightarrow \infty$, leading to very variable and non-reproducible sample paths although the mean of $W(t)$ is constant. For the integral it is important to define increments $\Delta W_k = W(t_{k+1}) - W(t_k)$, they consist of the following properties:

- (i) All increments ΔW_k are zero mean Gaussian random variables with variance $q \Delta t$ with $\Delta t = t_{k+1} - t_k$ and a diffusion constant q .

- (ii) Since the Wiener process is a Markov process, the increments ΔW_k are independent of each other for non-overlapping time spans. Moreover they are independent of $W(t_0)$.
- (iii) The process starts at $W(t_0) = 0$.

A further property of the Wiener process is that it is actually non-differentiable, but the white noise can be regarded as the weak derivative: $\xi(t) = dW(t)/dt$.

The same properties apply for the increments for each of the $i \in n$ of a multivariate Wiener process:

$$\mathbf{W}(t) = (W_1(t), W_2(t), \dots, W_n(t)), \quad (\text{A.16})$$

while the covariances of the increments are now $\mathbf{Q}\Delta t$, where \mathbf{Q} is the diffusion matrix of the Wiener process.

Still, because of the discontinuous derivative of $W(t)$, the second integral on the right-hand side in Eq. A.12 can not be solved by a Riemann-Stieltjes integral. The integral has to be solved as an *Itô stochastic integral*, defined by:

$$\int_{t_0}^t L(x, t) dW(t) = \lim_{n \rightarrow \infty} \left(\sum_{k=0}^n L(x(t_k), t_k) [W(t_{k+1}) - W(t_k)] \right), \quad (\text{A.17})$$

with $t_0 < t_1 < t_2 < \dots < t_n = t$. For the sake of completeness, another solution of the integral is the Stratonovich stochastic integral. However, it is not used in the CRWM and therefore not described here.

Now the integrals are solvable and Eq. A.13 can be rewritten by considering the second integral to be an Itô stochastic integral:

$$x(t) = x(t_0) + \int_{t_0}^t a(x, t') dt' + \int_{t_0}^t b(x, t') dW(t'). \quad (\text{A.18})$$

By assuming the differential limits to be very small, Eq. A.18 can be expressed by the *Itô stochastic differential equation* (SDE):

$$dx(t) = a[x(t), t] \cdot dt + b[x(t), t] \cdot dW(t). \quad (\text{A.19})$$

This SDE can be solved numerically by the *Euler-Maruyama method* with Δt and ΔW_k by:

$$x(t_{k+1}) = x(t_k) + a[x(t_k), t_k] \cdot \Delta t + b[x(t_k), t_k] \cdot \Delta W_k. \quad (\text{A.20})$$

A.2 Component equations in spherical coordinates

Eq. 4.10 would be sufficient for a planar migration, but since the migration occurs on a globe the velocity momentum equations need to be expanded into its scalar components (an analogue expansion of the velocity momentum equations of the wind speed can be found in [Holton and Hakim, 2013](#)). The Earth is assumed to be spherical, so the slight ellipsoidal deformation is neglected here. The momentum equations can then be defined in spherical coordinates with the Earth being a coordinate surface, so that the position is described by the longitude (λ), latitude (ϕ), and vertical distance above the surface of the Earth (z). The velocity is then described by the unit vectors \mathbf{i} , \mathbf{j} and \mathbf{k} that define the direction to the east, the north and upwards, respectively,

for a human moving on the surface of the Earth. With the velocity components:

$$u = r \cos \phi \cdot \frac{d\lambda}{dt}, \quad (\text{A.21})$$

$$v = r \cdot \frac{d\phi}{dt}, \quad (\text{A.22})$$

$$w = \frac{dz}{dt}, \quad (\text{A.23})$$

for $r = a + z$, and $a = 6371.000785$ km being the radius of the Earth, the velocity of the human becomes:

$$\mathbf{u} = u\mathbf{i} + v\mathbf{j} + w\mathbf{k}. \quad (\text{A.24})$$

Positional changes in \mathbf{k} direction are not taken into account in the CRWM, so $z = 0$ for all times t , and consequently $r = a$ and $w = 0$. To simplify calculations, x and y are introduced as the eastward and northward distance, calculated by $dx = a \cos \phi \cdot d\lambda$ and $dy = a \cdot d\phi$. The horizontal velocities can then be expressed by $u = dx/dt$ and $v = dy/dt$. The new coordinate system (x, y, z) is not stationary, the unit vectors \mathbf{i} , \mathbf{j} , \mathbf{k} change with the position of the human on the Earth. So when taking the timely total derivative of \mathbf{u} , this positional dependence must be taken into account:

$$\frac{d\mathbf{u}}{dt} = \frac{du}{dt}\mathbf{i} + \frac{dv}{dt}\mathbf{j} + u\frac{d\mathbf{i}}{dt} + v\frac{d\mathbf{j}}{dt}. \quad (\text{A.25})$$

To get the equations for each velocity component, the changes of the unit vectors have to be determined.

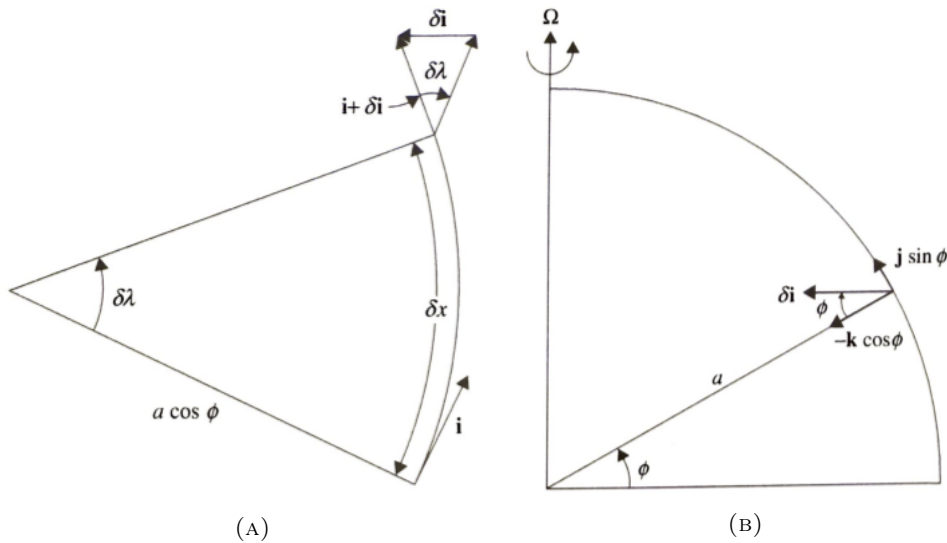


FIGURE A.2.1: (A) Change of the unit vector \mathbf{i} according to the longitude λ . (B) Division of $\delta \mathbf{i}$ into the northward and vertical components depending on the latitude ϕ . Both figures are from [Holton and Hakim \(2013\)](#).

As the eastward directed unit vector \mathbf{i} does not change its orientation if the motion is in y - or z -direction, the timely change only depends on the longitudinal components:

$$\frac{d\mathbf{i}}{dt} = u \frac{\partial \mathbf{i}}{\partial x}. \quad (\text{A.26})$$

On Fig. A.2.1a one can see that:

$$\tan \delta\lambda = \frac{\delta x}{a \cos \phi}, \quad \tan \delta\lambda = \frac{|\delta \mathbf{i}|}{|\mathbf{i}|} = |\delta \mathbf{i}|, \quad (\text{A.27})$$

from both equations, the magnitude of directional change can be estimated by:

$$\lim_{\delta x \rightarrow 0} \frac{|\delta \mathbf{i}|}{\delta x} = \left| \frac{\partial \mathbf{i}}{\partial x} \right| = \frac{1}{a \cos \phi}. \quad (\text{A.28})$$

As it is shown in Fig. A.2.1b, $\partial \mathbf{i} / \partial x$ is directed towards the axis of rotation of the Earth (Ω , shown for better orientation, the rotation of the Earth has no effect on human mobility) and can be expressed by:

$$\frac{\partial \mathbf{i}}{\partial x} = \frac{1}{a \cos \phi} (\sin \phi \mathbf{j} - \cos \phi \mathbf{k}). \quad (\text{A.29})$$

The derivative of \mathbf{i} therefore is:

$$\frac{d\mathbf{i}}{dt} = \frac{u}{a \cos \phi} (\sin \phi \mathbf{j} - \cos \phi \mathbf{k}). \quad (\text{A.30})$$

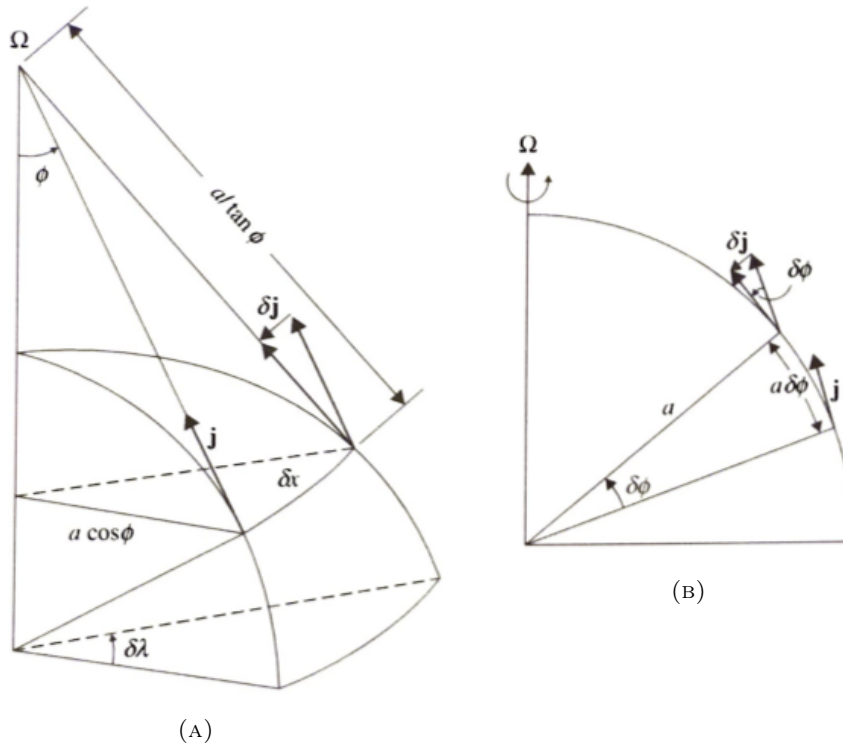


FIGURE A.2.2: (A) Longitudinal change of the unit vector \mathbf{j} . (B) Latitudinal change of unit vector \mathbf{j} . Both figures are from [Holton and Hakim \(2013\)](#).

The northward directed unit vector \mathbf{j} depends on the x - and y -directed motion:

$$\frac{d\mathbf{j}}{dt} = u \frac{\partial \mathbf{j}}{\partial x} + v \frac{\partial \mathbf{j}}{\partial y}. \quad (\text{A.31})$$

On Fig. A.2.2a is shown the change in direction of \mathbf{j} for changing x . The following equations directly follow from trigonometry:

$$\tan \delta\lambda = \frac{\delta x}{a/\tan \phi}, \quad \tan \delta\lambda = \frac{|\delta\mathbf{j}|}{|\mathbf{j}|} = |\delta\mathbf{j}|. \quad (\text{A.32})$$

From both equations and by noting that $\partial\mathbf{j}/\partial x$ is directed in negative x -direction, one gets:

$$\frac{\partial\mathbf{j}}{\partial x} = -\frac{\tan \phi}{a} \mathbf{i} \quad (\text{A.33})$$

In Fig. A.2.2b the change of \mathbf{j} for northward motion is illustrated. Shown is that:

$$\tan \delta\phi = \frac{a\delta\phi}{a} = \delta\phi, \quad \tan \delta\phi = \frac{|\delta\mathbf{j}|}{|\mathbf{j}|} = |\delta\mathbf{j}|, \quad (\text{A.34})$$

so $|\delta\mathbf{j}| = \delta\phi$. $\delta\mathbf{j}$ is directed downwards, so with $\delta y = a\delta\phi$:

$$\frac{\partial\mathbf{j}}{\partial y} = -\frac{\mathbf{k}}{a}. \quad (\text{A.35})$$

With both results together, the timely change of \mathbf{j} is defined by:

$$\frac{d\mathbf{j}}{dt} = -\frac{u \tan \phi}{a} \mathbf{i} - \frac{v}{a} \mathbf{k}. \quad (\text{A.36})$$

As mentioned above, all components in \mathbf{k} direction can be neglected, as no component is included in the CRWM and $w = 0$ for all time steps by default.

Inserting Eq. A.30 and A.36 in Eq. A.25 without the \mathbf{k} components gives the additional terms for the acceleration that come from the spherical coordinates:

$$\frac{d\mathbf{u}}{dt} = \left(\frac{du}{dt} - \frac{uv \tan \phi}{a} \right) \mathbf{i} + \left(\frac{Dv}{Dt} + \frac{u^2 \tan \phi}{a} \right) \mathbf{j}. \quad (\text{A.37})$$

With the gradient of Φ :

$$\nabla\Phi = \frac{\partial\Phi}{\partial x} \mathbf{i} + \frac{\partial\Phi}{\partial y} \mathbf{j}, \quad (\text{A.38})$$

the two-dimensional Wiener process:

$$\mathbf{W} = W_x \mathbf{i} + W_y \mathbf{j} \quad (\text{A.39})$$

and the new components inserted in Eq. 4.10, the final stochastic differential equations are:

$$du = \left[\frac{uv \tan \phi}{a} + \alpha \cdot \frac{\partial\Phi}{\partial x} - \gamma \cdot u \right] \cdot dt + \beta \cdot dW_x, \quad (\text{A.40})$$

$$dv = \left[-\frac{u^2 \tan \phi}{a} + \alpha \cdot \frac{\partial\Phi}{\partial y} - \gamma \cdot v \right] \cdot dt + \beta \cdot dW_y. \quad (\text{A.41})$$

The longitudinal and latitudinal positions are then calculated by:

$$d\lambda(t) = \frac{1}{a \cos \phi} \cdot u(t) \cdot dt, \quad (\text{A.42})$$

$$d\phi(t) = \frac{1}{a} \cdot v(t) \cdot dt. \quad (\text{A.43})$$

Appendix B

Impact of Heinrich Event 4 on human populations in Iberia

B.1 Climate maps

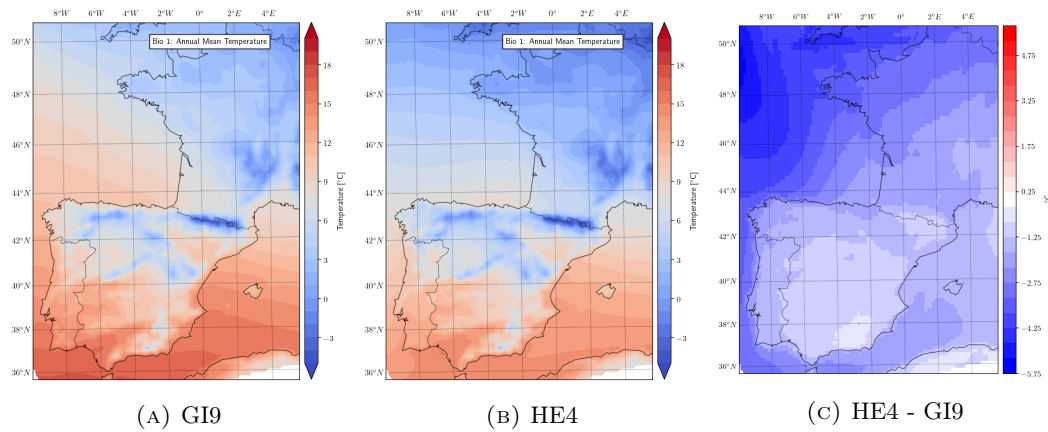


FIGURE B.1.1: Annual mean temperature (Bio1)

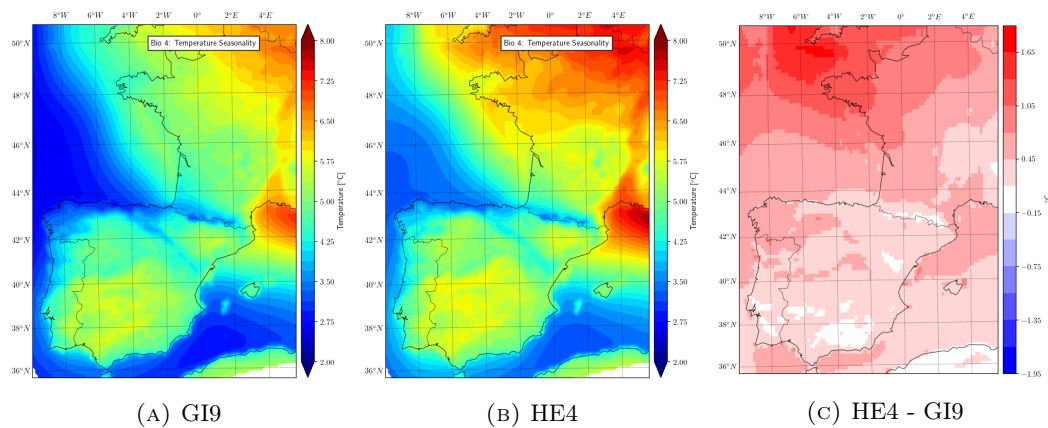


FIGURE B.1.2: Temperature seasonality (Bio4)

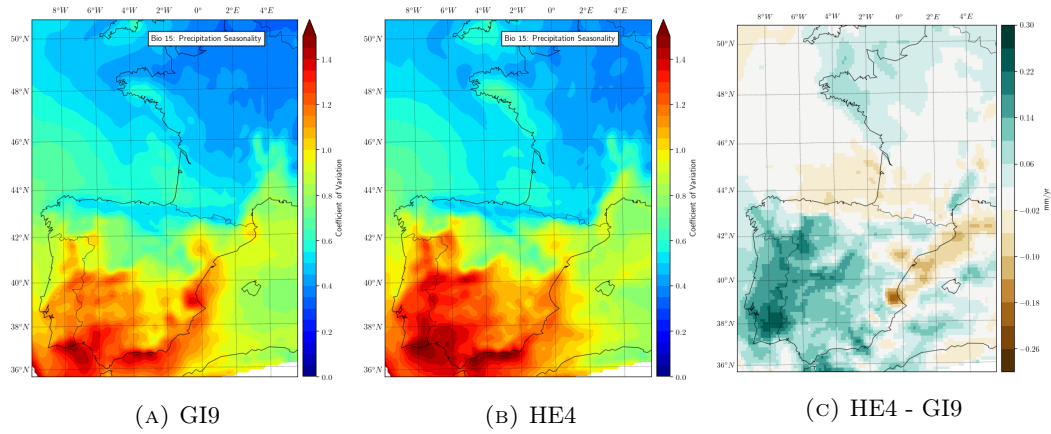


FIGURE B.1.3: Precipitation seasonality (Bio15)

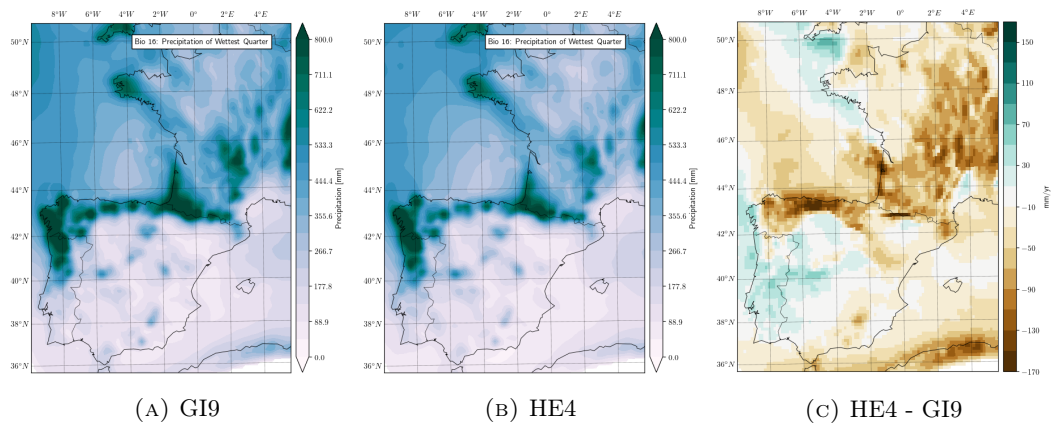


FIGURE B.1.4: Precipitation of wettest quarter (Bio16)

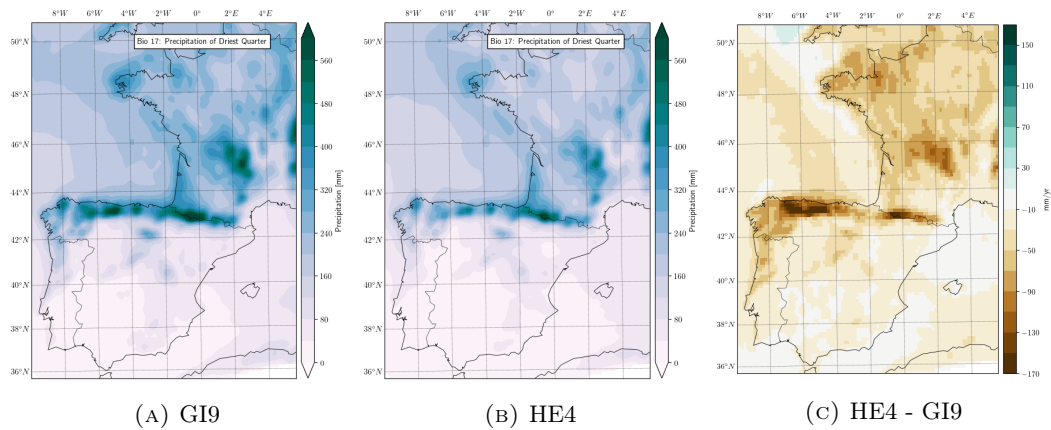


FIGURE B.1.5: Precipitation of driest quarter (Bio17)

B.2 HEP estimation

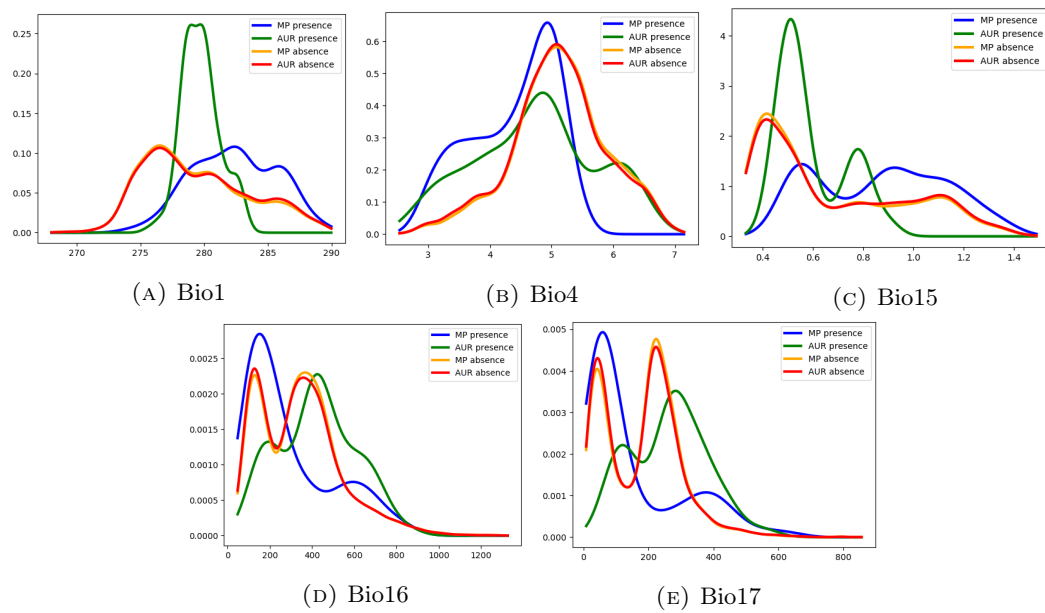


FIGURE B.2.1: Climatic conditions at the presence and absence points based on the sites distribution of the Aurignacian (AUR All) and Middle Paleolithic (MP) technocomplexes for the GI9 climate simulation. Human presence is considered in a radius of 20 km around each archaeological site, human absence everywhere else.

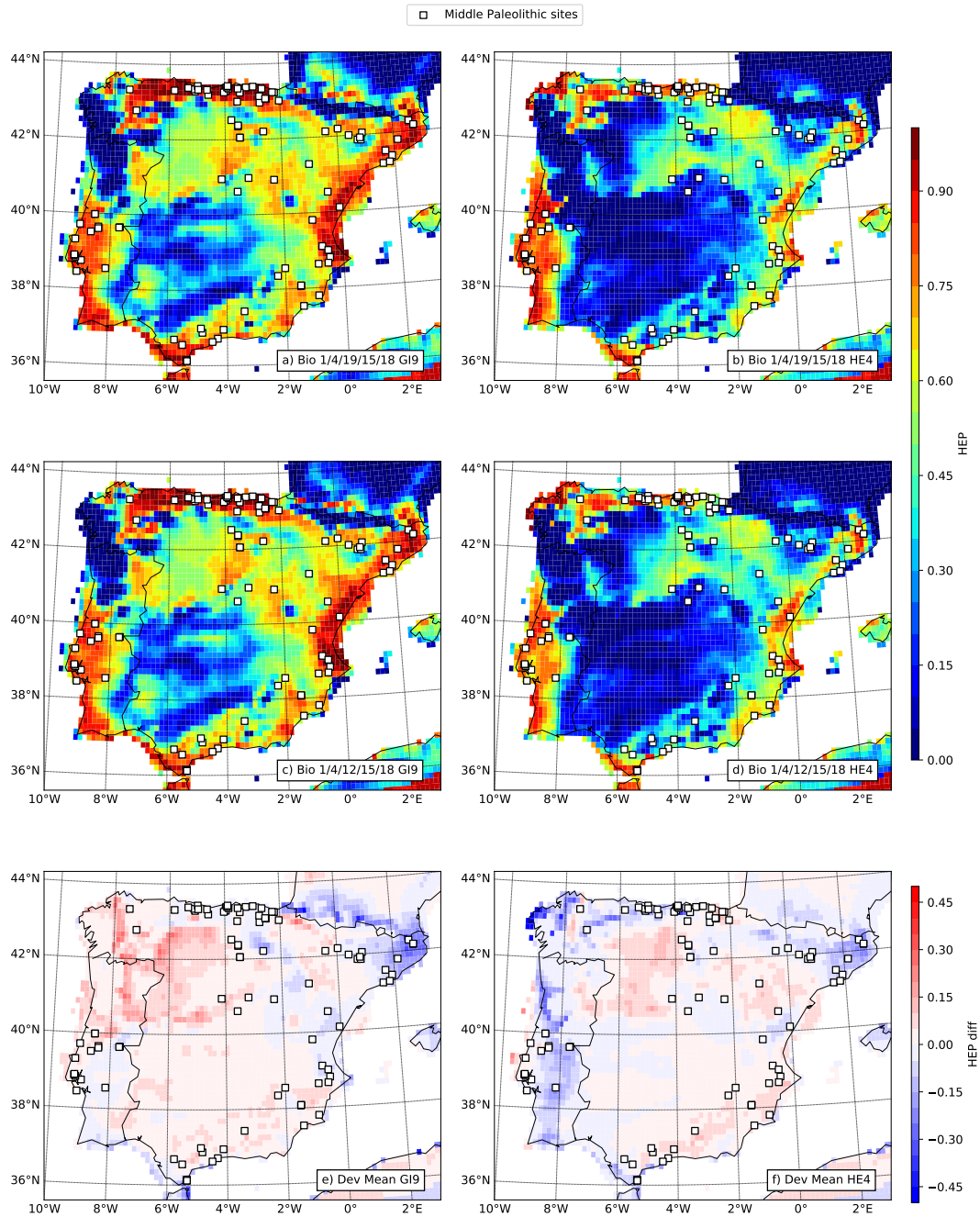


FIGURE B.2.2: MP HEP derived by the bioclimatic variables Bio 1/4/19/15/18 (a) and (b) and Bio 1/4/12/15/18 (c) and (d) for GI9 (a) and (c) and HE4 (b) and (d) estimated by the GI9 bioclimatic variables. Deviation the HEP Bio 1/4/16/15/17 (Fig. 1) from the mean of the three runs for GI9 (e) and HE4 (f).

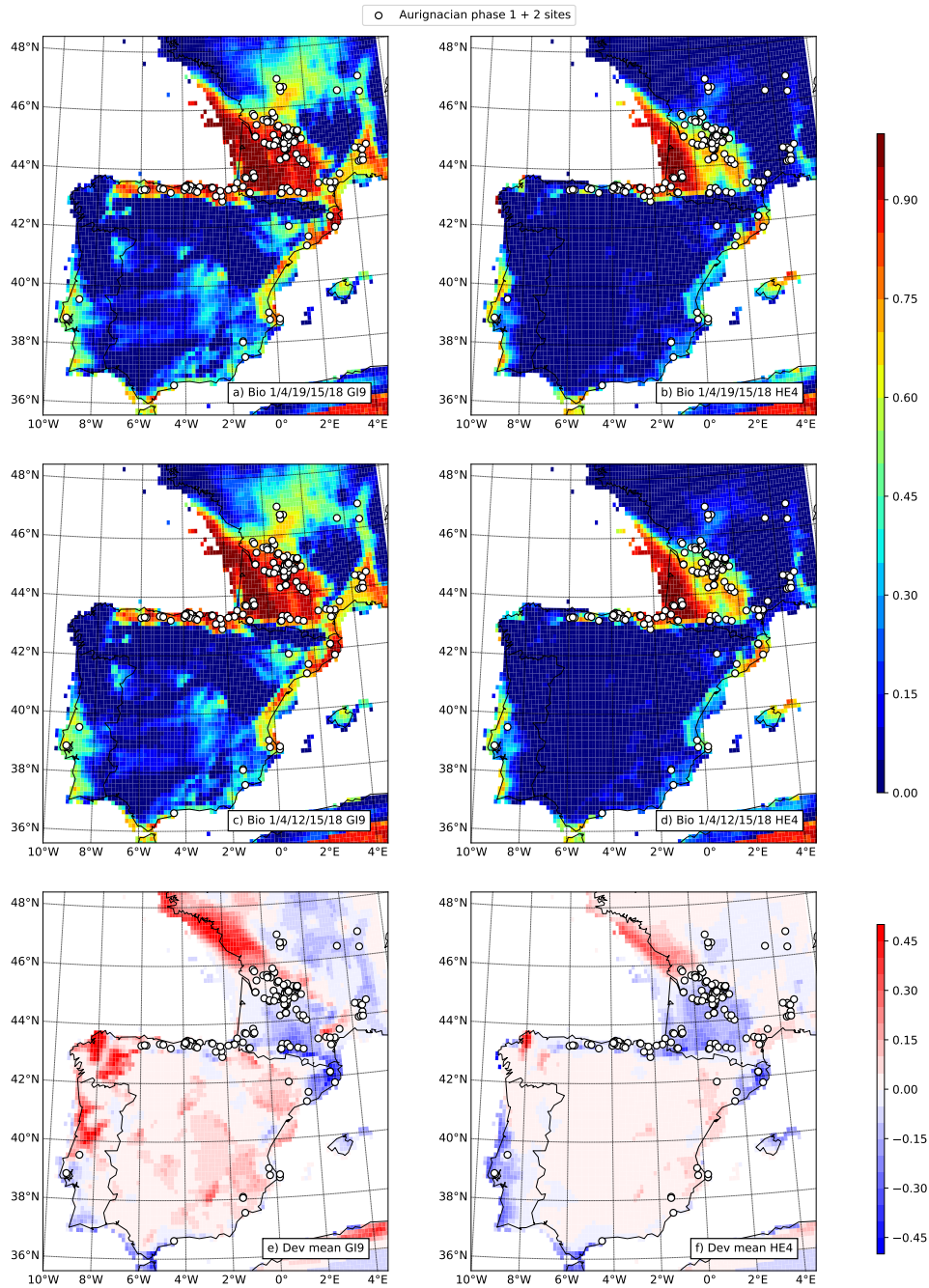


FIGURE B.2.3: Aur HEP derived by the bioclimatic variables Bio 1/4/19/15/18 (a) and (b) and Bio 1/4/12/15/18 (c) and (d) for GI9 (a) and (c) and HE4 (b) and (d) estimated by the GI9 bioclimatic variables. Deviation the HEP Bio 1/4/16/15/17 (Fig. 1) from the mean of the three runs for GI9 (e) and HE4 (f).

B.3 CRWM Iberia

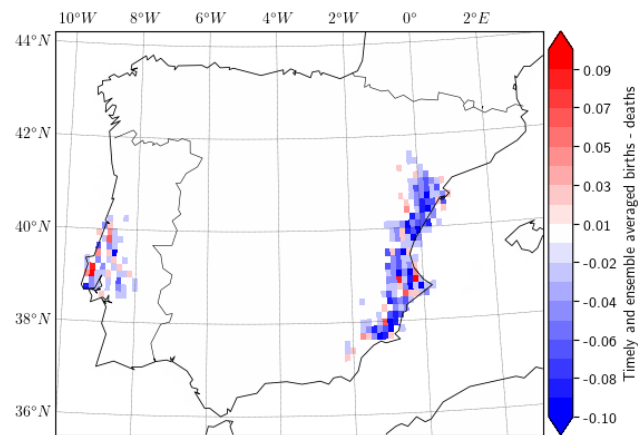


FIGURE B.3.1: Same as in Fig. 6.18b but calculated from 25k - 30k years.